UNIVERSITY OF CRETE

SCHOOL OF SCIENCES AND ENGINEERING

DEPARTMENT OF MATERIALS SCIENCE AND TECHNOLOGY

2D/2D LAYERED NANO-HETEROSTRUCTURES OF TRANSITION METAL DICHALCOGENIDES (MS_2, M = Mo, Sn) AND GRAPHITIC CARBON NITRIDE (g-C_3N_4) FOR PHOTOCATALYTIC HYDROGEN PRODUCTION AND ENVIRONMENTAL REMEDIATION

Ph.D. THESIS

EIRINI KOUTSOUROUBI

MATERIALS SCIENTIST

Supervisor: **Gerasimos S. Armatas**

HERAKLION 2021

ΠΑΝΕΠΙΣΤΗΜΙΟ ΚΡΗΤΗΣ
ΣΧΟΛΗ ΘΕΤΙΚΩΝ ΚΑΙ ΤΕΧΝΟΛΟΓΙΚΩΝ ΕΠΙΣΤΗΜΩΝ
ΤΜΗΜΑ ΕΠΙΣΤΗΜΗΣ ΚΑΙ ΤΕΧΝΟΛΟΓΙΑΣ ΥΛΙΚΩΝ

2D/2D ΦΥΛΛΟΜΟΡΦΕΣ ΝΑΝΟ-ΕΤΕΡΟΔΟΜΕΣ ΔΙΧΑΛΚΟΓΟΝΙΔΙΩΝ ΜΕΤΑΛΛΩΝ ΜΕΤΑΠΤΩΣΗΣ (MS_2, M = Mo, Sn) ΚΑΙ ΓΡΑΦΙΤΙΚΟ ΝΙΤΡΙΔΙΟ ΤΟΥ ΑΝΘΡΑΚΑ (g-C_3N_4) ΓΙΑ ΦΩΤΟΚΑΤΑΛΥΤΙΚΗ ΠΑΡΑΓΩΓΗ ΥΔΡΟΓΟΝΟΥ ΚΑΙ ΠΕΡΙΒΑΛΛΟΝΤΙΚΗ ΑΠΟΚΑΤΑΣΤΑΣΗ

ΔΙΔΑΚΤΟΡΙΚΗ ΔΙΑΤΡΙΒΗ

ΕΙΡΗΝΗ ΚΟΥΤΣΟΥΡΟΥΜΠΗ
ΕΠΙΣΤΗΜΩΝ ΥΛΙΚΩΝ

Επιβλέπων καθηγητής: **Γεράσιμος Αρματάς**

ΗΡΑΚΛΕΙΟ 2021

Doctoral Committee

Gerasimos S. Armatas (Supervisor)

Associate Professor, Dept. of Materials Science and Technology, University of Crete

George Kioseoglou

Associate Professor, Dept. of Materials Science and Technology, University of Crete

Ioannis Remediakis

Associate Professor, Dept. of Materials Science and Technology, University of Crete

Kelly Velonia

Assistant Professor, Dept. of Materials Science and Technology, University of Crete

George Kopidakis

Associate Professor, Dept. of Materials Science and Technology, University of Crete

Constantinos Stoumpos

Associate Professor, Dept. of Materials Science and Technology, University of Crete

Constantinos J. Milios

Professor, Dept. of Chemistry, University of Crete

To my loving parents, Dimitris and Argiro-Eirini

ACKNOWLEDGMENTS

First of all, I would like to express my unlimited gratitude to my supervisor Prof. Gerasimos Armatas for showing me trust from the very first time, his support, encouragement and insightful guidance through these years. He truly is a mentor and it was an honor for me to work with him and learn from him.

I would deeply like to thank Prof. George Kioseoglou, Prof. Ioannis Remediakis, Prof. Kelly Velonia, Prof. George Kopidakis, Prof. Constantinos Stoumpos and Prof. Constantinos Milios for accepting to be members of my doctoral committee and for their insightful evaluation.

My sincere thanks to Dr. Ioannis Papadas for the electrochemical measurements, Prof. Stella Kennou for X-ray photoelectron spectroscopy (XPS) measurements and Prof. George Kopidakis for theoretical (DFT) calculations.

Furthermore, I would like to thank the Department of Materials Science and Technology, University of Crete for providing me with the necessary infrastructure to accomplish the present thesis.

Moreover, I would like to thank former and present members of ChemMater Lab that contributed in different ways throughout these years. From the bottom of my heart, I would like to thank my friend and colleague Dr. Ioannis Vamvasakis for his precious advices and insight, and Dr. Euaggelia Skliri who, truly, is a sister for me, and always is by my side in every way. Also, special thanks to Dr. Alexandra Xylouri, Dr. Ioannis Papadas, Dr. Alexia Agiomyrgianaki, Dr. Georgia Velegraki, Evangelos Andreou, Chrysanthi Patriarchea and Sofia Bra. All these people made the laboratory feels like home. I would also like to express my deep love for my beloved friend, Dr. Ioannis Tamiolakis, who is no longer with us, but he will always be in our hearts.

I am also grateful to my friends Manos Fitsakis, Stelios Steiakakis and Fotini Kakaroni, who have always given me their generous love and support.

Last, but not least, I would like to thank my loving parents, Dimitris and Argiro-Eirini and my brother Giorgos for their love, encouragement and endless support during all these years, and also my heartwarming thanks to my future husband Pavlos, who is always there and caring for me. I will always do my best to make them proud.

FUNDING

We gratefully acknowledge financial support from the Hellenic Foundation for Research and Innovation (H.F.R.I.) under the "1st Call for H.F.R.I. Research Projects to support Faculty Members & Researchers and the Procurement of High-cost research equipment grant" (project number: 400). The present research work was also financially supported with the scholarship from I.P.T.O. (Independent Power Transmission Operator) - Α.Δ.Μ.Η.Ε. (Ανεξάρτητος Διαχειριστής Μεταφοράς Ηλεκτρικής Ενέργειας).

SUMMARY

Highly efficient and cost-effective photocatalysts are among the most prominent targets in the field of clean energy production and environmental remediation. The understanding of photochemical charge transfer mechanisms at the nanoscale is essential to develop effective catalysts for energy conversion and environmental remediation applications. Photocatalytic hydrogen generation through water splitting is regarded as a promising solution to future energy demands. This approach utilizes a semiconductor-based catalyst that absorbs sunlight and splits water, producing hydrogen. Alongside, water pollution is on top of the most permeative threats worldwide, risking human health and quality life. This is because voluminous amounts of toxic metals, such as hexavalent chromium, Cr(VI), are released directly or incidentally to the environment. Therefore, finding an effective way for remediation of Cr(VI)-contaminated solutions is undoubted of high priority in the field of environmental and health protection.

In this dissertation, new and cost-effective synthetic strategies for preparing 2D/2D layered nano-heterostructures of transition metal dichalcogenides (MS_2, M = Mo, Sn) and graphitic carbon nitride (g-C_3N_4) have been successfully developed and the resulting materials have been tested against photocatalytic production of hydrogen and reduction of toxic Cr(VI). A controllable synthesis method and a combination of electron microscopy, optical absorption, photoluminescence, and electrochemical impedance spectroscopic studies have been utilized to investigate the effect of MoS_2 nanosheet lateral dimension and edge length size on the photochemical behavior of MoS_2-modified g-C_3N_4 heterojunctions. These nano-heterostructures, which comprise interlayer junctions with variable area, i.e., MoS_2 lateral size ranges from 18 nm to 52 nm, provide a size-tunable interfacial charge transfer through the MoS_2/g-C_3N_4 contacts, while exposing a large fraction of surface MoS_2 edge sites available for the hydrogen evolution reaction. Importantly, modification of g-C_3N_4 with MoS_2 layers of 39±5 nm lateral size (20 wt % loading) creates interfacial contacts with relatively large number of MoS_2 edge sites and efficient electronic transport phenomena, yielding a high photocatalytic H_2-production activity of 1497 μmol h^{-1} g_{cat}^{-1} and an apparent QY of 3.3 % at 410 nm light irradiation. This study offers a design strategy to improve light energy conversion efficiency of catalysts by engineering interfaces at the nanoscale in 2D-layered heterojunction materials.

By modifying the above MoS_2 layers with nickel, a novel series of 2D/2D layer heterostructures composed of exfoliated Ni-doped MoS_2 nanosheets and g-C_3N_4 layers have been prepared. These hybrid materials can carry out photocatalytic Cr(VI) reduction in aqueous solutions with outstanding activity, exhibiting apparent QYs as high as 29.6 % and 23.7 % at 375 and 410 nm. Ni doping of MoS_2 markedly increases the photochemical activity, which, together with electrochemical spectroscopy and theoretical DFT studies, arises from the enhanced carrier density and mobility at the Ni-MoS_2/g-C_3N_4 interface. In addition to the favorable charge transport properties, delineation of the photoinduced oxidation reactions by control catalytic experiments and gas monitoring techniques reveals that the high efficiency also arises from fast water oxidation kinetics. Due to the efficient dissociation and transport of free excitons, surface-reaching holes effectively oxidize water to form molecular oxygen. The results of this work mark an important step forward in understanding and designing low-cost and earth-abundant catalysts for detoxification of Cr(VI)-contaminated industrial effluents.

Additional subject of the present research work is the synthesis of 2D/2D SnS_2/g-C_3N_4 layered heterostructures with reduced interfacial resistance and improved charge transfer kinetics. The realization of these materials was accomplished by using a photochemical deposition method. These newly developed catalysts, which consist of exfoliated g-C_3N_4 flakes and SnS_2 nanosheets (~25–30 nm in lateral diameter), demonstrate outstanding photocatalytic Cr(VI) reduction (with a 21.2 μmol h^{-1} conversion rate) and water oxidation (with a 15.1 μmol h^{-1} O_2 evolution rate) activity. The SnS_2/g-C_3N_4 heterostructures reach energy conversion efficiencies of up to 16.4% and 12.1% at 375 nm and 410 nm, respectively, that is among the best known Cr(VI) reduction catalysts reported to date. Based on X-ray photoelectron, UV–vis optical absorption, and electrochemical and photoelectrochemical measurements, we provide detailed mechanistic insight into the photochemical redox reactions and charge transport dynamics in this catalytic system. The results demonstrate the great potential of the SnS_2-decorated g-C_3N_4 nano-heterostructures as viable photocatalysts for environmental protection, including remediation of Cr(VI)-contaminated industrial effluents.

ΠΕΡΙΛΗΨΗ

Οι εξαιρετικά αποδοτικοί και οικονομικοί φωτοκαταλύτες είναι από τους πιο σημαντικούς στόχους στον τομέα της παραγωγής καθαρής ενέργειας και της περιβαλλοντικής αποκατάστασης. Η κατανόηση των μηχανισμών μεταφοράς φορτίου στη νανοκλίμακα είναι αναγκαία για την ανάπτυξη αποτελεσματικών καταλυτών για μετατροπή ενέργειας και εφαρμογές περιβαλλοντικής αποκατάστασης. Η φωτοκαταλυτική παραγωγή υδρογόνου μέσω διάσπασης νερού θεωρείται ως μια πολλά υποσχόμενη λύση για μελλοντικές ενεργειακές ανάγκες. Η προσέγγιση αυτή χρησιμοποιεί έναν ημιαγώγιμο καταλύτη που απορροφά ηλιακό φως και διασπά το νερό, παράγοντας υδρογόνο. Παράλληλα, η ρύπανση των υδάτων βρίσκεται στην κορυφή των σημαντικότερων απειλών παγκοσμίως, θέτοντας σε κίνδυνο την ανθρώπινη υγεία και την ποιότητα ζωής. Αυτό οφείλεται στο γεγονός ότι μεγάλες ποσότητες τοξικών μετάλλων, όπως το εξασθενές χρώμιο, Cr(VI), απελευθερώνονται άμεσα ή τυχαία στο περιβάλλον. Ως εκ τούτου, η εύρεση ενός αποτελεσματικού τρόπου για την αποκατάσταση των μολυσμένων υδάτων με Cr(VI) είναι αναμφίβολα υψηλής προτεραιότητας στον τομέα της προστασίας του περιβάλλοντος και της υγείας.

Στην παρούσα διδακτορική διατριβή έχουν αναπτυχθεί επιτυχώς νέες και οικονομικά αποδοτικές συνθετικές στρατηγικές για την παρασκευή 2D/2D φυλλόμορφων νανο-ετεροδομών από διχαλκογονίδια μετάλλων μετάπτωσης (MS_2, M = Mo, Sn) και γραφιτικό νιτρίδιο του άνθρακα (g-C_3N_4) και τα προκύπτοντα υλικά έχουν δοκιμαστεί ως καταλύτες στη φωτοκαταλυτική παραγωγή υδρογόνου και στην αναγωγή του τοξικού Cr(VI). Μια ελεγχόμενη μέθοδος σύνθεσης και ένας συνδυασμός ηλεκτρονικής μικροσκοπίας, οπτικής απορρόφησης, φωτοφωταύγειας και ηλεκτροχημικής φασματοσκοπίας εμπέδησης έχουν χρησιμοποιηθεί για τη διερεύνηση της επίδρασης της πλευρικής διάστασης καθώς και του μεγέθους του μήκους των ακμών των νανοφύλλων MoS_2 στη φωτοχημική συμπεριφορά των ετεροδομών MoS_2/g-C_3N_4. Αυτές οι νανο-ετεροδομές, οι οποίες περιλαμβάνουν διαστρωματικές επαφές με μεταβλητή επιφάνεια, όπου το πλευρικό μέγεθος MoS_2 κυμαίνεται από 18 nm έως 52 nm, παρέχουν μια ρυθμιζόμενη ως προς το μέγεθος διεπιφανειακή μεταφορά φορτίου μέσω των επαφών MoS_2/g-C_3N_4, ενώ εκθέτουν ένα μεγάλο αριθμό θέσεων ακμής MoS_2 που είναι διαθέσιμες για την αντίδραση παραγωγής υδρογόνου. Σημαντικά, η τροποποίηση του g-C_3N_4 με φύλλα MoS_2 μεγέθους 39±5 nm (20 wt% περιεκτικότητα) δημιουργεί διεπαφές με σχετικά μεγάλο αριθμό καταλυτικών κέντρων

MoS_2 και αποτελεσματικά φαινόμενα μεταφοράς ηλεκτρονίου, αποδίδοντας μια υψηλή φωτοκαταλυτική δραστικότητα παραγωγής H_2 1497 μmol h^{-1} g_{cat}^{-1} και μια βελτιωμένη κβαντική απόδοση 3.3% σε ακτινοβολία φωτός 410 nm. Η μελέτη αυτή προσφέρει μια στρατηγική σχεδιασμού για τη βελτίωση της απόδοσης μετατροπής ηλιακής ενέργειας σε των καταλυτών μέσω μηχανικών διεπαφών στη νανοκλίμακα σε 2D φυλλόμορφες ετεροδομές.

Τροποποιώντας τα παραπάνω στρώματα MoS_2 με νικέλιο, έχει παρασκευαστεί μια νέα σειρά 2D/2D φυλλόμορφων ετεροδομών που αποτελούνται από αποφλοιωμένα νανοφύλλα MoS_2 ντοπαρισμένα με νικέλιο και στρώματα g-C_3N_4. Αυτά τα υβριδικά υλικά εμφανίζουν εξαιρετική φωτοκαταλυτική δράση στην αναγωγή του Cr(VI) σε υδατικά διαλύματα, εμφανίζοντας κβαντικές αποδόσεις 29.6% και 23.7% στα 375 και 410 nm, αντίστοιχα. Η πρόσμιξη Ni στο MoS_2 αυξάνει αισθητά τη φωτοχημική δραστικότητα, η οποία, σε συνδυασμό με ηλεκτροχημικές, φασματοσκοπικές και θεωρητικές μελέτες DFT, προκύπτει από την αυξημένη πυκνότητα και κινητικότητα των φορέων φορτίου στη διεπαφή Ni-MoS_2/g-C_3N_4. Εκτός από τις ευνοϊκές ιδιότητες μεταφοράς φορτίου, η διερεύνηση των φωτοεπαγόμενων αντιδράσεων οξείδωσης με ελεγχόμενα καταλυτικά πειράματα και τεχνικές ανίχνευσης αερίων επιβεβαιώνει ότι η υψηλή απόδοση προκύπτει επίσης από τη γρήγορη κινητική οξείδωσης του νερού. Λόγω της αποτελεσματικής διάσπασης και μεταφοράς των ελεύθερων εξιτονίων, οι οπές που φτάνουν στην επιφάνεια του καταλύτη οξειδώνουν αποτελεσματικά το νερό για να σχηματίσουν μοριακού οξυγόνου. Τα αποτελέσματα αυτής της εργασίας σηματοδοτούν ένα σημαντικό βήμα για την κατανόηση και το σχεδιασμό καταλυτών χαμηλού κόστους για την απορρύπανση βιομηχανικών λυμάτων μολυσμένων με Cr(VI).

Επιπλέον αντικείμενο μελέτης της παρούσας ερευνητικής εργασίας είναι η σύνθεση 2D/2D SnS_2/g-C_3N_4 φυλλόμορφων ετεροδομών με μειωμένη αντίσταση διεπαφής και βελτιωμένη κινητική μεταφοράς φορτίου. Η ανάπτυξη αυτών των υλικών επιτεύχθηκε με τη χρήση μεθόδου φωτοχημικής εναπόθεσης. Οι καινοτόμοι αυτοί καταλύτες, οι οποίοι αποτελούνται από αποφλοιωμένο g-C_3N_4 και νανοστρώματα SnS_2 (~25–30 nm σε διάμετρο), επιδεικνύουν εξαιρετική φωτοκαταλυτική δραστικότητα αναγωγής Cr(VI) (με ρυθμό μετατροπής 21.2 μmol h^{-1}) και οξείδωσης νερού (με ρυθμό παραγωγής O_2 15.1 μmol h^{-1}). Οι ετεροδομές SnS_2/g-C_3N_4 επιτυγχάνουν αποδόσεις μετατροπής ενέργειας έως και 16.4% και 12.1% στα 375 και 410 nm, αντίστοιχα, που

είναι μεταξύ των αποδοτικότερων καταλυτών αναγωγής Cr(VI) που έχουν αναφερθεί μέχρι σήμερα στη βιβλιογραφία. Με βάση τη φασματοσκοπία φωτοηλεκτρονίων ακτίνων-Χ, την οπτική απορρόφηση UV-vis και τις ηλεκτροχημικές και φωτοηλεκτροχημικές μετρήσεις, παρέχουμε λεπτομερή μηχανιστική εικόνα των φωτοχημικών αντιδράσεων οξειδοαναγωγής και της δυναμικής μεταφοράς φορτίου στο παρόν καταλυτικό σύστημα. Τα αποτελέσματα καταδεικνύουν την εξαιρετική δυνατότητα εφαρμογής των νανο-ετεροδομών SnS_2/g-C_3N_4 ως βιώσιμοι φωτοκαταλύτες στη προστασία του περιβάλλοντος, συμπεριλαμβανομένης της αποκατάστασης των βιομηχανικών αποβλήτων που περιέχουν Cr(VI).

TABLE OF CONTENTS

Chapter 1 - Introduction

1.1 2D materials

There is a wide assortment of materials that show layered structures and loan themselves exceptionally well to being mechanically cleaved along the layers.[1] By continuous cleaving of the stacked layers, one can promptly thin them down to a single layer[2], which comes about within the realization of new properties completely diverse from the bulk counterpart. The most highly studied 2D material is graphene because of its exceptional electronic, optoelectronic, electrochemical and biomedical applications. Graphene is a basic building component for graphitic materials and is a flat monolayer of carbon atoms firmly packed into a two-dimensional (2D) honeycomb lattice (**Figure 1**).[3] Novoselov and Geim's (re)discovery of single-layer graphene in 2004 demonstrated not only that stable and single-atom or single-polyhedral thick 2D materials can be exfoliated from van der Waals solids, but that these materials can also exhibit unique and fascinating physical features. It was not until 2004 that physicists were able to first isolate individual graphene planes using just a simple adhesive tape to obtain flakes that exhibited unique electronic characteristics. Discovery of monolayer graphene and its impressive properties has led to open a novel group of materials known as "2D materials".[4] The last 15 years have also shown us that these materials are too astonishingly interesting for electronic and optoelectronic applications.[5]

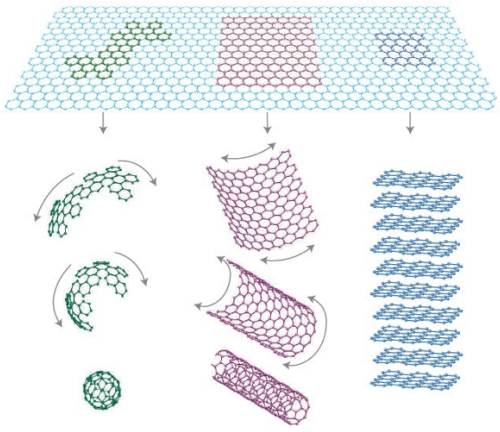

Figure 1. Origin of all graphitic forms. Graphene can be wrapped up into 0D buckyballs, twirled into 1D nanotubes or piled into 3D graphite. Graphene (top) and related structures: fullerene (bottom left); carbon nanotubes (bottom centre); and graphite (bottom right). (Copyright © 2007, Nature Publishing Group).

Inspired by the success invention of graphene, alternative layered materials have been discovered being the center of attention due to their unique physical and chemical properties. Some of the as-discovered materials are transition metal-dichalcogenides (TMDs, e.g., MoS_2), carbon nitrides (a class of polymeric materials consisting mainly of carbon and nitrogen), hexagonal boron-nitride (h-BN), which was theoretically predicted to induce a bandgap in graphene when graphene was deposited onto it[6], and layered metal oxides (**Figure 2**).[7] There are also 2D tungsten diselenide (WSe_2), tungsten disulphide (WS_2), molybdenum diselenide ($MoSe_2$) and tin disulfide (SnS_2), which are chemically, structurally and electronically similar to MoS_2.

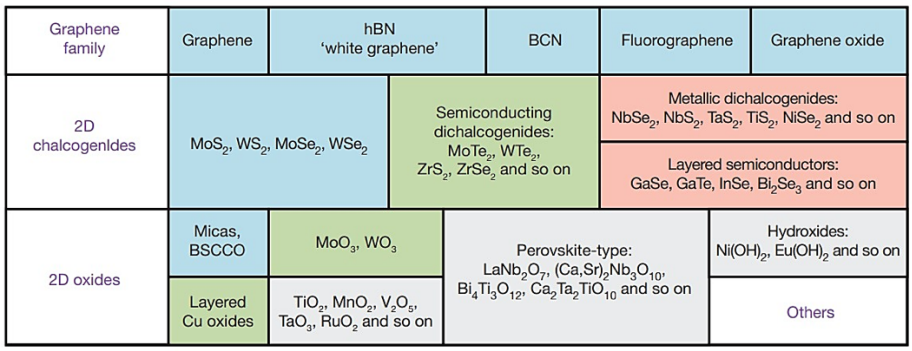

Figure 2. Current 2D materials family (blue shade: monolayers that are stable in ambient conditions (room temperature in air), green shade: monolayers that are stable in air but may only be stable in inert atmosphere are shaded pink, gray shade: monolayers that have been exfoliated, with no more information). (Copyright © 2013, Nature Publishing Group, a division of Macmillan Publishers Limited. All Rights Reserved).

Due to the special properties, 2D nanostructures are expected to have an important implication to a diverse set of applications, extending from catalysis and electronics to gas separation and storage and high-performance biological sensors. There are numerous layered materials with solid in-plane chemical bonds and frail coupling between layers. These layered structures give the opportunity to be cleaved into characteristic single atomic layers. When the thickness of the layered material is decreased to single or few layers, some extraordinary varieties happen in their electronic structure. The layers with one dimension strictly restricted to a single layer are called two-dimensional (2D) materials. The density of states for 2D materials exhibits a quasi-continuous step-like increase with increasing excitation energy.[8] These changes in the density of states for exciting electrons changes the way that the excitation energy interacts with the valence electrons - in a way similar that the principal

properties of quantum restricted nanomaterials are changed with size and shape of particles. Thus, band-gap engineering can be carried out by changing the number of layers in a given material.[9] Current materials research includes fabrication of 2D materials, determining an important field because of the physicochemical characteristics that are way different from the bulk analogue. Primarily, such materials with distinct architectures show exclusive shape-dependent features and successful application in nanoelectronic devices.[10] Other interesting features of 2D materials is not only for basic understating of growth mechanism, but also for developing contemporary applications in photocatalysis, chemical sensors and nanoreactors - properties that are so unique to outshine the inevitable inconveniences of transitioning to a new technology.

1.2 2D transition-metal dichalcogenide materials

Two-dimensional (2D) transition-metal dichalcogenide materials (TMDs), a group of graphene-like nanosheets with single-layer or few-layer structure, have lately emerged as a newsworthy area of physical science and engineering, facing fundamental scientific and technological challenges. TMDs are a subdivision of the layered materials family, where the inter-layer bonding consists of Van den Waals forces, while the intra-layer forces are covalent-bonded. Highly anisotropic properties are escorted by this kind of bond structure, where in-plane electrical, thermal and mechanical effects outstandingly exceed the out-plane properties.[11] Compared with the relatively simple composition and structure of graphene, 2D TMD materials exhibit rich structural and compositional varieties.[12] The general chemical formula of TMDs is MX_2 (**Figure 3**)[13] where M is a transition metal, i.e., Mo, W, Nb or Ta and X can be S, Se or Te.

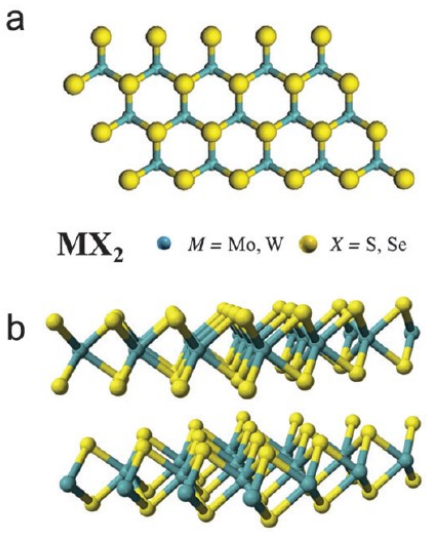

Figure 3. Schematic representation of the lattice structure of bulk and monolayer TMDs. (a) Monolayer TMD crystal from the top. (b) MX_2 bulk and even-layer structure schematic representation (Adapted from ref. [13] with permission from Royal Society of Chemistry).

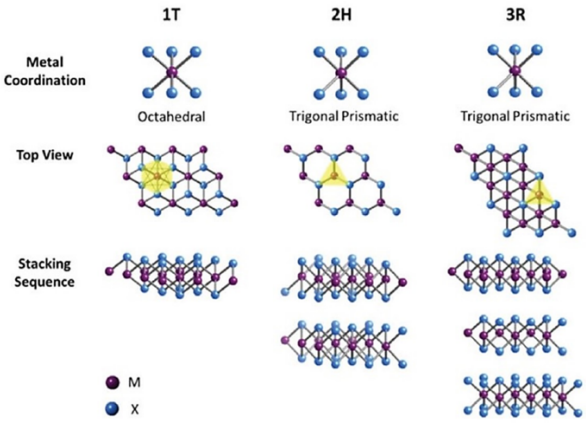

Figure 4. TMD structural unit cell metal coordinations and stacking sequences. Octahedral or trigonal prismatic metal coordination is possible. The octahedral coordination permits sequences to be stacked, resulting in tetragonal symmetry (1T). Different symmetries can result from different stacking sequences of trigonal prismatic single layers: hexagonal symmetry (2H) and rhombohedral symmetry (3R) (Reproduced from ref. [14]).

TMD materials show various polymorphs in crystalline structures, including 1H or 1T for monolayer and 1T (octahedral), 2H (trigonal prismatic) or 3R (trigonal prismatic) for a few layer structures (**Figure 4**).[14] The 2H phase corresponds to a stacking in which chalcogen atoms in different atomic planes occupy the same position and are located on top of each other in the direction perpendicular to the layer. By contrast, the 1T phase is characterized by a different stacking order. Depending on the

particular combination of transition metal (group IV, V, VI, VII, IX or X) and chalcogen (S, Se or Te) elements, the thermodynamically stable phase is either the 2H or 1T phase. A characteristic example is shown in **Figure 5**, where the "periodic table" displays that for five of six possible chemically distinct TMDs formed by a group VI transition metal (Mo or W) and a chalcogen (S, Se or Te), the 2H phase is thermodynamically stable and the 1T phase can be obtained as a metastable phase. An exception is represented by WTe_2, for which the stable bulk phase at room temperature is the orthorhombic $1T_d$ phase.[15] Unlike graphene, which is a semi-metal material with no band gap structure[16], 2D TMD materials, such as MoS_2, $MoSe_2$, WS_2 and WSe_2, have a band gap with a size comparable to that observed in ordinary group IV, II-VI and III-V semiconductors.[17]

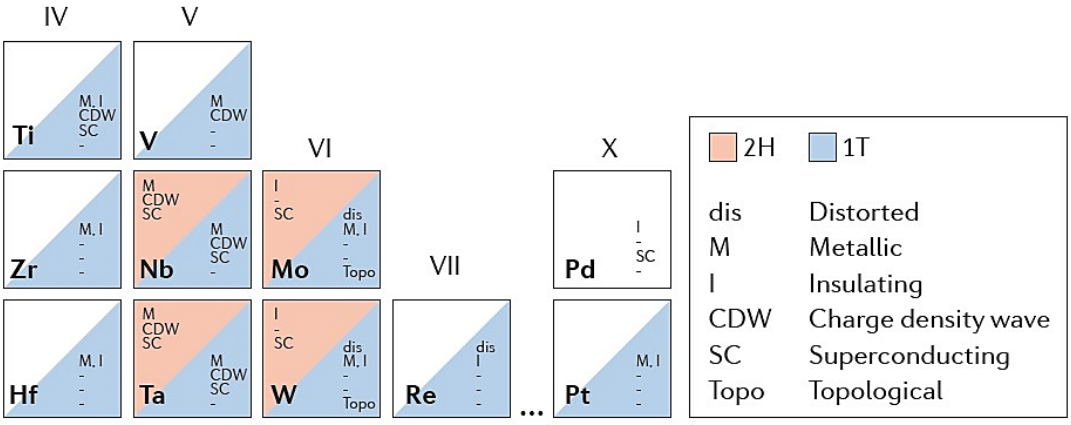

Figure 5. "Periodic table" of known layered TMDs, organized based on the transition metal element involved, summarizes the existing structural phases (2H, 1T or other) and indicates the presence of distorted structural phases (Copyright © 2017, Macmillan Publishers Limited).

1.3 Layered van der Waals solids

The most common class of crystalline structures that can be exfoliated as stable single layers are the layered van der Waals solids. After quantum dots, nanowires and nanotubes, two-dimensional (2D) materials in the form of sheets with atomic-scale thickness represent the most recent nanoscale material family under intense study. These materials appear in their bulk form as stacks of layers held together via van der Waals interaction in the crystal structure. Single layers with atomic-scale thickness can be extracted from such crystals. These materials exhibit strong in-plane covalent or

ionic bonding and weak out of the plane van der Waal or hydrogen bonding. 2D materials under pressure or strain display especially unique behaviors thanks to its bond strength contrast between strong intra-layer covalent bonds and weak inter-layer van der Waals bonds. The weak van der Waals interactions can be exploited to achieve epitaxial growth, in which the lattice structure of the substrate can be used to align the orientation of the overlayer[18] – an essential requirement for growing high-quality films. Van der Waals solids feature neutral, single-atom-thick or polyhedral-thick layers of atoms that are covalently or ionically connected with their neighbors within each layer, whereas the layers are held together via van der Waals bonding along the third axis. The weak nature of van der Waal bonding (~40–70 meV) and surface tension (~60–90 mJ/m^2) in a range of common solvents are used for the exfoliation of bulk parent crystals into individual nanosheets.[19] Besides graphite, TMDs are a well-studied system for layering van der Waals solids, especially MoS_2, $MoSe_2$ and WS_2. At the present time, over 40 disparate TMDs have been referred in layered form.[20] Due to their fascinating properties, single and few layered materials have been used in a plethora of applications, such as water splitting for hydrogen production[21], detoxification of Cr(VI)-containing wastewaters[22], thermo-electric devices[23] etc. As mentioned before, in TMDs the transition metal engages trigonal prismatic coordinates and octahedral coordinates and in 2H and 1T crystal phase, respectively. These facilitates share edges with closest neighbors within each layer and frame hexagonal honeycomb-like structure.

1.4 Processing methods of 2D materials

1.4.1 Mechanical exfoliation

The Scotch tape method

As mentioned before, graphene research has speeded up since 2004 when pristine graphene was isolated and characterized from Geim and Novoselov employing for the first time the widely accepted terminology known as the "Scotch tape method"[24] (2010 Nobel Prize in Physics). Putting an adhesive tape on graphite (or mica), the top layer of the material is peeled, remaining on the tape (**Figure 6**).[25] By folding the tape in half, sticking it to the flakes, splitting them again and by repeating this procedure for several times, each time the flakes split into thinner and thinner flakes, leaving by the end very

thin flakes attached to the tape that are directly dispersed in a solution by dissolving the tape into it. This method results to a variety of flakes including monolayers due to the cleavage of weak van der Waal forces between the layers. Using this method, commercially available inorganic layered materials are peeled off against scotch tape tests. This method has been employed to obtain monolayers of WS_2[26], MoS_2[27] and h-BH[28] from the bulk solids. Although this process is relatively simple, fast and cost effective, this strategy of production seems to be a relevant problem with graphene as the initial adhesive tape method can only isolate small amounts of graphene and, thus, the monolayer yield of this process is extremely low. Therefore, this method is only suitable for laboratory scale studies and cannot be utilized for large-scale production of monolayer materials. On the other hand, since this process does not prerequisite any chemicals and only depends on the shear force applied during the peeling process, high crystallinity and structural integrity of the initial structures are maintained.

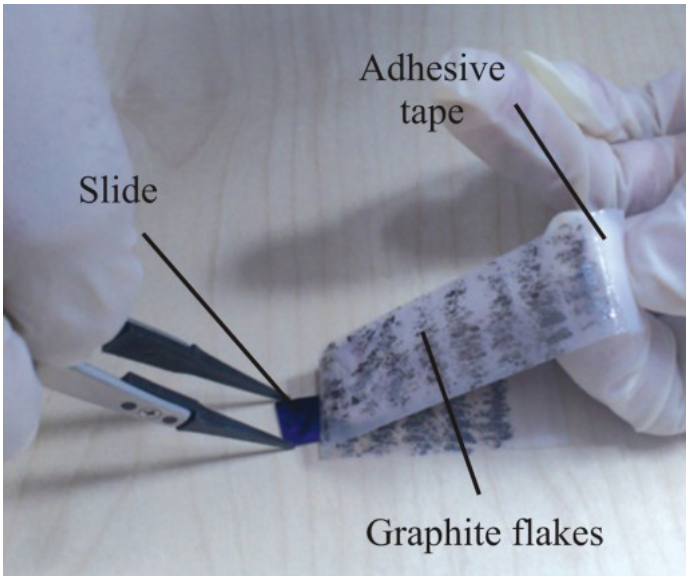

Figure 6. The 'Scotch tape' procedure (Copyright © 2012, Nature Publishing Group, a division of Macmillan Publishers Limited. All Rights Reserved).

1.4.2 Liquid-phase exfoliation

Liquid-phase exfoliation, a mild organic solvent-based (i.e., isopropyl alcohol, *o*-dichlorobenzene, *N*-methylpyrrolidone) exfoliation technique[29] (**Figure 7**)[30], is an alternative to mechanical exfoliation and permits the fabrication of arrangements of flakes with controllable thickness, producing single and few layers 2D sheets at bulk

scale. This method has been broadly used to isolate mono and few layer nanosheets of MoS_2[31], C_3N_4[32], WS_2[33] and so on. The liquid exfoliation method has four alternative forms: (i) oxidation, (ii) intercalation (iii) ion exchange and (iv) ultrasonic cleavage. Contrast to the mechanical exfoliation, liquid-phased exfoliation presents great advantages of reliability, scalability and versatility for the mass (industrial scale) production of 2D materials.

(i) One of the oldest methods is the oxidative liquid exfoliation, an established technique followed by subsequent dispersion into suitable solvents. The best example of that is the graphene oxide, where graphite flakes are treated with oxidizers, such as sulfuric acid and potassium permanganate, to passivate the surface of individual graphite layers with the addition of surface hydroxyl or epoxide functional groups and their upcoming dispersion/exfoliation in polar solvents. Layered materials having low reduction potential are best befitted for this oxidative liquid exfoliation.

(ii) Intercalation methodologies have been applied to 2D materials as means of exfoliating from their bulk equivalents in large quantities. The increased interlayer spacing between individual 2D layers by entering external species play a key role for the intercalation-based exfoliation method. These species weaken the interlayer adherence, while reducing the energy barrier to exfoliation. Similar to graphite, this method has been mainly applied for TMDs. A major drawback of this method is that it introduces a significant amount of chemical groups and structural defects on the exfoliated materials, thus, the physical properties of 2D materials are quite different from those of its pristine form.

(iii) Ion exchange liquid exfoliation has been widely used to exfoliate oxide nanosheets for optoelectronic applications.[34] For example, in the ion exchange exfoliation process, layered europium ($Eu(OH)_{2.5}Cl_{0.5}\bullet 0.9H_2O$) first react with dodecyl sulfate by replacing Cl^- ions in an ion exchange process followed by ultrasonication to separate the positively charged sheets.[35] Similar to europium hydroxide, TiO_2 layered crystals are tend to be negatively charged and their charge neutrality is maintained by Cs^+ ions. Therefore, negatively charged oxides are treated with bulkier cations such as Cs^+ and tetrabutylammonium (TBA). This method is widely known as proton exchange and has used in the exfoliation of perovskite type oxides, for example $Cs_{0.7}Ti_{1.825}O_4$.[36]

(iv) Ultrasonic cleavage of weak out-of-plane bonding is another liquid exfoliation process to acquire mono and few layer nanosheets. The bulk layered material is

dispersed in a suitable solvent, while the waves propagate through the solvent generating alternating high- and low-pressure cycles that promote exfoliation. These cycles provoke two different forms of energy inputs, vibration and cavitation forces, causing cavitation bubbles in the solvent. These bubbles generate high energy via release of pressure followed by an exfoliation of layers in the solvent. This procedure exposes the crystals to energetic forces until dispersed TMD nanosheets can be isolated from the unexfoliated material.[37] Some of the crucial parameters that prescribe the quality of the resultant solution are the centrifugation rate and the ultrasonication time. Another essential key parameter for the ultrasonic exfoliation of 2D materials is the selection of the optimum solvent. Over 25 different solvents have been studied on the exfoliation of a wide range of 2D materials based on the yield, crystallinity, thickness and size of the resultant layers. It has been proved that solvents having surface tension ~40 mJ/m^2 maximize the exfoliation rate. On the contrary, using a solvent with a surface tension similar to the surface energy of the layered 2D material not only the energetic cost of exfoliation is minimized, but also the restacking of nanosheets is prevented.[38] Isopropyl alcohol (IPA), dimethyl sulfoxide (DMSO), dimethylformamide (DMF), *N*-methyl-2-pyrrolidone (NMP), cyclohexyl-pyrrolidinone, *N*-dodecyl-pyrrolidone, *N*-vinylpyrrolidone are used as common solvents for ultrasonic exfoliation of *h*-BN[39], VS_2[40] and MoS_2[41] materials.

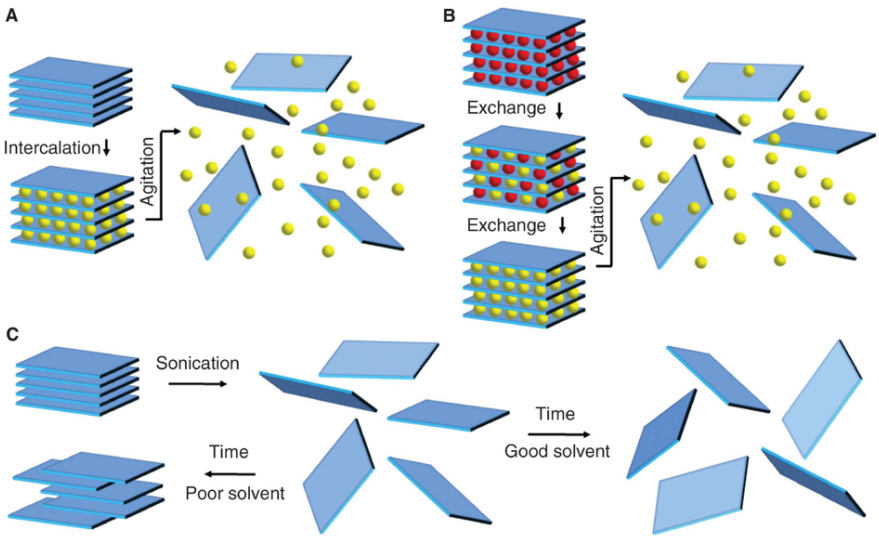

Figure 7. Schematic representation of variation in liquid exfoliation process: (A) intercalation, (B) ion exchange and (C) ultrasonic exfoliation (Copyright © 2013, The American Association for the Advancement of Science).

1.4.3 Hydrothermal synthesis

Apart from scotch tape based micromechanical exfoliation, intercalation assisted exfoliation, liquid-phase exfoliation, physical vapor deposition, micro-domain reaction and thermolysis of single precursors, have been used to prepare 2D thin-layer TMDs. Also, the hydrothermal method, a versatile wet chemical process, has been widely used to prepare layered 2D materials at high temperature and vapor pressure from an aqueous or an organic solution. This process is suitable for precursors having good solubility and stability at high temperature and pressure. Materials having high vapor pressure near the melting point can also be synthesized by the referred process. As an example, chemical reaction between ammonium molybdate [$(NH_4)_6Mo_7O_{24}•4H_2O$] and sulfur and/or selenium in hydrazine solution at 150–180 °C for 48 h results in the synthesis of single monolayer MoS_2 and $MoSe_2$.[42] Inspired by the synthesis of single and few MoS_2 layers, the use of hydrothermal method has been extended to obtain other 2D layered materials. Single-layer MoS_2@amorphous carbon (a-C) composites using thiacetamide as the sulfur source and reductant[43], few-layer WS_2/graphene using WCl_6 and thioacetamide in the presence of GOS[44], and L-cysteine-assisted SnS_2/GNS composites[45] have been produced by the hydrothermal synthesis. These synthesized 2D materials can be redispersed in the desired solvent, and can be deposited to prepare thin film nanocomposites and functional nanodevices.

1.5 Properties of TMDs

1.5.1 Crystal and electronic band structures

1.5.1.1 Molybdenum disulfide (MoS_2)

Molybdenum disulfide (MoS_2) has a crystal structure consisting of weakly coupled of S–Mo–S layers, where a Mo atom layer is packed between two layers of S atoms and each single layer has a thickness of about 6.5 Å (**Figure 8**). MoS_2 crystals are composed of vertically stacked, weakly interacting layers held together by van der Waals interactions[46], making it possible to produce monolayers of MoS_2 using the well-established micromechanical cleavage and liquid exfoliation techniques. So far, four poly-types of MoS_2 structures have been identified: 1H, 1T, 2H and 3R, and the structural changes are directly connected to the physical properties of MoS_2.[47] 1T MoS_2

and 3R MoS_2 are meta-stable (not occurring naturally) and the 1H phase is the most stable among all the poly-types. The 1T MoS_2 has the Mo atoms coordinated octahedrally by the sulfur and Mo atoms to form a unit cell. 1H phase (the basic unit of MoS_2 monolayer) has the Mo atoms coordinated octahedrally by the sulfur atoms and sandwiched in layers of S–Mo–S. 2H MoS_2 has a trigonal prismatic coordination around the Mo atom and exhibits two S–Mo–S units per elemental cell. The metastable 1T has one layer per unit cell with Mo atoms in octahedral symmetric arrangement. Because of the metastable nature, 1T-MoS_2 can be readily transformed to 2H phase via intralayer atomic gliding under specific conditions. The 2H-MoS_2 solid is semiconductor while 1T-MoS_2 is metallic in nature. The 3R MoS_2 also has trigonal prismatic coordination, the same as the 2H MoS_2 but with three S–Mo–S units per elemental cell arranged along the c-axis direction (**Figure 9**).[48]

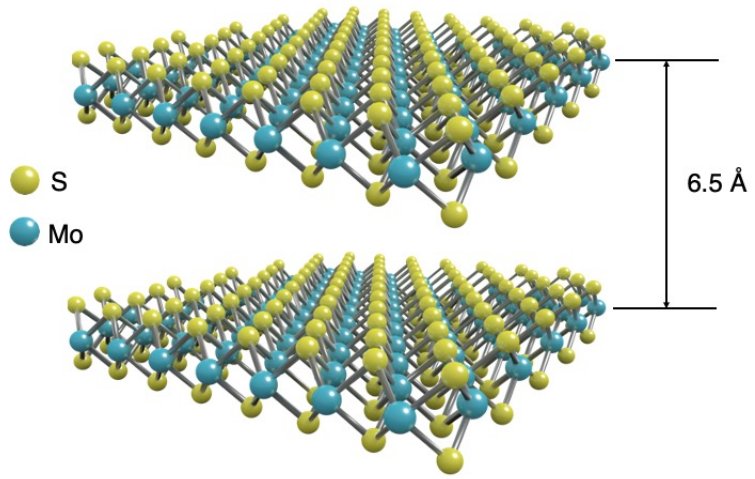

Figure 8. Chemical structure of two layers of MoS_2.

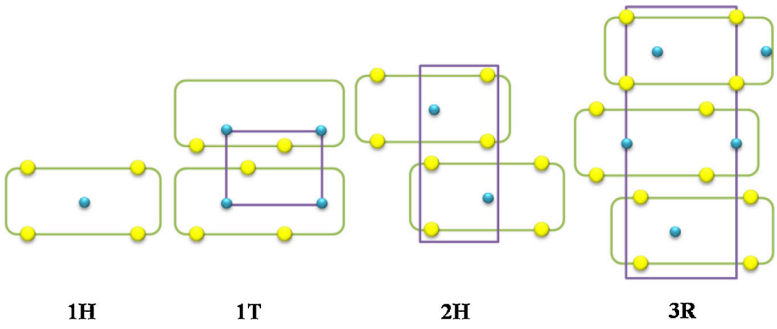

Figure 9. Schematic drawing of common poly-types for MoS_2 (Copyright © 2016 Elsevier Ltd. All rights reserved).

MoS_2 has an energy band gap (E_g) from 1.2 (indirect bandgap) to 1.9 (direct bandgap) eV for multi- to single-layer sheets, respectively[49], and exhibits high electron mobility (typically > 100 $cm^2 V^{-1} s^{-1}$)[50] and unique S–Mo–S coordination in the layered structure that forms atomically undercoordinated edge sites with high photochemical and electrochemical reactivity.[51] For the applications of MoS_2 nanosheets, electronic structure is the key determinant. In **Figure 10**, the band structures of MoS_2 in bulk, bilayer and monolayer form are compared. We can observe that as the layer number of 2H-MoS_2 nanosheets decreased from bulk to monolayer, the conduction band (CB) minimum is down-shifting from the middle of Γ-K line towards K point. At the same time, the valence band (VB) energy at the K point also up-shifting, and becomes the valence band maximum as same as the Γ point. Predominantly, the VB maximum and the CB minimum are located at the two inequivalent high-symmetry points K and K′, which correspond to the corners of the hexagonal Brillouin zone. This property is common to monolayer 2H-MoS_2 (and other group VI monolayer 2H-TMDCs) and to graphene, and enables the observation of valley-dependent physical phenomena and potential valleytronics applications. MoS_2 with different thicknesses has been utilized as cocatalyst to enhance photocatalytic activity using many different types of photoactive host semiconductors.

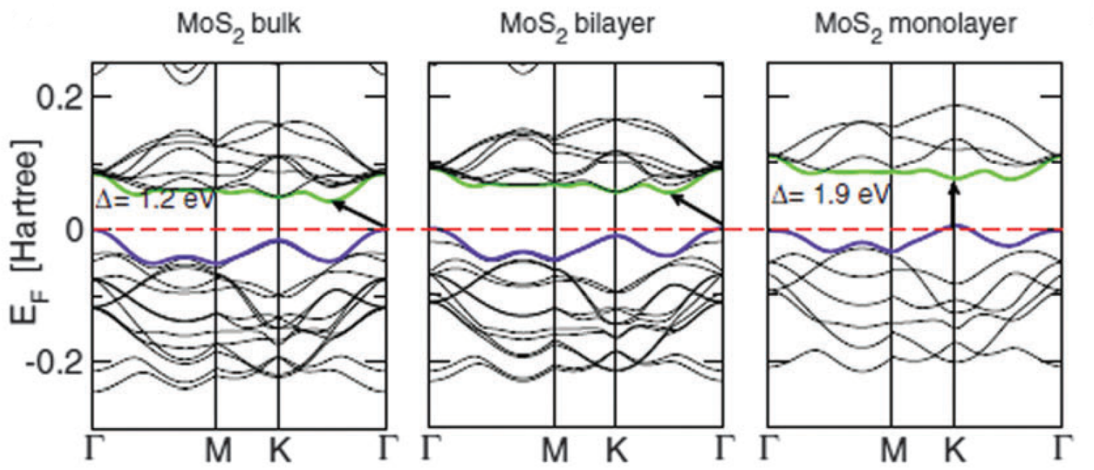

Figure 10. Calculated band structures of bulk, bilayer, and monolayer MoS_2 calculated at the DFT/PBE level. The horizontal dashed lines indicate the Fermi level. The arrows indicate the fundamental band-gap (direct or indirect) for a given system (Reproduced from ref. [13] with permission from Royal Society of Chemistry).

1.5.1.2 Carbon nitride (C_3N_4)

Carbon nitrides are a class of polymeric materials consisting mainly of carbon and nitrogen, including α-C_3N_4, β-C_3N_4, cubic-C_3N_4, pseudocubic-C_3N_4 and graphitic-C_3N_4 (g-C_3N_4).[52] g-C_3N_4 is not only the most stable allotrope of carbon nitrides at ambient atmosphere, but it also has rich surface properties that are attractive for many applications, including catalysis, due to the presence of basic surface sites. It also comprises a π-conjugated polymeric layered structure of sp^2-hybridized carbon and nitrogen atoms. In general, g-C_3N_4 can be prepared from nitrogen-rich and carbon-rich precursors, such as cyanamide, dicyandiamide, melamine, urea, and thiourea. The structure contains a small amount of hydrogen, present as primary and/or secondary amine groups on the terminating edges (**Figure 11**). The existence of hydrogen indicates that g-C_3N_4 is incompletely condensed and that a number of surface defects exist, which can be useful in catalysis – such defects are believed to promote electron relocalization on the surface, inducing Lewis-base character towards photocatalysis. Because of the presence of hydrogen and to the fact that nitrogen has one more electron than carbon, g-C_3N_4 has rich surface properties that are important to catalysis, such as basic surface functionalities, electron-rich properties and H-bonding motifs. Its high thermal (stable up to 600 ºC in air)[53] and hydrothermal (insoluble either in acidic, neutral or basic solvents)[54] stability, enables g-C_3N_4 to function as catalyst either in liquid or gaseous environments, and at elevated temperatures.

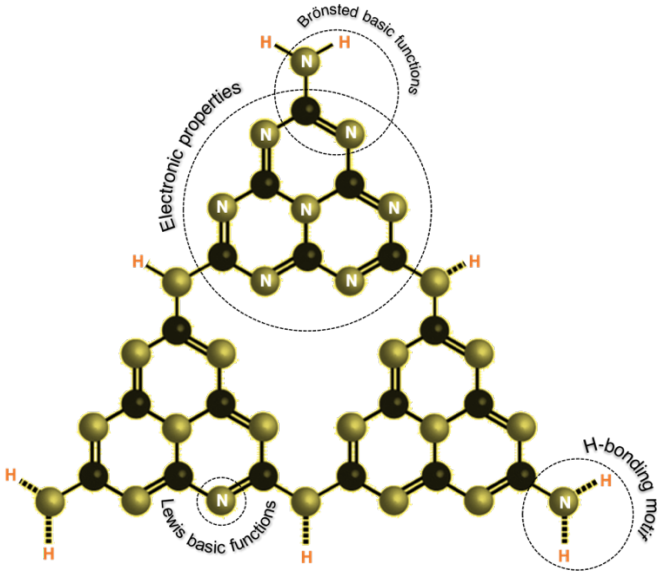

Figure 11. Chemical structure of g-C_3N_4 and multiple surface functionalities found on g-C_3N_4.

g-C_3N_4 is a nontoxic and novel semiconductor catalyst, having a CB at around –1.23 V vs normal hydrogen electrode (NHE) at pH 7, which is more negative that the potential of H_2 evolution (−0.41V vs NHE at pH 7).[55] However, the photocatalytic H_2 production efficiency of g-C_3N_4 is limited due to the large optical band gap (~2.7 eV, which corresponds to a utilization of solar energy at $\lambda < 460$ nm) and the fast recombination rate of photogenerated electron−hole pairs.[56] Thus, to facilitate the spatial dissociation of the photogenerated charges, a cocatalyst or other semiconductor materials can be loaded on the surface of g-C_3N_4 to form a hybrid nanocomposite. These heterostructures can exhibit improved charge separation and, thus, higher photochemical stability due to the charge transfer between the different components.

1.5.1.3 Tin disulfide (SnS_2)

Tin sulfide (SnS) is a non-toxic and inexpensive material that exhibit interesting mixed valence properties. The thermodynamic balance between the oxidation states of Sn is subtle, and both Sn(II)S and Sn(IV)S_2 compounds are known to exist. The lower oxidation state is associated with a Sn lone pair[57], which is the origin of the structural distortion found in the orthorhombic phase of SnS (**Figure 12**).[58]

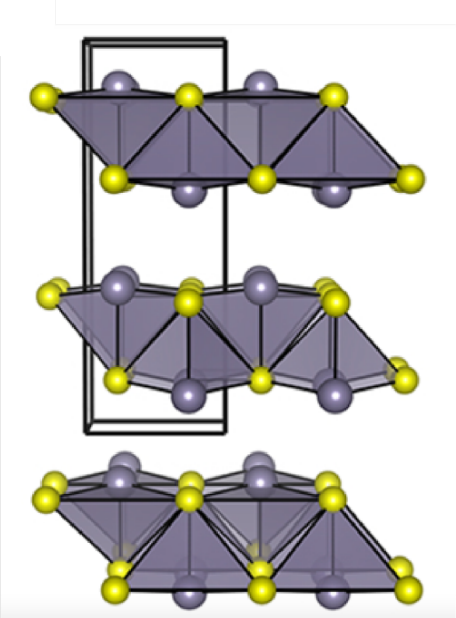

Figure 12. Ground-state crystal structure of SnS (the tin atoms are displayed as gray spheres and the sulfur atoms as yellow spheres) (Adapted from ref. [59]. Copyright © 2013 American Chemical Society).

In terms of conductivity, a reducible cation (i.e., tetravalent Sn) is generally associated with electron conduction (n-type), while an oxidizable cation (i.e., divalent Sn) is associated with hole conduction (p-type). For example, SnS is typically p-type, while SnS_2 is n-type. As mentioned before, SnS is intrinsically a p-type semiconductor owing a high absorption coefficient (a) of > 10^4 cm^{-1} above the band gap[59], a direct band gap of 1.2–1.5 eV[60], indirect gap of 1.1 eV[61] and high free carrier concentration around 10^{17}–10^{18} cm^{-3} [62]. SnS can take the form of several phases, but its stable phase at room temperature is a distorted rock salt structure. The α-SnS phase -which has the mineral name herzenbergite- adopts a layered orthorhombic structure with *Pnma* symmetry at ambient conditions. Upon increasing the pressure and/or temperature, α-SnS is known to experience a structural transformation to β-SnS which is semi-metallic phase with an orthorhombic structure (*Cmcm* space group symmetry) (**Figure 13**).[63] Only α-SnS is stable at room temperature, while the other phase is formed at higher temperatures.

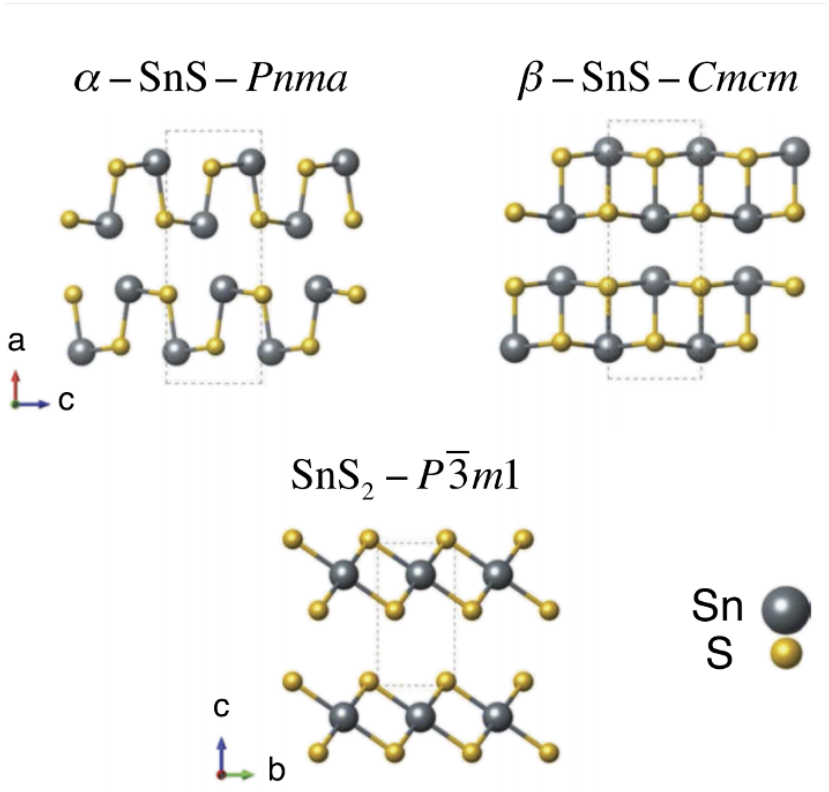

Figure 13. Crystal structures of α-SnS, β-SnS and SnS_2 (Adapted from ref. [64]. Rights managed by AIP Publishing).

Another important material is SnS_2 (**Figure 13**), a well-known semiconductor, which adopts a layered structure with *P*-3*m*1 symmetry at ambient conditions.[64] SnS_2 has a band gap of ~2.1 eV and thus exhibits photoabsorption ability in visible and near infrared regions, making it suitable for photocatalysis applications. Unlike α-SnS, SnS_2 can adopt various polytypes (i.e., 2H, 4H, and 3R) with different stacking sequences arising from different growth conditions.[65] **Figure 14** shows the energy band structure of monolayer and bi-layer SnS_2, calculated by using DFT method, emerging that it is an indirect band gap semiconductor.[66] It can be seen that the calculated bandgap of bulk SnS_2 is 2.14 eV, and the monolayer reserves the indirect semiconducting characteristic with a bandgap down to 1.65 eV. SnS_2 has received much attention due to its possible applications in optoelectronics, solar cells and, in the latest few years, in photocatalysis.

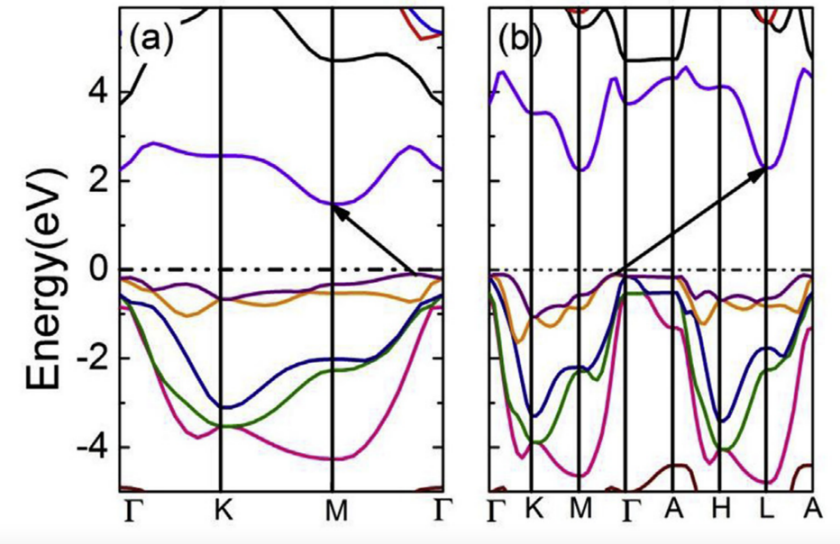

Figure 14. Band structures of (a) monolayer and (b) bulk SnS_2 (the black arrows indicate the indirect bandgaps) (Adapted from ref. [67]. Copyright © 2017 Elsevier Ltd. All rights reserved).

1.6 Fabrication of 2D heterostructures

Since the successful preparation of graphene in 2004, the properties and applications of 2D materials have attracted much attention. However, a number of issues limit the application of single 2D materials. Developing new hybrid materials by combining 2D layered materials in vertical stacks or epitaxial grown planar (where the monolayers are held together by Van der Waals forces) displays a plethora of possibilities to expand

the adaptability of 2D materials, allowing for achieving prevalent and unusual material properties that cannot be obtained in any other way. Critical points to achieve practical junctions (e.g., p-n, p-n-p etc.) are a stable and tunable doping capability over the natural tendency of TMDs (n-type and p-type for MoS_2 and WSe_2, respectively), key functions that are required for electronic and optoelectronic devices. If p- and n-doped materials are used in such devices, then atomically sharp p-n junctions can be created.[67] Such systems are extremely efficient in carrier separation, so it is anticipated to achieve very high quantum efficiency. As referred in previous section, one of the most powerful methods for preparing graphene, which can also be extended to other materials, is liquid-phase exfoliation. By solution synthesis of 2D materials or by controlling the charge of individual flakes in suspensions, heterostructures (e.g., MoS_2-WS_2) can be formed straight in the liquid phase (**Figure 15**).[68] Such kind of 2D materials can be used for energy storage and catalytic applications. For instance, $MoSe_2$/graphene heterostructures have been used for Li-ion battery applications[69], MoS_2/g-C_3N_4/Pt nanosheets for enhanced photocatalytic H_2 production from water[70] and GO/g-C_3N_4/MoS_2 flower-like heterojunctions for water remediation[71].

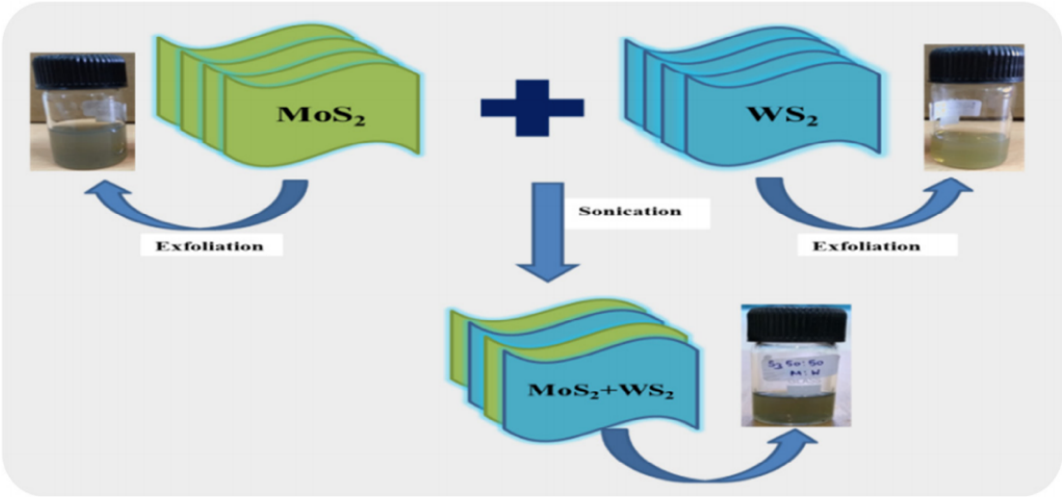

Figure 15. Schematic representation for the formation of the MoS_2-WS_2 van der Waals heterostructure from the exfoliated TMD dispersions (Copyright © 2019 Elsevier Ltd. All rights reserved. Peer-review under responsibility of the scientific committee of the Interntional Symposium on Functional Materials (ISFM-2018): Energy and Biomedical Applications).

1.7 Photocatalysis with 2D materials

Compared to the conventional thermal catalysis, semiconductor photocatalysis has attracted prodigious attention for its promising potential to induct incurable environmental and energy issues using solar energy.[72] The solar energy is an endless and environmentally friendly source, which makes photocatalysis an attractive technology for solving environmental and energy problems, such as water contaminants degradation[73], water splitting[74] and CO_2 reduction[75]. The overall process of a semiconductor-sensitized photoreaction can be summarized as follows:

$$A + D \xrightarrow[h\nu \geq E_g]{semiconductor} A^- + D^+ \quad (1)$$

where E_g is the semiconductor's band gap, A is an electron acceptor (usually oxygen) and D is an electron donor (usually an inorganic contaminant).

If an electron acceptor and electron donor are adsorbed on the semiconductor particle, a series of reactions may occur. Usually, electrons get excited from valence band to conduction band by heating or light irradiation. If $h\nu > E_g$, a photon can be absorbed, creating a free electron and a free hole. It is known that catalysis belongs to a class of surface reactions, and is sensitive to the surface structure and morphology of the catalyst.

One of the most effective methods of water decomposition involves heterogeneous photocatalysts. During the past few years, increased attention is being paid to this particular method in order to develop an environment-friendly technology to purify polluted air and water without electricity or other energy consuming sources. Heterogeneous photocatalytic process involves at least five separate reaction steps, including (i) transfer of the reactants in the fluid phase to the catalyst surface, (ii) adsorption of reactants onto the surface of semiconductor, (iii) reaction in the adsorbed phase, (iv) desorption of products from the surface of the semiconductor, and (v) removal of the products from the interface region. Heterogeneous photocatalysis appears as a viable method that can compete economically compared with other UV oxidation processes for water treatment. Key steps of a heterogeneous photocatalytic process are the photoinduced charge separation, charge migration, and interfacial electron exchange and interaction with reactants.

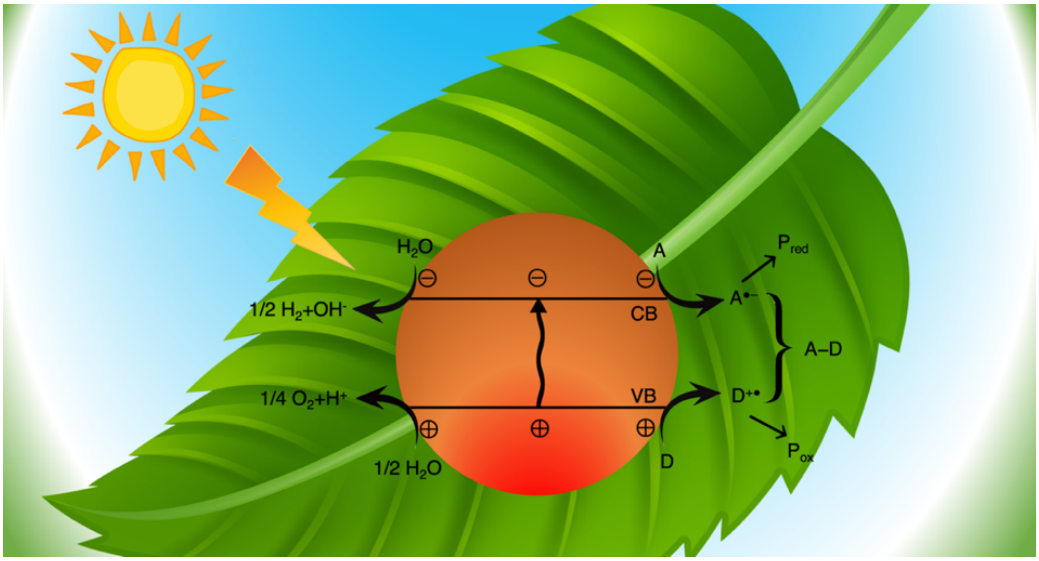

Figure 16. Schematic diagram of semiconductor photocatalysis.

As seen in **Figure 16**, activation of the semiconductor photocatalyst for reaction is achieved through the absorption of a photon of ultra-bandgap energy, which results in the promotion of an electron (e^-) from the valence band to the conduction band, with the concomitant generation of a hole (h^+) in the valence band. For a semiconductor photocatalyst to be efficient, the interfacial processes involving e^- and h^+ must compete effectively with the major deactivation process involving e^-–h^+ recombination. In general, recombination of the electron-hole pair on the surface can be prevented to a significant degree by adding suitable scavengers.

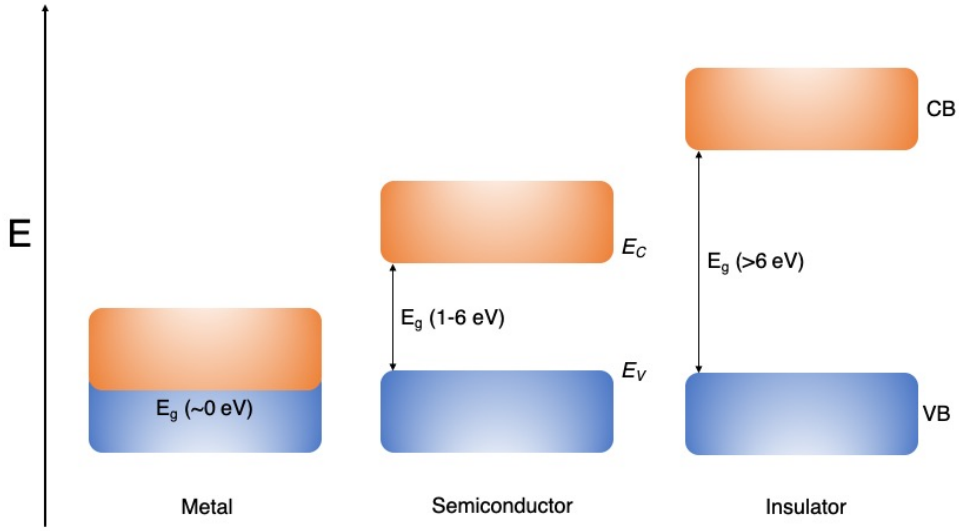

Figure 17. Energy band diagrams for metals, semiconductors and insulators.

In order for a material to be conductive, both free electrons and empty states must be available. Systems with an energy-level-free zone (forbidden zone) are called semiconductors and insulators if the bandgap is in the range of 1–6 eV and above 6 eV, respectively. Semiconductors have similar band structure as insulators but with a much smaller band gap (**Figure 17**). Some electrons can jump to the empty conduction band by thermal or optical excitation. Thus, a semiconductor becomes an electronic conductor when irradiated with light of energy equal to or larger than E_g – thus, an ideal semiconductor cannot absorb light of energy smaller than its bandgap. The position of semiconductor's conduction band (CB) and valence band (VB) edges relative to the redox potentials of the adsorbed substrates (reactants) determines the efficiency of the electron transfer reaction as mentioned before. In order to photo-reduce a chemical species, the CB of the semiconductor must be more negative than the reduction potential of the chemical species, while to photo-oxidize a chemical species, the potential of the VB of the semiconductor must be more positive than the oxidation potential of the chemical species (**Figure 18**).[76,77,78]

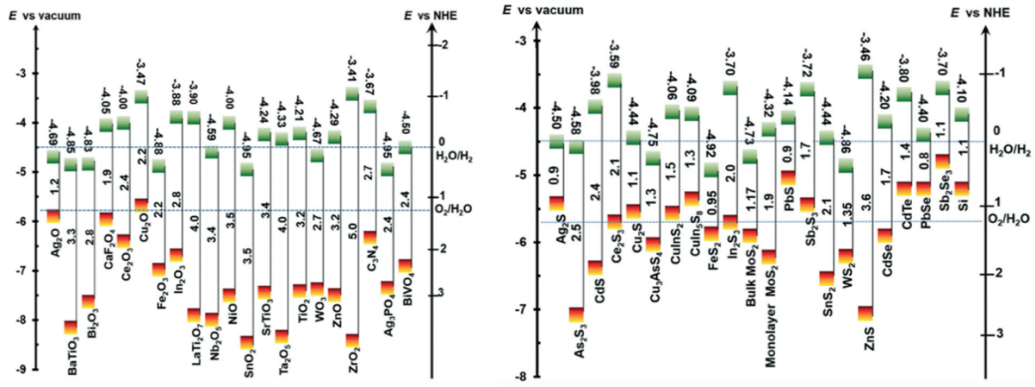

Figure 18. Band edge positions of semiconductors in contact with the aqueous electrolyte at pH=0 relative to NHE and the vacuum level, accompanied with redox couples for comparison (Adapted from ref. [79] with permission from Royal Society of Chemistry).

The band structure of a material is calculated with various numerical methods and plotted as E vs *k*, where *k* is the wave vector. In general, two characteristic cases are relevant for the interpretation of electronic absorption spectra. As seen in **Figure 19a**, the maximum of the VB and the minimum of the CB are located at the same value of *k* (*k*=0). In this case, the absorption of a photon is fully allowed and the material is called a direct semiconductor. In an indirect semiconductor, the minimum of the CB is

displaced to a larger *k* value and the law of momentum requires that in addition to the photon also a phonon has to be absorbed (**Figure 19b**). The resulting "three-part process" (photon, electron and phonon) is of lower probability than the "two-part" process of a direct transition. Therefore, a direct semiconductor displays a much abrupt absorption on set than an indirect one.

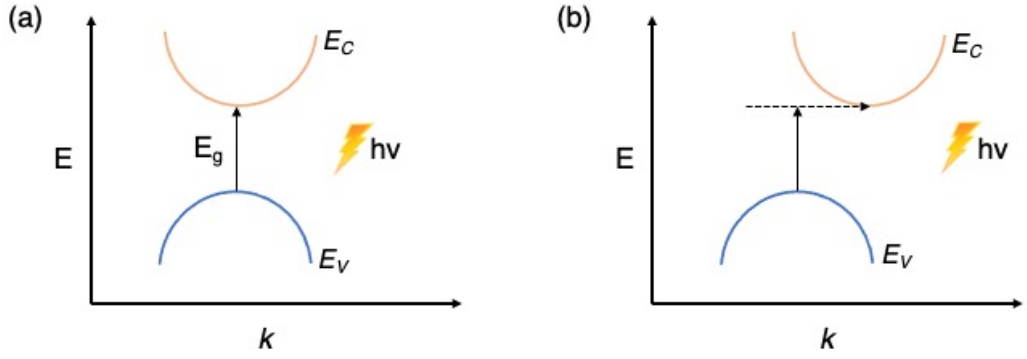

Figure 19. (a) Direct and (b) indirect band-to-band transitions in semiconductors. The dashed arrow represents the absorption of a phonon.

The location of the Fermi level (E_F) respect to the semiconductor band edges, determines the electronic characteristics of the semiconductor. In common, the understanding of the physical processes affecting the Fermi energy is a complex issue, which requires an extensive knowledge of mechanisms leading to the introduction of electrically active impurities and/or native defects. It is well known that the generation of native defects affects the Fermi energy.[79] From a statistical point of view it is defined as the energy at which the probability of an energy level being occupied by an electron is 50%. Instead, from the viewpoint of thermodynamics, the Fermi level corresponds to the electrochemical potential of an electron in a solid. In an ultrapure intrinsic semiconductor, it is located in the middle of the bandgap. When impurities are present or introduced through doping with electron-donating and electron-accepting atoms, E_F is located close to CB (large number of free electrons in the CB) and VB (large number of holes in the VB), respectively (**Figure 20**). The corresponding materials are called n-type and p-type semiconductors since the majority charge carriers are electrons (e^-) and holes (h^+), respectively. The precise position of E_F depends basically on the dopant concentration, and typical distances to the band edges (CB or VB) are 0.1–0.3 eV.

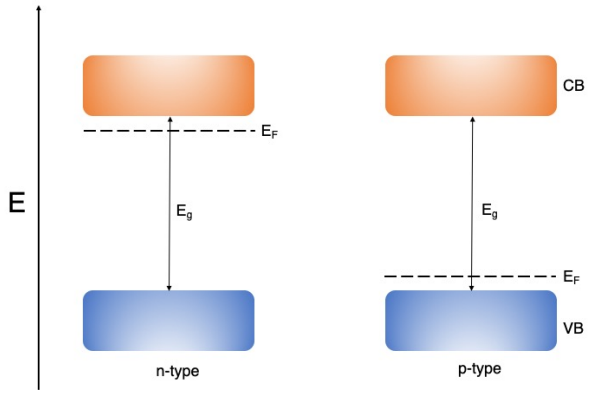

Figure 20. Position of the Fermi level (E_F) in an n-type and a p-type semiconductor in thermal equilibrium.

Given that the enhanced catalytic activity of 2D materials emanates from the modification of their electronic structure, different atomic monolayer TMDs can be combined to create heterostructures that are held together with van der Waals interactions. In these materials the monolayers of multiple 2D materials are stacked vertically layer-by-layer or stitched together in-plane to create lateral heterojunctions. A semiconductor structure in which more than one semiconductor components is used and the structure contains interfaces or junctions between two different semiconductors is called heterostructure. 2D materials and their heterostructures can be used as a catalyst, catalytic support or even an electron donor to the active centres.[80] Semiconducting monolayer TMDs can also serve as building blocks for p-n or n-n junctions and Van der Waals heterostructures by stacking different 2D materials using mechanical transfer techniques.[81] Once a junction is formed (heterostructure interface between a wide bandgap and a narrow bandgap semiconductor), electrons will flow from the side with higher Fermi level to the side with lower Fermi level, while the holes will flow to the opposite direction (**Figure 21**).

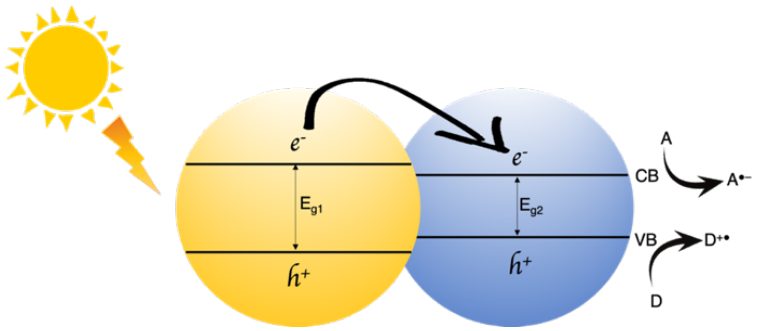

Figure 21. Schematic diagram of a semiconductor-semiconductor heterostructure.

1.8 Hydrogen production by photocatalytic water splitting

Photocatalytic hydrogen generation through water splitting can be viewed as a promising solution to future energy demands.[82] This approach utilizes a semiconductor-based photocatalytic system, which absorbs sunlight and splits water, producing hydrogen. In recent years, considerable scientific effort has been devoted to designing efficient catalysts for electrochemical and photochemical production of hydrogen. As a result, a number of organic–metal complexes, metal oxides and transition-metal chalcogenides have been synthesized and used as potential cathode materials to split water by the hydrogen evolution reaction (HER).[83] To be of practical use, however, HER catalysts need to fulfill several requirements: (i) efficient absorption of sunlight, (ii) fast transport of charge carriers to the solid–electrolyte interface, (iii) high surface-area-to-volume ratio structure that provides a large number of active sites, and (iv) appropriate potential of photocarriers to sustain the HER. Moreover, the photocatalyst needs to remain stable in solution and must be cost-effective for widespread application. Sunlight and water are the most abundant, clean, renewable and natural energy resources on Earth. The transformation of solar energy into chemical energy, particularly hydrogen, has become a challenging and attractive subject during the past years.[84] Hydrogen has been acknowledged as a promising substitute form of storable and clean energy for the future. H_2 is mainly produced from petroleum and natural gas steam reforming process, method that is not sustainable in the long term.[85] Thus, there has been a growing interest in the development of new methods to generate H_2 from renewable and sustainable resources to avoid the production of greenhouse gases from fossil fuel utilization. Hydrogen production from solar water-splitting processes generally can be categorized into thermochemical water splitting, photo-biological water splitting and photocatalytic water splitting.[86] Among them, the most efficient is the production of hydrogen by water splitting using sunlight (Equation (2)) because it does not have the inadequacies associated with thermal transformations or with the conversion of solar energy to electricity followed by electrolysis. This reaction is therefore sometimes referred to as artificial photosynthesis:

$$H_2O + h\nu \rightarrow H_2 + {}^1/_2O_2 \qquad (2)$$

The conversion of water to H_2 using sunlight has been described as an ideal solution to counter the depletion of and environmental issues associated with fossil fuels.[87] As pure water does not absorb solar radiation, the water splitting needs a semiconductor material (photocatalyst) capable of efficiently absorbing solar energy to produce electrons and holes that can reduce and oxidize, respectively, the water molecules adsorbed on the photocatalyst surface (**Figure 22**).

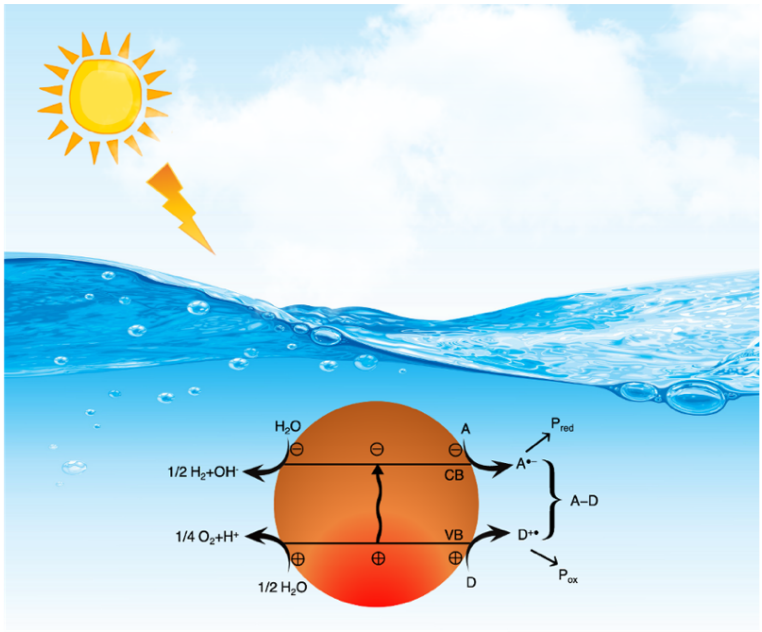

Figure 22. Sketch diagram showing the basic principle of overall water splitting on a semiconductor-based surface.

Sustainable hydrogen production by water splitting has been pioneered by Honda and Fujishima in 1972, who demonstrated the photoelectrochemical splitting of water using TiO_2 photoanode under ultraviolet irradiation.[88] Water splitting into H_2 and O_2 is classified as an "uphill" photocatalytic reaction because it is accompanied by a large positive change in the Gibbs free energy (ΔG^0 = 237 kJ/mol; 2.46 eV per molecule). One of the biggest challenges in water splitting is to overcome that thermodynamically 'uphill' hydrogen and oxygen evolution half reactions which involve four-electron transfer reactions.[89] Cocatalysts loaded on the surface of semiconductors (creating heterojunctions) have been proven to be able to facilitate photocatalytic reactions by accommodating excited electrons or holes and promoting redox reaction kinetics, in contrast to single-component photocatalysts. Under irradiation with energy greater than the band gap (E_g) of the semiconductor photocatalyst, an electron (e^-) is promoted to

the CB, while a positive hole (h^+) is formed in the VB. The excited electrons and holes can recombine and dissipate the input energy as heat, get trapped in metastable surface states or react with electron donors and electron acceptors adsorbed on the semiconductor surface. Under suitable reaction conditions the generated electrons and holes can participate in the process of oxidation and reduction of water, resulting in the formation of gaseous oxygen and hydrogen.[90] The irradiation of the semiconductor leads to the evolution of hydrogen and oxygen at the surface of the cathode and anode, respectively. In a water splitting system, the reducing CB electrons become important, as their role is to reduce protons to hydrogen molecules. Thus, the CB level should be more negative than the hydrogen evolution level (E_{H_2/H_2O}) to initiate hydrogen production (0 V vs. NHE at pH=0), while the VB should be more positive than the water oxidation level (E_{O_2/H_2O}) for efficient oxygen production (1.23 V vs. NHE at pH=0) from water by photocatalysis (**Figure 23**).[91] Apart from the suitable position of the VB and CB, the recombination of photogenerated charge carriers can limits the overall photocatalytic efficiency. To avoid these problems some researchers suggested that the addition of electron donors (hole scavenger or sacrificial agents), which react faster than water with the photogenerated VB holes will increase the electron/hole separation and improve the H_2 production rate. Methanol, ethanol, phenol, EDTA, citric acid, lactic acid and formaldehyde have been tested as electron donors and proved to be effective to enhance H_2 generation.

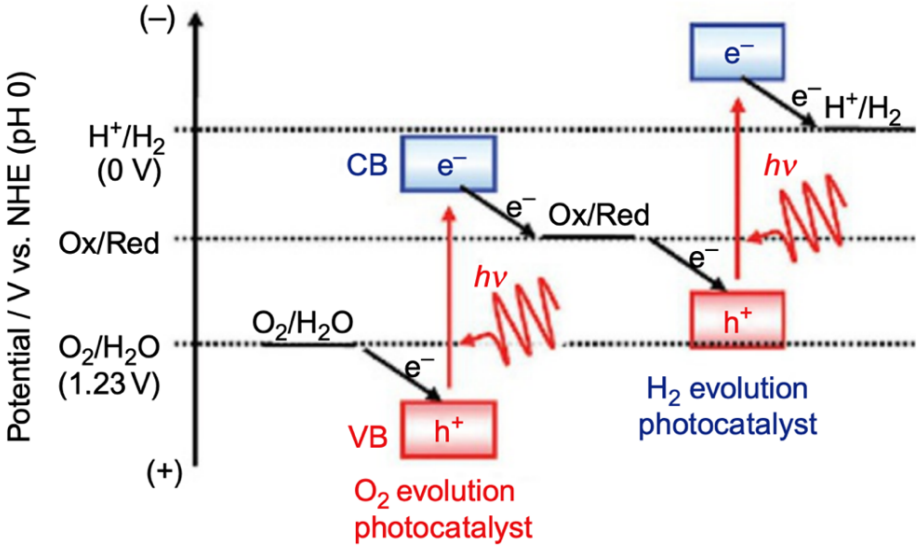

Figure 23. Energy diagrams of photocatalytic water splitting (Adapted from ref. [92]. Copyright © 2018 Elsevier Inc. All rights reserved).

The rational design of new photochemical systems for efficient water reduction is of critical importance and has attracted continuous attention over the past few years.[92] Through this pursuit, a diverse set of metal oxide (such as TiO_2, Ta_2O_5, $SrTiO_3$, $K_4Nb_6O_{17}$ etc.) and metal sulfide (such CdS, ZnS, NiS etc.) semiconductors have been investigated as potential hydrogen-evolving catalysts under solar or visible light irradiation. Unfortunately, the realization of these materials for light energy conversion often coincides with poor visible light absorption (that is, the main portion of solar radiation), low charge separation yield, pronounced susceptibility to photo-corrosion and high cost. Recently, the layered transition-metal dichalcogenides, such as MoS_2, SnS_2 and WSe_2, have emerged as a new front in the fields of electronics, optoelectronics and chemical sensor devices.[93] Among them, molybdenum disulfide (MoS_2) possesses a combination of intriguing attributes for use in electro- and photocatalysis, including low cost, tunable electronic structure (it adopts metallic 1T as well as semiconducting 2H structures[94], and its band gap (E_g) varies from 1.2 to 1.9 eV for multi- to single-layer sheets, respectively)[95], high electron mobility (typically > 100 $cm^2 V^{-1} s^{-1}$)[96] and unique S–Mo–S coordination in the layered structure that forms atomically undercoordinated edge sites with high photochemical and electrochemical reactivity.[97] Between different phases of MoS_2 (2H, 1T/2H and 1T/3R), 2H MoS_2, although possesses lower charge carrier mobility than the metallic 1T MoS_2, shows higher stability and interesting semiconducting characteristics make it attractive material for applications in light energy conversion and opto-electronics.[98] Nonetheless, the photoconversion efficiency of multilayer 2H MoS_2 is largely limited by its indirect bandgap transition, which depress the absorption coefficient and anisotropic charge transport property, which shorten the carrier lifetime (~200 10^{-12} s).[99] To circumvent the above limitations, researchers strive to integrate MoS_2 with various layered metal-free materials, such as graphitic carbon nitride (g-C_3N_4), carbon nanofibers, graphene and graphite. In fact, 2D/2D heterostructural architectures with large contact areas may offer a significant advantage for photochemical catalysis because of their large exposed surface area and facile dissociation of photogenerated excitons across the junction. Earlier studies have shown that g-C_3N_4 is a beneficial material for light energy conversion due to the good optical absorption (it has a bang gap (E_g) of ~ 2.7 eV), excellent photostability, low cost and high exposure of catalytically active sites.[100] Remarkably, over the past few years, rising improvements in the light-irradiated

hydrogen evolution catalysis have been achieved by using thin-layered MoS_2/g-C_3N_4[101], MoS_2/S-doped g-C_3N_4[102], MoS_2/pyridine-modified g-C_3N_4[103], MoS_2/mesoporous g-C_3N_4[104], MoS_2/oxygenated g-C_3N_4[105] and g-C_3N_4/Ag/MoS_2[106] heterojunction composites. The catalytic propensity of these hybrid materials to produce hydrogen has been mainly related to the synergistic coupling effects caused by strong electronic interactions at the interface between MoS_2 and g-C_3N_4 layers. Such interfacial interactions, which arise due to the weak interlayer van der Waals forces and possibly strong electronic coupling among MoS_2 and g-C_3N_4 adjacent layers, was envisaged to improve electron transfer from photoexcited g-C_3N_4 to MoS_2, thus leading to the enhancement of electron-hole pair separation. In this sense, the photocatalytic function of MoS_2/g-C_3N_4 heterostructures for hydrogen evolution may be significantly improved compared to single-components g-C_3N_4 and MoS_2, standing out promising perspectives in the search for highly active and cost-efficient photocatalysts. However, although some important progress has been made in synthesis of MoS_2-modified g-C_3N_4 semiconductors, there is no literature reporting the fabrication of MoS_2/g-C_3N_4 nano-heterojunctions with different interfacial contact area between two semiconductors, importantly, at a fixed chemical composition. In addition, the electronic behavior of MoS_2 nanolayers and their underlying role in affecting the charge carrier separation dynamics and, thus, the photocatalytic propensity of MoS_2/g-C_3N_4 nanojunctions for hydrogen generation remain poorly understood. In consequence, to address these limitations, the fabrication of 2D/2D nanojunction networks consisting of exfoliated g-C_3N_4 flakes and 2H MoS_2 nanosheets (NSs) with variable lateral sizes provides an efficient way. These, MoS_2/g-C_3N_4 nano-heterostructures, where the tuning parameter is only the dimension of MoS_2 layers, provide a good platform to study and understand the effect of interfacial area and exposed catalytic MoS_2 edge sites on their charge transport properties and photochemical activities. Thus, these layered materials, which possess size-tunable photocarrier properties in MoS_2/g-C_3N_4 contacts and large number of exposed catalytic MoS_2 edge sites can exhibit favorable photocatalytic hydrogen evolution performance.

1.9 Hexavalent chromium wastewater treatment

Water pollution is on top of the most permeative threats worldwide, risking human health and quality life. This is because voluminous amounts of toxic metals, such as hexavalent chromium (Cr(VI)) are released directly or incidentally to the environment.[107] Cr(VI) discharges in wastewaters usually from industrial processes, such as leather tanning, chrome plating and polishing, stainless-steel production, chromate manufacturing, pigment production, and other industrial production activities[108], and is one of the dominant concerns in environmental restoration plant. Chromium exists in trivalent (Cr(III)) and hexavalent oxidation states in aquatic systems, having extremely different physical, chemical and toxicity properties.[109] At acidic conditions (pH < 6), $HCrO_4^-$ and $Cr_2O_7^{2-}$ oxyanions are the most predominant species of Cr(VI)[110], which are sparingly soluble, making their precipitation unattainable (**Figure 24**).[111,112] In fact, Cr(VI) oxo species are particularly harmful pollutants causing carcinogenesis and mutagenesis in biological cells.[113] According to the International Agency for Research on Cancer (IARC), Cr(VI) is classified as a Group 1 carcinogen with a harmful dose (LD_{50}) of 50–150 mg Kg^{-1} for an adult.[114] Because of the carcinogenicity and genotoxicity of Cr in human cells, the World Health Organization (WHO) recommends guideline value of 5 μg L^{-1} in drinking water.[115]

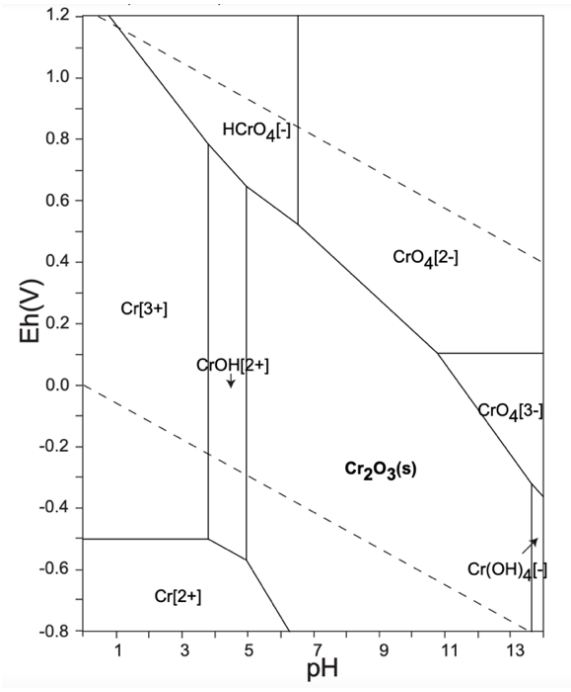

Figure 24. The Eh-pH diagram of Cr–O–H system (Reproduced from ref. [113]).

In the recent few years, semiconductor photocatalysis has enticed great attention due to its wide applications in puzzling out environmental problems associated with contaminated wastewaters by hazardous pollutants.[116,117] For instance, reduction of toxic Cr(VI) to less harmful Cr(III) by light-excited CB electrons of a photocatalyst is a viable approach that holds great potential for environmental remediation applications. In this regard, a wide spectrum of metal oxide and sulfide semiconductors, such as TiO_2[118], $BiGeO_{20}$[119], SnS_2[120], CdS[121] and MoS_2[122], have been investigated as potential Cr(VI)-reducing catalysts under solar or visible light irradiation. Although these materials have a well-suited band structure for photoreduction of Cr(VI), they suffer from prejudicial charge-carrier recombination and/or poor photon-to-electron conversion efficiency, which are detrimental for catalytic implementations. Up to today, various visible-light-driven semiconductor photocatalysts have been developed and examined for photocatalytic Cr(VI) reduction, such as metal-doped TiO_2[123], MoS_2[124], ZrO_2[125], Bi_2VO_4[126] and SnS_2[127]. However, some of these materials are expensive, unstable and potentially hazardous. Furthermore, many photocatalysts exhibit sluggish kinetics for the water oxidation reaction, so that the use of sacrificial electron donors, such as ascorbic acid, oxalates and tertiary amines, is necessary. In fact, the photocatalytic reduction of Cr(VI) with the aid of sacrificial reagents is a complex and costly issue, which severely limits the application options of the catalyst, for example in the detoxification of Cr(VI)-enriched effluents. This urgent need for efficient remediation of aqueous pollutants has stimulated a great deal of research interest in recent years.

Environmentally-friendly and low-cost graphitic carbon nitride (g-C_3N_4) has recently emerged as an attractive candidate for water splitting and environmental protection applications. g-C_3N_4 absorbs a substantial fraction of the visible spectrum (it has an energy gap of ~2.7–2.8 eV) and possesses favorable CB and VB positions for direct solar-to-chemical conversion, including organic fine synthesis and H_2 production.[128,129] Nevertheless, single-ingredient g-C_3N_4 catalyst suffers from high recombination ratio of photoexcited carriers and low electron transportation kinetic, which result in insufficient photoconversion efficiency.[130] To satisfy the requirements for high-performance photocatalysts, researchers endeavor to integrate g-C_3N_4 with various layered materials, such as MoS_2[131]. As mentioned above, 2H MoS_2 is a well-known two-dimensional layered metal dichalcogenide material that has received

scrutiny for potential application in the fields of optoelectronics and electrocatalysis, particularly in the hydrogen evolution reaction (HER)[132,133] Recent reports indicated that the coordinately unsaturated S-edge sites of 2H MoS_2 are the active sites for electrochemical reactions (HER, oxygen evolution (OER)/reduction (ORR) reactions).[134] Moreover, the interfacial electron transfer in few layer MoS_2 correlates with the number of layers and it could be significantly improved due to the interlayer electron hopping effect.[135] Owing to these characteristics, 2H MoS_2 nanostructures are well suited as photoactive materials in high-performance light energy conversion, field-effect transistors (FETs) and electroluminescent sensors.[136,137,138] Even though great progress has been made, the design and synthesis of few-layered MoS_2 nanostructures with ultrasmall lateral dimension (less than 50 nm) remains highly challenging. Conventional fabrication techniques for few layer MoS_2 nanoarchitectures involve different physical treatment processes of bulk MoS_2 solids, such as solvothermal-assisted liquid-phase exfoliation, electrochemical exfoliation and mechanical grinding.[139,140,141] Another promising photocatalyst for photocatalytic Cr(VI) reduction is tin disulfide (SnS_2), an inexpensive and nontoxic, layered semiconductor, which has attracted a great deal of scientific interest due to its suitable narrow band gap ($E_g \sim 2.2$ eV), significant chemical steadiness and safeness[142], and high CB potential (–0.114 V vs. NHE)[143]. It has lately pulled in awesome inquire about interest as a promising visible-light photocatalyst due to its low cost, nontoxicity, great stability and relatively high visible-light photocatalytic efficiency.[144,145,146] Nevertheless, SnS_2 shows generally low effectiveness in photocatalysis due to the increased recombination rate of its photoinduced holes and electrons.[147] It is presently acknowledged that, in contrast to a single-phase semiconductor, utilizing semiconductor composites can improve photocatalytic activity due to the successful separation of photogenerated electrons and holes.[148] To prevent the above limitations, researchers endeavor to integrate SnS_2 with various layered metal-free materials, such as g-C_3N_4.[149] Although g-C_3N_4 has rich surface properties that are attractive for catalysis, its photocatalytic efficiency is still limited due to the large optical band gap (2.7 eV) and the fast recombination rate of photogenerated electron−hole pairs.[150] The different position between the CB edge potentials of SnS_2 and g-C_3N_4 may allow electron transfer from the g-C_3N_4 to SnS_2 in SnS_2-modified g-C_3N_4 nano-heterostructures, improving the carriers' separation efficiency and, thus, the overall photocatalytic activity.

1.10 Thesis statement and objectives

Photocatalytic hydrogen generation through water splitting can be viewed as a promising solution to future energy demands. This approach utilizes a semiconductor-based photocatalytic system, which absorbs sunlight and splits water, producing hydrogen. In recent years, considerable scientific effort has been devoted to designing efficient catalysts for photo- and electro-chemical H_2 production. As a result, a number of organic–metal complexes and metal oxide and transition-metal chalcogenide nanostructures have been synthesized and used as potential cathode materials to split water by the hydrogen evolution reaction. On the other hand, aquatic environmental problems are mainly occurred by the water pollution caused by highly toxic metal ions– besides organic pollutants, which are difficult to deduct from ordinary chemical and biological methods. Consequently, heavy metal ions are concentrated in drinking water risking human health and well-being. Chromium is one of the major environmental pollutants, frequently entering into the aqueous ecosystem from natural and industrial sources. In natural environment, chromium exists in two oxidation states: trivalent Cr(III) and hexavalent Cr(VI), having distinctive chemical and toxicological characteristics. In the recent few years, semiconductor photocatalysis has enticed great attention due to its wide applications in puzzling out environmental problems associated with contaminated wastewaters by hazardous pollutants. For instance, reduction of toxic Cr(VI) to less harmful Cr(III) by light-excited CB electrons of a photocatalyst is a viable approach that holds great potential for environmental remediation applications. In this regard, a wide spectrum of metal oxide and sulfide semiconductors have been investigated as potential Cr(VI)-reducing catalysts under solar or visible light irradiation.

The scope of this doctoral dissertation is to produce a series of 2D/2D layered nano-heterostructures of transition metal dichalcogenides (MS_2, M = Mo, Sn) and graphitic carbon nitride (g-C_3N_4) and to investigate their photocatalytic activity for water splitting and reduction of Cr(VI) under UV and visible light irradiation. To this end, a combination of hydrothermal sulfurization route and liquid-phase exfoliation process to isolate 2D/2D nanojunction networks consisting of exfoliated g-C_3N_4 flakes and 2H MoS_2 nanosheets (NSs) with variable lateral sizes (i.e., ranging from 18 to 52 nm) was developed. The obtained MoS_2/g-C_3N_4 nano-heterostructures, where the tuning parameter is only the dimension of MoS_2 layers, provide a good platform to study and

understand the effect of interfacial area and exposed catalytic MoS_2 edge sites on their charge transport properties and photochemical activities. We use a combination of electron microscopy, photoluminescence and electrochemical spectroscopic studies to correlate the lateral dimension of MoS_2 layers with the charge separation efficiency and the observed photocatalytic hydrogen generation enhancement. These results of this work provide a fundamental understanding of the interface charge carrier dynamics and structural characteristics of MoS_2-modified g-C_3N_4 nano-heterostructures for efficient hydrogen evolution catalysis. Thereinafter, new 2D/2D nanojunction networks consisting of exfoliated g-C_3N_4 and Ni-doped MoS_2 nanosheets were successfully prepared and, for the first time, their effectiveness in photocatalytic detoxification of Cr(VI) (in $HCrO_4^-$ form) aqueous solutions was demonstrated. To prepare these materials we used a simple hydrothermal sulfurization method for the Ni-doped MoS_2 nanosheets and a subsequent liquid-phase exfoliation process for few-layer Ni-MoS_2/g-C_3N_4 composites. Using a combination of spectroscopic and electrochemical characterization techniques as well as theoretical computational (DFT) studies, we highlight the effect of Ni doping on the electronic band structure and photochemical activity of layered Ni-MoS_2/g-C_3N_4 heterostructures. Our results indicated that Ni-doped MoS_2 nanosheets not only effectively facilitate electron extraction from the g-C_3N_4, thus improving electron-hole separation, but also increase the charge density in Ni-MoS_2/g-C_3N_4 junctions, thus enhancing the photocatalytic efficiency notably without the use of any sacrificial reagent. The results exhibit the great potential of the Ni-doped MoS_2/g-C_3N_4 nano-heterostructures as excellent photocatalysts for practical application in environmental remediation. In addition, also for the first time, a simple and cost-effective photochemical method for 2D/2D nanojunction structures consisting of exfoliated g-C_3N_4 flakes and SnS_2 nanosheets is proposed. The functionality of these new materials for the detoxification of aqueous Cr(VI) solutions under UV and visible light illumination is also addressed. Actually, under photochemical deposition, the growth of SnS_2 nanosheets would preferentially take place at the active sites (photocatalytic redox centers) of the g-C_3N_4 surface. Therefore, the resulting SnS_2/g-C_3N_4 heterostructures can offer several advantages for photocatalysis due to the unique electronic communication and interfacial charge dissociation between SnS_2 and g-C_3N_4 components. By using a combination of spectroscopic techniques, we provide an understanding of the charge transport dynamics and the photochemical reaction kinetics

at the catalyst interface. We demonstrate that charge carrier transport through SnS_2–g-C_3N_4 interface effectively suppresses charge recombination, instigating Cr(VI) photoreduction and water oxidation reactions with high efficiency. The results of this work demonstrate the great potential of the SnS_2-decorated g-C_3N_4 nano-heterostructures as viable photocatalysts for environmental applications, including detoxification of Cr(VI)-contaminated aquatic systems.

Chapter 2 – Experimental Section

2.1 Synthesis of C_3N_4

In a typical synthesis of C_3N_4, 10 g of urea (≥99.5%, Sigma-Aldrich) was put into a porcelain crucible covered with a glass petri plate. The crucible was directly placed in a pre-heated high-temperature furnace and kept at 550 °C for 1 h. The final yellow product was collected after the furnace reached room temperature.

2.2 Synthesis of MoS_2 nanosheets

In a typical experiment, 12-phosphomolybdic acid ($H_3PMo_{12}O_{40}$, PMA, ≥99.99%, Sigma-Aldrich) was dissolved in 10 mL of deionized water with stirring. Next, 50 equivalents (relative to PMA concentration) of thioacetamide (TAA, ≥99%, Aldrich) was slowly added to the PMA solution. After being stirred for 1 h at room temperature, the resulting dark green solution was then placed in a Teflon-lined autoclave reactor and heated in an oven at 200 °C for 12 h. The black precipitate (MoS_2) was collected by centrifugation, and subsequently washed with water and dried at 60 °C. A series of MoS_2 NSs with different sizes of lateral width (i.e., 18, 32, 39 and 52 nm) were prepared following the above-mentioned procedure, by varying the concentration of PMA (from 13 to 27 to 55 to 82 μmol) and TAA (50 equivalents). Bulk-like MoS_2 flakes were also prepared following the same procedure, with the exception that 0.09 mmol of $(NH_4)_6Mo_7O_{24}\cdot 4H_2O$ (≥99%, Alfa Aesar) and 2.7 mmol of TAA were used as initial reactants.

2.3 Preparation of MoS_2/g-C_3N_4 nano-heterostructures

The graphitic carbon nitride (g-C_3N_4) sheets were produced by liquid exfoliation of the C_3N_4 powder in isopropanol (IPA, ≥99.7%, Honeywell). Briefly, 100 mg of as-made C_3N_4 was added to 50 mL of IPA into a 100-mL beaker, and the mixture was sonicated for 2 h at room temperature, giving a light-yellow suspension. In a separate vial, 0.12 mmol of MoS_2 NSs was added to a 2:1 water:IPA solution (30 mL) into a 50-mL beaker

and the mixture was sonicated for 2 h at room temperature, forming a homogeneous black suspension. After that, the above solutions were mixed together and sonicated for another 2 h. Finally, the product was collected by centrifuging and dried at 60 °C. A series of 2D/2D MoS_2/g-C_3N_4 heterostructures with different loading amounts and lateral sizes (denoted as MSCN-n; all these samples contain 20 wt% MoS_2) of MoS_2 were fabricated following the method as referred above. The amount of MoS_2 NSs used in reactions was varied between 31, 62, 125 and 187 μmol to give a series of hybrid materials with 5, 10, 20 and 30 wt % MoS_2 loading.

2.4 Synthesis of Me-doped MoS_2 nanosheets

Metal-doped MoS_2 nanosheets with different doping level (denotes as *n*-MeMS, where *n* refers to Me content (Ni, Co, In, Sn, Zn), *n* (mol% Me) = Me/(Me + Mo) x 100) were prepared by hydrothermal sulfurization of monovacant Keggin $[PMo_{11}O_{39}]^{7-}$ clusters in the presence of $NiCl_2$, $CoCl_2$, $InCl_3$, $SnCl_4$ or $ZnCl_2$ compound. Monovacant Keggin-type phosphomolybdate $Na_7PMo_{11}O_{39}$ (denoted as PMo_{11}) clusters were prepared following a similar procedure reported previously.[151] For a typical synthesis of the Me-doped MoS_2 nanosheets, PMo_{11} (43 μmol) and pre-weighed amount of $NiCl_2{\cdot}6H_2O$ (98%, abcr GmbH), $CoCl_2{\cdot}6H_2O$ (≥98%, Alfa Aesar), $InCl_3{\cdot}4H_2O$ (97%, Aldrich), $SnCl_4{\cdot}5H_2O$ (98%, Aldrich) or $ZnCl_2$ (≥98%, Honeywell) were dissolved in 10 mL of deionized (DI) water, followed by the addition of 120 equivalents (relative to PMo_{11}) of thioacetamide (TAA, ≥99%, Aldrich). The resulting mixture was stirred for about 1 h and then placed in a Teflon-lined autoclave (50 mL) and heated to 200 °C for 12 h. After cooling the solution to room temperature, the black precipitate was collected by centrifugation, washed with water and dried at 60 °C overnight. A series of metal-doped MoS_2 nanosheets with 3% doping level (denotes as 3-MeMS, where 3 refers to metal content (mol% Ni, Co, In, Sn or Zn) = Me/(Me + Mo) x 100) was prepared following the above-mentioned procedure, using 3.6, 3.6, 3.6, 5.3 and 2.1 mg of $NiCl_2{\cdot}6H_2O$, $CoCl_2{\cdot}6H_2O$, $InCl_3{\cdot}4H_2O$, $SnCl_4{\cdot}5H_2O$ and $ZnCl_2$, respectively.

2.5 Preparation of Me-MoS_2/g-C_3N_4 heterostructures

A series of 2D/2D Me-doped MoS_2/g-C_3N_4 nano-heterostructures (Me = Ni, Co, In, Sn and Zn) containing 3% Me doping (denoted as 3-MeMS/GCN; all these samples feature 20 wt% Me-MoS_2 content) was prepared by depositing Me-doped MoS_2 nanosheets on the surface of g-C_3N_4 via a liquid-phase exfoliation method. The C_3N_4 sheets used in this study were synthesized by thermal decomposition of urea at 550 °C, according to the previously reported method. Graphitic carbon nitride (g-C_3N_4) was produced by liquid exfoliation of the C_3N_4 powder in isopropanol solution. In a typical experiment, as-made C_3N_4 sample (100 mg) was suspended in 50 mL of isopropanol (IPA, ≥99.7%, Honeywell) in a 100-mL beaker, and the mixture was sonicated for 2 h at room temperature, giving a light-yellow suspension. In a separate vial, Me-doped MoS_2 nanosheets (0.09 mmol) was added to a water:IPA mixture (2:1 v/v, 30 mL) with sonication for 2 h to obtain a homogeneous suspension. Afterwards, the above solutions were mixed together and then sonicated for another 2 h at room temperature. The final products containing 20 wt% Me-MoS_2 were collected using a centrifuge and dried overnight at 60 °C.

2.6 Synthesis of Ni-doped MoS_2 nanosheets

Ni-doped MoS_2 nanosheets with different Ni doping level were prepared by hydrothermal sulfurization of monovacant Keggin $[PMo_{11}O_{39}]^{7-}$ clusters in the presence of $NiCl_2$. Monovacant Keggin-type phosphomolybdate $Na_7PMo_{11}O_{39}$ (denoted as PMo_{11}) clusters were prepared following a similar procedure reported previously. For a typical synthesis of the Ni-doped MoS_2 nanosheets, PMo_{11} (43 μmol) and pre-weighed amount of $NiCl_2 \cdot 6H_2O$ (98%, abcr GmbH) were dissolved in 10 mL of deionized (DI) water, followed by the addition of 120 equivalents (relative to PMo_{11}) of thioacetamide (TAA, ≥99%, Aldrich). The resulting mixture was stirred for about 1 h and then placed in a Teflon-lined autoclave (50 mL) and heated to 200 °C for 12 h. After cooling the solution to room temperature, the black precipitate was collected by centrifugation, washed with water and dried at 60 °C overnight. A series of Ni-MoS_2 nanosheets with different Ni doping level (denotes as *n*-NMS, where *n* refers to

different Ni content, *n* (mol% Ni) = Ni/(Ni + Mo) x 100 = 1, 3, 5, 10 and 15%) was prepared following the above-mentioned procedure, by varying the Ni amount from 6 to 15 to 30 to 60 to 90 μmol.

Besides, for comparison, undoped MoS_2 nanolayers (denotes as MS) were also prepared with a similar procedure, but without addition of Ni.

2.7 Preparation of Ni-MoS_2/g-C_3N_4 heterostructures

A series of 2D/2D Ni-doped MoS_2/g-C_3N_4 nano-heterostructures with different Ni content (denoted as *n*-NMS/GCN, where *n* refers to the mole percent of Ni doping; all these samples contain 30 wt% Ni-MoS_2) was prepared by depositing Ni-doped MoS_2 nanosheets on the surface of g-C_3N_4 via a liquid-phase exfoliation method. The carbon nitride (g-C_3N_4) sheets used in this study were synthesized by thermal decomposition of urea at 550 °C, according to our previously reported method see ref. [30] in the main text. Graphitic carbon nitride (g-C_3N_4) was produced by liquid exfoliation of the C_3N_4 powder in isopropanol solution. In a typical experiment, as-made C_3N_4 sample (100 mg) was suspended in 50 mL of isopropanol (IPA, ≥99.7%, Honeywell) in a 100-mL beaker, and the mixture was sonicated for 2 h at room temperature, giving a light-yellow suspension. In a separate vial, Ni-doped MoS_2 nanosheets (0.14 mmol) was added to a water:IPA mixture (2:1 v/v, 30 mL) with sonication for 2 h to obtain a homogeneous suspension. Afterwards, the above solutions were mixed together and then sonicated for another 2 h at room temperature. The product was collected using a centrifuge and dried overnight at 60 °C. A series of 2D/2D Ni-doped MoS_2/g-C_3N_4 nano-heterostructures with different Ni content (denoted as *n*-NMS/GCN, where *n* refers to the mole percent of Ni doping; all these samples contain 30 wt% Ni-MoS_2) were synthesized following the method as referred above. The amount of Ni-doped MoS_2 nanosheets (3 mol% Ni content) used in reactions was also varied between 45, 90, 140 and 180 μmol to give a series of hybrid materials with 10, 20, 30 and 40 wt% Ni-MoS_2 concentration.

For comparison, undoped MoS_2/g-C_3N_4 heterostructure with 30 wt% MoS_2 concentration (denoted as MS/GCN) was also synthesized under similar condition,

using MoS_2 nanosheets. A bulk heterostructure consisting of 3% Ni-doped MoS_2 microflakes (30 wt%) and exfoliated g-C_3N_4 layers (denoted as 3-NMS/GCN-*b*) was also prepared through a similar wet deposition process. The 3% Ni-doped MoS_2 microflakes were synthesized following a similar procedure as described for *n*-NMS, with the exception that 0.068 mmol of $(NH_4)_6Mo_7O_{24}\cdot 4H_2O$ (≥99%, Alfa Aesar) and 5.3 mmol of TAA were used as initial reactants. All the as-prepared materials were dried at 130 °C under vacuum for at least 3 h to remove residual IPA molecules.

2.8 Photodeposition of SnS_2

In a typical synthesis process, 50 mg of C_3N_4 were added in a solution containing 1:1 deionized water:ethanol (30 mL) in a 50 mL beaker and the resulting mixture was first stirred overnight at room temperature, and then sonicated for 2 h to give a light-yellow suspension. A series of 2D/2D SnS_2/g-C_3N_4 heterostructures with different SnS_2 loading amounts were prepared following the consequential procedure. For a typical synthesis, a precise amount of $SnCl_4\cdot 5H_2O$ were dissolved in 2 mL deionized water and directly were added dropwise into the g-C_3N_4/water/ethanol mixture, followed by the addition of sulfur (S_8). The final solution was put into an air-tight Pyrex glass reactor and was de-aerated by Ar gas for at least 40 min under stirring. After that, the solution was irradiated with a 50 W LED (λ=375 nm) for 2 h. The resulting light brown product was collected by centrifugation, washed several times with ethylenediamine and deionized water, and dried at 130 °C for 3 h under vacuum.

The amounts of $SnCl_4\cdot 5H_2O$ and sulfur powder used in the above reaction were varied between 31, 68, 117 and 183 μmol (referred to $SnCl_4\cdot 5H_2O$) and 306, 683, 1179 and 1825 μmol (referred to sulfur powder) to give a series of hybrid *n*-SnS_2/GCN heterostructures with different weight percent of SnS_2 (*n*), i.e., 10, 20, 30 and 40 wt%, respectively.

For comparison, we also prepared a SnS_2 microstructured sample through direct reaction of $SnCl_4$ (1 mmol) and Na_2S (2.5 mmol) compounds in water (5 mL) for 2 h. The brown-colored product was isolated by centrifugation, wasted with water and ethanol, and dried at 80 °C for 6 h. The phase purity of the as-prepared sample was verified by X-ray diffraction (XRD).

2.9 Photocatalytic H_2 evolution experiments

Photocatalytic experiments for hydrogen evolution were performed in an airtight Pyrex glass reactor. In a typical experiment, 20 mg of the catalyst was dispersed with stirring in 20 mL of water/methanol (4:1 v/v) solution, and then the mixture was deaerated by Ar gas for at least 30 min. The reaction solution was cooled to 20 ±2 °C using a water-cooling system and irradiated at $\lambda > 360$ nm light using a 300-W Xenon lamp (Variac Cermax). The generated H_2 was detected by taking 100 μL of gas from the headspace of the reactor using a gastight syringe and analyzed by a Shimadzu GC-2014 gas chromatograph equipped with a thermal conductivity detector (TCD), using Ar as the carrier gas.

The apparent quantum yield, $QY = (2 \times N_{H2})/N_{hv}$ where N_{H2} and N_{hv} are the numbers of evolved H_2 molecules and incident photons, respectively, were estimated by obtaining the amount of evolved hydrogen at a $\lambda = 410 \pm 10$ nm irradiation wavelength. The incident photon number was determined with a StarLite power meter equipped with a FL400A-BB-50 thermal sensor (Ophir Optronics Ltd).

2.10 Photocatalytic Cr(VI) reduction experiments

In a typical experiment, the photocatalyst was suspended in an aqueous solution (50 mL) containing Cr(VI) (50 mg L^{-1}) in a Pyrex glass cell. The Cr(VI) solution was prepared by dissolving $K_2Cr_2O_7$ in DI water, and the pH was adjusted to 2 by adding small aliquots of concentrated H_2SO_4. The temperature of the suspension was maintained at 20 ±2 °C by using a water-cooling system. The reaction solution was stirred in the dark for 20 minutes to establish adsorption/desorption equilibrium and then irradiated with a 300-W Xenon lamp (Variac Cermax) equipped with a long-pass filter ($\lambda > 360$ nm). During the reaction, the concentration of Cr(VI) in the mixture was determined using the 1,5-diphenylcarbazide (DPC) colorimetric method. The color change was monitored using a Perkin Elmer Lambda 25 UV–vis spectrometer. The normalized concentration (C_t/C_o) of Cr(VI) solution at different illumination times was considered in proportion to the absorbance of DPC-Cr(VI) complex at 540 nm.

For a three-electron reduction of Cr(VI) to Cr(III), the apparent quantum yield (QY) of the reaction was determined by evaluating the amount of reduced Cr(VI) at λ = 365 and 410 ±10 nm irradiation wavelengths using LED light sources.

$$QY = \frac{3 \text{ x number of reduced Cr(VI)}}{\text{number of incident photons}} \quad (3)$$

The power density of the incident light was determined by using a StarLite power meter equipped with a FL400A-BB-50 thermal detector (Ophir Optronics Ltd).

2.11 Photocatalytic water oxidation reaction

A photocatalytic Cr(VI) reduction experiment was performed as described above in a vacuum-tight cell containing 1 g L^{-1} of catalyst and 50 mL of $K_2Cr_2O_7$ aqueous solution (50 mg L^{-1}, pH = 2). Prior to experiment, the reaction solution was deaerated by purging with He for at least 40 min. The gas-phase effluent was analyzed using a gas chromatograph (Shimadzu GC-2014, He carrier gas) equipped with thermal conductivity detector (TCD). The evolved O_2 was also monitored in situ with a Hiden HPR-20 QIC mass spectrometer.

2.12 Physical characterization

Powder X-ray diffraction (XRD)

Powder X-ray diffraction (XRD) patterns were recorded on a PANalytical X´Pert Pro X-ray diffractometer with a Ni-filtered Cu Kα source (λ = 1.5418 Å) operating at 45 kV and 40 mA using.

X-ray photoelectron spectroscopy (XPS)

X-ray photoelectron spectroscopy (XPS) experiments were conducted on a Leybold EA-11 analyzer with Al Kα radiation as the energy source (1486.6 eV). Samples were prepared by pressing the powder on a Pb sheet in order to be introduced in an ultra-high vacuum chamber. The analyzed area was approximately 2×5 mm^2 and the XPS spectra was collected at a 0 degrees take-off angle. All the binding energies were referenced to the C 1s line at 284.8 eV.

Transmission electron microscopy (TEM)

Transmission electron microscopy (TEM) images were taken on a JEOL JEM-2100 electron microscope (LaB_6 filament) operated at 200 kV. Samples were finely ground, ultrasonic dispersed in ethanol and then drop-casted on a holey carbon-coated Cu grid.

Nitrogen physisorption

N_2 adsorption-desorption isotherms were obtained at –196 °C using a Quantachrome NOVA 3200*e* analyzer. Before analysis, all the samples were outgassed at 100 °C for 12 h under vacuum ($<10^{-5}$ Torr). The specific surface areas were calculated by applying the Brunauer-Emmett-Teller (BET) method to the adsorption data in relative pressure (P/P_o) range 0.04–0.24, and the total pore volumes were estimated from the amount of adsorbed N_2 at a P/P_o of 0.98.

Elemental analysis

Elemental microprobe analyses were performed by a JEOL JSM-6390LV scanning electron microscope (SEM) equipped with an Oxford INCA PentaFETx3 energy dispersive X-ray spectroscopy (EDS) detector (Oxfordshire, UK). Data acquisition was performed at least five times for each sample using an accelerating voltage of 20 kV and a 100-s accumulation time.

Raman spectroscopy

Raman spectra were collected on a Nicolet Almega XR micro-Raman spectrometer using a laser line at 473 nm wavelength.

Infrared (IR) spectroscopy

Infrared (IR) spectra of dried samples pressed into KBr pellets were obtained on a Perkin Elmer Model Frontier FT-IR spectrometer with 2 cm^{-1} resolution.

UV–vis/near-IR spectroscopy

Diffuse reflectance UV–vis/near-IR spectra were measured on a Perkin Elmer Lambda 950 optical spectrophotometer with $BaSO_4$ as a reference. The absorption spectra were converted from diffuse reflectance data using the Kubelka-Munk function: $f(R) = (1-R)^2/(2R)$, where R is the measured reflectance.[152] The energy bandgap (E_g) of semiconductors were derived from Tauc plot analysis, that is, the x-intercept of the linear portion of the $(f(R)hv)^r$ versus photon energy (hv) data, where h is the Planck's constant, v is the light frequency, and r is equal to 2 or ½ for direct and indirect allowed transitions, respectively.[153]

Photoluminescence (PL) spectroscopy

Photoluminescence (PL) spectra were recorded at room temperature on a lumina fluorescence spectrometer (Thermo scientific) equipped with a 150 W Xenon lamp.

2.13 Electrochemical measurements

Electrochemical impedance spectroscopy (EIS) and Mott-Schottky measurements were performed in a 0.5 M Na_2SO_4 aqueous electrolyte (pH 7) using a Metrohm Autolab PGSTAT 302N potentiostat. A three-electrode electrochemical cell with a Pt wire as the counter electrode and an Ag/AgCl (3M KCl) as the reference electrode was used to study the samples. Mott-Schottky plots were obtained at 1 kHz, using a 10-mV alternating current (AC) voltage amplitude. For Nyquist plots, the different current output was measured throughout a frequency range of 1 Hz to 1 MHz using a small AC perturbation of 20 mV, under open-circuit potential conditions. All the EIS experiments were conducted in the dark. The measured flat-band potentials were converted to the normal hydrogen electrode (NHE) scale using the Nernst equation, $E_{NHE} = E_{Ag/AgCl} + 0.197 + 0.059 \times pH$.

The working electrodes were fabricated as follows: 10 mg of each sample was ultrasonically mixed with 1 mL of deionized water to form a homogeneous suspension. Glass slides (1.5 × 2 cm^2) coated with fluorine-doped tin oxide (FTO, 9 Ω sq^{-1}) were cleaned thoroughly by sonication in acetone and then in isopropanol for 15 min and dried at 100 ºC for 10 min. Next, the FTO substrates were further treated with a UV-ozone plasma for 5 min. The samples were drop-casted onto FTO substrates, which were masked with an epoxy resin to leave an exposure area of 1.0 cm × 1.0 cm, and heated for 30 min at 60 ºC.

For Nyquist plots, the different current output was measured throughout a frequency range of 1 Hz to 1 MHz using a small AC perturbation of 10 mV, under open-circuit potential conditions. The electrochemical impedance data were fitted to an equivalent circuit model using ZView Software.

For semiconductor-electrolyte interface, the capacitance C_{sc} of the space charge region can be described as follows:

$$\frac{1}{C_{SC}^2} = \frac{2(E-E_{FB})}{\varepsilon\varepsilon_o A^2 e_o N_d} \quad (4)$$

where, C_{SC} is the space charge capacitance, E is the applied potential, E_{FB} is the flat band potential of the semiconductor, N_d is the donor density of electrode material, ε is the relative dielectric constant (4.6 for g-C_3N_4), ε_o is the permittivity under the vacuum (8.8542×10^{-10} F cm^{-1}), A is the area of the electrode, and e_o is the elementary charge (1.602×10^{-19} C).

The donor concentration (N_d) of the samples can be calculated using the following equation:

$$N_d = \frac{2(E-E_{FB})\cdot C_{SC}^2}{\varepsilon\varepsilon_o e_o} \quad (5)$$

where the term $(E - E_{FB})\cdot C_{SC}^2$ is the reciprocal of the slope of the Mott-Schottky plot.

2.14 Photoelectrochemical measurements

Chronoamperometric and open-circuit photovoltage decay measurements were performed on a VersaSTAT 4 electrochemical workstation (Princeton Applied Research, USA) in a 0.5 M Na_2SO_4 solution (pH = 6.8). The photoelectrochemical studies were conducted in an air-tight three-electrode cell, consisting of a catalyst-coated FTO working electrode, an Ag/AgCl (saturated KCl) reference electrode, and a Pt wire counter electrode. Photochronoamperometric data were obtained at a bias voltage of 0.2 V (vs Ag/AgCl).

2.15 Theoretical calculations

Density functional theory calculations (DFT) calculations were performed using the Vienna ab initio Simulation Package (VASP)[154] with the projector augmented wave method (PAW) for treating core electrons and nuclei.[155] For the exchange–correlation functional, we adopted the generalized gradient approximation (GGA) of Perdew–Burke–Ernzerhof (PBE)[156], which is well suited to our system. For the pristine MoS_2 monolayer, we find a lattice constant of 3.18 Å and an electronic energy band gap of 1.61 eV. Defected structures were studied using supercells of varying size in order to simulate systems with different defect concentrations. In supercell calculations, wave functions were expanded on a plane wave basis set with a 660-eV kinetic energy cutoff and Γ-centered Monkhorst-Pack k-point mesh for the Brillouin zone sampling was

employed. Periodic boundary conditions and a large vacuum in the perpendicular to the surface plane direction were applied. Atomic positions were fully relaxed for all structures.

Chapter 3 – Results & Discussion

3.1 MoS_2-modified g-C_3N_4 heterostructures

3.1.1 Structure and morphology of MoS_2/g-C_3N_4

2H MoS_2-modified few-layered g-C_3N_4 nanostructures with different lateral-sized MoS_2 nanosheets (NSs) were prepared using a two-step synthetic protocol, which involves low-temperature sulfurization and liquid-phase exfoliation process.[157] A schematic illustration of the synthesis of MoS_2/g-C_3N_4 nano-heterostructures is shown in **Figure 25**. Briefly, 2D nanolayers of MoS_2 were first obtained through chemical conversion of 12-phosphomolybdic acid ($H_3PMo_{12}O_{40}$, PMA) using thioacetamide (TAA). During the synthesis, TAA is readily decomposed and acts as sulfur source (generating S^{2-} ions) and reducing agent for the formation of MoS_2. We found that this newly developed synthetic route is highly reproducible and permits control over the grain size of MoS_2 nanolayers, which is directly related to the concentration of PMA; particularly, by taking advantage of this chemistry, the lateral dimension of MoS_2 NSs could be readily controlled within the 18–52 nm range with very small polydispersity (typically within 4–6 nm). During the sulfidation process, the thioacetamide is hydrolyzes to form H_2S, which causes the decomposition of 12-phosphomolybdic clusters to MoO_x oxide species and their consequent conversion into MoS_2 nanosheets. We believe that the concentration of the PMA precursor affects the nucleation and growth of small MoO_x oligomers and, thus, the size of the final MoS_2 particles.

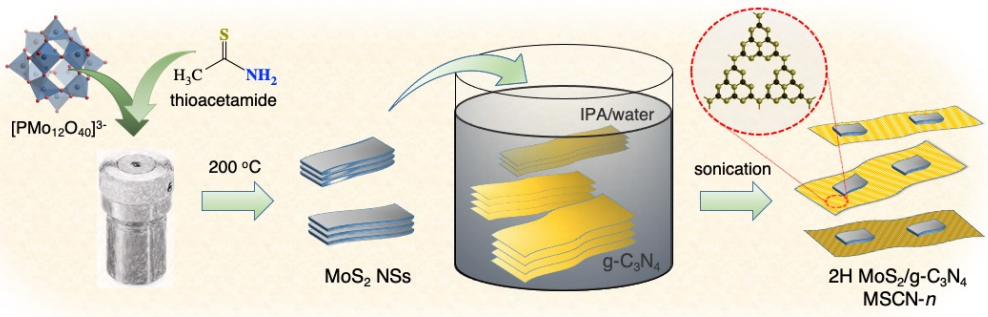

Figure 25. Schematic representation of the synthesis of MoS_2 NSs and MoS_2/g-C_3N_4 (MSCN-*n*) nano-heterostructures.

The crystallinity and phase purity of the as-made MoS_2 NSs were confirmed by X-ray diffraction (XRD) and Raman spectroscopy. The XRD pattern in **Figure 26** indicates that the MoS_2 NSs have a hexagonal (2H) phase (JCPDS card no. 77-1716; space group *P*63/*mmc*).[158] In addition, the XRD pattern shows broad reflections consistent with the small grain composition of MoS_2.

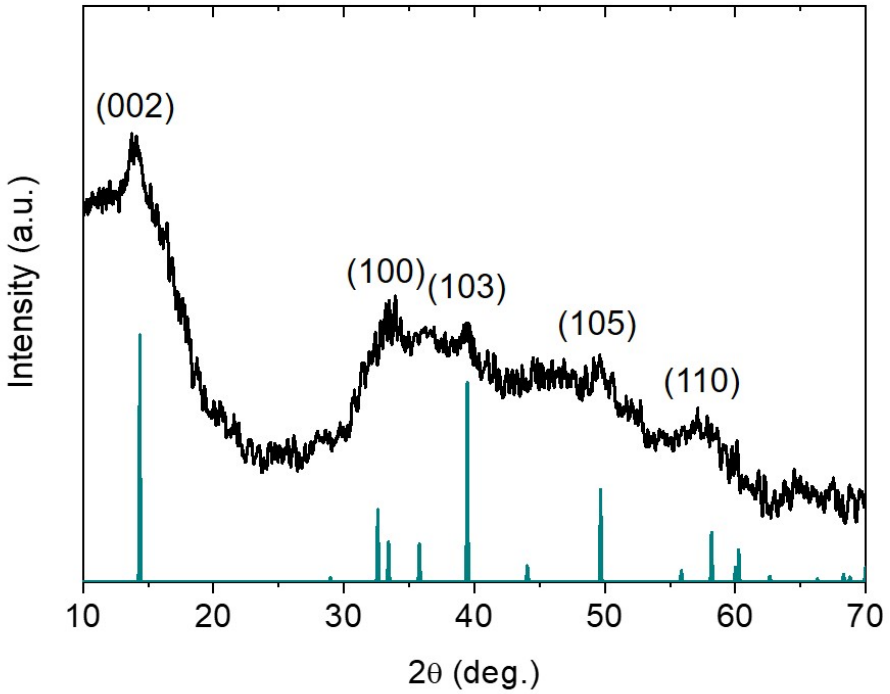

Figure 26. XRD pattern of the MoS_2 NSs with 39 nm lateral size. The peaks correspond to the hexagonal phase of MoS_2 according to the JCPDS card no. 77-1716.

A 2H crystal phase of MoS_2 is also confirmed by the characteristic in-plane (E^1_{2g}) and out-of-plane (A_{1g}) Mo–S vibration modes[159] at 384 and 407 cm^{-1}, respectively, in the Raman spectrum shown in **Figure 27**. Of none, the MoS_2 NSs exhibit a variable shift in the frequency between the E^1_{2g} and A_{1g} Raman peaks close to 22.8 cm^{-1}, which is lower relative to bulk MoS_2 (ca. 25.4 cm^{-1}). We interpret this small, but distinct, red shift as the weak interlayer coupling (along the c-axis) in MoS_2 NSs, which reduces the out-of-plane restoring forces operating on the atoms.[160] The Raman spectra and the XRD results together indicate that the PMA compound was indeed successfully decomposed into MoS_2 under the present liquid-phase conditions. Next, a series of 2D/2D MoS_2/g-C_3N_4 nano-heterojunctions with adjustable loading and lateral dimension of MoS_2 layers were realized by deposition of MoS_2 NSs onto a few-layered g-C_3N_4 sheets. Bulk g-C_3N_4 can be chemically delaminated into few-layered sheets by

a sonication-assisted liquid exfoliation technique; this process is sufficient to break the interlayer van der Waals and hydrogen bonding interactions in g-C_3N_4.[161] The obtained catalysts with 20 wt % MoS_2 loading content are labelled as MSCN-*n*, where n denotes heterostructures with different MoS_2 lateral dimensions.

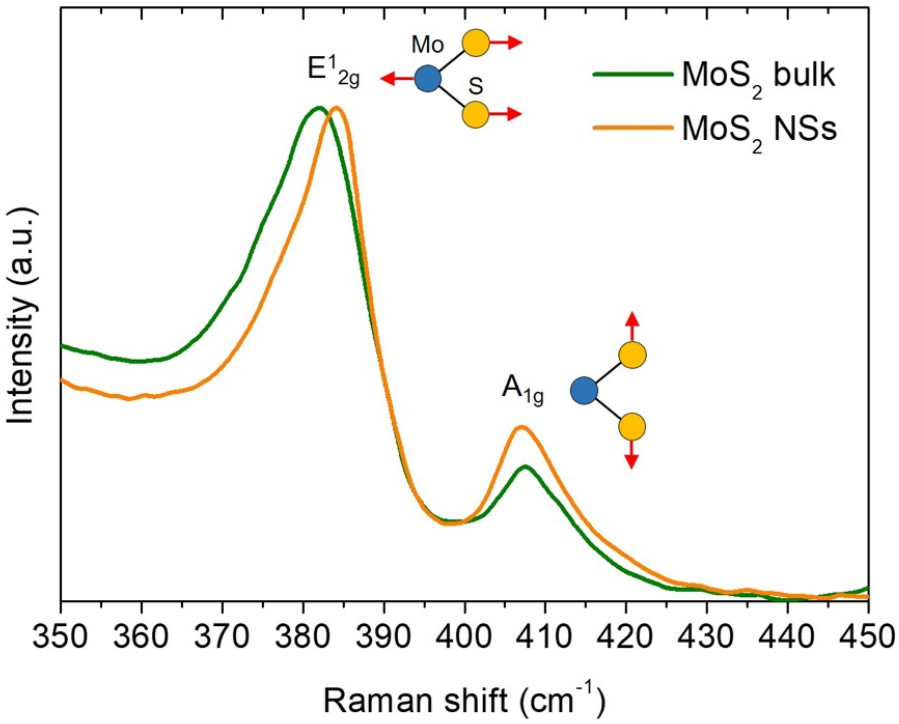

Figure 27. Raman spectra of the 39 nm-sized MoS_2 layers and bulk MoS_2 flakes. The Raman shifts at ~384 cm^{-1} and ~407 cm^{-1} are assigned to the in-plane (E^1_{2g}) and out-of-plane (A_{1g}) modes of Mo–S, respectively.

The morphological features of the MSCN-*n* materials (20 wt % MoS_2 loading) were investigated by transmission electron microscopy (TEM). **Figure 28a** and **b** show typical TEM images taken of the MSCN-3 sample, which is the most active catalyst of this series. The TEM micrographs of other samples are given in **Figure 29**. The images affirm the presence of few-layered MoS_2 nanostructures that are spread over the surface of the graphitic C_3N_4. In addition, close inspection of the heterojunction network with high-resolution TEM (HRTEM) reveals an interlayer spacing (along the (002) direction) of 6.5 Å for MoS_2 NSs (appeared as dark spots) and ~3.2 Å for g-C_3N_4 (appeared as light areas), **Figure 28b**. These results suggest a small expansion in the interlayer spacing of MoS_2 NSs relative to the bulk MoS_2 (6.2 Å)[162], possibly due to the very small grain size.[163] Selected-area electron diffraction (SAED) pattern recorded

on a small area of the MSCN-3 structure further confirms the nanocrystallite size of MoS_2, showing two broad concentric Debye-Scherrer diffraction rings. Associated with XRD and Raman results, the angular position of these rings corroborates to the hexagonal phase of MoS_2, as reasonably assigned to the (100) and (110) crystal planes of 2H MoS_2. Through this analysis, we also obtained the MoS_2 lateral-size distribution of MSCN-*n* samples, and the corresponding results are presented in insets of **Figures 28a** and **29**. The size histograms (based on the analysis of more than 80 individual MoS_2 layers) unveils a strong correlation of reaction conditions with the lateral dimension of MoS_2, in which the MoS_2 layers show an incremental growth in the size from 18 to 52 nm as the concentration of PMA increases.

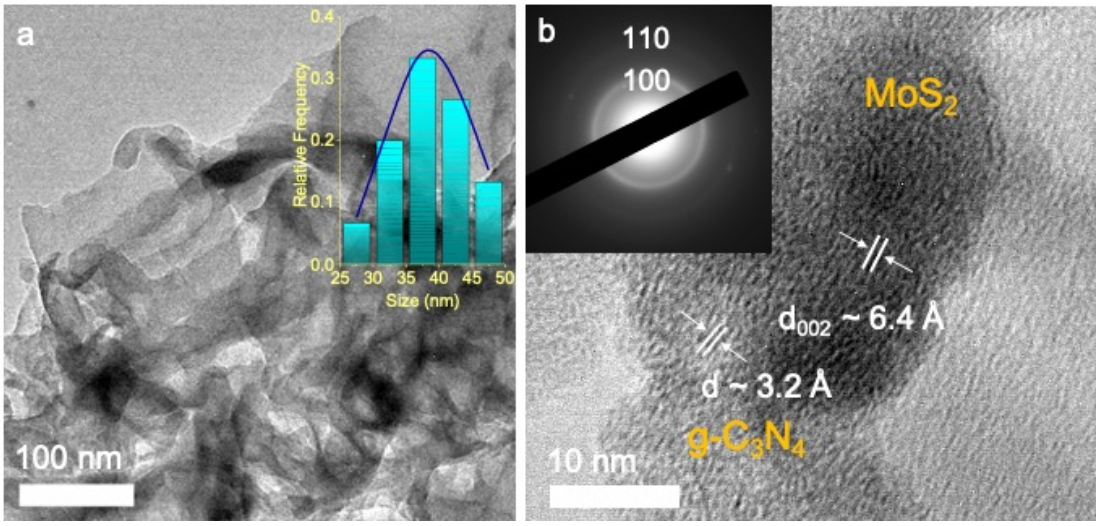

Figure 28. (a) Typical TEM image showing the layers morphology (Inset: Histogram of the MoS_2 lateral-size distribution) and (b) high-resolution TEM (Inset: SAED pattern displaying the (100) and (110) lattice planes of the hexagonal 2H MoS_2) of an isolated MoS_2 NSs.

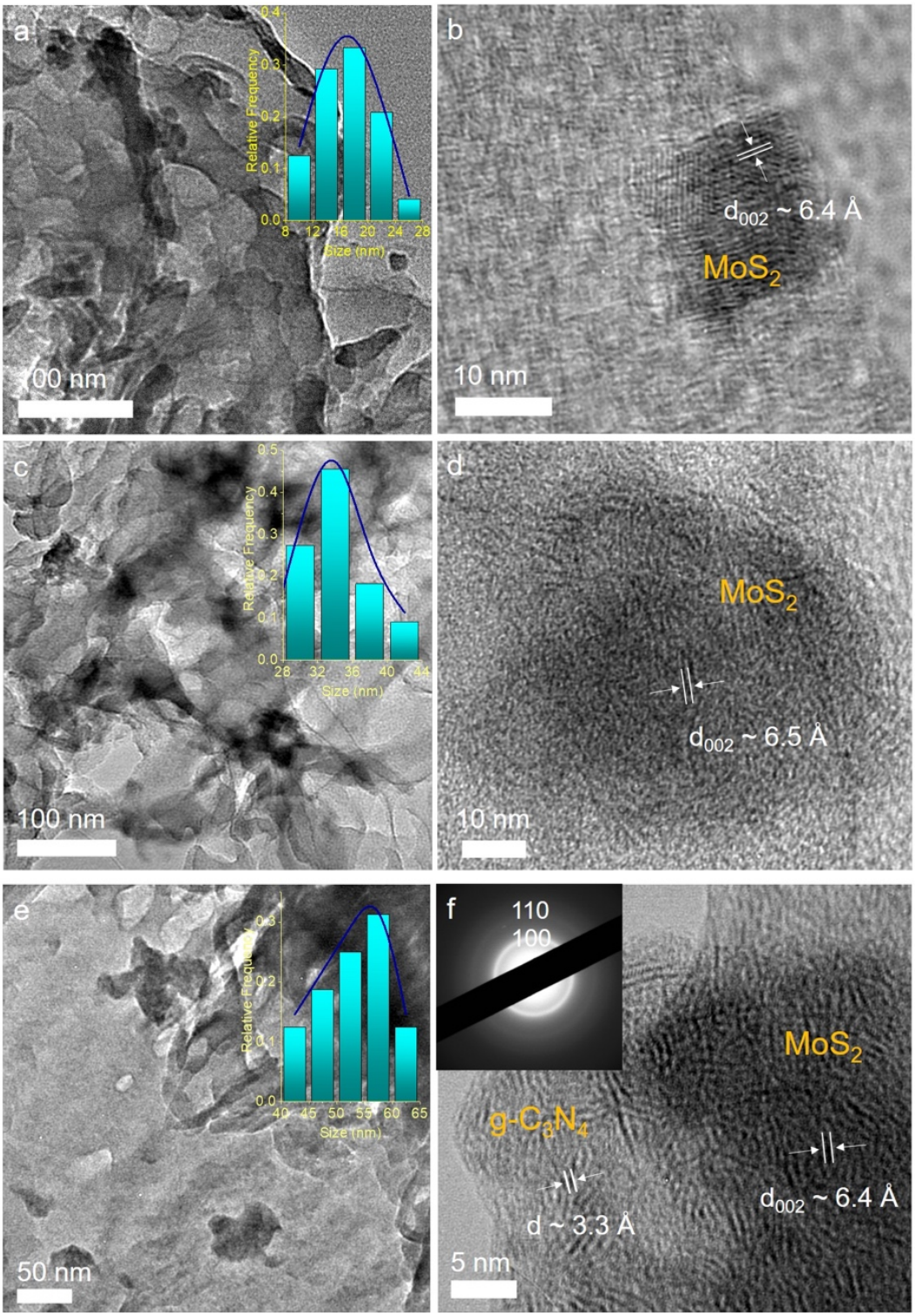

Figure 29. Typical TEM images and (insets of panels (a), (c) and (e)) the corresponding lateral-size distribution histograms of the MoS_2 NSs for the MSCN-*n* (*n* = 1, 2 and 4) catalysts. The inset of panel (f) shows typical SAED pattern of the hexagonal 2H MoS_2.

In addition to TEM analysis, X-ray diffraction was also carried out to examine the layered structure of the exfoliated g-C_3N_4. A typical XRD pattern of the MSCN-3

sample is shown in **Figure 30**. It shows a strong diffraction peak at 27.6° and a weak feature at 13.2°, which are assigned to the (002) interlayer stacking of the conjugated aromatic rings and (100) in-plane tri-s-triazine packing motif, respectively, of the graphitic C_3N_4 (JCPDS card no. 87-1526).[164] By comparing the XRD patterns of samples MSCN-3 and g-C_3N_4, it is apparent that the intensity of the (002) peak decreases after MoS_2 deposition, implying that MoS_2 layers are mostly studded on the g-C_3N_4 (002) surface. Also, the relative intensity of the (100) reflection over the high-index (002) diffraction line is reduced in the MSCN-3 heterostructure, which could be ascribed to the strong interactions between the MoS_2 and g-C_3N_4 layers, in consistent with TEM observation.[165] Meanwhile, we did not observe any diffraction peaks from MoS_2 in XRD pattern of MSCN-3, possibly due to the nanoscale size and high dispersion of the MoS_2 layers. In good accordance with the XRD results, Fourier transform infrared (FT-IR) spectroscopy further corroborates the poly-condensation structure of g-C_3N_4, judging from the characteristic vibration bands of s-triazine (C_3N_3) units at 812 cm^{-1} (ν(C=N–C)) and heptazine (C_6N_7) units at 1240 cm^{-1} (ν(C–N)) and 1637 cm^{-1} (ν(C=N))[166], as seen in **Figure 31**. The FT-IR analysis also revealed the presence of un-reacted amino groups (–NH_2 and/or =NH) by broad peaks at 3170–3450 cm^{-1}.

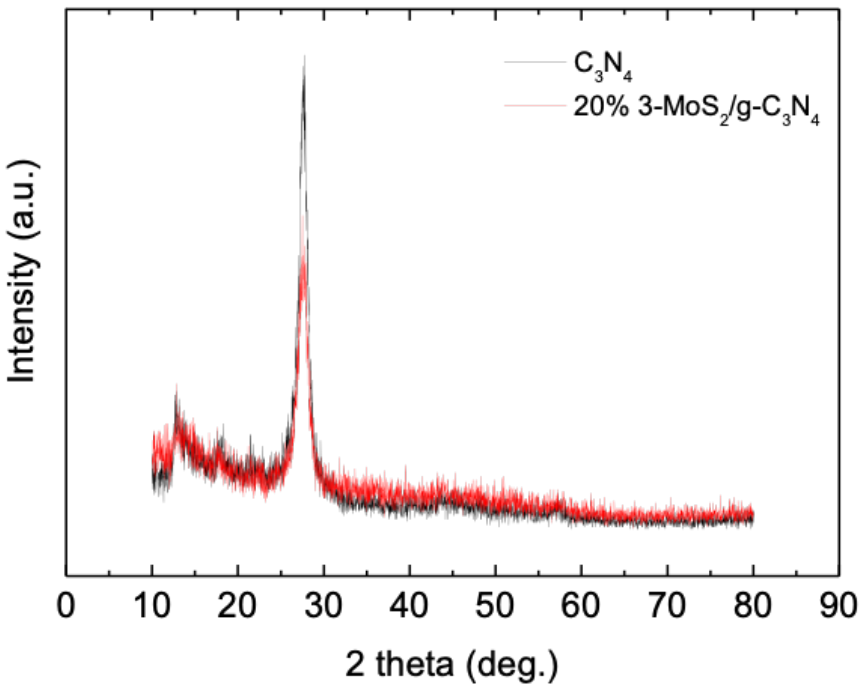

Figure 30. XRD patterns of the MSCN-3 and g-C_3N_4 catalysts.

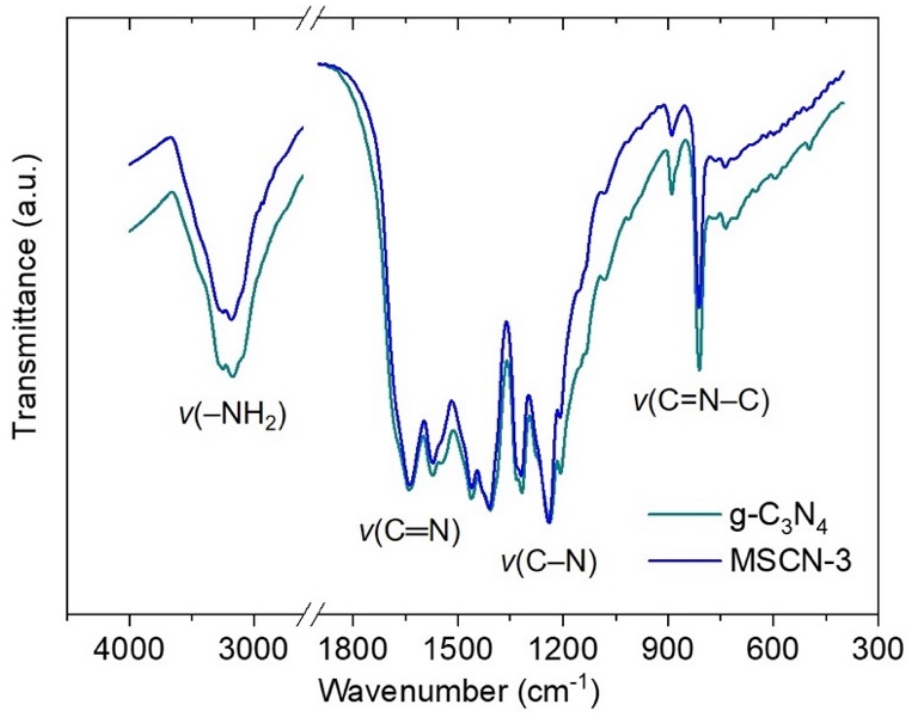

Figure 31. FTIR spectra of the as-prepared g-C_3N_4 and MSCN-3 materials.

The porosity of the MSCN-*n* materials (20 wt% MoS_2 loading) was determined by N_2 physisorption experiments. As seen in **Figure 32**, all samples exhibited typical type IV adsorption and desorption isotherms with a small H_3 hysteresis loop according to the IUPAC classification, suggesting mesoporous structures with slit-shaped pores[167]. On the basis of the adsorption data, specific surface areas of 62–84 $m^2\ g^{-1}$ and total pore volumes of 0.10–0.12 $cm^3\ g^{-1}$ were determined for the MSCN-*n* using the Brunauer–Emmett–Teller (BET) model, which are slightly lower than that obtained for pristine g-C_3N_4 (106 $m^2\ g^{-1}$, 0.14 $cm^3\ g^{-1}$). The lower specific surface area of the MSCN-*n* samples compared to g-C_3N_4 can be explained by the heavy elements (Mo and S) that compose the structure. A summary of the N_2 physisorption results is shown in **Table 1**.

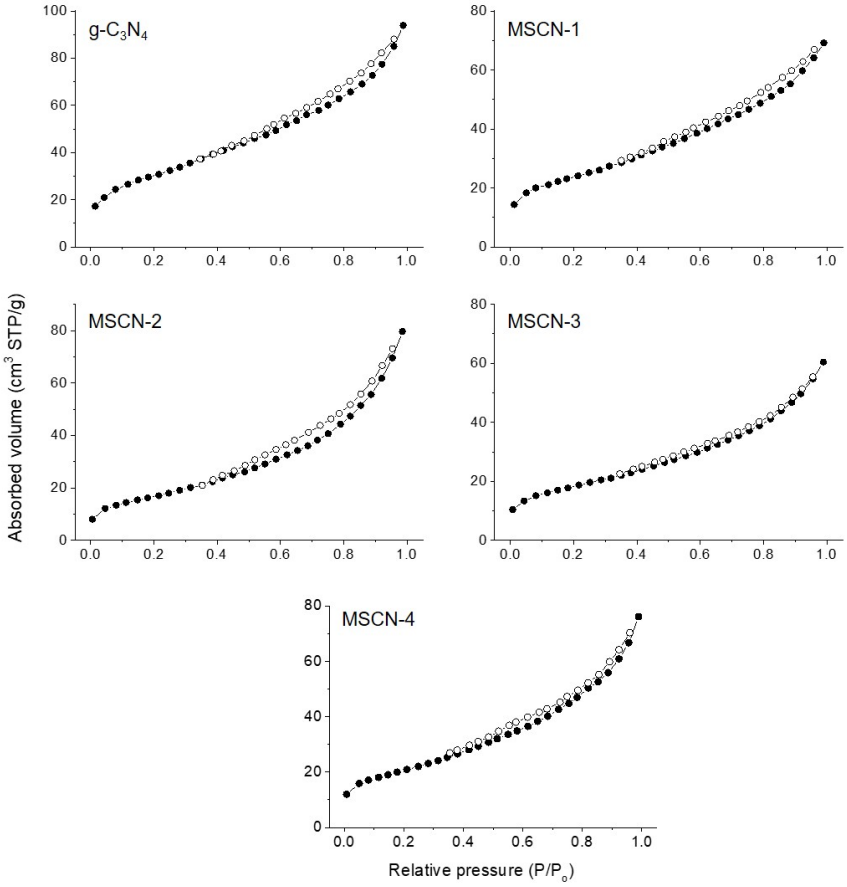

Figure 32. N_2 adsorption-desorption isotherms at –196 ºC for g-C_3N_4 and MSCN-*n* nano-heterostructures (20 wt% MoS_2 loading).

Table 1. Morphological properties of the g-C_3N_4 and MSCN-n (20 wt% MoS_2 loading) catalysts.

Sample	**MoS_2 lateral size[a] (nm)**	**BET surface area ($m^2\ g^{-1}$)**	**Pore volume ($cm^3\ g^{-1}$)**
g-C_3N_4	-	106	0.14
MSCN-1	18 ±4	84	0.11
MSCN-2	32 ±4	62	0.12
MSCN-3	39 ±5	65	0.10
MSCN-4	52 ±6	73	0.12

[a] Based on the TEM analysis.

X-ray photoelectron spectroscopy (XPS) measurements were performed to investigate the surface chemical sates of the prepared materials. **Figures 33a** and **b** show typical C 1s and N 1s core-level spectra, respectively, obtained from MSCN-3 catalyst. Deconvolution of the C 1s spectrum reveals three symmetrical peaks at 284.8,

286.3 and 288.2 ±0.2 eV binding energies, which correspond to the aliphatic carbon and the sp^2-bonded and sp^3-bonded C atoms in triazine (N–C=N and C–N linkages) units of g-C_3N_4, respectively.[168] In the N 1s region, a prominent peak at around 399.8 ±0.3 eV and a broad shoulder at 400.7 ±0.3 eV were detected, which can be assigned to the pyridinic (C–N sp^2) and pyrrolic like (C–N sp^3) nitrogen, respectively, in accordance with the C 1s peaks.[169] As for the Mo 3d XPS signal (**Figure 33c**), deconvolution of the spectrum shape revealed a doublet peak at 229.1 and 232.0 ±0.2 eV due to the Mo $3d_{5/2}$ and Mo $3d_{3/2}$ spin-orbit components of the Mo^{4+} in MoS_2.[170]

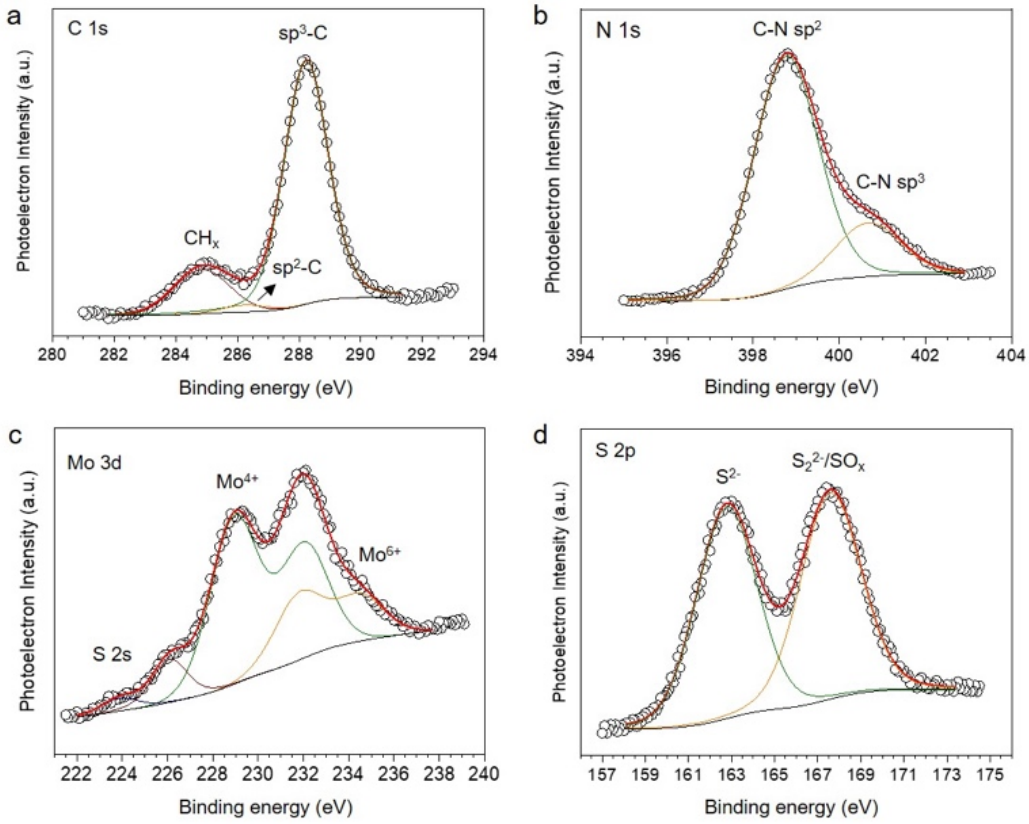

Figure 33. (a) C 1s, (b) N 1s, (c) Mo 3d and (d) S 2p core-level XPS spectra of MSCN-3 catalyst. Embedded peaks for different components are represented as green, orange, wine and blue curves. The red lines are fits to the experimental data.

Furthermore, we observed weak Mo signals at relatively higher binding energies (Mo $3d_{5/2}$, 232.0 ±0.2 eV; Mo $3d_{3/2}$, 235.0 ±0.2 eV) most likely due to defect Mo^{4+} (unsaturated Mo atoms)[171] and/or the formation of some surface suboxide MoO_{3-x} species during the synthesis process and sample exposure to air.[172] Besides, the small features close to 224.2±0.2 eV and 226.5±0.2 eV are assigned to the S 2s lines corresponding to the S^{2-} ions of MoS_2 and SO_x species, respectively, as indicated by

the S 2p peak analysis. The XPS spectrum of the S 2p region (**Figure 33d**) shows two peaks assigned to sulfide (S^{2-}) ions of MoS_2 (162.8 ±0.2 eV) and bridging S_2^{2-} atoms of MoS_2 and/or SO_x species (167.5 ±0.2 eV) from partial surface oxidation of MoS_2.[173]

3.1.2 Photocatalytic study

3.1.2.1 Photocatalytic H_2 evolution study

The photocatalytic H_2 production activity of the MSCN-*n* nano-heterostructures was evaluated by UV-vis light irradiated (λ > 360 nm) reduction of water. Initially, we optimized the reaction conditions by performing a series of photocatalytic water reduction tests with different concentrations of MSCN-3 suspended in water/methanol (4:1 v/v) solution. As shown in **Figure 34**, the H_2 generation rate of MSCN-3 increased with increasing mass addition until reaching a maximum at 1 mg mL^{-1}. The catalyst concentration-dependent activity can be interpreted as a result of increase in light absorption, until a saturation level is reached due to the scattering of incident photons by the colloidal particles. Remarkably, following various catalytic tests, a markedly enhancement of H_2 evolution rate was observed in the presence of methanol (29.9 μmol h^{-1}) compared to triethylamine (17.6 μmol h^{-1}) and Na_2S/Na_2SO_3 pairs (ca. 2 μmol h^{-1}) as sacrificial electron donors (**Figure 35**).

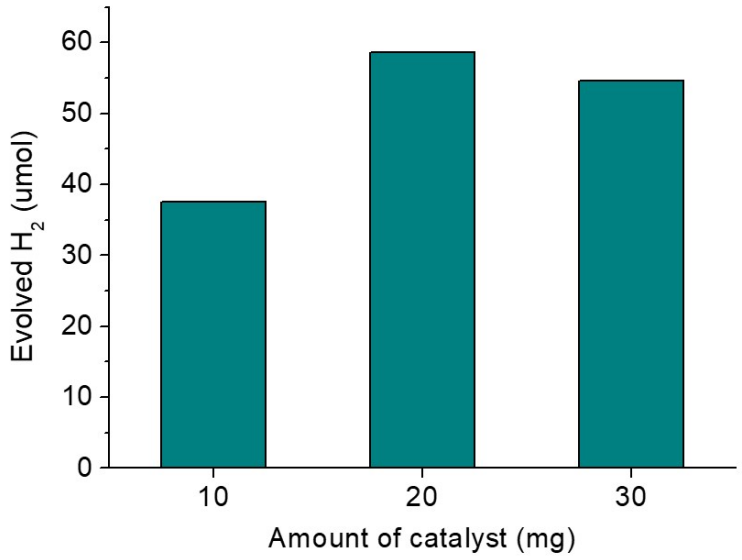

Figure 34. Photocatalytic H_2 evolution for different concentrations of MSCN-3 catalyst. The photocatalytic reactions were performed as follows: 10–30 mg of catalyst were dispersed in 20 mL aqueous solution containing 20% (v/v) methanol, 300-W Xenon light radiation with a long-pass cut-off filter allowing λ > 360 nm, 3 h reaction time.

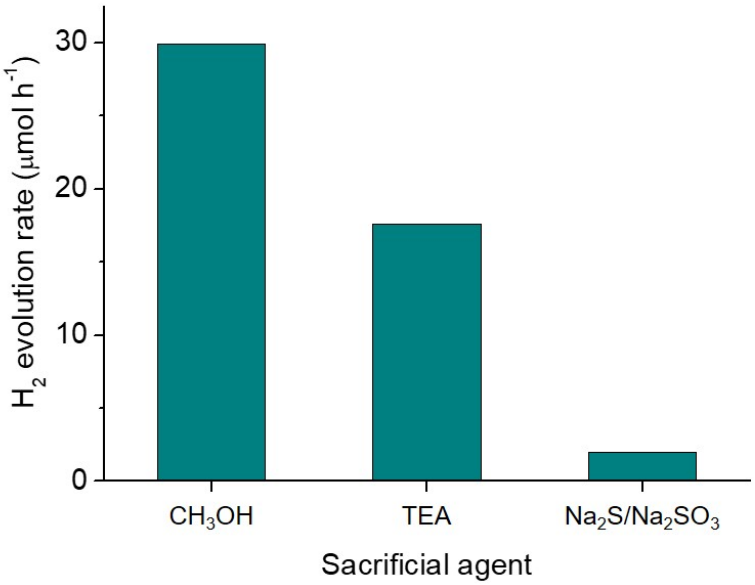

Figure 35. Photocatalytic H_2 evolution rates for MSCN-3 catalyst using different sacrificial reagents: 20% (v/v) methanol, 20% (v/v) triethanolamine (TEA) and 0.35 M Na_2S – 0.25 M Na_2SO_3 aqueous solution. All photocatalytic reactions were performed as follows: 20 mg of catalyst was dispersed in 20 mL aqueous solution containing the sacrificial reagent, 300-W Xenon light radiation with a long-pass cut-off filter allowing $\lambda > 360$ nm. The H_2-evolution rates were averaged over 3-h irradiation periods.

Afterward, further control experiment over the catalyst composition showed that the production rate of H_2 for MoS_2/g-C_3N_4 drastically increases with increasing MoS_2 content and attains a maximum value at 20 wt%, see **Figure 36**. The reduced activity at lower and higher levels of MoS_2 loadings could be attributed to the insufficient MoS_2 amount and light shading effect of excessive MoS_2, respectively. In contrast, single-component g-C_3N_4 and MoS_2 samples show almost no H_2-production activity under identical conditions due to the fast recombination of photogenerated charge carries; in particular, an amount of 0.78 μmol of hydrogen was detected in 3 h with g-C_3N_4, while no reaction observed with MoS_2 NSs. This observation is clearly consistent with the photochemical activity of MoS_2/g-C_3N_4 nanocatalysts being originated from the synergistic action of their components.

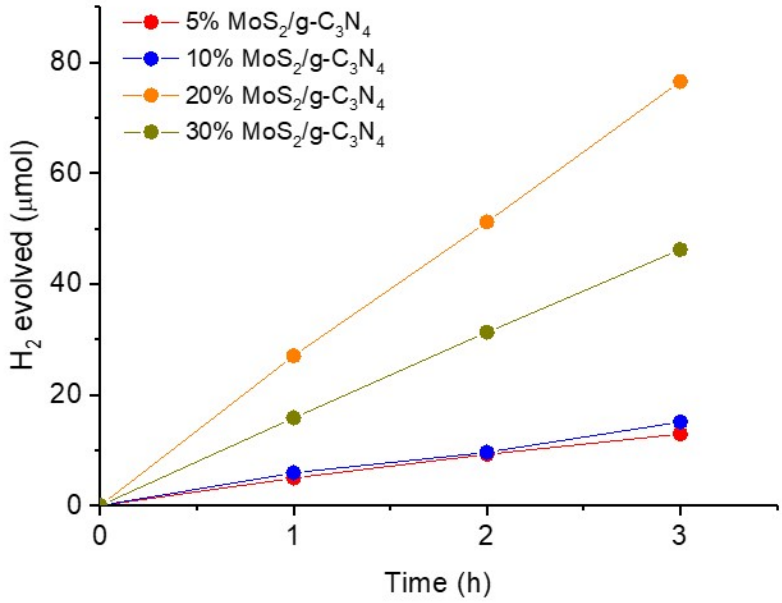

Figure 36. Time courses for photocatalytic H_2 evolution from MoS_2-modified g-C_3N_4 catalysts containing different loadings of MoS_2 NSs with 39 nm lateral size. All photocatalytic reactions were performed as follows: 20 mg of catalyst was dispersed in 20 mL of aqueous solution containing 20% (v/v) methanol, 300-W Xenon light radiation with a long-pass cut-off filter allowing $\lambda > 360$ nm.

To investigate the effect of MoS_2 dimensional confinement on the H_2-production performance of MSCN-*n* comparative H_2 evolution experiments for MSCN-*n* catalysts containing MoS_2 layers of different lateral sizes at a fixed chemical composition were examined, all of them containing 20 wt% MoS_2 loading (**Figure 37**). All catalytic reactions were performed by stirring a water/methanol (4:1 v/v) solution containing 1 mg mL^{-1} of catalyst under $\lambda > 360$ nm light irradiation. It can be seen that MoS_2 nanolayers exert a prominent effect on the photoactivity of MSCN-*n*, in which the rate of H_2 generation progressively increases with increasing MoS_2 lateral size up to 39 nm, and then decreases. The MoS_2 layer size results are graphically associated with the corresponding hydrogen photogeneration activities in **Figure 37**. Overall, the activity for the MSCN-3 catalyst surpasses the activity obtained for other MoS_2-modified samples, corresponding to an average H_2-production rate of 1497 μmol h^{-1} g_{cat}^{-1} in the initial 3 h. Assuming all incident photons are absorbed by the catalyst suspension, the apparent quantum yield (QY) for this reaction is 3.3% by irradiation of 410 ± 10 nm light. Moreover, assuming all MoS_2 atoms are involved in catalysis, the turnover frequency (defined as 2 × H_2 evolution amount/MoS_2 amount/reaction time) for hydrogen evolution in the first 3 h reached 2.4 h^{-1}. To our knowledge, this efficiency

ranks among the highest reported values for MoS_2-loaded g-C_3N_4 photocatalysts, and it is comparable to the efficiency achieved with three junctional g-C_3N_4 catalysts.

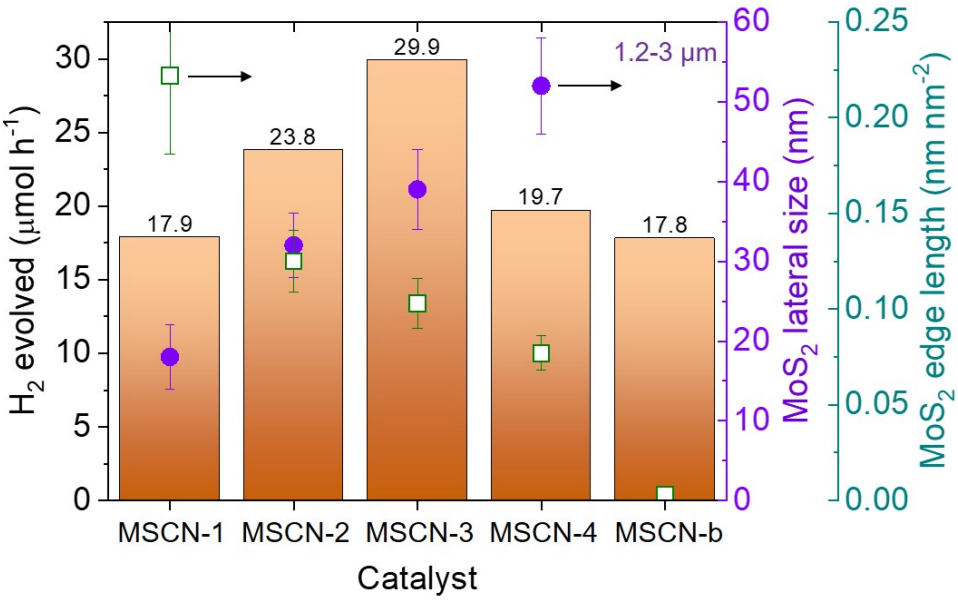

Figure 37. Photochemical H_2 evolution (columns) and MoS_2 lateral size (filled symbols) and edge length density (open symbols) evolution for MSCN-*n* catalysts. The H_2 evolution rates were averaged over 3-h irradiation periods.

To further elucidate the morphological effects, we prepared microstructured MoS_2-modified g-C_3N_4 (MSCN-b) catalyst by depositing bulk-grown MoS_2 on exfoliated g-C_3N_4 flakes, and its photocatalytic performance was investigated under identical conditions (20 mg of MSCN-b was dispersed in 20 mL of water/methanol (4:1 v/v) solution; $\lambda > 360$ nm irradiation, 20 °C). As shown by TEM images in **Figure 38**, this catalyst is composed of approximately 1.2–3 μm-sized MoS_2 flakes standing on the surface of g-C_3N_4. Interestingly, the reference MSCN-b catalyst during the first 3 h of irradiation entails a 1.7-fold lesser activity (17.8 μmol h^{-1}) compared to MSCN-3 sample despite having similar composition (20 wt % MoS_2 loading), see **Figure 37**. This distinct change in H_2 generation activity is highly related to the nanoscale grain size of MoS_2 layers, which concurrently increases the density of active MoS_2 edge sites and facilitates the charge separation at the MoS_2/g-C_3N_4 interface. This interpretation is supported by further studies with photoluminescence and electrochemical methods as will be discussed below.

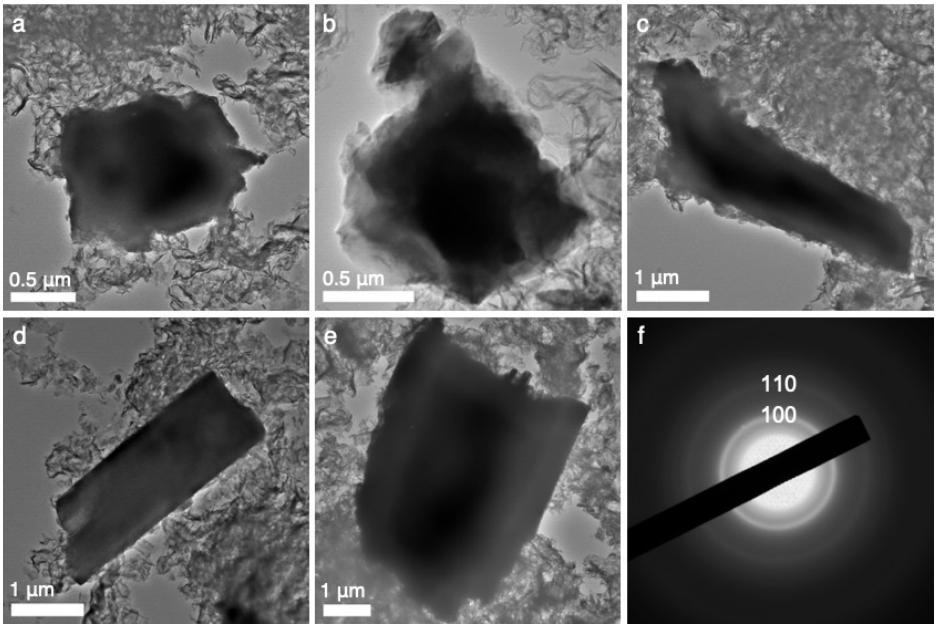

Figure 38. (a-e) Typical TEM images and (f) SAED pattern showing two concentric Debye-Scherrer diffraction rings corresponding to the (100) and (110) planes of hexagonal 2H MoS_2 of bulk-like MoS_2/g-C_3N_4 (MSCN-b) catalyst.

Moreover, the MSCN-3 catalyst could be recycled at least three times without obvious loss of activity. After each photocatalytic test, the catalyst was collected by centrifugation, washed with deionized water, dried under vacuum at 80 ºC, and replenished with a fresh water/methanol (4:1 v/v) solution. As shown in **Figure 39**, the MSCN-3 exhibits very similar activity during the tested periods, giving an average H_2-production rate of about 25 µmol h^{-1} (ca. 8.2 mL at STP) after 15 h of illumination. XPS spectra indicate no significant changes in the chemical state of the reused catalyst, confirming its stability under the examined conditions. In particular, after catalysis the intensity of the S 2p XPS peak assigned to oxidized SO_x species is remarkably decreased. Moreover, an additional weak S 2p feature observed at 160.1 ±0.2 eV binding energy probably due to unbound sulfide (S^{2-}) atoms present on the surface of MoS_2[174], see **Figure 40**.

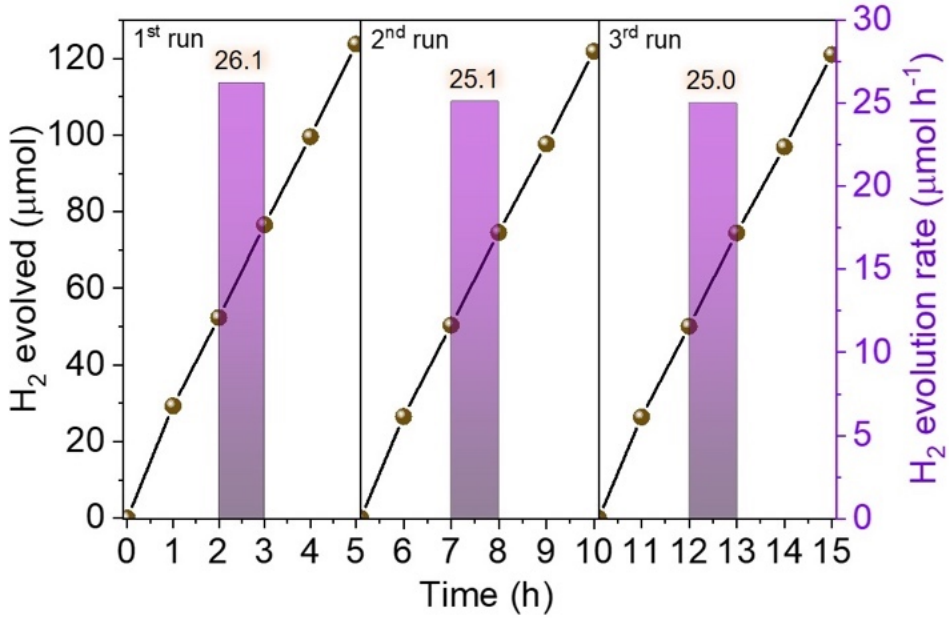

Figure 39. Photocatalytic regeneration of the MSCN-3 sample. Reaction conditions: 20 mg of catalyst, 20 mL of water/methanol (4:1 v/v) solution, 300-W Xenon lamp (λ > 360 nm) irradiation, 20 °C.

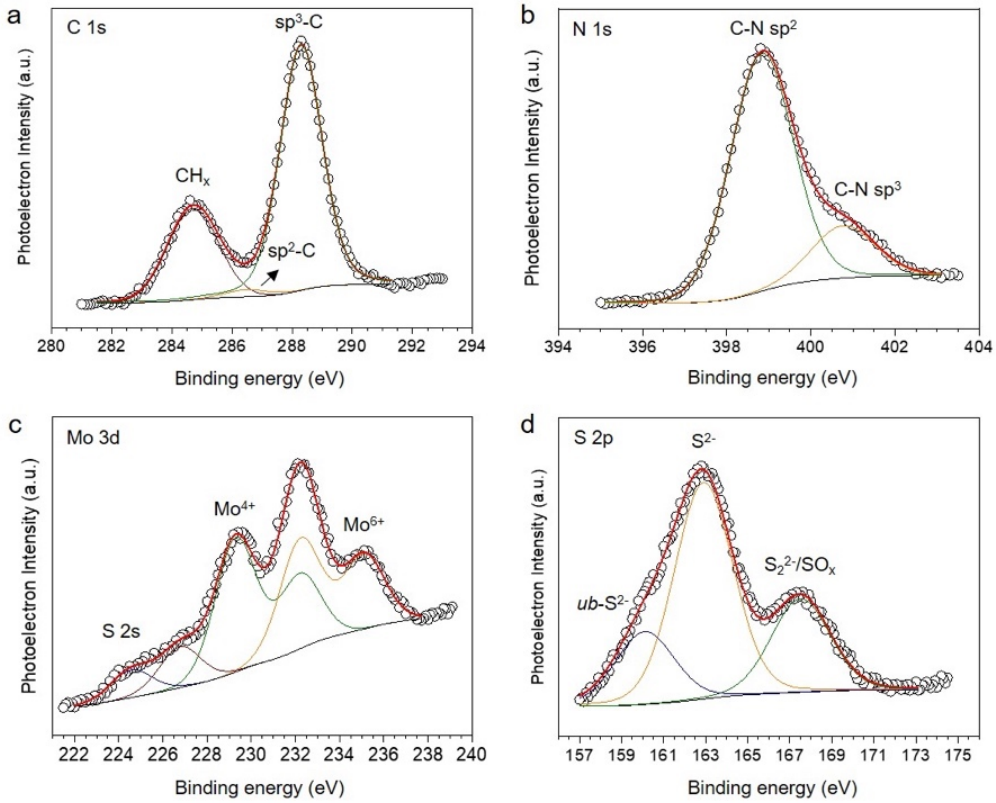

Figure 40. (a) C 1s, (b) N 1s, (c) Mo 3d and (d) S 2p XPS spectra for the reused MSCN-3 catalyst. The additional S 2p emission at 160.1±0.2 eV is attributed to the free (unbound) sulfide ions present on the MoS_2 surface. The weak S 2p feature observed at 167.5±0.2 eV binding energy is related to bridging S_2^{2-} atoms and/or surface oxidation (S–O) of MoS_2.

3.1.2.2 Effect of lateral MoS_2 NSs size on the photochemical activity

To understand the electronic interactions at the MoS_2/g-C_3N_4 interfaces and to investigate the quantum size effect on the reactivity of MoS_2 NSs, we measured the flat-band potentials (E_{FB}) using electrochemical impedance spectroscopy (EIS). **Figure 41** shows the Mott-Schottky plots of the as-prepared catalysts (drop-casted onto FTO glass substrates), that is, $1/C_{SC}^2$ versus applied voltage (E) curves measured using a three-electrode cell in 0.5 M Na_2SO_4 solution (pH 7). From these plots, the E_{FB} potential is obtained as linear extrapolation of the $1/C_{SC}^2$ to zero. All samples exhibited positive slopes of the $1/C_{SC}^2$ – E lines indicating that electrons are the majority carriers (n-type conduction). By combining EIS and optical absorption spectroscopy results, we calculated the band-edge positions for each catalyst and the corresponding energy level diagrams are illustrated in **Figure 42**.

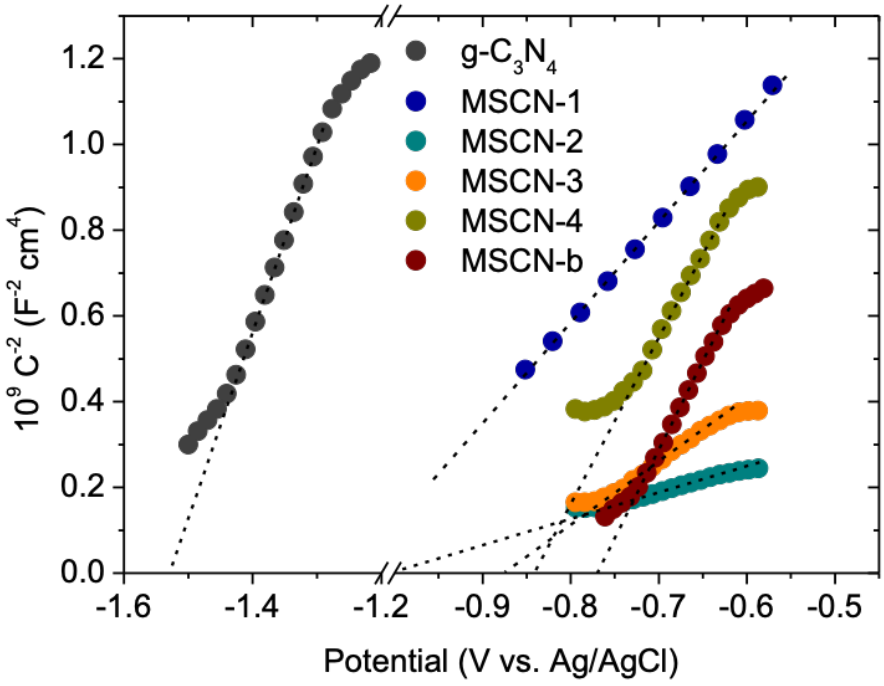

Figure 41. Mott-Schottky plots of pristine and MoS_2-modified g-C_3N_4 (MSCN-*n*) catalysts.

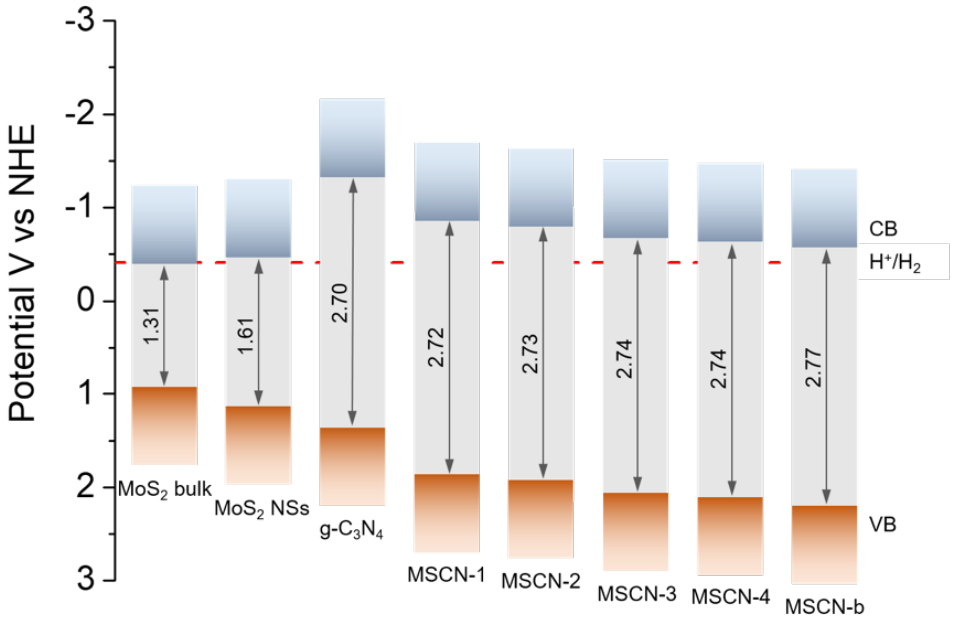

Figure 42. Approximate band-edge positions of pristine and MoS_2-modified g-C_3N_4 (MSCN-*n*) catalysts.

The absorption spectra of as-prepared samples were acquired using UV–vis/NIR diffuse reflectance spectroscopy, from which the bandgap energies (E_g) of MSCN-*n* are estimated to be 2.72–2.74 eV according to the Tauc method, values which are very close to that of the pristine g-C_3N_4 sample (2.70 eV) (**Figure 43**). The absorption spectra argue that the energy gap of g-C_3N_4 does not change significantly and remains comparable after deposition of MoS_2 NSs within the uncertainty of the measurement. Accordingly, this implies that the electronic structure of g-C_3N_4 is dominated by the electron transfer from the N 2p states in VB to the C 2p and N 2p states in CB and remains almost unaffected by the interlayer coupling of MoS_2/g-C_3N_4. For the construction of energy diagrams in **Figure 42**, we assumed that flat band level lies very close to the CB edge for heavily doped n-type g-C_3N_4, and thus the valence band potential (E_{VB}) was calculated by subtracting the energy gap (E_g) from the E_{FB} level. These results show that, unlike the bandgap, the E_{VB} edge position of g-C_3N_4 progressively up-shifts with the lateral dimension of MoS_2 layers, i.e., from 1.36 V for the 18 nm sized to 2.12 V for the 52 nm sized MoS_2 sheets, making them better electron acceptors for oxidation reaction. All potentials are reported versus normal hydrogen electrode (NHE) at pH 7. Moreover, as inferred from the change in slope of the $1/C_{SC}^2$ versus E lines, deposition of MoS_2 increases the donor density (N_d) of MoS_2-modified g-C_3N_4. The EIS measurements yield N_d values for MSCN-*n* from 7.80×10^{17} to

5.13×10^{18} cm^{-3}, which are larger than that obtained from pristine g-C_3N_4 sample (7.10×10^{17} cm^{-3}), see **Table 2**.

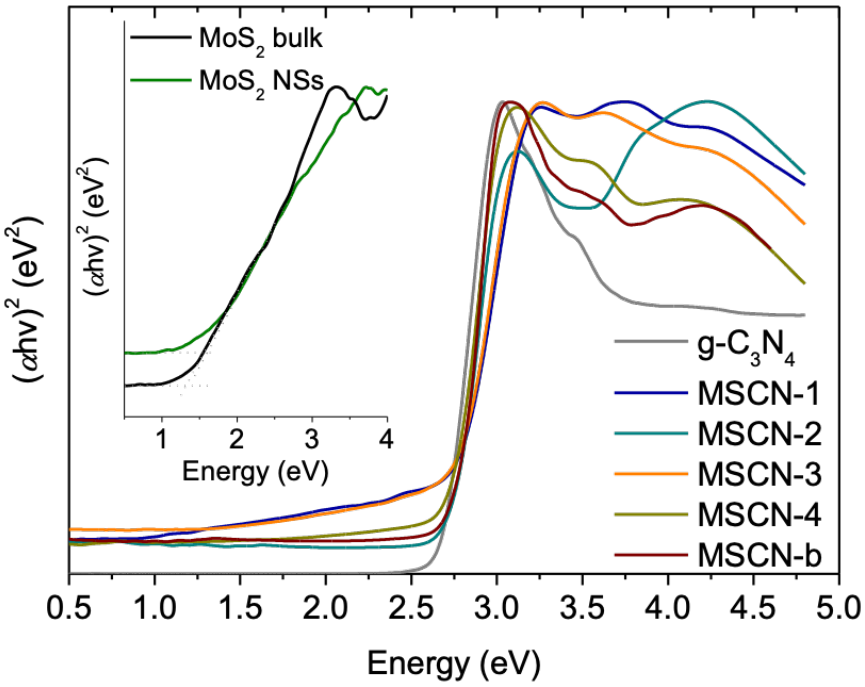

Figure 43. Tauc plots showing the bandgap transitions of pristine and MoS_2-modified g-C_3N_4 (MSCN-*n*) catalysts (inset: the corresponding Tauc plots of as-made MoS_2 nanolayer and bulk materials).

Table 2. Electrochemical data obtained from Mott-Schottky measurements for pristine g-C_3N_4 and MoS_2-modified g-C_3N_4 catalysts with 20 wt% MoS_2 (MSCN-*n*), and MoS_2 nanolayer and bulk materials. Density of edge length of the deposited MoS_2 NSs with different lateral size.

Catalyst	**E_{FB}**	**E_{VB}**	**Energy gap (eV)**	**Carrier density[a] (N_d, cm^{-3})**	**MoS_2 edge length[b] (D_{Ls}, 10^{-1} nm nm_{cat}^{-2})**
	(V vs NHE, pH=7)				
g-C_3N_4	–1.33	1.37	2.70	7.10×10^{17}	-
MoS_2 NSs[c]	–0.47	1.14	1.61	7.02×10^{17}	-
MoS_2 bulk	–0.39	0.92	1.31	4.86×10^{17}	-
MSCN-1	–0.85	1.87	2.72	1.30×10^{18}	2.22 ±0.41
MSCN-2	–0.80	1.93	2.73	5.13×10^{18}	1.25 ±0.16
MSCN-3	–0.67	2.07	2.74	2.03×10^{18}	1.03 ±0.13

MSCN-4	–0.63	2.11	2.74	7.80×10^{17}	0.77 ±0.09
MSCN-b	–0.57	2.20	2.77	7.39×10^{17}	<0.03[d]

[a] Carrier density (N_d) given by $N_d = 2(E–E_{FB})\cdot C_{SC}^2/\varepsilon\varepsilon_o e$, where E is the applied potential, E_{FB} is the flat-band potential, C_{sc} is the space charge capacitance, ε is the relative dielectric constant of g-C_3N_4 (4.6), ε_o is the dielectric permittivity (8.8542×10^{-10} F cm^{-1}) and e is the elementary charge (1.602×10^{-19} C). [b] Density of MoS_2 edge length (D_{Ls}) was calculated by dividing the edge size of MoS_2 layers [$L_c = 2\pi r$] by the geometric planar surface area [$A_c = \pi r^2$] according to the equation $D_{Ls} = L_c/A_c$, assuming spherical-shaped nanosheets with an average radius r. [c] MoS_2 NSs of 39 nm lateral size. [d] Based on the MoS_2 lateral size (>1.2 μm) as determined by TEM images.

Given that the CB potential of MoS_2 (i.e., –0.47 V and –0.39 V vs NHE for nanolayered and microstructured MoS_2, respectively, as determined from Mott-Schottky plots, as seen in **Figure 44**) is more positive than that of g-C_3N_4 (its CB potential is about –1.33 V vs NHE), an internal electric field across the MoS_2/g-C_3N_4 junction will be formed, which drives the electrons from the CB of g-C_3N_4 to MoS_2 until the Fermi levels of the two components reach equilibrium. Such an electron transfer creates a depletion region at the g-C_3N_4 surface (by subtraction of the CB electrons), which is consistent with the positive (anodic) shift of g-C_3N_4 E_{FB}. This intrinsic electric field is beneficial for photocatalysis because it improves the separation and prolongs the lifetime of photogenerated electron-hole pairs.

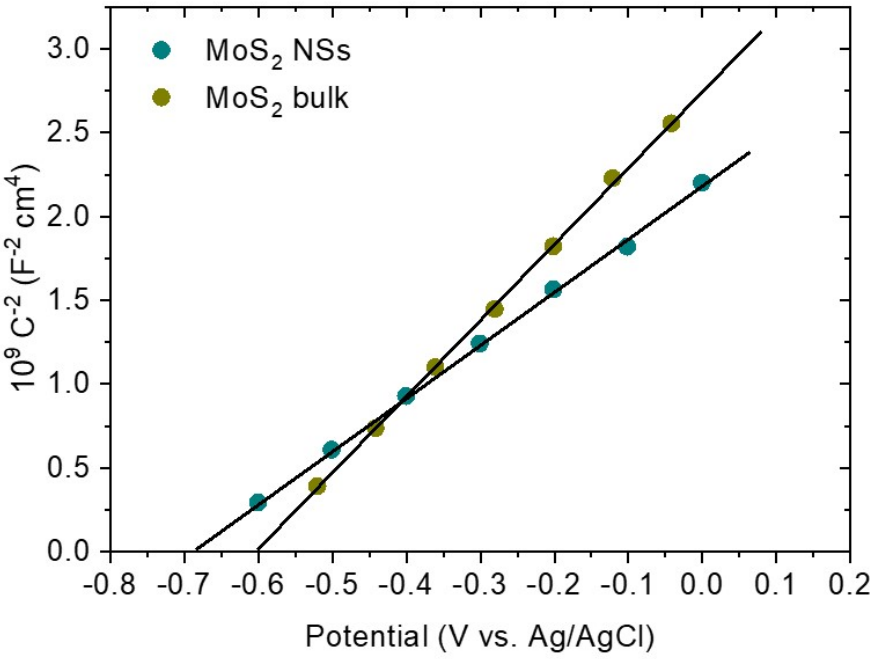

Figure 44. Mott-Schottky plots of the 39 nm-sized MoS_2 layers and bulk MoS_2 flakes.

Furthermore, the charge transfer properties of MSCN-*n* nano-heterostructures were investigated by EIS Nyquist measurements. **Figure 45** shows AC impedance spectra of the g-C_3N_4 and MSCN-*n* sample electrodes measured in the 0.5 M Na_2SO_4 electrolyte at open circuit potential. A typical electrical circuit that is illustrated in inset of **Figure 45** has been used to interpret the experimental results and to extract the charge-transport resistance (R_{ct}) of the electrodes. Analysis of the high-frequency range of Nyquist plots revealed that MoS_2-modified samples, except MSCN-1, exhibit lower R_{ct} values (from 94.7 to 99.5 Ω) than that for pristine g-C_3N_4 sample (102.6 Ω). The low degree of R_{ct} resistance indicates favorable charge transport and separation presumably along the MoS_2/g-C_3N_4 junction; consequently, this process may contribute to the enhanced photocatalytic efficiency. In addition, the EIS results reveal a little yet obvious descending trend in the charge transfer efficiency of MSCN-*n* samples with increasing MoS_2 lateral size (see **Table 3**). As for the higher R_{ct} resistance of MSCN-1 (113.7 Ω) relative to the unmodified g-C_3N_4 sample, this could be tentatively ascribed to the diminished electron-accepting ability of MoS_2 layers due to their very small lateral dimension (ca. 18 nm). Combined with photoluminescence measurements, this means that very small MoS_2–g-C_3N_4 interface areas suppress smooth electron transfer from photoexcited g-C_3N_4 to MoS_2, and thus resulting in lower photoactivity.

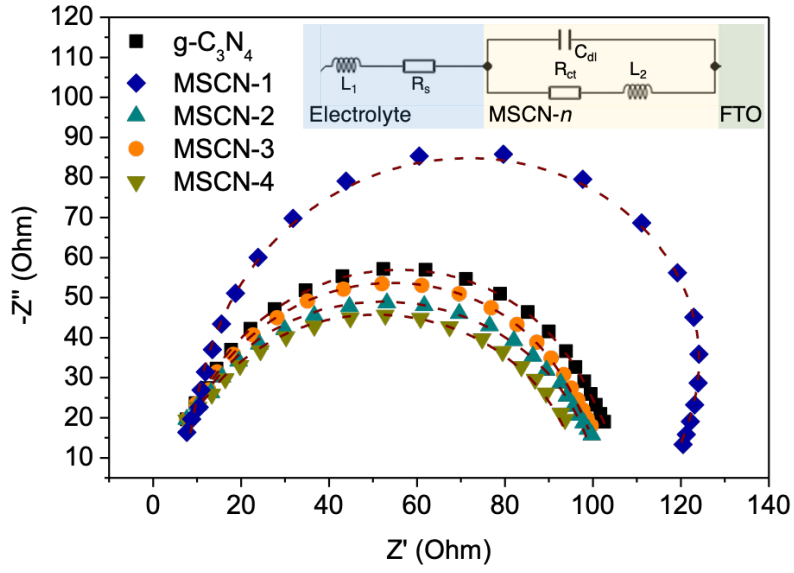

Figure 45. Nyquist plots of pristine and MoS_2-modified g-C_3N_4 (MSCN-*n*) catalysts (inset: equivalent circuit model $L_1R_s[C_{dl}/(R_{ct}L_2)]$, where R_s and R_{ct} are the electrolyte and the charge-transfer resistance, respectively, C_{dl} accounts for the double layer capacitance, and L_1 and L_2 inductors represent the pseudo-inductive behavior observed in the high frequency domain, arising respectively by disordered movement of redox species at the electrode surface and relaxation of carriers).[175]

Table 3. EIS equivalent circuit fitted parameters of pure and MoS_2-modified g-C_3N_4 catalysts.

Sample	R_{ct} (Ω)	L_1 (H)	R_s (Ω)	C_{dl} (F)	L_2 (H)	x^2
g-C_3N_4	102.6	0.40×10^{-6}	6.48	27.02×10^{-9}	41.47×10^{-6}	9.22×10^{-5}
MSCN-1	113.7	0.51×10^{-6}	5.92	29.16×10^{-9}	98.53×10^{-6}	6.44×10^{-4}
MSCN-2	99.6	0.50×10^{-6}	6.41	30.96×10^{-9}	39.38×10^{-6}	3.05×10^{-4}
MSCN-3	98.8	1.88×10^{-6}	2.98	6.73×10^{-9}	12.38×10^{-6}	2.46×10^{-3}
MSCN-4	94.7	1.56×10^{-6}	2.80	6.66×10^{-9}	9.66×10^{-6}	1.69×10^{-3}

Steady-state photoluminescence (PL) measurements were also performed to ascertain that there is a decrease of the interband exciton relaxation rate with increasing MoS_2/g-C_3N_4 coupling area. **Figure 46** shows PL emission spectra for pristine g-C_3N_4 and MSCN-*n* nano-heterostructures measured using 370 nm excitation wavelength. All the PL spectra show a broad peak at around 455 nm (2.72 eV) slightly above the band-edge absorption of g-C_3N_4 (~2.70 eV), which is related to the band-edge emission process. Apparently, deposition of MoS_2 layers with larger dimensions onto the g-C_3N_4 surface leads to a gradual quenching of the photoemission signal, indicating depressed electron-hole recombination rate. The spatial separation of photogenerated carriers and lower charge-transfer resistance, as evidenced by EIS and PL measurements, agree with the expected trends for better electrochemical interactions between large-sized MoS_2 and g-C_3N_4 layers; presumably they favor electron flow from CB of g-C_3N_4 to MoS_2. To the best of our knowledge, this is the first example of a size-dependent electronic band structure and charge separation concomitant with reduction of the MoS_2/g-C_3N_4 interfacial area at the nanoscale. These effects definitely have a great impact on the photochemical processes within the nanoscale junctions of MoS_2 and g-C_3N_4 and raise the possibility of designing new photocatalysts with improved performance.

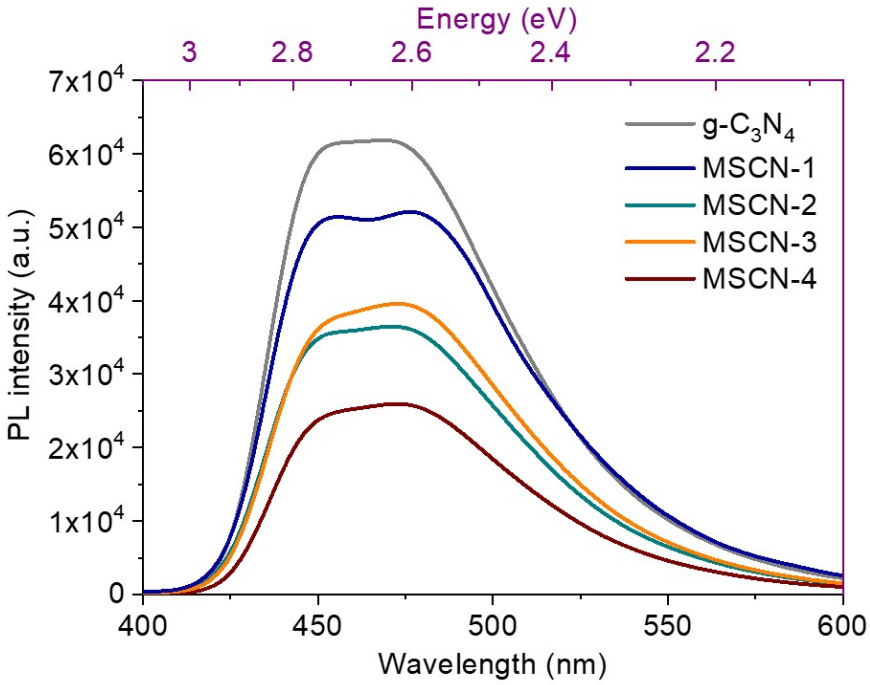

Figure 46. Room-temperature PL spectra of pristine g-C_3N_4 and MoS_2-modified g-C_3N_4 (MSCN-*n*) catalysts. PL emission spectra were obtained at a concentration of 1 mg/mL in water with an excitation wavelength of 370 nm.

However, band edge alignment and interfacial charge transfer processes do not explicitly explain the improved hydrogen generation efficiency of MSCN-*n* nano-heterostructures. Aside from efficient electronic interactions, the enhancement in photocatalytic activity of the present MoS_2/g-C_3N_4 system could be tentatively ascribed to the density of active sites at the edge region of MoS_2 NSs. It has been reported that, compared to the sulfur-terminated (0001) basal planes, the highly energetic edge sites of MoS_2 (particularly, undercoordinated Mo sites)[176] are much more catalytically active for hydrogen evolution catalysis.[177] To clarify this issue, we calculated the edge length per planar surface area of the MoS_2 NSs (D_{Ls}) based on the MoS_2 lateral size (as determined by TEM observations) and loading amount (20 wt% MoS_2). This analysis reveals a reverse trend where D_{Ls} values increase with decreasing MoS_2 lateral size, as expected in the context of the dimensional reduction layer; the D_{Ls} value for MSCN-1 is 2.22×10^{-1} nm nm_{cat}^{-2} but those for MSCN-4 and MSCN-b are only 0.77 and 0.04×10^{-1} nm nm_{cat}^{-2}, respectively (see **Table 2**). Such a behavior may have a profound influence on the photocatalytic activity of MSCN-*n* since a large fraction of surface-active sites is available for reaction. In order to verify that edge sites, instead of the basal-plane region of MoS_2, are responsible for H_2 evolution, we annealed the MSCN-

3 sample at 200 °C in air for 1 h to form partially oxidized MoS_2 edges (e.g., Mo=O bonds), and we performed the photocatalytic H_2 evolution reaction under the same conditions. It should be stressed that the activation energy barrier for the O_2 dissociation on the Mo- and S-edge sites of MoS_2 is much lower compared with that on the basal plane, and thus the atoms located at the edge region are more susceptible to oxidation.[178] Remarkably, the O_2-treated sample showed a very small hydrogen production activity (giving an average H_2 evolution rate of 7.2 μmol h^{-1} during the first 3 h), implicating that edge sites are the catalytic centers for hydrogen evolution. On the basis of these results, we thus conclude that the density of MoS_2 edge sites along with the efficient electronic communication between g-C_3N_4 and MoS_2 layers may competitively enhance the photochemical activity of the MoS_2/g-C_3N_4 nanojunctions. This suggests that the MoS_2 lateral size decrease, although provides large number of MoS_2 edge sites available for reaction, creates interfacial contacts with suppressed g-C_3N_4-to-MoS_2 electron transfer. In contrast, larger size MoS_2 layers, even though favor interfacial electron-transfer kinetics, contain decreased density of surface edge sites and, therefore, result in lower photocatalytic activity. As summarized in **Figure 37**, the MoS_2 layers of 39 nm lateral dimension implicate a balanced combination of relatively high electronic communication and large number of active sites at the MoS_2/g-C_3N_4 heterojunction and, therefore, induce highest activity.

3.2 Metal-doped MoS_2-modified g-C_3N_4 nanostructures

2D/2D metal (Me)-doped MoS_2/g-C_3N_4 layered heterostructures were prepared via a two-step chemical process. Small-sized Me-doped MoS_2 nanosheets were firstly prepared by a facile sulfurization of monovacant Keggin-type phosphomolybdate ($Na_7PMo_{11}O_{39}$) precursors with a hydrothermal reaction with thioacetamide and Me compounds. In this method, $[PMo_{11}O_{39}]^{7-}$ clusters are decomposed to form MoO_x oxide species, while thioacetamide acts as a sulfur source, which, in pair with Me^{x+} ions (where x refers to the oxidation state of the metal ion, x = 2, 3 or 4), leads to the formation of Me-doped MoS_2 nanosheets. This is a gentle procedure that permits control over the metal doping level of MoS_2. The composition of the Me-MoS_2

nanolayers was effectively modulated by simply tuning the mass ratio of metal ion to $[PMo_{11}O_{39}]^{7-}$ precursor. The resulting Me-MoS_2 nanosheets were subsequently deposited on the surface of g-C_3N_4 (denoted as GCN) via a liquid exfoliation route to give few-layer heterostructures of Me-doped MoS_2/g-C_3N_4. The obtained catalysts were denoted as 3-NMS/GCN, where 3 refers to the metal content (i.e., 3%) in Me-MoS_2 nanosheets; all these samples have 20 wt% Me-MoS_2.

3.2.1 Photocatalytic study of 3-MeMS/GCN

3.2.1.1 Photocatalytic Cr(VI) reduction

The photocatalytic Cr(VI) reduction activity of the 20% 3-MeMS/GCN heterostructures was initially investigated in a Cr(VI) aqueous solution (50 mg L^{-1}) that contained 0.6 g L^{-1} of catalyst without any additional hole scavenger under $\lambda > 360$ nm light irradiation. The catalytic results in **Figure 47** show that doping the MoS_2 lattice with Ni^{2+} leads to a significant improvement of the photoactivity, indicating that the Ni-MoS_2 nanosheets act as an efficient co-catalyst in the present system. In particular, the Cr(VI) photoreduction rate of 3-NMS/GCN outperforms the other Me-doped catalysts, achieving complete (>99%) reduction of the Cr(VI) in 70 min. To further examine the kinetics of the Cr(VI) reduction by the 3-MeMS/GCN catalysts, the pseudo-first-order reaction is plotted in **Figure 48**. Assuming that the reaction rate is proportional to the concentration of Cr(VI), the overall photocatalytic reaction can be expressed by the first-order kinetics of Langmuir-Hinshelwood model: $\ln(C_t/C_o) = -k_{app} \cdot t$, where C_t and C_o are the concentration of Cr(VI) at time t and initial time, respectively, and k_{app} is the apparent reaction rate constant. For all samples, the initial temporal evolution of the Cr(VI) concentration shows a good linear correlation with time, indicating that the reaction rate is first order with respect to Cr(VI) concentration. For instance, the k_{app} rate constant of 3-NiMS/GCN is improved to 3.21×10^{-2} min^{-1} which is about 2.9 and 3.8 times the rate of the 3-SnMS/GCN ($k_{app} = 1.12\times10^{-2}$ min^{-1}) and 3-ZnMS/GCN ($k_{app} = 0.84\times10^{-2}$ min^{-1}) samples, respectively. In addition, the k_{app} rate constant of 3-NiMS/GCN is about 1.3 and 1.4 times higher the rate of the 3-CoMS/GCN ($k_{app} = 2.46\times10^{-2}$ min^{-1}) and 3-InMS/GCN ($k_{app} = 2.33\times10^{-2}$ min^{-1}) samples, respectively.

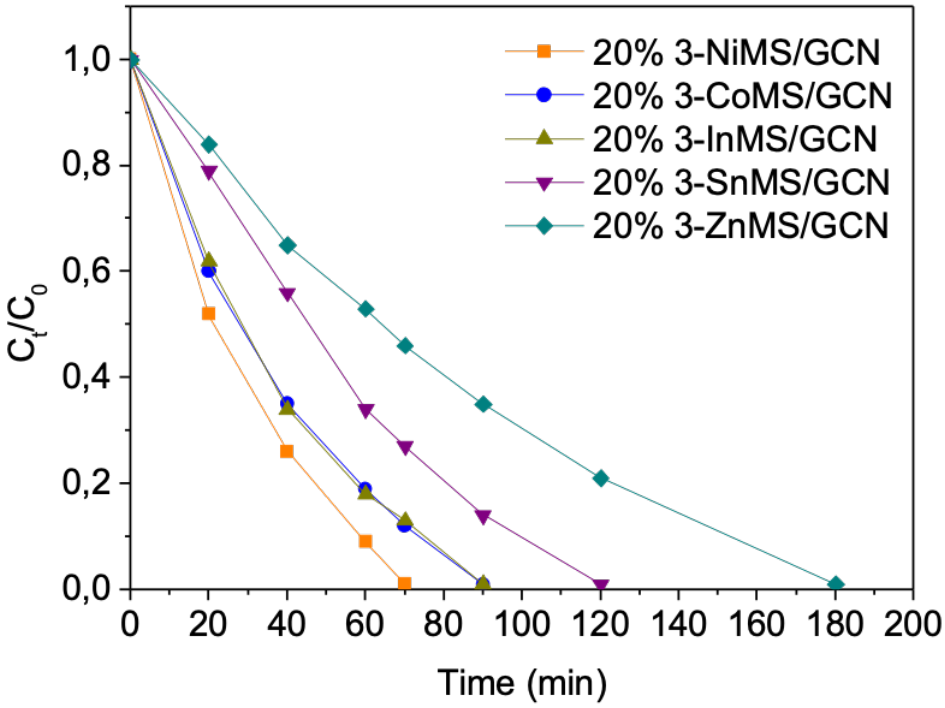

Figure 47. Photocatalytic reduction of aqueous Cr(VI) over different 20% 3-MeMS/GCN catalysts (Me = Ni, Co, In, Sn, Zn). The photocatalytic reactions were performed as follows: 0.6 g L^{-1} catalyst, 50 mg L^{-1} Cr(VI) solution, pH = 2, λ > 360 nm light irradiation, 20 °C.

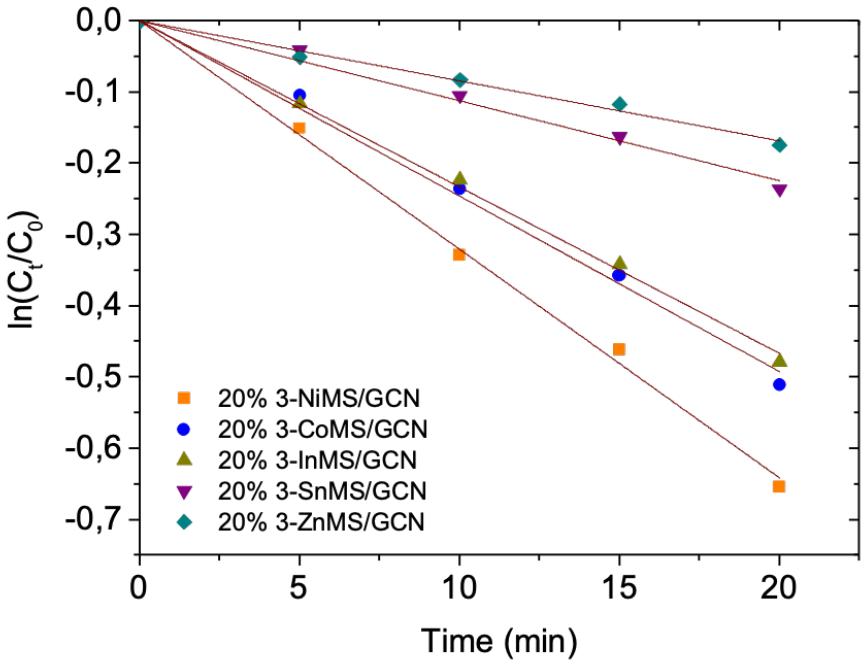

Figure 48. Kinetic profiles for the photocatalytic reduction of Cr(VI) over different 20% 3-MtMS/GCN catalysts. The red lines are fit to the data.

The above analysis thus clearly indicates that the reaction proceeds at a faster rate over 3-NiMS/GCN catalyst than the other samples (**Figure 49**). Based on these results, the Ni-doped MoS_2 system will be further studied and discussed in the next session by varying the synthesis parameters.

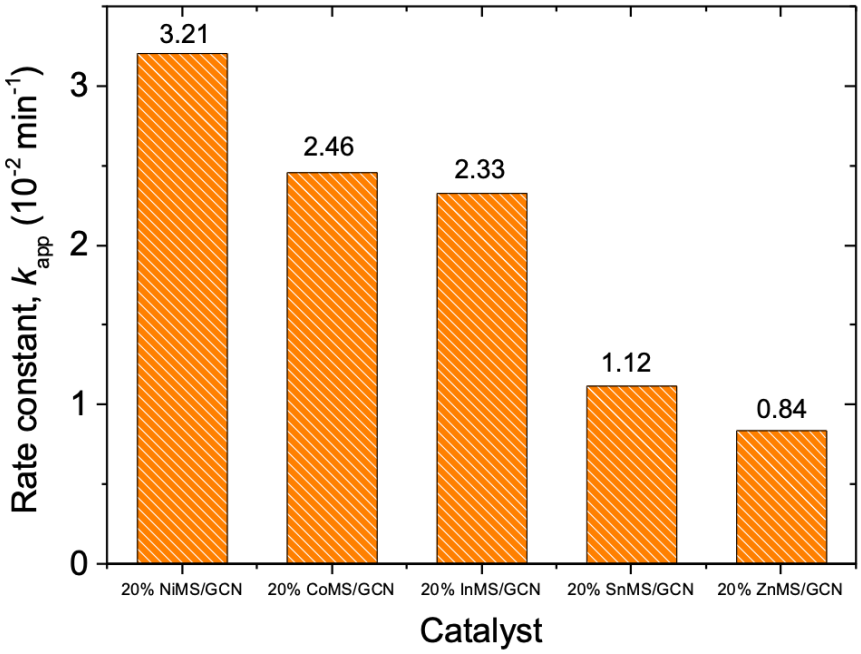

Figure 49. Pseudo-first-order reaction rate constants (k_{app}) over different 3-MeMS/GCN catalysts.

3.3 Ni-doped MoS_2/g-C_3N_4 hetero-nanostructures

3.3.1 Structure and morphology of n-NMS/GCN

2D/2D Ni-doped MoS_2/g-C_3N_4 layered heterostructures were prepared via a two-step chemical process[179], as illustrated in **Figure 50**. Small-sized Ni-doped MoS_2 nanosheets were firstly prepared by a facile sulfurization of monovacant Keggin-type phosphomolybdate ($Na_7PMo_{11}O_{39}$) precursors with a hydrothermal reaction with thioacetamide and $NiCl_2$ compounds. In this method, $[PMo_{11}O_{39}]^{7-}$ clusters are decomposed to form MoO_x oxide species, while thioacetamide acts as a sulfur source, which, in pair with Ni^{2+} ions, leads to the formation of Ni-doped MoS_2 nanosheets. This is a gentle procedure that permits control over the Ni doping level of MoS_2. The composition of the Ni-MoS_2 nanolayers (*n* (mol% Ni) = 100 x Ni/(Ni + Mo) = 1, 3, 5, 10 and 15%) was effectively modulated by simply tuning the mass ratio of $NiCl_2$ to

$[PMo_{11}O_{39}]^{7-}$ precursor. The resulting Ni-MoS_2 nanosheets were subsequently deposited on the surface of g-C_3N_4 (denoted as GCN) via a liquid exfoliation route to give few-layer heterostructures of Ni-doped MoS_2/g-C_3N_4, as displayed in **Figure 50**. The interlayer coupling between g-C_3N_4 and MoS_2 layers can be realized through strong van der Waals stacking interactions and possible out-of-plane Mo–N bonding[180,181]. The obtained catalysts were denoted as *n*-NMS/GCN, where *n* refers to the Ni content in Ni-MoS_2 nanosheets; all these samples have 30 wt% Ni-MoS_2.

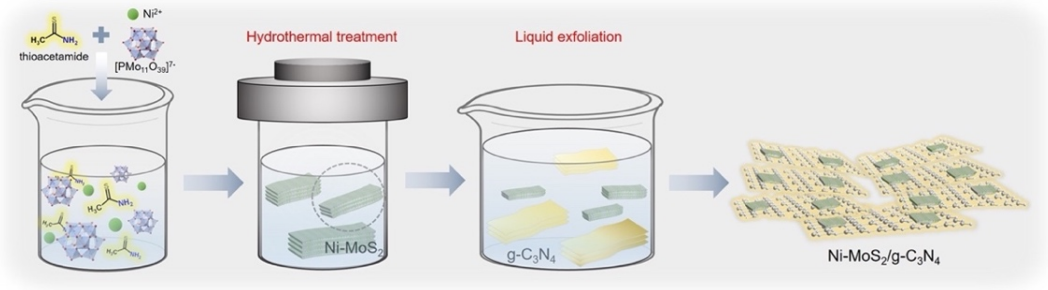

Figure 50. Schematic representation of the preparation of layered Ni-doped MoS_2/g-C_3N_4 (*n*-NMS/GCN) materials.

Insights into the crystal structure and morphology of as-prepared materials were obtained by employing powder X-ray diffraction (XRD) and transmission electron microscopy (TEM). **Figure 51** shows a typical XRD pattern of the composite material made using 30 wt% Ni-MoS_2 (3-NMS/GCN), which is the most active catalyst of this study, along with that of pristine GCN sample. The XRD patterns present a strong diffraction peak at 27.8° and the weak feature at 13.2°, which are assigned to the (002) interlayer stacking of the conjugated aromatic rings and the (100) in-plane tri-s-triazine packing motif of the graphitic C_3N_4, respectively (JCPDS card no. 87-1526).[182] The XRD analysis also manifests that compared with pristine g-C_3N_4, there is a decrease in the (002) peak intensity for the Ni-MoS_2 loaded sample. This could result from the smaller constructive interference from adjacent crystal planes due to the Ni-MoS_2 deposition on the (002) surface of g-C_3N_4. Also, the reduced intensity ratio of the (100) and (002) reflections in 3-NMS/GCN as compared to that in GCN suspects strong interaction between the Ni-MoS_2 and g-C_3N_4 layers.[183]

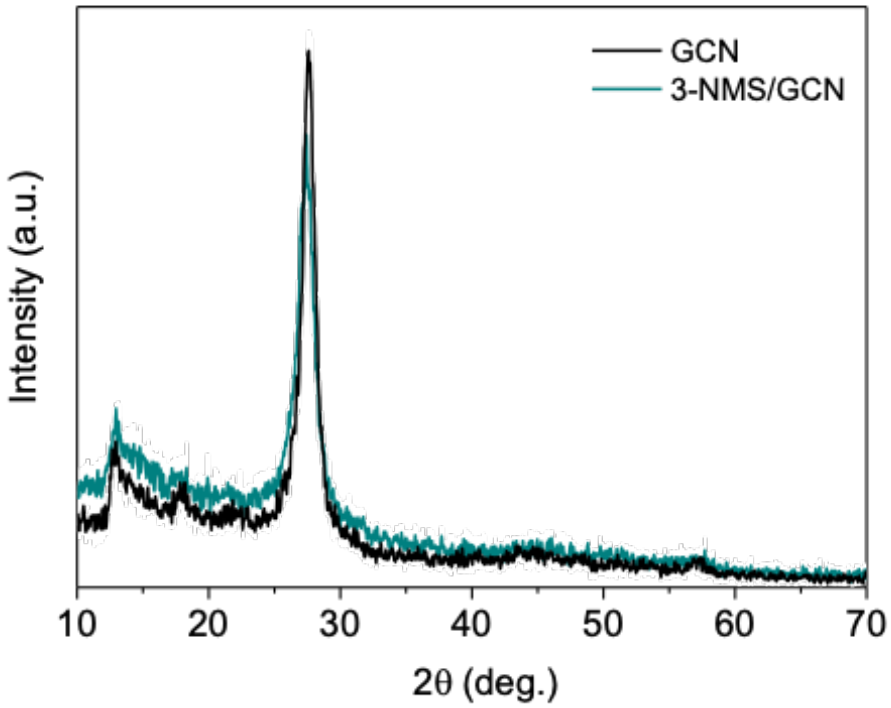

Figure 51. Typical XRD pattern of g-C_3N_4 (GCN) and 3-NMS/GCN heterostructure.

The intimate contact of the Ni-MoS_2 and g-C_3N_4 components is beneficial for photoelectron conversion since creates multiple electron-transfer pathways through the Ni-MoS_2/g-C_3N_4 interface. Despite the crystalline nature of Ni-MoS_2 layers, as seen in high-resolution TEM and electron diffraction studies (see below), it is difficult to observe MoS_2 diffraction peaks in the composite materials because of the small grain size and high dispersion of the Ni-MoS_2 nanosheets. Infrared (IR) spectroscopy further verified the π-conjugated structure of g-C_3N_4, showing the characteristic peaks of the tri-s-triazine (C_3N_3) and heptazine (C_6N_7) units (**Figure 52**). The infrared (IR) spectroscopy confirms the conjugated structure of g-C_3N_4, showing the characteristic vibration bands of tris-s-triazine (C_3N_3) rings at 810 cm^{-1} (ν(C=N–C)) and heptazine (C_6N_7) units at 1238 and 1408 cm^{-1} (ν(C–N)) and 1638 cm^{-1} (ν(C=N))[184]. The IR spectra also implies the presence of uncondensed amino (–NH_2 and =NH) groups by broad peaks at 3100–3300 cm^{-1}. However, from IR analysis is difficult to discern any noticeable chemical difference between the 3-NMS/GCN and GCN samples, showing similar profiles possibly due to the low amount and small lateral dimension of the Ni-MoS_2 nanosheets.

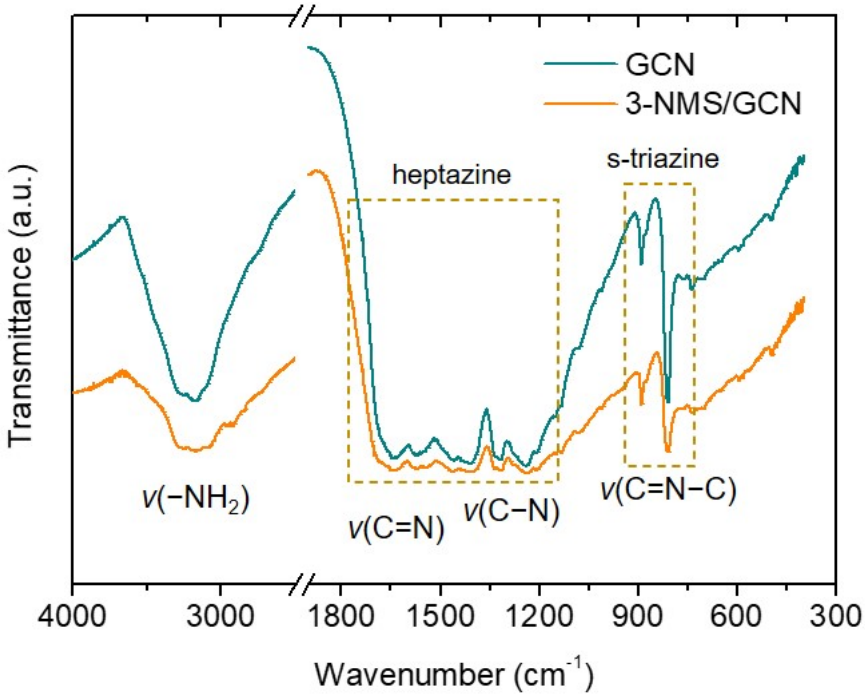

Figure 52. IR spectra of the as-prepared 3-NMS/GCN and GCN materials.

Table 4. EDS results and chemical formulas of as-prepared *n*-NMS/GCN catalysts (30 wt% Ni-MoS_2).

Sample	**Atomic ratios Ni/Mo/S**	**Ni content in Ni-MoS_2 nanosheets (at%)**	**Chemical formula**
1-NMS/GCN	0.4:35.2:64.4	1.0	$Ni_{0.01}Mo_{0.99}S_{1.81}$/g-$C_3N_4$
3-NMS/GCN	1.2:36.5:62.4	3.1	$Ni_{0.03}Mo_{0.97}S_{1.66}$/g-$C_3N_4$
5-NMS/GCN	1.9:36.2:61.9	4.9	$Ni_{0.05}Mo_{0.95}S_{1.62}$/g-$C_3N_4$
10-NMS/GCN	4.0:37.3:58.7	9.7	$Ni_{0.10}Mo_{0.90}S_{1.43}$/g-$C_3N_4$
15-NMS/GCN	6.4:36.9:56.7	14.8	$Ni_{0.15}Mo_{0.85}S_{1.32}$/g-$C_3N_4$
3-NMS/GCN[a]	1.2:37.5:61.4	3.0	$Ni_{0.03}Mo_{0.97}S_{1.60}$/g-$C_3N_4$

[a]Retrieved after photocatalytic reactions.

Clear evidence of the presence of Ni-MoS_2 in the heterostructures comes from energy dispersive X-ray spectroscopy (EDS) and atomic absorption (AAS) spectroscopy. Through this technique, we determined atomic ratios of Mo, Ni and S, which are very close to the nominal compositions of the prepared nanosheets (**Table 4**). This suggests the complete incorporation of Ni^{2+} into the MoS_2 lattice during the hydrothermal synthesis. Moreover, EDS analysis also verifies that these materials are S deficient with a composition of $Ni_xMo_{1-x}S_y$; $x \sim 0.01$ to 0.15, $y \sim 1.32$ to 1.81. Indeed,

the sulfur content in the Ni-doped MoS_2 decreased obviously with increasing amount of Ni, see **Table 4**. In fact, the incorporation of Ni^{2+} ions into the MoS_2 structure may cause the formation of S-defect sites according to Equation (6). In this equation replacement of one Mo^{4+} with Ni^{2+} involves the formation of one S vacancy ($V_s^{\cdot\cdot}$) in the Mo-S-Ni lattice for charge balance.

$$MoS_2 + xNi^{2+} \rightarrow xNi_{Mo}'' + xV_s^{\cdot\cdot} + Ni_xMo_{1-x}S_{2-x} \quad (6)$$

Such S vacancies can improve the carrier transport efficiency and electrochemical performance of MoS_2 nanosheets by introducing mid-gap localized states in the band structure as well as creating new active edge sites (S-terminated edge) in the catalytically inactive basal plane of MoS_2[185]. These interband states may activate new optical transitions in the visible range, thus improving light harvesting ability[186]. Therefore, controlling the quantity of defects in MoS_2 is critical in photochemical reactions.

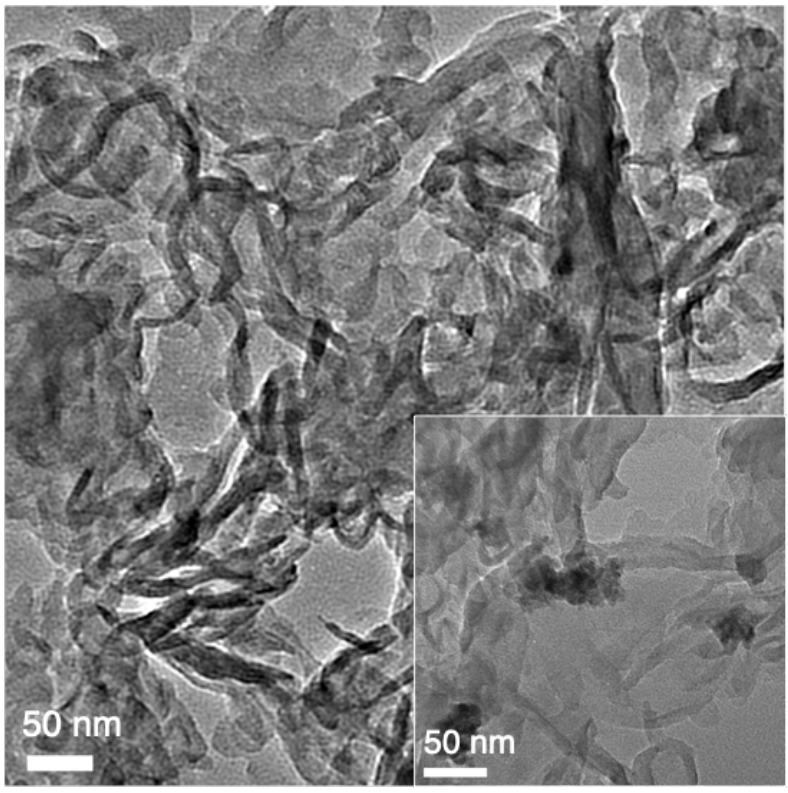

Figure 53. Typical TEM images of 3-NMS/GCN heterostructure.

Typical TEM images of the 3-NMS/GCN catalyst are shown in **Figure 53**. The images show that this material exhibits a layered network structure that is composed of

Ni-MoS_2 nanosheets (appeared as dark small areas) with a 27 ± 4 nm lateral size (**Figure 54**) that spread over the surface of graphitic C_3N_4 (appeared as light areas). A high-resolution TEM (HRTEM) image taken on the surface of a single Ni-MoS_2 nanosheet shows crystal lattice fringes throughout the entire layered structure with a 3.2 Å interplanar distance (**Figures 55a** and **b**), corresponding to the (004) planes of hexagonal MoS_2. The hexagonal lattice symmetry of MoS_2 was further affirmed by selected-area electron diffraction (SAED); the three concentric Debye-Scherrer diffraction rings in **Figure 55c** are well assigned to the (100), (110) and (200) crystal planes of 2H MoS_2 (JCPDS card no. 77-1716; space group P63/*mmc*).[187]

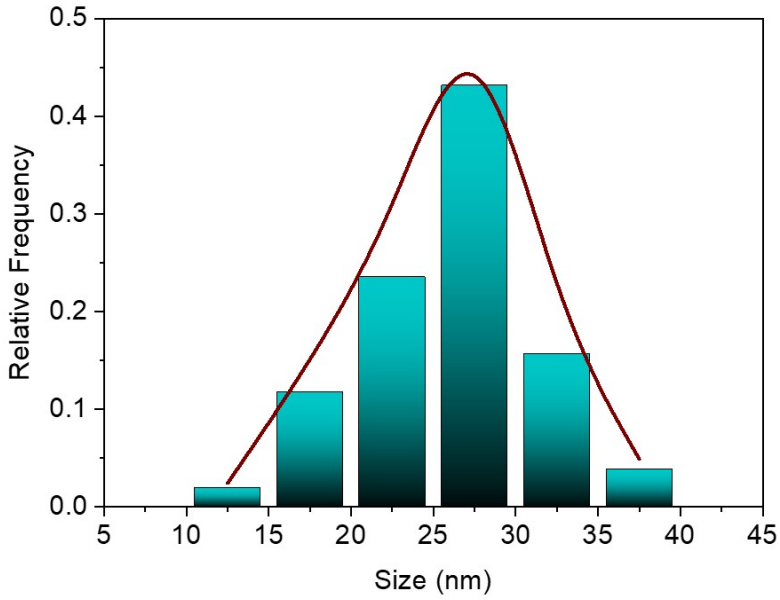

Figure 54. The lateral size distribution of the 3% Ni-MoS_2 nanosheets for the 3-NMS/GCN catalyst (based on the analysis of more than 70 individual Ni-MoS_2 layers).

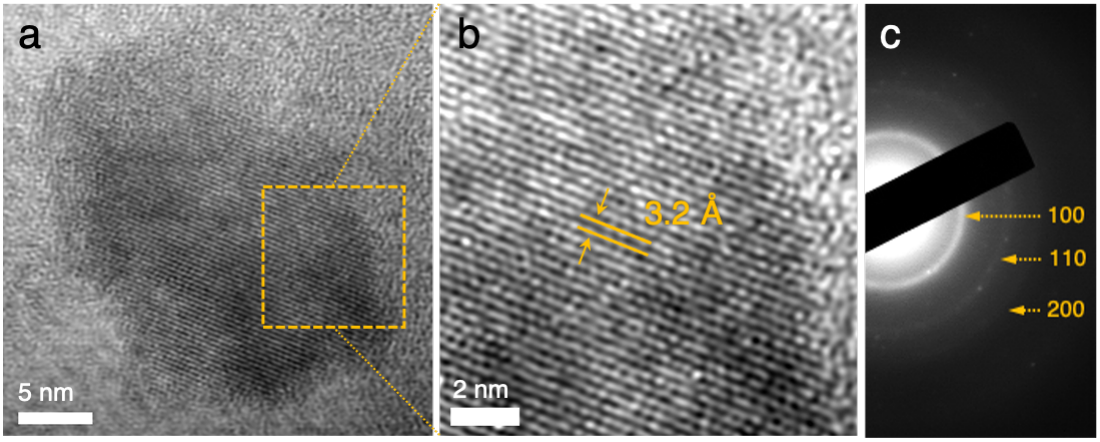

Figure 55. Typical (a and b) high-resolution TEM and (c) SAED pattern of 3-NMS/GCN heterostructure.

Further chemical information for the as-prepared MoS_2 based nanosheets was obtained from X-ray photoelectron spectroscopy (XPS) measurements. **Figures 56** show the Mo 3d and S 2p core-level signals for the undoped and Ni-doped MoS_2 samples. In **Figure 56a**, deconvolution of the Mo 3d spectrum reveals a prominent doublet peak (229.1 and 232.3 ±0.2 eV) with a spin-orbit splitting of 3.2 eV due to the Mo $3d_{5/2}$ and $3d_{3/2}$ spin-orbit components of the Mo^{4+} in MoS_2[188]. Furthermore, it displays a weak doublet peak at 232.4 ± 0.2 eV (Mo $3d_{5/2}$) and 235.6 ±0.2 eV (Mo $3d_{3/2}$) binding energies most likely due to unsaturated Mo^{4+} atoms[189] and/or the formation of some surface suboxide MoO_x species caused by the synthesis and surface oxidation in air.[190] The small singlet peaks at 226.1, 227.6 and 233.0 ±0.2 eV are assigned to the S 2s lines, corresponding to metal sulfur bonds (Ni/Mo–S), S^{2-} ions of defective MoS_2 and SO_x species owing to surface oxidation, respectively.[191]

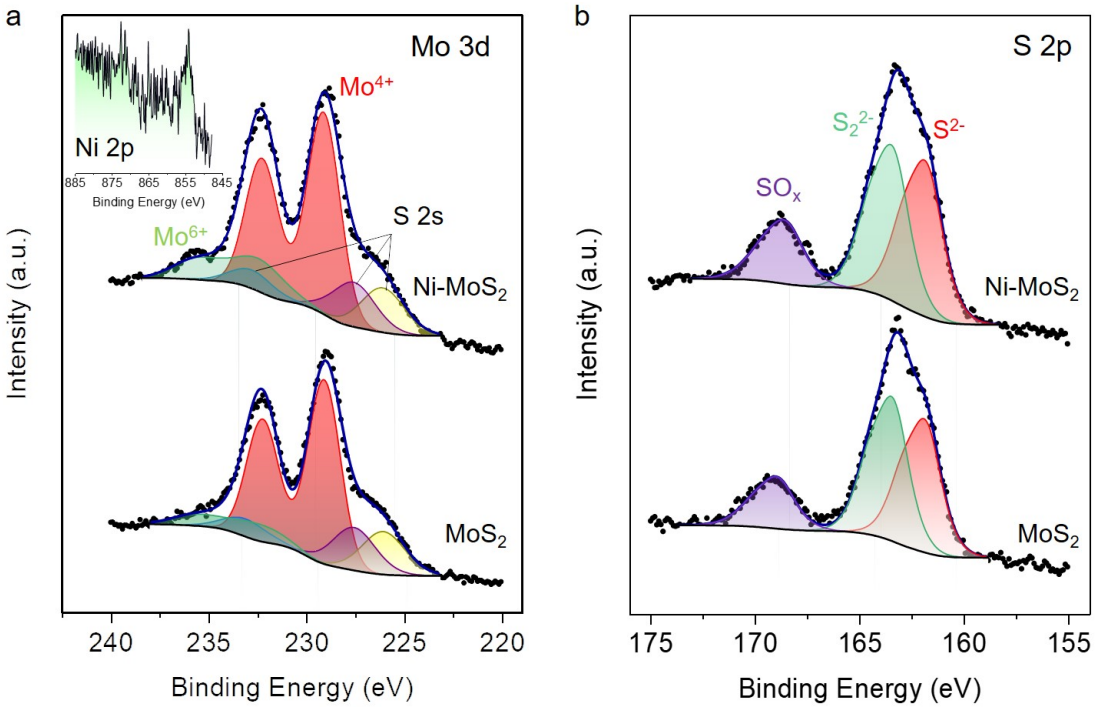

Figure 56. (a) Mo 3d and (b) S 2p core-level XPS spectra of as-prepared MoS_2 and Ni-doped MoS_2 nanosheets. Inset of panel (a): the Ni 2p XPS spectrum for Ni-MoS_2 sample. Embedded peaks for different components are presented as green, red, yellow and purple curves. The blue lines are fits to the experimental data.

For the Ni-doped MoS_2 sample, due to the low signal-to-noise ratio, fitting of the Ni 2p spectrum is difficult to perform. The Ni 2p region shows a broad Ni $2p_{3/2}$ photoelectron peak at around 854.8 ± 0.3 eV (inset of **Figure 56a**), which can be attributed to Ni–S

bonds, corroborating the inclusion of Ni^{2+} ions into the MoS_2 lattice by the formation of Ni–S–Ni and/or Ni–S–Mo bonds. **Figure 56b** shows two prominent doublet peaks (shown as asymmetric single peaks with a spin-orbit splitting of 1.16 and an area ratio of 1:2) for the S 2p spectrum at 161.7 ±0.2 eV and 163.3 ±0.2 eV assigned to metal-sulfur bonds (Ni/Mo–S) and bridging S_2^{2-} moieties of (Ni)MoS_2, respectively.[192] In addition, a small amount of sulfur species at certain higher oxidation states is, however, observed in the surface of MoS_2 and Ni-MoS_2 nanosheets, deducing from the weak peaks at 168.6 ±0.2 eV.

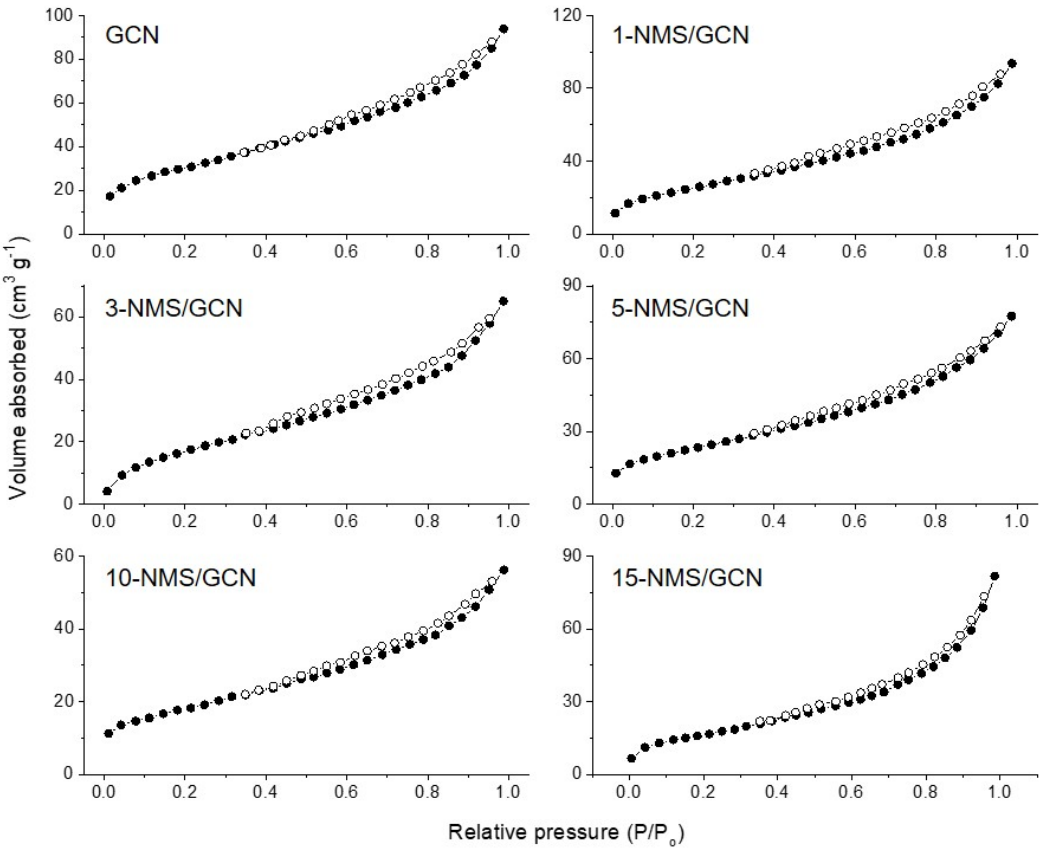

Figure 57. N_2 adsorption-desorption isotherms at –196 °C of the GCN and *n*-NMS/GCN catalysts.

N_2 physisorption was carried out to examine the porosity of the prepared materials. The N_2 adsorption–desorption isotherms of the GCN and *n*-NMS/GCN samples show typical type-IV curves accompanied with a small H_3-type hysteresis loop according to the IUPAC classification (**Figure 57**), suggesting mesoporous structures with slit-shaped pores, possible derived from the interstitial voids among the stacked layers.[193] On the basis of the adsorption data, the specific surface area of the *n*-NMS/GCN was

estimated to be 63–95 m^2 g^{-1}, using the Brunauer–Emmett–Teller (BET) model fit of the adsorption data, which are slightly lower than the surface area of pristine GCN sample (ca. 104 m^2 g^{-1}), see **Table 5**. The lower surface area of the Ni-MoS_2 loaded materials is presumably due to the heavy elements (Mo, Ni and S) that compose the structure.

Table 5. Textural properties of the GCN and *n*-NMS/GCN catalysts.

Catalyst	Surface area (m^2 g^{-1})	Pore volume (cm^3 g^{-1})	Average pore size[a] (nm)
GCN	104	0.15	2.9
1-NMS/GCN	95	0.15	3.2
3-NMS/GCN	73	0.11	3.0
5-NMS/GCN	82	0.12	2.9
10-NMS/GCN	65	0.10	3.1
15-NMS/GCN	63	0.11	3.5

[a]The average pore width is given by $w = 2V_p/S_p$, where V_p is the total pore volume at $P/P_o = 0.98$ and S_p is the pore surface area, assuming slit-shaped pores.

3.3.2 Photocatalytic study of n-NMS/GCN

3.3.2.1 Photocatalytic Cr(VI) reduction

The photocatalytic Cr(VI) reduction activity of the *n*-NMS/GCN heterostructures was initially investigated in a Cr(VI) aqueous solution (50 mg L^{-1}) that contained 1 g L^{-1} of catalyst without any additional hole scavenger under $\lambda > 360$ nm light irradiation. The catalytic results in **Figure 58** show that doping the MoS_2 lattice with Ni^{2+} leads to a significant improvement of the photoactivity, indicating that the Ni-MoS_2 nanosheets act as functional co-catalysts in the present system. In particular, the Cr(VI) photoreduction rate of *n*-NMS/GCN heterostructures increases with increasing Ni dopant level and attains a maximum at 3 at%; the 3-NMS/GCN outperforms the other catalyst, achieving complete (>99%) reduction of the Cr(VI) in 40 min. For comparison, under analogous conditions, the undoped MS/GCN (containing 30 wt% MoS_2) and pure GCN samples exhibited inferior performance to *n*-NMS/GCN, yielding a respective Cr(VI) conversion of ~87% and ~54% in 3 h. Meanwhile, control experiments showed no obvious changes in the Cr(VI) concentration in the dark or

absence of catalyst, suggesting that Cr(VI) elimination occurs via photocatalytic process (inset of **Figure 58**).

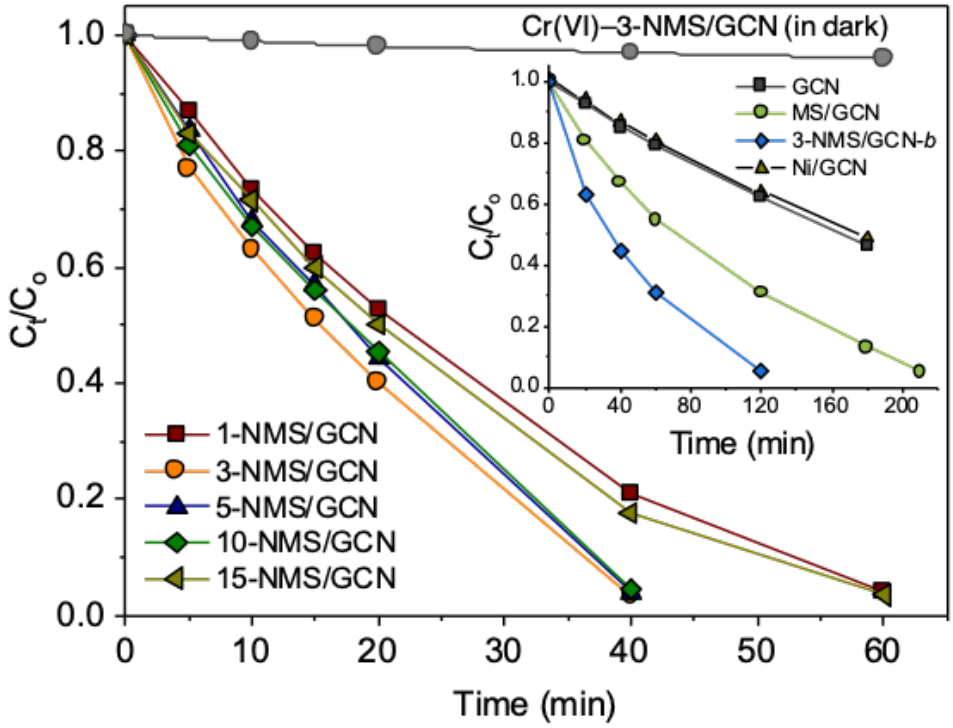

Figure 58. Photocatalytic reduction of aqueous Cr(VI) over different GCN, MS/GCN, *n*-NMS/GCN and 3-NMS/GCN-*b* catalysts (inset: photocatalytic Cr(VI) reduction activity of Ni/GCN). The photocatalytic reactions were performed as follows: 1 g L^{-1} catalyst, 50 mg L^{-1} Cr(VI) solution, pH = 2, λ > 360 nm light irradiation, 20 ºC.

As we shall discuss below, the superior catalytic performance of the present system can be justified by the enhanced charge carrier density and mobility at the interface of Ni-MoS_2/g-C_3N_4 junctions. Also, the lower photocatalytic activity of the highly Ni-doped samples could be attributed the to the relative lower reduction potential of the CB electrons and the deteriorated charge transport over the Ni-MoS_2/g-C_3N_4 interface. To further examine the kinetics of the Cr(VI) reduction, the pseudo-first-order reaction is plotted in **Figure 59**. Assuming that the reaction rate is proportional to the concentration of Cr(VI), the overall photocatalytic reaction can be expressed by the first-order kinetics of Langmuir-Hinshelwood model: $\ln(C_t/C_o) = -k_{app} \cdot t$, where C_t and C_o are the concentration of Cr(VI) at time t and initial time, respectively, and k_{app} is the apparent reaction rate constant. For all samples, the initial temporal evolution of the Cr(VI) concentration shows a good linear correlation with time, claiming that the reaction rate is first order with respect to Cr(VI) concentration. The above analysis thus

indicates that the reaction proceeds at a faster rate over 3-NMS/GCN catalyst than the other samples (**Figure 60**). For instance, the k_{app} rate constant of 3-NMS/GCN is improved to 4.57×10^{-2} min^{-1}, which is about 4.7 and 11.4 times the rate of the MS/GCN (k_{app} = 0.98×10^{-2} min^{-1}) and GCN (k_{app} = 0.40×10^{-2} min^{-1}) samples (**Figure 61**), respectively.

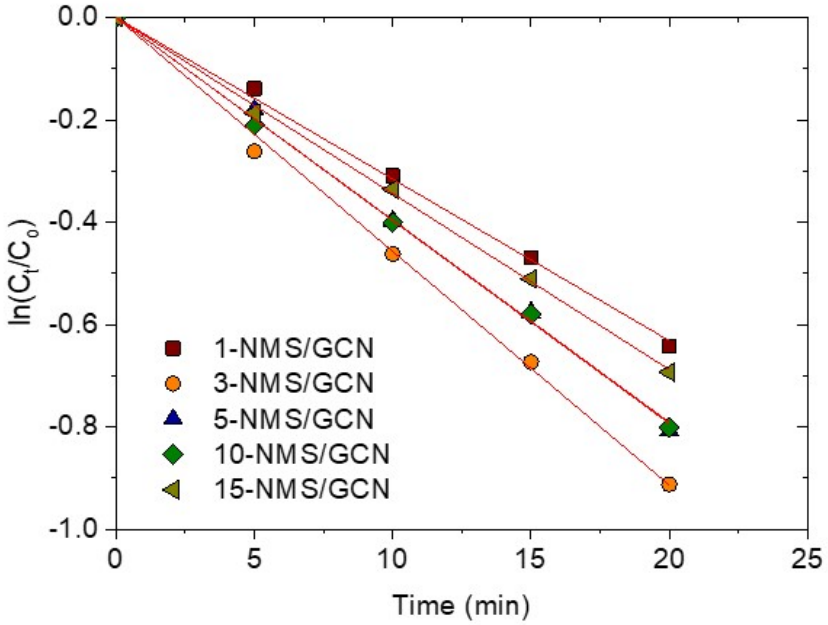

Figure 59. Kinetic profiles for the photocatalytic reduction of Cr(VI) over different *n*-NMS/GCN catalysts. The red lines are fit to the data.

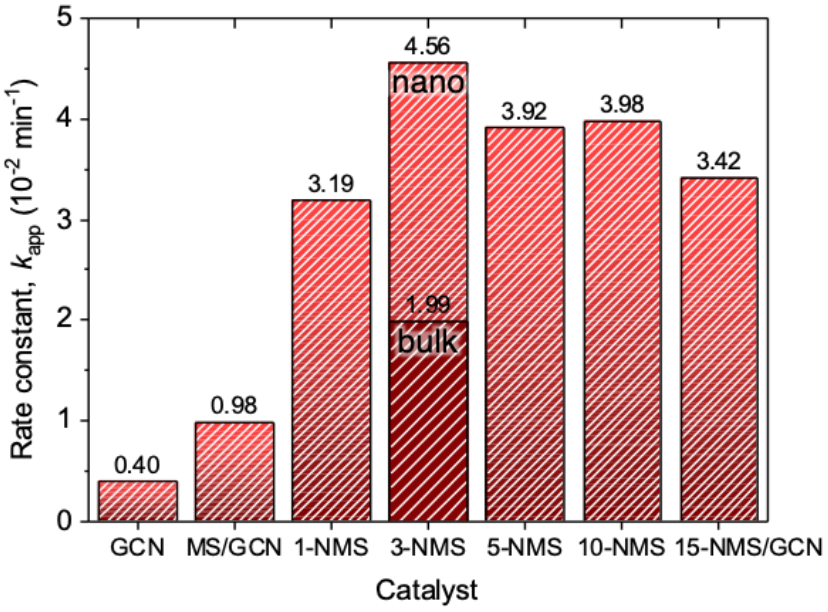

Figure 60. Pseudo-first-order reaction rate constants (k_{app}) over different GCN, MS/GCN, *n*-NMS/GCN and 3-NMS/GCN-*b* catalysts.

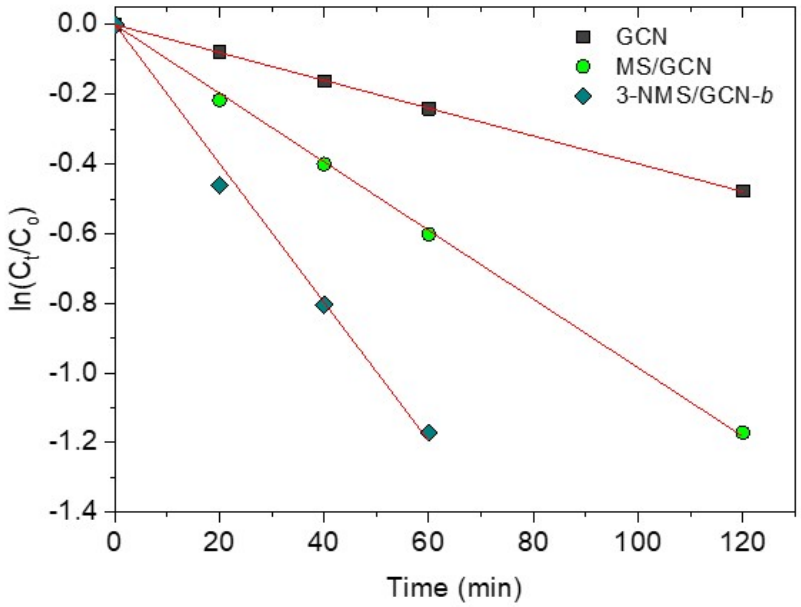

Figure 61. Pseudo-first-order kinetic plots for the photocatalytic reduction of Cr(VI) over different GCN, MS/GCN, 3-NMS/GCN-*b* catalysts. The red lines are fit to the data.

The photocatalytic effectiveness of the nanoscale Ni-MoS_2 layers was also evidenced by comparing the 3-NMS/GCN to a bulk analogue with respect to their corresponding Cr(VI) photoreduction performance. We thus prepared Ni-doped MoS_2/g-C_3N_4 heterostructure (denoted as 3-NMS/GCN-*b*) by depositing 3% Ni-doped MoS_2 microflakes (30 wt%) on the surface of exfoliated g-C_3N_4. Interestingly, the Cr(VI) photoreduction efficiency with 3-NMS/GCN is even higher that of 3-NMS/GCN-*b*, although both catalysts possess similar composition. In particular, bulk 3-NMS/GCN-*b* heterostructure reduces ~95% of Cr(VI) in 2 h with a reaction rate constant (k_{app}) of 1.99×10^{-2} min^{-1} (**Figures 58, 60** and **61**). In addition, a newly designed 3% Ni-loaded g-C_3N_4 (Ni-GCN) catalyst, which prepared by impregnating the exfoliated g-C_3N_4 with an ethanol solution of $NiCl_2$, showed similar catalytic activity to GCN (inset of **Figure 58**), indicating that Ni^{2+} ions have negligible effect towards the photocatalytic reduction of Cr(VI). These results explicitly demonstrate that both Ni doping and small grain size of Ni-MoS_2 layers have a decisive effect in enhancing the Cr(VI) photoreduction performance.

In the following, we optimize the photocatalytic performance of 3-NMS/GCN by performing a series of Cr(VI) photoreduction tests with different concentrations of Ni-MoS_2 nanosheets (from 10 to 40 wt%) and different loads of catalyst (from 0.6 to 1.2 g

L^{-1}). As shown in **Figure 62**, at a fixed mass of catalyst, a higher photocatalytic Cr(VI) reduction activity is observed with heterostructure containing 30 wt% Ni-MoS_2.

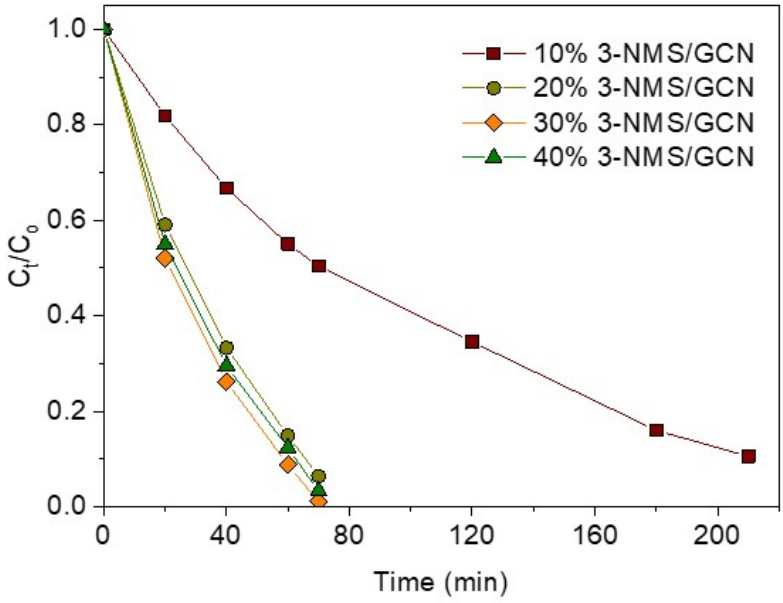

Figure 62. Time courses for photocatalytic Cr(VI) reduction for 3-NMS/GCN catalyst containing different amounts (wt%) of 3% Ni-doped MoS_2 nanosheets (3-NMS). The photocatalytic reactions were performed by suspending 30 mg of catalyst in 50 mL of water containing 50 mg L^{-1} Cr(VI) (pH = 2), under $\lambda > 360$ nm light irradiation.

Also, there is an increase of the Cr(VI) conversion efficiency with catalyst dosage increasing up to 1 g L^{-1} (keeping the Ni-MoS_2 loading concentration constant), as shown in **Figure 63**. This may result from the increased absorption of the incident light by the catalyst. At higher catalyst addition (1.2 g L^{-1}), however, the Cr(VI) photoreduction rate is slightly lower, possibly due to the full absorption of the incident light and/or light scattering by the catalyst's particles. Aside from catalyst loading, the pH of the solution has a pronounced effect on the photocatalytic activity. As shown in **Figure 64**, the 3-NMS/GCN catalyst exhibits a remarkably increased Cr(VI) photoreduction yield as the solution pH decreases from 6 to 1. Notably, in pH 1 solution, 3-NMS/GCN reduces Cr(VI) (50 mg L^{-1}) with a >99% conversion yield after 20 min. This behavior can be attributed to the favorable adsorption of Cr(VI) on the catalyst surface. In particular, at low pH values (less than 4), the Cr(VI) species, mainly as $HCrO_4^-$ anions, tend to interact more extensively with the positively charged surface of g-C_3N_4 (the point of zero charge (pH_{pzc}) of g-C_3N_4 ranges from 4 to 5)[194] and, therefore, this process can increase the Cr(VI) photoreduction effect.

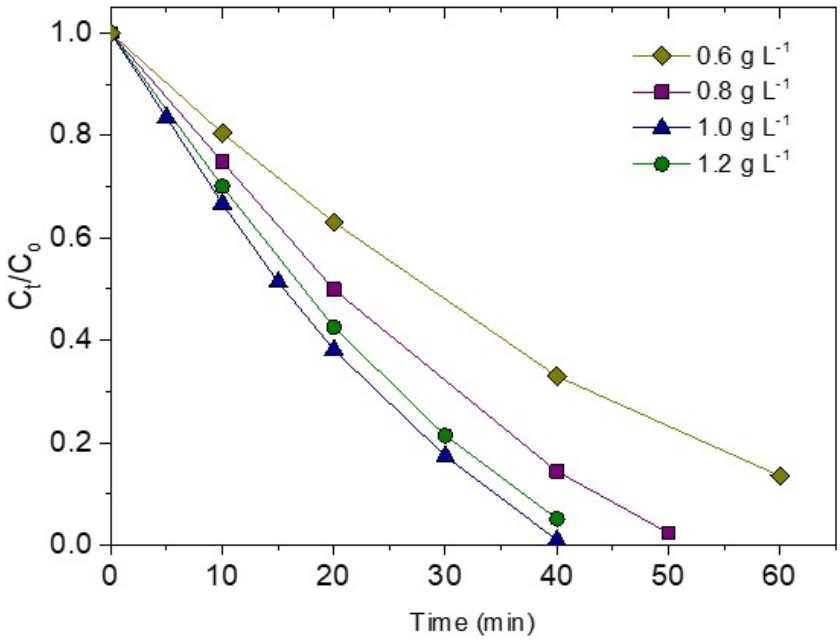

Figure 63. Concentration dependent photocatalytic Cr(VI) reduction activity of 3-NMS/GCN catalyst. Reaction conditions: 0.6–1.2 g L^{-1} of catalyst, 50 mgL^{-1} Cr(VI) aqueous solution, pH = 2, UV-visible light (λ>360 nm) irradiation, 20 °C.

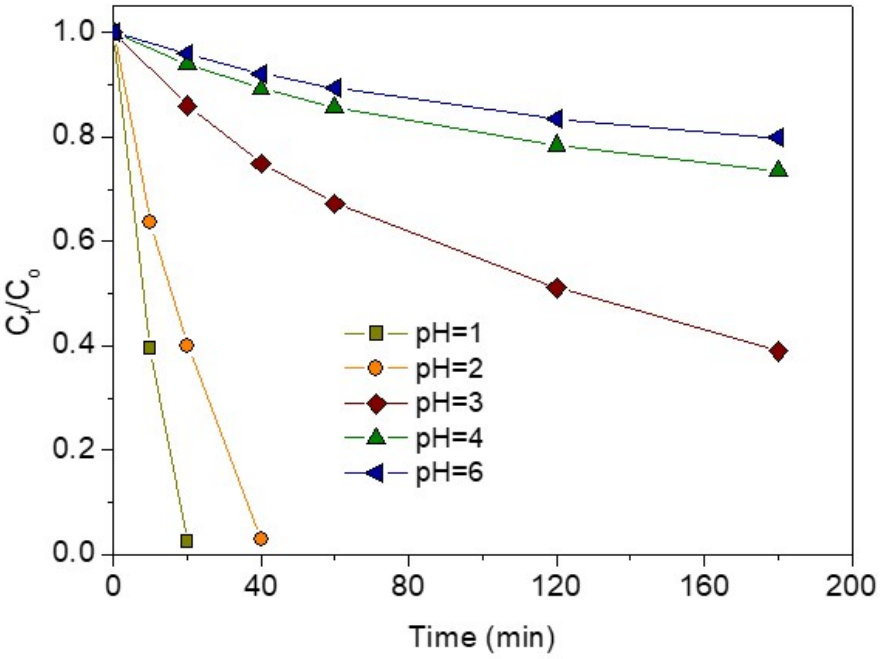

Figure 64. Effect of the solution pH on the photocatalytic Cr(VI) reduction performance. Reaction conditions: 1 g L^{-1} catalyst (3-NMS/GCN), 50 mg L^{-1} Cr(VI) aqueous solution, pH = 1–6, λ > 360 nm light irradiation, 20 °C. The pH of the solution was adjusted with 2 M H_2SO_4 or 2 M NaOH.

Moreover, in acidic solutions, the excessive concentration of hydronium ions (H_3O^+) is beneficial to the reduction of Cr(VI) to Cr(III) (see Equation (9)). Thus, under optimal

conditions (1 g L^{-1} catalyst, pH = 2), the Cr(VI) reduction rate for this system reaches 38.8 μmol h^{-1} within 40 min under UV-visible light. When using monochromatic light sources, the apparent quantum yield (QY) for the system is estimated to be as high as 29.6% at 375 ± 10 nm and 23.7% at 410 ± 10 nm, assuming all incident light is absorbed by the catalyst particles. This activity is superior to that of other state-of-the-art Cr(VI) reduction catalysts reported to date, even with sacrificial electron donors, such as the Ag_3PO_4/AgBr/$Ti_3C_2T_x$ composite (15 mg L^{-1} Cr(VI)/EDTA; QY ~ 12.5% at λ > 420 nm)[195], AgCl:Ag hollow nanocrystals (10 mg L^{-1} Cr(VI)/10 mM EDTA, QY ~ 7.5% at λ > 420 nm)[196], porous Ag/Ag_3PO_4/rGO microspheres (10 mg L^{-1} Cr(VI)/methylene blue (MB), QY ~ 2.37% at λ > 400 nm)[197], $CuFe_2O_4$/CdS heterostructure (0.5 mM Cr(VI)/0.5 mM salicylic acid, QY ~ 1.1% at λ = 430 nm)[198], TiO_2/formic acid (FA) composite (1.92 mM Cr(VI)/286 mM FA, QY ~ 1.58% at λ = 365 nm)[199], Co_3O_4/g-C_3N_4 heterojunction (15 mg L^{-1} Cr(VI)/tetracycline, QY~ 30% at λ = 420 nm)[200], mesoporous $Co_{1-x}Ni_xO$ nanoparticles (50 mg L^{-1} Cr(VI), QY ~ 1.5% at λ = 375 nm, QY ~ 0.8% at λ = 410 nm)[201], mesoporous CoO nanoparticle assemblies (50 mg L^{-1} Cr(VI), QY ~ 1.61% at λ = 375 nm)[202] and Au/TiO_2-Pt nanocomposites (1 mM Cr(VI), QY ~ 1% at λ = 550 nm)[203], as well as other g-C_3N_4-based catalysts (**see Table 6**), further manifesting the excellent photocatalytic activity of 3-NMS/GCN towards Cr(VI) reduction.

Table 6. Comparison of photocatalytic efficiency between 3-NMS/GCN and other reported g-C_3N_4-based photocatalysts.

Photocatalyst	**Reaction conditions**	**Photocatalytic reduction of Cr(VI)**		**Ref.**
		C/C_0	**Time (min)**	
Sulfonic acid-modified g-C_3N_4	50 mg catalyst, 100 mL Cr(VI) solution (10 mg L^{-1}), 50 mg citric acid, 300 W Xe lamp (λ>400 nm), pH=2	>86%	40	[204]
BUC-21/g-C_3N_4 composite	50 mg catalyst, 200 mL Cr(VI) solution (10 mg L^{-1}), tartaric acid, 500 W Xe lamp (λ>400 nm), pH=2	100%	80	[205]
g-C_3N_4/Graphene Oxide/$BiFeO_3$	0.5 g catalyst, 200 mL Cr(VI) solution (5 mg L^{-1}), 0.01 M or 0.1 M NaOH and HCl solution, 300 W Xe lamp (λ>400 nm), pH=2	95%	240	[206]

3.0 wt% g-C_3N_4/MIL-53(Fe)	20 mg catalyst, 50 mL Cr(VI) solution (10 mg L^{-1}), 500 W Xe lamp, (420<λ<760 nm), pH=3	100%	180	[207]
ZnS/g-C_3N_4	800 mg L^{-1} catalyst, 250 mL Cr(VI) solution (10 mg L^{-1}), 500 W Xe lamp, pH=7	91%	120	[208]
Ag/Bi_4O_7/g-C_3N_4 nanosheets	15 mg catalyst, 50 mL Cr(VI) solution (50 mg L^{-1}), 300 W Xe lamp (λ>420 nm), pH=3	98%	60	[209]
Polyaniline@g-C_3N_4/$ZnFe_2O_4$	200 mg catalyst, 20 mL Cr(VI) solution (20 mg L^{-1}), 20 mg L^{-1} phenol, 300 W Xe lamp, pH=3	98%	120	[210]
90 wt% g-C_3N_4/rGH	30 mg catalyst, 30 mL Cr(VI) solution (30 mg L^{-1}), 400 W metal halide lamp (λ>420 nm)	100%	120	[211]
GO/g-C_3N_4/MoS_2	20 mg catalyst, Cr(VI) solution (10 mg L^{-1}), 300 W Xe lamp (λ>420 nm)	80%	120	[212]
BPCMSs(40)/g-C_3N_4 NSs	50 mg catalyst, 50 mL Cr(VI) solution (10 mg L^{-1}), 4-fluorophenol, 300 W Xe lamp (λ>420 nm), pH=2	~70%	240	[213]
g-C_3N_4/PMDA	50 mg catalyst, 50 mL As(III) and Cr(VI) solution ($[As(III)]_0$ = 100 μM, $[Cr(VI)]_0$ = 100 μM, 300 W Xe lamp (λ>420 nm), pH=4	>90%	120	[214]
2D/3D g-C_3N_4/UiO-66 composite	100 mg catalyst, 200 mL Cr(VI) solution (10 mg L^{-1}), 300 W Xe lamp, pH=2	~99%	40	[215]
50 wt% CoFe-LDH/g-C_3N_4	50 mg catalyst, 50 mL Cr(VI) solution (50 mg L^{-1}), 300 W Xe lamp (λ > 420 nm), pH=2	100%	100	[216]
TiO2/g-C3N4/rGO	50 mg catalyst, 100 mL Cr(VI) solution (100 mg L^{-1}), 300 W Xe lamp (λ > 360 nm), pH=3	97%	240	[217]
B-doped g-C_3N_4/$BiVO_4$	50 mg catalyst, 20 mL Cr(VI) solution (20 mg L^{-1}), 150 W Xe lamp (λ>420 nm), pH=2	85%	30	[218]
Fe^0-doped g-C_3N_4/MoS_2	30 mg catalyst, 50 mL Cr(VI) solution (20 mg L^{-1}), RhB, 500 W Xe lamp (λ>420 nm)	91%	120	[219]
30 wt% g-C_3N_4/SnS_2	40 mg catalyst, 100 mL Cr(VI) aqueous solution (50 mg L^{-1}), 300 W Xe lamp (λ>420 nm)	>99%	50	[220]
2 wt% Cu-(1:4) MoO_3/g-C_3N_4	20 mg catalyst, 20 mL Cr(VI) (20 mg L^{-1}), citric acid, sunlight, pH=3	95%	~50	[221]
Fe_3O_4/C/g-C_3N_4	10 mg catalyst, 50 mL Cr(VI) solution (20 mg L^{-1}), 300 W Xe lamp (λ>420 nm), pH=2	100%	100	[222]

1D/2D $Ag_xH_{3-x}PMo_{12}O_{40}$/Ag NRs/g-$C_3N_4$	20 mg catalyst, 40 mL Cr(VI) solution (80 mg L^{-1}), isopropanol, 300 W Xe lamp (λ>420 nm)	85.4%	40	[223]
$CaFe_2O_4$/g-C_3N_4/CNT	100 mg catalyst, 100 mL Cr(VI) and tetracycline (10 mg L^{-1}), 300 W Xe lamp (λ>420 nm), pH=3	97%	120	[224]
g-C_3N_4@NH_2-MIL-88B(Fe)	25 mg catalyst, 50 mL Cr(VI) aqueous solution (25 mg L^{-1}), 500 W Xe lamp, pH=7	100%	40	[225]
g-C_3N_4/ MIL-88B(Fe)	20 mg catalyst, 50 mL Cr(VI) aqueous solution (10 mg L^{-1}), 300 W Xe (λ>420 nm)	100%	105	[226]
3-NMS/GCN	**50 mg catalyst, 50 mL Cr(VI) aqueous solution (50 mg L^{-1}), 300 W Xe lamp, pH=2**	**>99%**	**40**	**In this work**

In order to explore the applicability of the present catalytic system for practical detoxification of wastewaters, the Cr(VI) photoreduction ability of 3-NMS/GCN was examined in the presence of various interfering ions. These experiments made by using the same dose of catalyst (1 g L^{-1}) in 50 mL of Cr(VI) aqueous solution (100 mg L^{-1}) containing 50 mg L^{-1} for each SO_4^{2-}, CO_3^{2-}, NO_3^-, Cl^-, Na^+, Cu^{2+}, Zn^{2+} and Mn^{2+} ion, which represent typical concentrations in industrial wastewaters.[227,228] In general, the coexistence of interfering ions (such as SO_4^{2-}, NO_3^-, Cl^-, Zn^{2+} and Mn^{2+}) with Cr(VI) in wastewaters is a challenge as they decrease the reduction rate of Cr(VI) due to the competitive adsorption and redox behavior at the catalyst surface, as well as the light screening effect.[229,230] **Figure 65** shows the time courses of photocatalytic reduction of Cr(VI) (100 mg L^{-1}) in aqueous solutions without and in the presence of different interfering ions. The results demonstrate that there is no significant change in the Cr(VI) (in form of $HCrO_4^-$ and $Cr_2O_7^{2-}$ oxyanions) photoreduction performance of 3-NMS/GCN even though overwhelming amounts of interfering ions are present; Cr(VI) oxyanions are completely reduced after irradiation for 90 min in both contaminated solutions. Recent studies indicated that the presence of hydrated anions with high charge and large size (like SO_4^{2-} and NO_3^-) can severally deteriorate the reduction efficiency of the catalyst by inhibiting the diffusion of $HCrO_4^-$ ions[231]. However, we did not observe such a behavior in our catalytic system, confirming the strong photocatalytic ability of the prepared catalysts for Cr(VI) reduction.

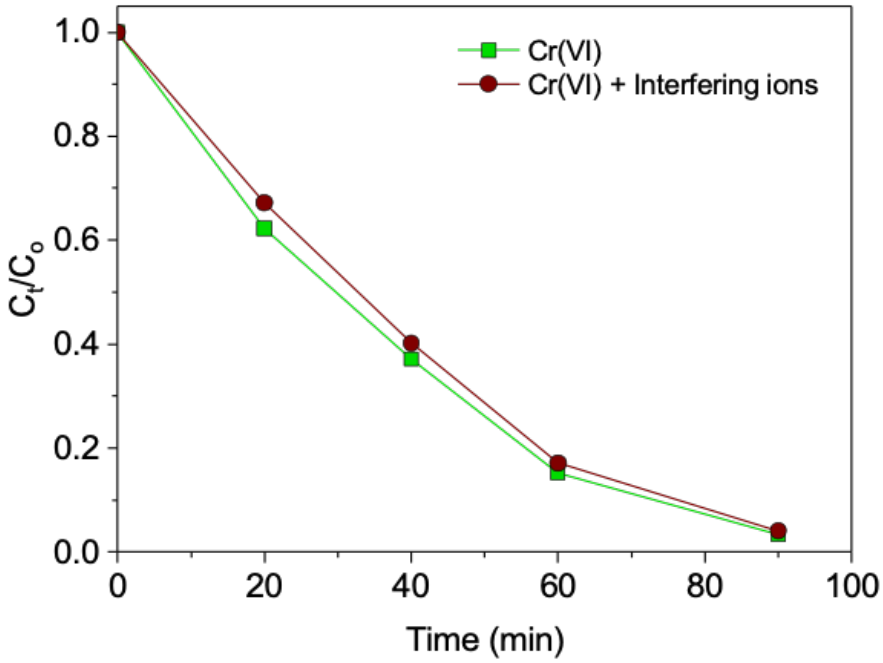

Figure 65. Photocatalytic reduction of aqueous Cr(VI) solution (100 mg L^{-1}) over 3-NMS/GCN catalyst in the absence and presence of different interfering ions (50 mg L^{-1} for each ion: SO_4^{2-}, CO_3^{2-}, NO_3^-, Cl^-, Na^+, Cu^{2+}, Zn^{2+} and Mn^{2+}). The photocatalytic reactions were performed as follows: 1 g L^{-1} catalyst, 50 mg L^{-1} Cr(VI) solution, pH = 2, $\lambda > 360$ nm light irradiation, 20 °C.

Moreover, 3-NMS/GCN catalyst exhibited high photochemical stability over three consecutive recycling tests. After the completion of catalytic reaction, the catalyst was isolated from the reaction mixture by centrifugation, washed with water, and re-dispersed in a fresh Cr(VI) solution. As seen in **Figure 66**, 3-NMS/GCN largely maintained its operation performance (within 5% experimental error) throughout the entire tested period, giving an a Cr(VI) reduction efficiency of >98% after three 40 min cycles of reuse. In addition, kinetic analysis indicated that the rate of Cr(VI) reduction remains stable, and no significant changes were observed ($k^1_{app} = 4.4\times10^{-2}$ min^{-1}; $k^2_{app} = 4.4\times10^{-2}$ min^{-1}; $k^3_{app} = 4.5\times10^{-2}$ min^{-1}, **Figure 67**). The durability of the 3-NMS/GCN catalyst was further explored by EDS and XRD measurements after repeated photocatalytic tests. The EDS analysis demonstrated that the dopant structure of Ni-MoS_2 nanosheets is well maintained after cycle reactions; it shows a 1.2:37.5:61.4 Ni/Mo/S atomic ratio that corresponds to a Ni content in MoS_2 of about 3 at% (see **Table 4**). In addition, XRD data confirm the graphitic structure of C_3N_4 host matrix, thus providing further evidence for the durability of the catalyst (**Figure 68**). These results attest the stability of the catalyst under the examined conditions.

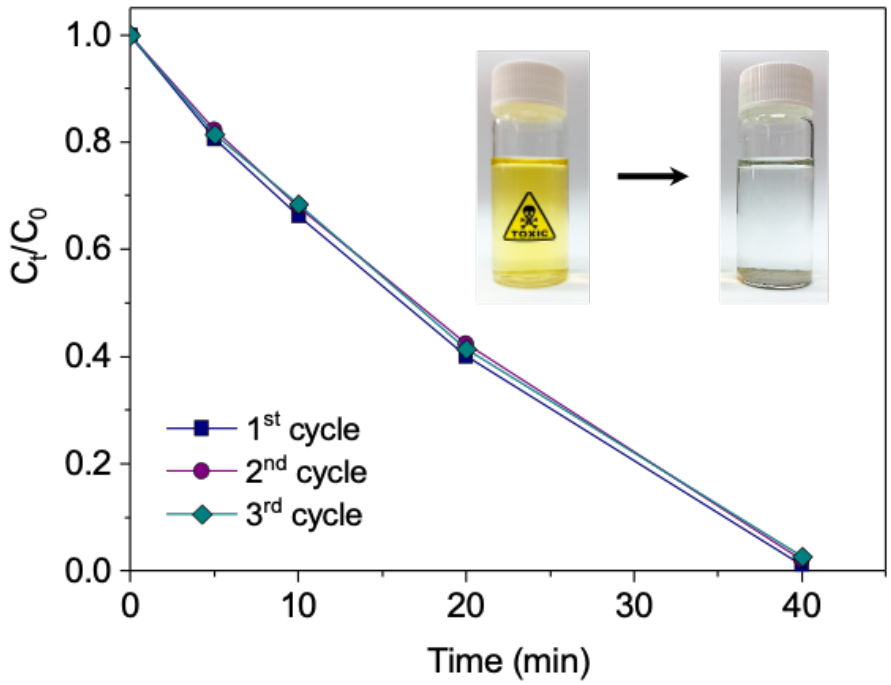

Figure 66. Recycling study of the 3-NMS/GCN catalyst (inset: typical photographic images of Cr(VI)-containing solution before and after catalysis). The photocatalytic reactions were performed as follows: 1 g L^{-1} catalyst, 50 mg L^{-1} Cr(VI) solution, pH = 2, λ > 360 nm light irradiation, 20 °C.

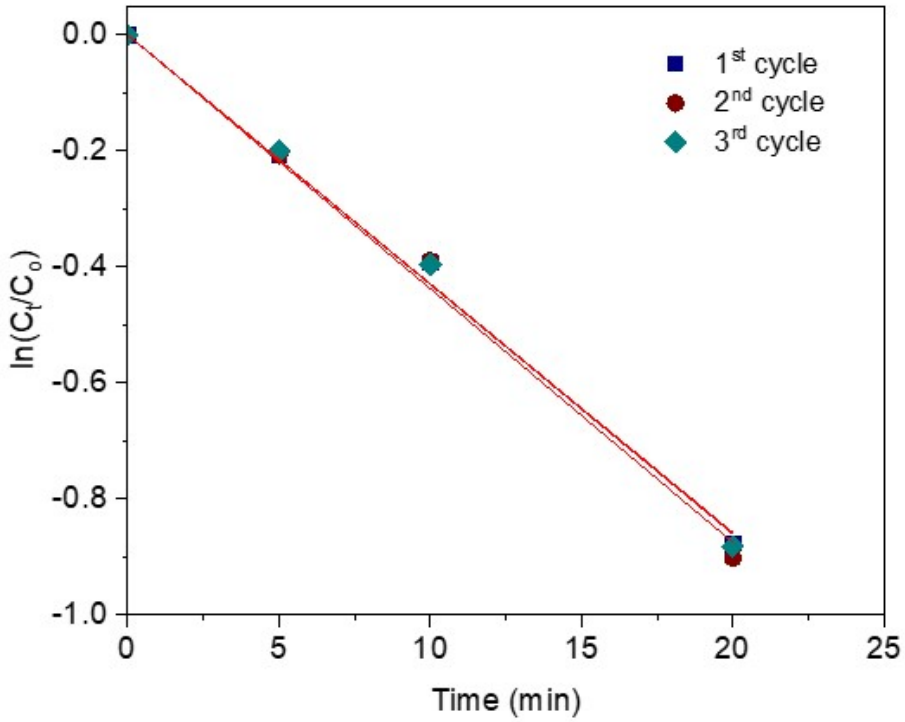

Figure 67. Kinetic profiles for the photocatalytic reduction of Cr(VI) over 3-NMS/GCN catalysts. The red lines are fit to the data.

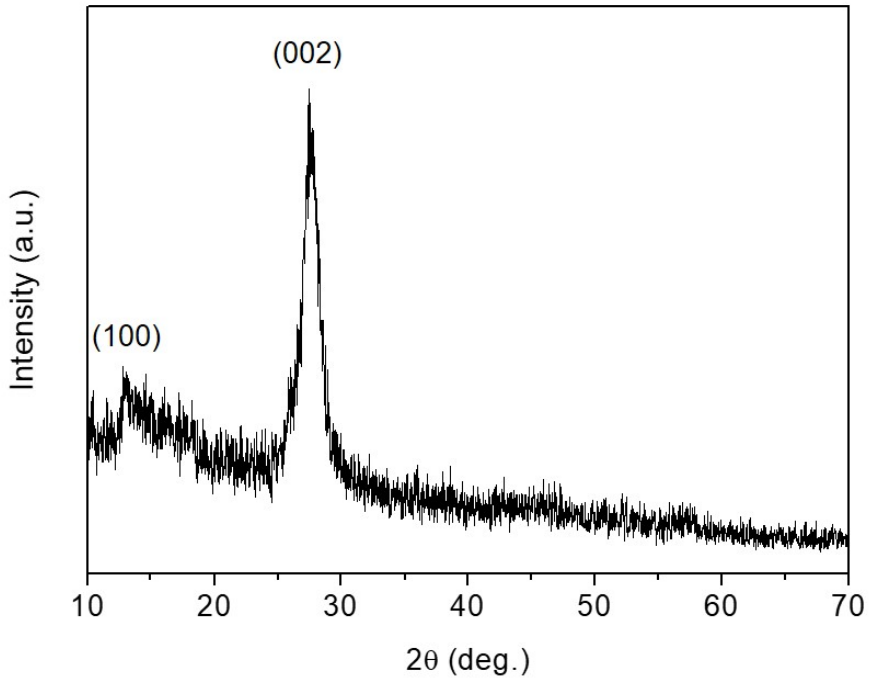

Figure 68. XRD pattern of the 3-NMS/GCN sample after photocatalytic recycle tests.

3.3.2.2 Mechanism of photocatalytic reaction

To elucidate the hole transfer processes during photocatalytic reaction, 3-NMS/GCN catalyst was examined for oxygen evolution under our previously described experimental conditions. In particular, the photocatalytic reduction of Cr(VI) along with H_2O oxidation was carried out in an air-tight cell containing 50 mg L^{-1} Cr(VI) solution and 1 g L^{-1} catalyst under irradiation of $\lambda > 360$ nm light; in this experiment, the concentration of Cr(VI) was determined using the colorimetric method and the amount of evolved O_2 was measured using a gas chromatograph. Prior to photocatalysis, the reaction solution was purged with He for at least 45 min to remove dissolved oxygen. The results indicate that 3-NMS/GCN is effective to reduce Cr(VI) to Cr(III) and oxidize water to molecular oxygen, yielding a Cr(VI) consumption rate of ~31.6 μmol h^{-1} (as $HCrO_4^-$ ions) and an O_2 evolution rate of ~21.4 μmol h^{-1} after 40 min irradiation. Further verification that the evolved O_2 indeed comes from the photochemical oxidation of water ($2H_2O \rightarrow O_2 + 4H^+ + 4e^-$) was provided by in situ monitoring the effluent gas with a mass spectrometer. For the purpose of this study, the Cr(VI) reduction experiment was performed as described above in a vacuum-tight cell and the evolved oxygen gas was detected by an on-line connected gas analyzer. **Figure**

69 shows the transient partial pressure of oxygen when light on and off conditions were applied to a 3-NMS/GCN suspension.

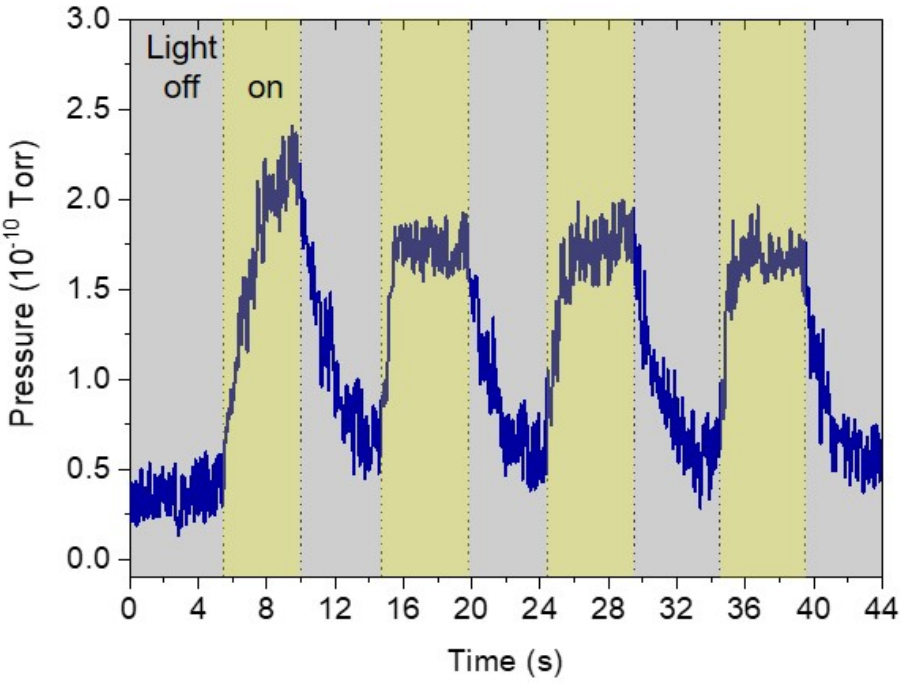

Figure 69. Oxygen evolution transient for 3-NMS/GCN catalyst under light on/off conditions. The dashed lines indicate the light on and off states. Reaction conditions: 1 g L^{-1} catalyst, 50 mg L^{-1} Cr(VI) solution, pH = 2, λ > 360 nm light irradiation, 20 °C.

It is apparent that there is a quick oxygen formation under UV-visible light illumination, while no oxygen evolution was observed in the dark. Meanwhile, no detectable trace of N_2 was observed during the course of the experiment, indicating that the reaction cell was air tight. Taken together, these results explicitly confirm the feasibility of the 3-NMS/GCN catalyst for multi-electron oxidation of water to dioxygen. Therefore, the half-reactions and overall reaction for photocatalytic reduction of Cr(VI) in acidic solution (in pH < 4 solution, Cr(VI) predominately exists as hydrogen chromate ($HCrO_4^-$) anions) can be expressed by the following equations:

$$HCrO_4^-{}_{(aq)} + 7H^+{}_{(aq)} + 3e^- \rightarrow Cr^{3+}{}_{(aq)} + 4H_2O_{(l)} \text{ (cathode)} \quad (7)$$

$$3H_2O_{(l)} + 6h^+ \rightarrow {}^3/_2O_{2(g)} + 6H^+{}_{(aq)} \text{ (anode)} \quad (8)$$

$$2HCrO_4^-{}_{(aq)} + 8H^+{}_{(aq)} \rightarrow 2Cr^{3+}{}_{(aq)} + {}^3/_2O_{2(g)} + 5H_2O_{(l)} \text{ (overall reaction)} \quad (9)$$

If we use the stoichiometry shown in Equation (9) to estimate the rate of oxygen production from the photocatalytic consumption of 31.6 μmol h^{-1} $HCrO_4^-$ (as inferred from photo-oxidation results), we obtain a theoretical value of 23.7 μmol h^{-1}, which is close to the experimental O_2 evolution rate obtained by the 3-NMS/GCN catalyst (ca. 21.4 μmol h^{-1}). Given that the redox potentials of H_2O/·OH (1.92 V) and –OH/·OH (1.58 V) pairs are located above the VB of *n*-NMS/GCN catalysts (see below), photo-oxidation of absorbed water molecules (H_2O_{abs}) and/or surface hydroxyl ($–OH_{abs}$) groups to hydroxyl radicals (·OH) also appears feasible.

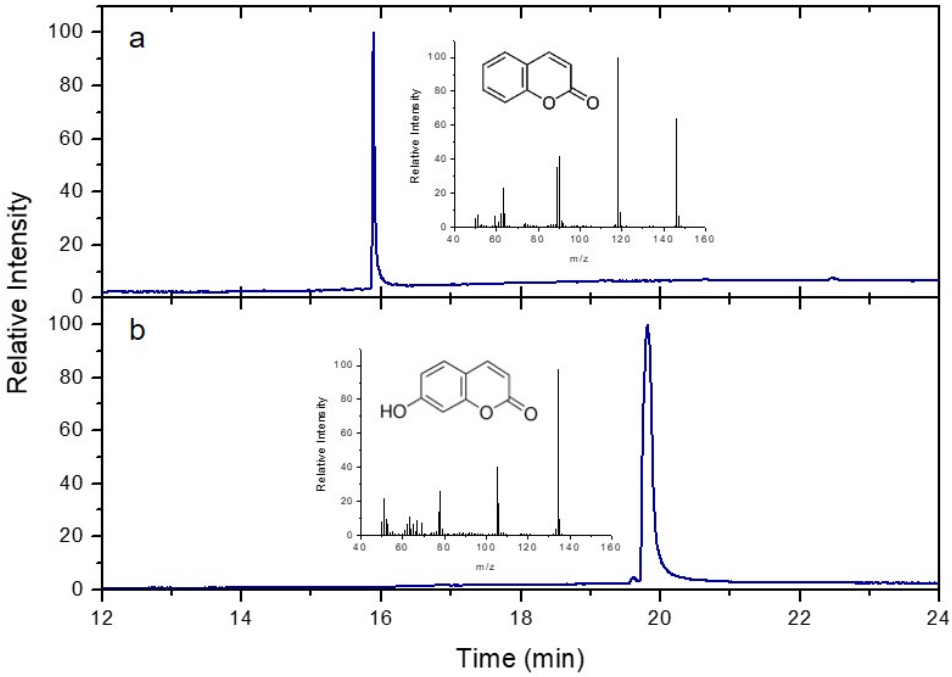

Figure 70. (a) GC chromatograph of the 40 min reaction product obtained from Cr(VI) (50 mg L^{-1}) reduction with 3-NMS/GCN catalyst (1 g L^{-1}) in the presence of coumarin (10 mM) at 20 °C under λ > 360 nm light irradiation. (b) GC chromatograph of the umbelliferone solution (10 mM). Insets of panels (a) and (b) are the MS spectra of coumarin and umbelliferone compounds, respectively.

To clarify this, Cr(VI) photoreduction experiment was carried out in the presence of coumarin and the products obtained at certain reaction times were study by gas chromatography-mass spectroscopy (GC-MS). Coumarin reacts readily with ·OH to form umbelliferone[232] and, therefore, identification of these substances in the reaction medium enables investigation of the free ·OH radicals' formation. It is noted that, because of the similar fluorescence emission spectra of umbelliferone (ca. 455 nm) and catalyst, the direct verification of umbelliferone through fluorescence spectroscopy is difficult. The GC-MS chromatograph in **Figure 70** reveals no signs of umbelliferone in

the reaction mixture even after completion of the reaction, signalling that ·OH radical formation does not occur during the photochemical process. These findings, together with oxygen evolution results, consistently verify that, under the photocatalytic Cr(VI) reduction conditions, the majority of the surface-reaching holes of the catalyst participate in water oxidation reaction, producing molecular oxygen.

The hole-transfer kinetics at the catalyst/solution interface were also investigated in the presence of ethylenediaminetetraacetic acid (EDTA), citric acid and phenol, which served as sacrificial hole acceptors. Since hole transfer to these organic compounds can overcome the kinetic limitations of the multi-electron water oxidation process (oxidation of H_2O involves a four electron transfer process combining with sluggish absorption/dissociation steps)[233], the overall photochemical reduction of Cr(VI) is expected to proceed more readily. In support to this, results of catalytic experiments indicated that the rate of Cr(VI) reduction (50 mg L^{-1}) can be considerably enhanced after addition of small amount (2 equiv. relative to the Cr(VI) concentration) of the above pollutants in the solution. For example, in these conditions, 3-NMS/GCN catalyst reaches a quantitative (>99%) conversion of Cr(VI) within only 5 to 15 min (**Figure 71**). To the best of our knowledge, this is the first example reporting Cr(VI) photoreduction at so faster rates. The rate enchantment in the photoreduction of Cr(VI) can be ascribed to the fast oxidation kinetics of organic compounds, which deplete the surface-reaching holes and thus reduce electron-hole recombination.

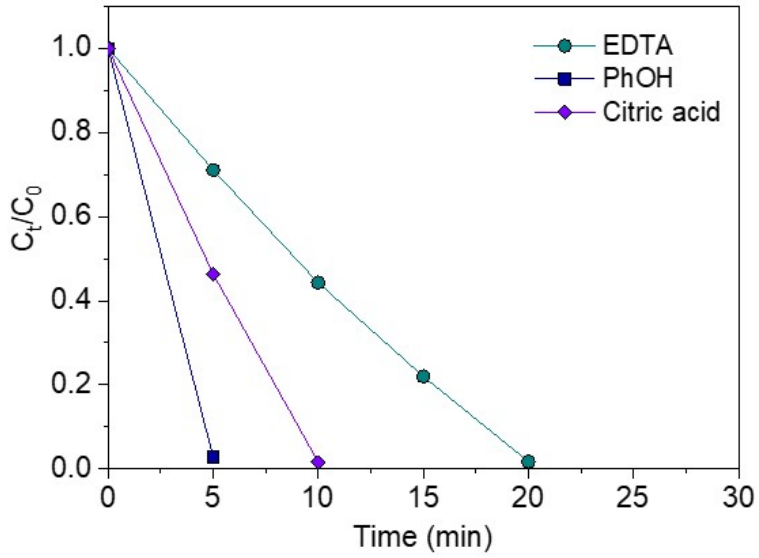

Figure 71. Photocatalytic reduction of aqueous Cr(VI) over 3-NMS/GCN catalyst in the presence 2 equiv. of ethylenediaminetetraacetic acid (EDTA), citric acid and phenol (PhOH) under $\lambda > 360$ nm light irradiation. Reaction conditions: 1 g L^{-1} catalyst, 50 mg L^{-1} Cr(VI) solution, pH = 2, 20 ºC.

3.3.2.3 Electronic band structure of the catalysts

To better understand and interpret the variations in the Cr(VI) photoreduction activity of *n*-NMS/GCN heterostructures, it is important to establish the electronic band structure of the catalysts. **Figure 72** shows the Mott-Schottky plots of GCN, MS/GCN and *n*-NMS/GCN sample electrodes (fabricated as thin films on FTO substrates), that is, $1/C^2$ as a function of applied voltage (E) curves. The flat band potentials (E_{FB}) of the samples are obtained as extrapolation of the linear fits of $1/C^2$ versus E curves to zero. Positive slopes of the Mott-Schottky plots indicate typical n-type semiconductor behavior. Moreover, as inferred from the slope of the $1/C^2$–E lines, the *n*-NMS/GCN catalysts exhibit a much higher donor density (N_d) compared to undoped MS/GCN and pristine GCN samples. Specifically, analysis of the $1/C^2$ versus E data yields values for N_d of ~5.5–6.1×10^{18} cm^{-3} for *n*-NMS/GCN, ~4.8×10^{18} cm^{-3} for MS/GCN and ~7.1×10^{17} cm^{-3} for GCN, see **Table 7**. This is most likely due to the n-type doping effect of Ni on MoS_2 and the improved charge dissociation at the Ni-MoS_2/g-C_3N_4 interface.

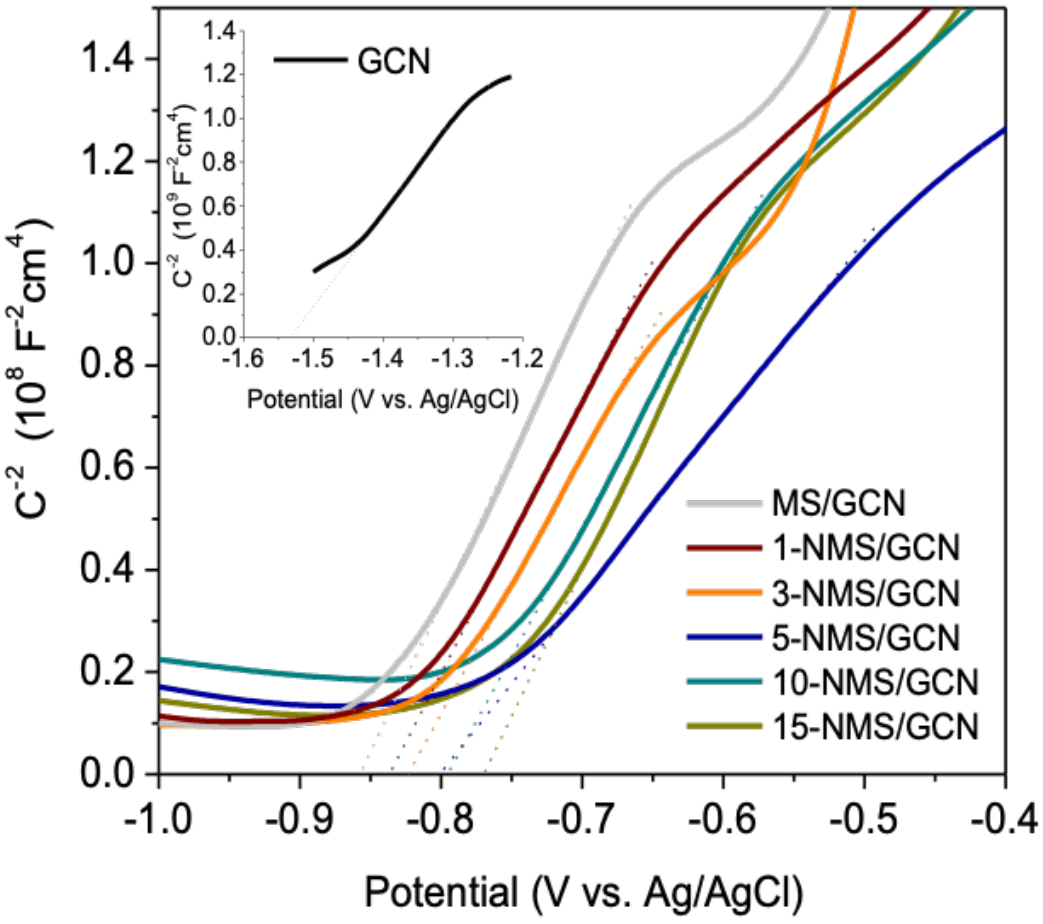

Figure 72. Mott-Schottky plots for the GCN, MS/GCN and *n*-NMS/GCN catalysts.

Table 7. Optical absorption and electrochemical data for the GCN, MS/GCN and *n*-NMS/GCN (30 wt% Ni-MoS_2) catalysts, and undoped and 3% Ni-doped MoS_2 nanosheets.

Catalyst	**E_{FB}**	**E_{VB}**	**Energy gap**	**Carrier density**	**R_{ct}**
	(V vs NHE, pH=7)		**(eV)**	**(N_d, cm^{-3})**	
MoS_2	–0.47	1.14	1.61	7.02×10^{17}	
3% Ni-MoS_2	–0.39	1.17	1.56	3.29×10^{18}	
GCN	–1.33	1.37	2.70	7.10×10^{17}	101.4
MS/GCN	–0.65	2.07	2.72	4.84×10^{18}	100.0
1-NMS/GCN	–0.62	2.12	2.74	5.19×10^{18}	100.4
3-NMS/GCN	–0.61	2.12	2.73	6.11×10^{18}	97.4
5-NMS/GCN	–0.59	2.14	2.73	8.76×10^{18}	102.9
10-NMS/GCN	–0.58	2.17	2.75	6.24×10^{18}	98.6
15-NMS/GCN	–0.56	2.19	2.75	5.49×10^{18}	98.9

One plausible mechanism for the increased carrier density is the formation of sulfur vacancies in MoS_2 matrix caused by the charge-balanced replacement of Mo^{4+} with Ni^{2+}, see Equation (6). Such defect centers can serve as electron donors to the CB of MoS_2, increasing the carrier density and mobility in Ni-doped MoS_2. Measurements of the optical band gap (E_g) were performed using ultraviolet-visible (UV–vis) diffuse reflectance spectroscopy, as shown in **Figure 73**. The UV–vis absorption spectra indicated that the heterostructured catalysts have an energy band gap of 2.72 to 2.75 eV, while the pristine GCN has an energy gap of 2.70 eV. This small, yet notable, hypsochromic shift in energy gap is attributed to the strong interlayer coupling between the g-C_3N_4 and (Ni)MoS_2 layers which allows for electronic interactions to develop. Moreover, compared to GCN, the composite catalysts show an apparent absorption tail below 1.8 eV ($\lambda > 690$ nm), most likely due to the interband electronic transitions in MoS_2; the energy gap of MoS_2 and Ni-MoS_2 nanosheets was estimated to be 1.61 and 1.56 eV, respectively, according to UV-vis spectra (**Figure 74**).

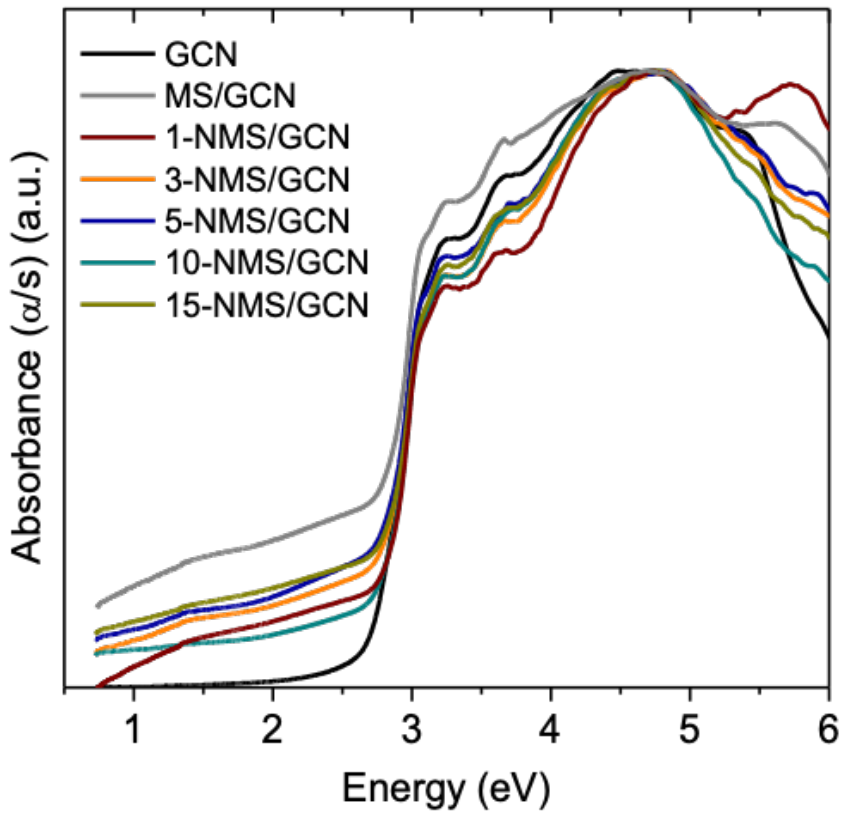

Figure 73. Optical absorption spectra for the GCN, MS/GCN and *n*-NMS/GCN catalysts.

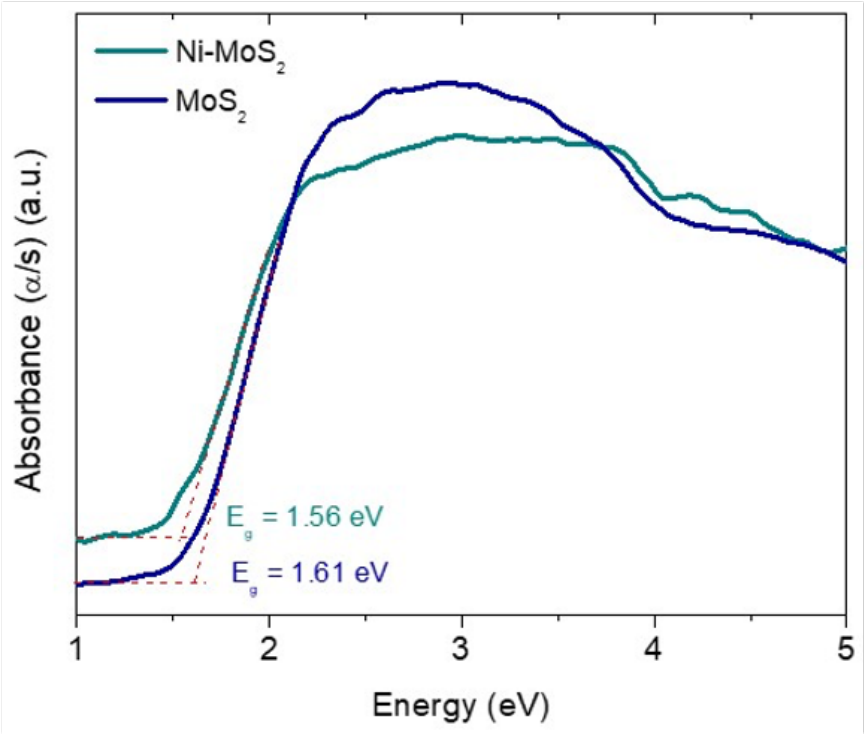

Figure 74. UV-vis absorption spectra of as-prepared MoS_2 and Ni-MoS_2 nanosheets.

Considering the heavily n-type doped nature of the *n*-NMS/GCN catalysts, it is appropriate to assume that the flat band position lies very close to the CB edge (particularly, E_{FB} potential lies at 0.1–0.3 V below the CB minimum).[234] Thus, we obtained the energy diagram for each catalyst and the corresponding results are illustrated in **Figure 75**. In this study, the valence band energy (E_{VB}) for each catalyst was determined from $E_{FB} + E_g$. As schematically shown by **Figure 75**, Ni doping of MoS_2 causes a remarkable downshift of the CB edge position of *n*-NMS/GCN by ca. 0.1 V (particularly, from –0.65 V to –0.56 V, see **Table 6**). All electrochemical potentials are referred to the normal hydrogen electrode (NHE) at pH 7. As g-C_3N_4 has a higher Fermi level (E_F) than Ni-MoS_2 nanosheets (specifically, for heavily n-type semiconductors the E_F lies close to the CB edge position, which is determined as –1.33 V for GCN and –0.39 V for 3% Ni-doped MoS_2 nanosheets through Mott-Schottky measurements, see **Figure 76**), a built-in electric field is formed near the Ni-MoS_2/g-C_3N_4 interface, which causes electron flow from g-C_3N_4 to Ni-MoS_2 until the Fermi levels reach equilibrium. Such an electron transfer creates a depletion layer close to the g-C_3N_4 surface, which is consistent with the anodic (positive) shift of the g-C_3N_4 E_{FB}. This intrinsic electric field may contribute to the enhanced photocatalytic efficiency because it helps electron-hole pair dissociation.

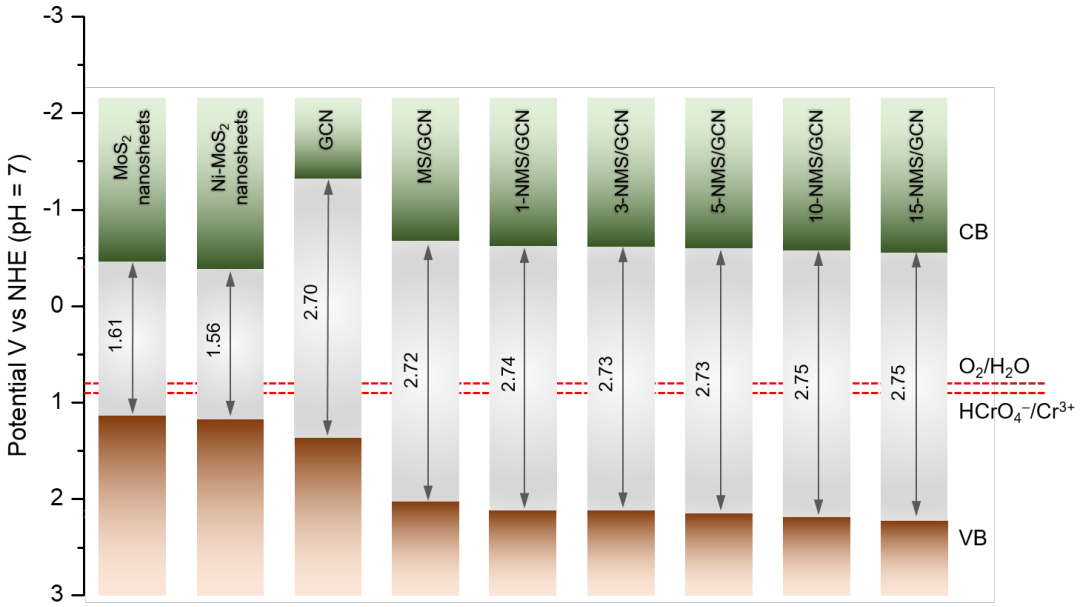

Figure 75. Energy band diagrams for the GCN, MS/GCN and *n*-NMS/GCN catalysts (the redox potential levels of the O_2/H_2O and $HCrO_4^-/Cr^{3+}$ pairs are also presented).

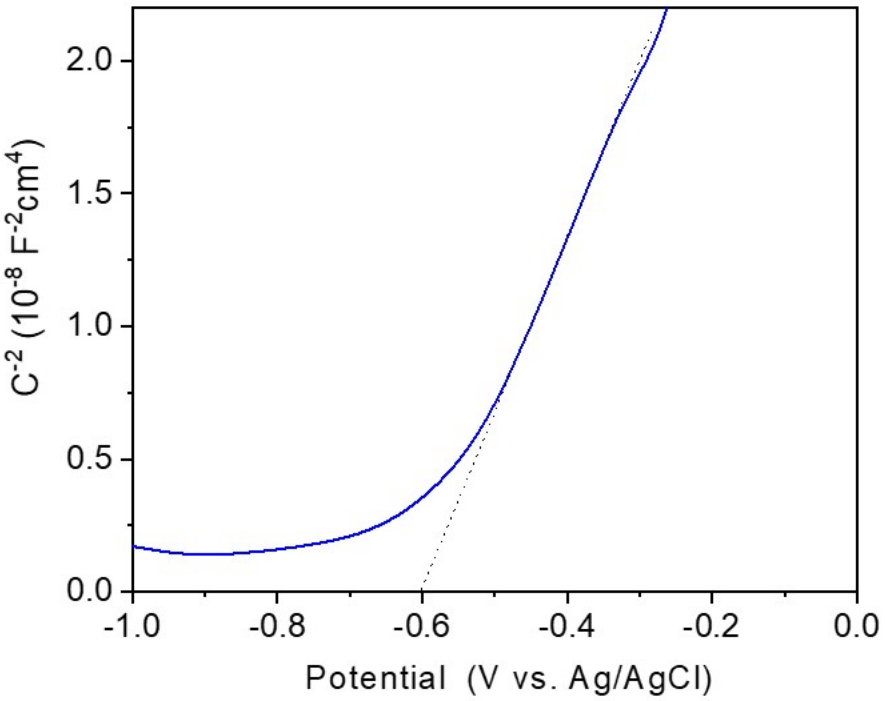

Figure 76. Mott-Schottky plot of the 3% Ni-doped MoS_2 nanosheets.

The effect of Ni substitutional doping and sulfur vacancies on the electronic structure of MoS_2 was studied using density functional theory (DFT) calculations. DFT results indicate that, when both Ni dopant and sulfur vacancy defects are present DFT results indicate that both Ni dopant and sulfur vacancy defects are present in MoS_2. There are relatively small structural changes near defects, mostly around substitutional Ni impurities. Substitutional Ni defect (Ni-MoS_2) has a formation energy close to 5 eV, much higher than the S vacancy (MoS_2-Vs) formation energy, which is 1.3 eV. When both defects are created simultaneously (Ni-MoS_2-Vs) the formation energy is approximately 3.9 eV, while when substitutional Ni follows S vacancy formation into the MoS_2 structure this value is close to 2.5 eV (**Figure 77**), suggesting that Ni-doping associated with S vacancies is energetically favorable. It should be stressed that defect formation energies are very similar for all of the relatively small Ni concentrations we examined (i.e., from 2.78 to 11.11 at%), but this may not be the case for high Ni concentrations (there is already a small difference for 11.11%). In order to study several defect concentrations with DFT, we used simulation cells of different sizes, with the MoS_2 monolayer unit cell repeated 3 to 6 times in each plane direction. Nickel doping was simulated by replacing a Mo atom by a Ni atom. S vacancy was created by removing one S atom from the supercells. The corresponding substitutional and

vacancy defects concentrations are 11.11% for 3x3, 6.25% for 4x4, 4.00% for 5x5, 2.78% for 6x6 supercells, respectively.

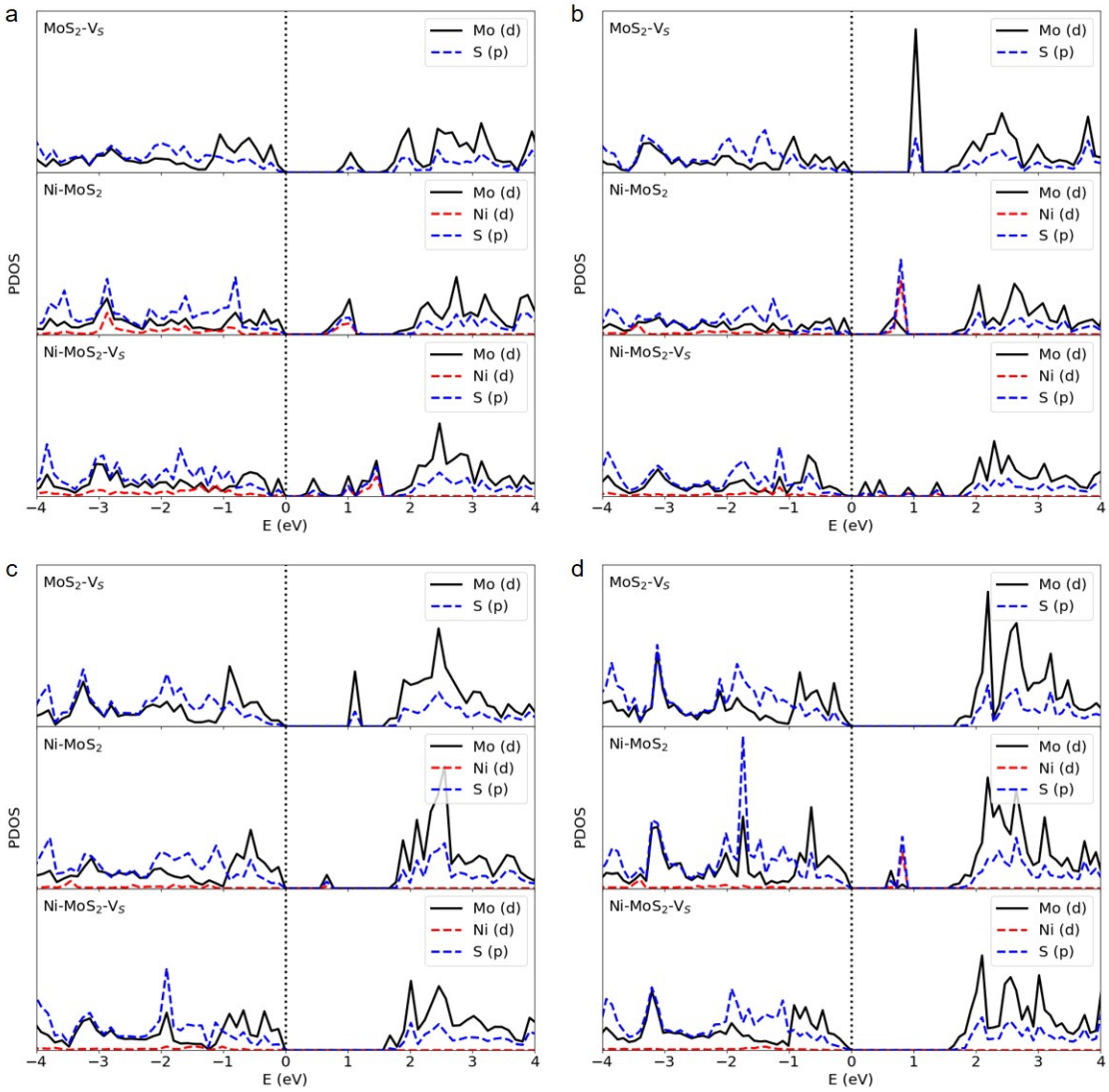

Figure 77. Projected electronic density of states (PDOS) for the defected structures MoS_2 with S vacancy, MoS_2 with Ni dopant, and MoS_2 with Ni dopant and S vacancy for defect concentration of (a) 11.11%, (b) 6.25%, (c) 4.00% and (d) 2.78%.

Defect formation energies are defined as $E_f = E_{def} + \sum\mu_i - E_{ref} - \sum\mu_j$, where E_{ref} is the total energy of the reference system without defects, E_{def} is the total energy of the defected system, μ_i and μ_j are reference chemical potentials for atoms removed from or added to the reference system. For instance, in the substitution of a Mo atom by a Ni atom, the formation energy is $E_{Nid} = E_{Ni\text{-}MoS2} + \mu_{Mo} - E_{MoS2} - \mu_{Ni}$, where E_{MoS2} and $E_{Ni\text{-}MoS2}$ are the energies of pristine and Ni containing supercells, respectively, μ_{Ni} and μ_{Mo} are the energies of Ni and Mo atoms in the pristine fcc Ni and bcc Mo lattices,

respectively. The formation energy for the S-vacancy is defined as $E_{Vsd} = E_{MoS2\text{-}Vs} + \mu_S - E_{MoS2}$, where E_{MoS2} and $E_{MoS2\text{-}Vs}$ are the energies of pristine and vacancy containing MoS_2 supercell, respectively, and $\mu_S = (\mu_{MoS2} - \mu_{Mo})/2$. In the plots of the projected electronic density of states (PDOS) of **Figure 77**, the defect states are located in the electronic band gap for the larger defect concentrations and merge with the band edges for the smaller concentrations we examined. In **Figure 78**, we present results for optimal doping of Ni, that is, close to 3%. It can be observed that the electronic band gap for 2.78% Ni-MoS_2-Vs becomes 1.56 eV, from 1.61 for pristine MoS_2, in good agreement with the experimental data. Another remarkable aspect is that incorporation of Ni/S-vacancy defect centers in MoS_2 lattice leads to the appearance of defect states in the gap toward the CB edge (see **Figure 77**), suggesting an enhanced n-type conductivity, in line with the Mott-Schottky results. The excellent agreement between DFT calculations and experimental data suggests that Ni/Mo substitution and sulfur vacancies confer to Ni-MoS_2 nanolayers' improved photochemical properties.

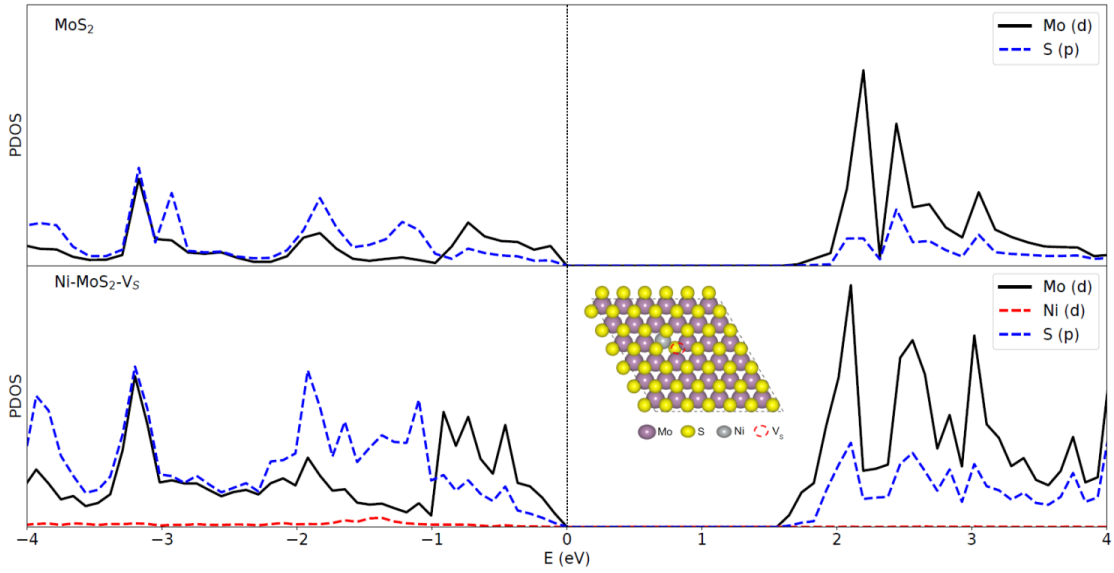

Figure 78. Projected electronic density of states (PDOS) for pristine MoS_2 and Ni-MoS_2-Vs (Inset: atomic structure) for defect concentration 2.78 at%.

In addition, electrochemical impedance spectroscopy (EIS) Nyquist measurements were performed to extract the charge-transfer rate of the different GCN, MS/GCN and *n*-NMS/GCN catalysts (drop-casted onto FTO glass substrates). **Figure 79** displays the Nyquist plots of each electrode recorded in a 0.5 M Na_2SO_4 electrolyte (pH 6.8) at open circuit potential. A typical electric circuit (inset of **Figure 79**) consisting of the

electrolyte resistance (R_s), charge-transfer resistance at the electrode/electrolyte interface (R_{ct}), double layer capacitance (C_{dl}) and high-frequency pseudo-inductor (L_1)[235,236] has been used to interpret the experimental data. Fitting analysis indicated that R_{ct} values for Ni-MoS_2-modified samples are lower, especially for 3-NMS/GCN catalyst (see **Tables 7** and **8**), suggesting an accelerated charge transfer rate at the interface between electrode and electrolyte. In fact, Ni-MoS_2 layers act as electron acceptors from photoexcited g-C_3N_4, suppressing the recombination of g-C_3N_4 photogenerated carriers, as indicated by the Mott-Schottky plots (**Figure 72**). This may facilitate the charge transportation within the heterojunction interface. Further information about the charge transfer processes on Ni-MoS_2/g-C_3N_4 interface was obtained from steady-state photoluminescence (PL) spectra of GCN and 3-NMS/GCN samples studied under 370 nm excitation wavelength.

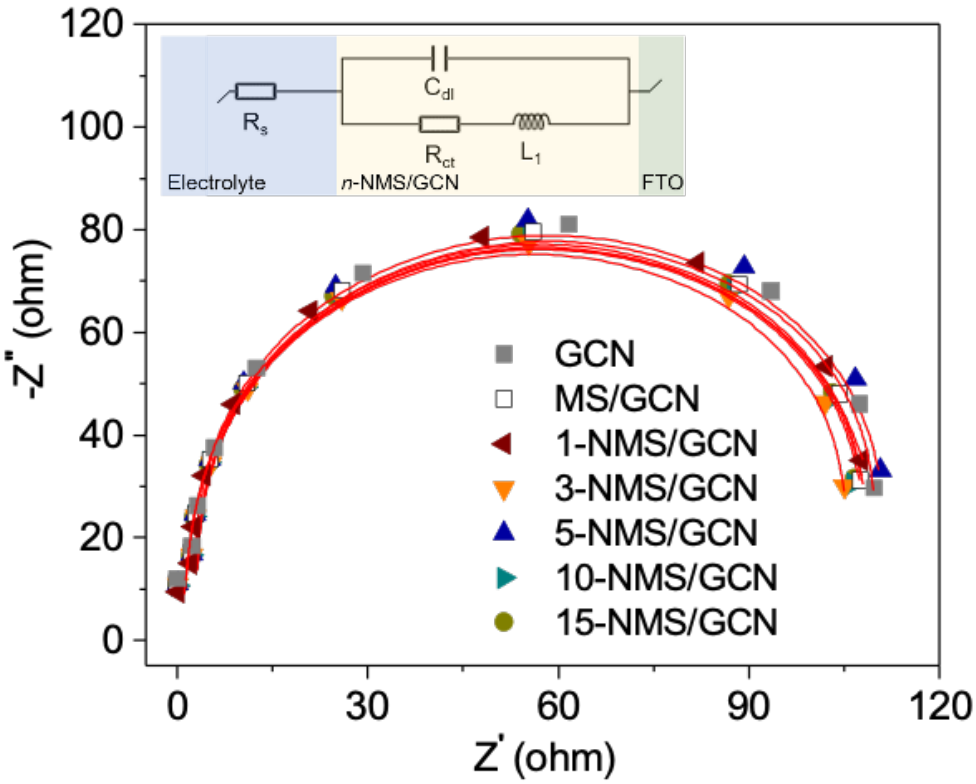

Figure 79. Nyquist plots of GCN, MS/GCN and *n*-NMS/GCN catalysts.

Table 8. EIS equivalent circuit fitted parameters for GCN, MS/GCN and *n*-NMS/GCN catalysts.

Sample	**R_s (Ω)**	**C_{dl} (F)**	**R_{ct} (Ω)**	**L_2 (H)**	**x^2**
GCN	2.64	11.19×10^{-9}	101.4	73.35×10^{-6}	9.3×10^{-5}
MS/GCN	2.49	11.79×10^{-9}	99.95	74.29×10^{-6}	2.8×10^{-4}
1-NMS/GCN	2.33	12.58×10^{-9}	100.4	79.66×10^{-6}	3.4×10^{-4}
3-NMS/GCN	2.49	12.03×10^{-9}	97.36	72.03×10^{-6}	1.9×10^{-3}
5-NMS/GCN	2.43	11.68×10^{-9}	102.9	78.20×10^{-6}	1.5×10^{-3}
10-NMS/GCN	2.38	11.93×10^{-9}	98.58	73.69×10^{-6}	3.4×10^{-4}
15-NMS/GCN	2.32	12.02×10^{-9}	98.97	74.79×10^{-6}	3.5×10^{-4}

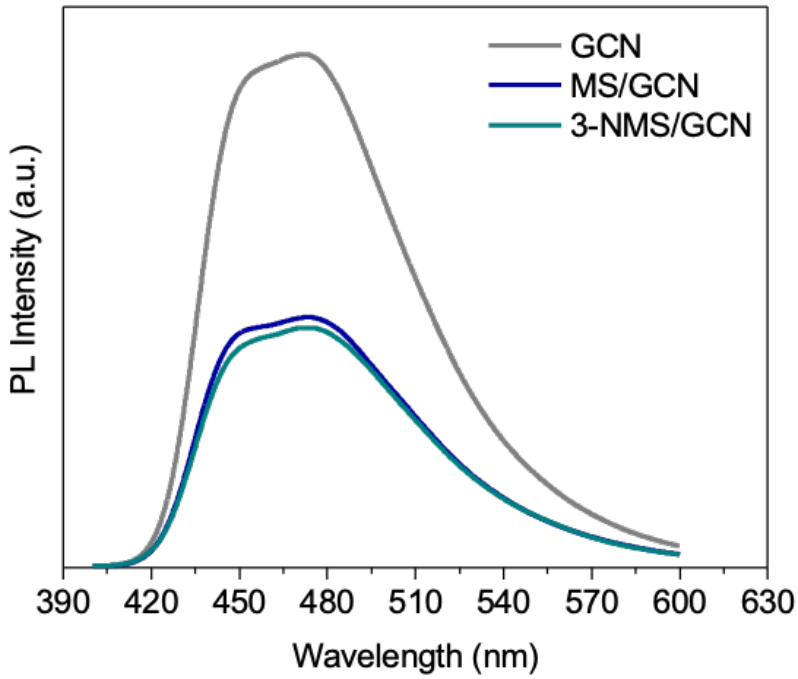

Figure 80. Room-temperature PL emission spectra of the 3-NMS/GCN, MS/GCN and GCN catalysts. PL experiments were carried out in water (0.5 mg mL^{-1}) with 370 nm excitation wavelength.

As seen from **Figure 80**, the GCN spectrum displays a prominent peak at 455 nm (2.72 eV), which is related to the band-edge absorption of g-C_3N_4 (E_g ~ 2.70 eV), and a weak shoulder around 480 nm (ca. 2.60 eV), which is attributed to the mid-gap photoemission processes due to defect levels. Comparatively, the 455 nm emission of both MS/GCN and 3-NMS/GCN samples decreased notably, indicating that electron-hole dissociation within the layered heterostructure is improved. This means that the

interband electron-hole transitions can be suppressed to a large extent by the electronic interactions between the Ni-MoS_2 and g-C_3N_4 layers, further demonstrating that the Ni-MoS_2/g-C_3N_4 junctions promote electron injection from photoexcited g-C_3N_4 to Ni-MoS_2, in line with the above EIS experiments.

Moreover, photoelectrochemical measurements were also performed to obtain further information about the different charge transport properties of (Ni)MoS_2/g-C_3N_4 heterostructures compared to those of pristine g-C_3N_4. Chronoamperometric curves are shown in **Figure 81**, and indicate that both 3-NMS/GCN and MS/GCN electrodes respond more strongly to light, emerging a higher photocurrent density than GCN under visible (380–780 nm) light irradiation. This affirms a higher charge separation efficiency and better electron conductivity within the (Ni)MoS_2/g-C_3N_4 junctions. The slightly lower photocurrent observed for 3-NMS/GCN sample, although Ni-doped MoS_2 enables faster redox kinetics as a cocatalyst, may be due to the interface recombination at the Ni-MoS_2/g-C_3N_4 junction. In addition, the efficient charge transport and separation of photogenerated charge carriers along the Ni-doped MoS_2/g-C_3N_4 heterostructure was also verified by open-circuit photovoltage (OCP) decay analysis. OCP is a useful technique to probe the lifetime of photoexcited carriers in the semiconductors, and can provide important information about the transport lifetime of electrons (both free and trapped electrons) in the CB of the catalyst. The potential-dependent photoelectron lifetime (τ_n) can be calculated according to the Equation (10)[237]:

$$\tau_n = -(k_B T/e)(dV_{oc}/dt)^{-1} \quad (10)$$

where, k_B is the Boltzmann's constant, e is the electron charge, T is the temperature and V_{oc} is the photovoltage at time t when the light is turned off.

Figure 82 displays the photoelectron lifetime (τ_n) versus V_{oc} plots for different catalysts obtained from the OCP decay profiles (**Figure 83**). Consistent with PL spectra and EIS Nyquist plots, these results demonstrate that the 3-NMS/GCN catalyst promotes better separation of photoexcited electron-hole pairs, exhibiting a markedly prolonged electron lifetime; the OCP analysis yields τ_n values of ~14, ~65 and ~119 s for GCN, MS/GCN and 3-NMS/GCN, respectively. This indicates an electron-transfer channel from photoexcited g-C_3N_4 to Ni-MoS_2 nanosheets that prolongs the electron lifetime

and eventually improves the utilization of charge carriers for chemical reactions, in line with the enhanced photocatalytic performance of 3-NMS/GCN.

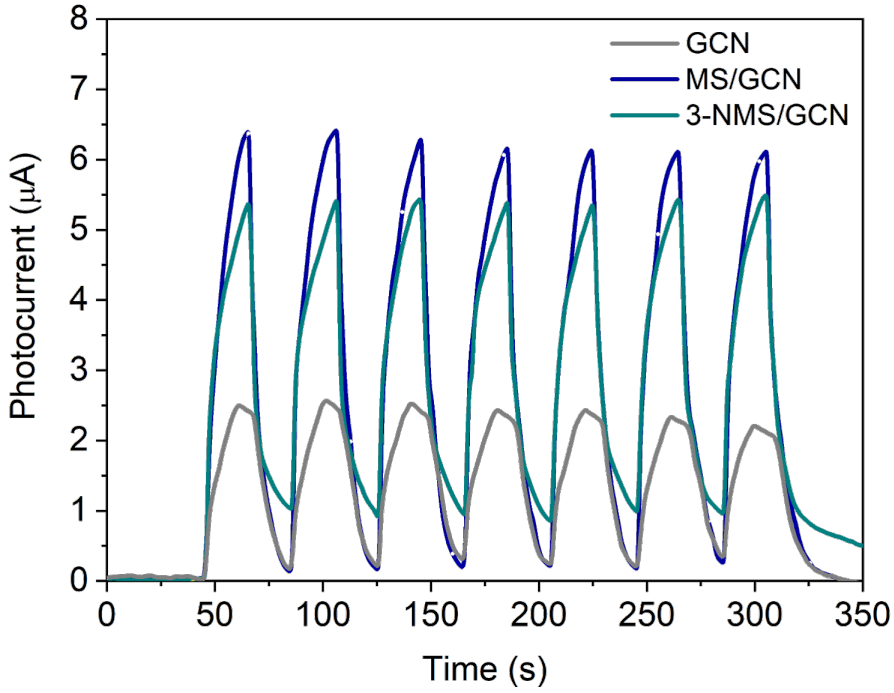

Figure 81. Transient photocurrent responses measured at a bias of 0.2 V (vs Ag/AgCl) under visible light (380–780 nm) irradiation and dark conditions of the 3-NMS/GCN, MS/GCN and GCN electrodes.

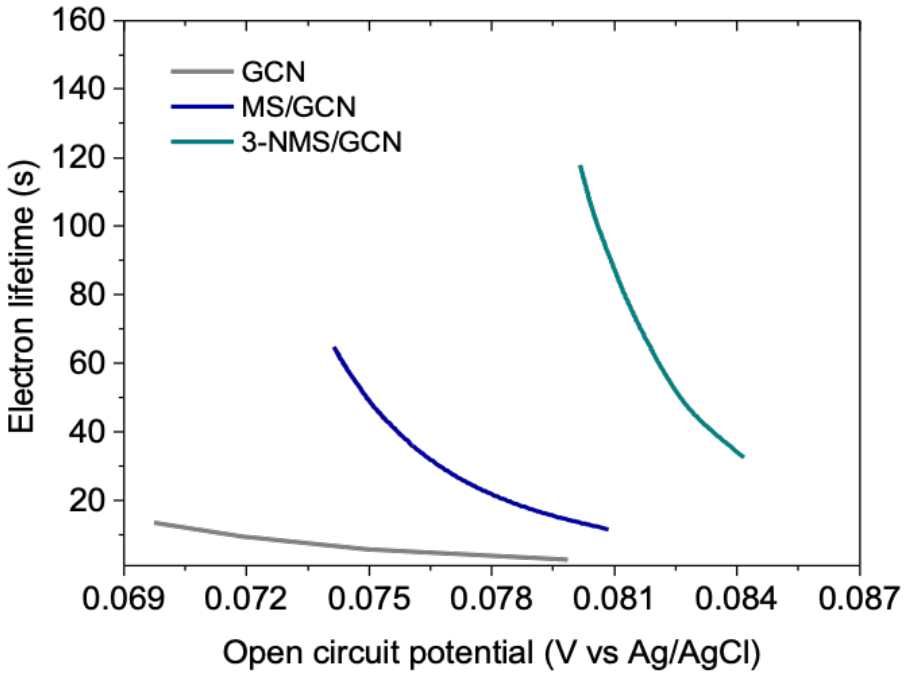

Figure 82. Electron lifetime determined from the OCP decay curves (Figure 76) of the 3-NMS/GCN, MS/GCN and GCN electrodes.

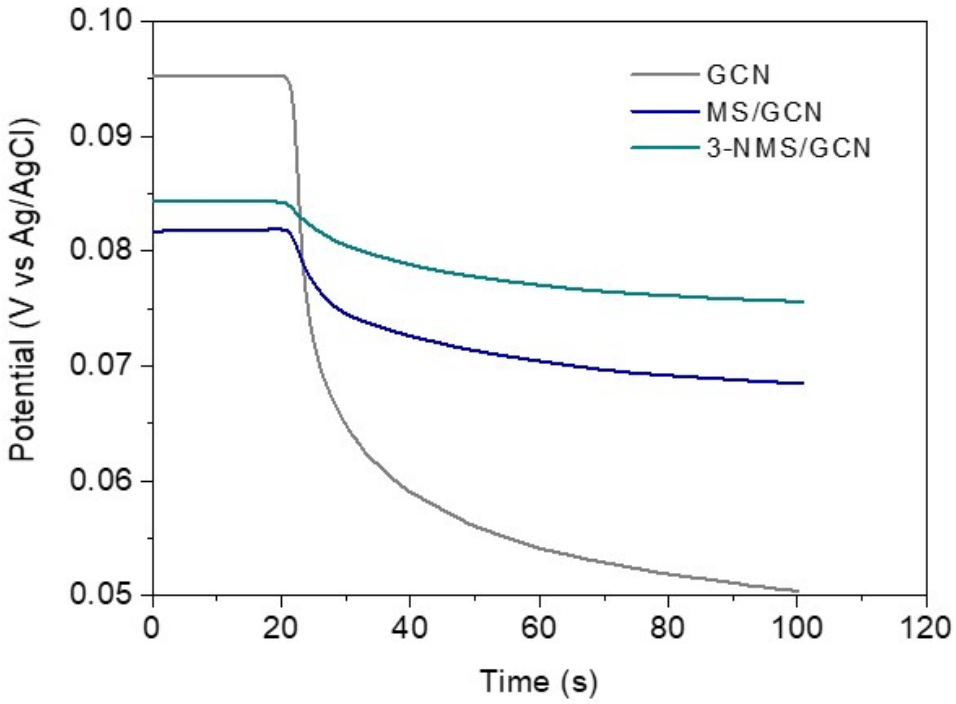

Figure 83. Open-circuit photovoltage (OCP) decay curves of GCN, MS/GCN and 3-NMS/GCN catalysts in 0.5 M Na_2SO_4 solution.

A plausible mechanism for the photocatalytic reduction of Cr(VI) by NMS/GCN catalysts is schematically depicted in **Figure 84**. In short, under UV-vis light irradiation, electrons and holes are generated in the CB and VB of g-C_3N_4. Because of the built-in electric field, excited electrons transferred through the Ni-MoS_2/g-C_3N_4 interface tend to localize in Ni-MoS_2 nanosheets, where they reduce Cr(VI) to less toxic Cr(III), as shown in Equation (9). Therefore, the anchored Ni-MoS_2 nanosheets on the g-C_3N_4 surface serve as effective co-catalysts and active sites for reduction of Cr(VI). On the other hand, the photoinduced holes in the VB of g-C_3N_4 react with surface absorbed water molecules to form O_2, as revealed by in-situ gas analysis techniques. Although *n*-NMS/GCN can perform efficient water oxidation, capture of the surface-reaching holes by organic pollutants (such as ETDA, phenol and citric acid) can accelerate the overall photocatalytic reaction. As a result, the photocatalytic Cr(VI) reduction efficiency was enhanced due to the efficient dissociation of electron-hole pairs. Evidence for this was obtained from photo-electrochemical and PL investigations.

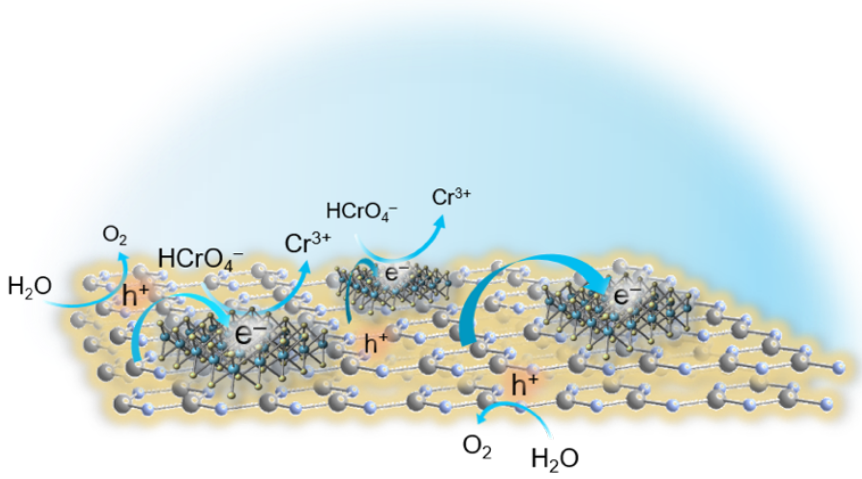

Figure 84. Proposed mechanism for the photocatalytic reduction of Cr(VI) by *n*-NMS/GCN catalysts under UV-visible light irradiation.

3.4 Photochemical deposition of SnS_2 on g-C_3N_4

3.4.1 Synthesis and structural characterization

The synthesis of SnS_2-containing g-C_3N_4 heterostructures with different SnS_2 content (denoted as *n*-SnS_2/GCN, where *n* refers to the different weight percent of SnS_2) was accomplished by a sulfur-mediated photochemical deposition of SnS_2 nanosheets on the g-C_3N_4 surface, which seems to be a redox reaction. Namely, g-C_3N_4 was excited under 375 nm light irradiation in the 1:1 water:ethanol solution (ethanol serves as the hole scavenger) containing tin chloride ($SnCl_4$) and sulfur (S_8) powder. During the irradiation the photogenerated electrons in the conduction band (CB) of g-C_3N_4 reduce Sn^{4+} to Sn^{2+} and/or Sn^0 species on the surface of g-C_3N_4, which in turn react with adsorbed S to form SnS_2, according to the following chemical reactions. Meanwhile, the photogenerated holes left on the valence band (VB) of g-C_3N_4 can oxidize the sacrificial ethanol.

$$g\text{-}C_3N_4 + hv \rightarrow g\text{-}C_3N_4(e^- + h^+) \quad (11)$$

$$g\text{-}C_3N_4(e^-) + Sn^{4+} \rightarrow g\text{-}C_3N_4 + Sn^{2+}/Sn^0 \quad (12)$$

$$Sn^{2+}/Sn^0 + xS_{ads} \rightarrow SnS_2 \quad (13)$$

$$g\text{-}C_3N_4(h^+) + CH_3CH_2OH \rightarrow g\text{-}C_3N_4 + CH_3CHO + 2H^+ \quad (14)$$

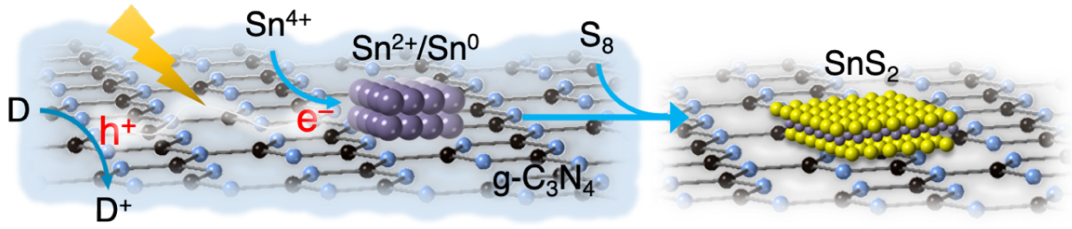

Figure 85. Schematic representation of the fabrication of $SnS_2/g\text{-}C_3N_4$ (SnS_2/GCN) layered heterostructures by photo-deposition method.

Given the standard redox potentials of Sn^{2+}/Sn^{4+} (0.15 V) and Sn^0/Sn^{2+} (–0.13 V) couples are located below the CB edge of $g\text{-}C_3N_4$ (ca. –0.92 V vs NHE, pH=0, see below), electron transfer from $g\text{-}C_3N_4$ to Sn^{4+}/Sn^{2+} thus appears feasible. Moreover, the redox potentials for the sulfur to mono- or poly-sulfide reduction range from 2.1 to 2.5 V[238], indicating that conversion of Sn^{2+}/Sn^0 species to SnS_2 is a thermodynamically favorable redox reaction. A schematic illustration of the synthetic procedure of SnS_2/GCN heterostructures is shown in **Figure 85**. The success of this process was verified by the color change of the suspension from light yellow to light brown. A similar reaction scheme has been proposed for synthesis of Me_xS_y/MIL-125(Ti) (Me_xS_y = Ag_2S, CuS, CdS, MoS_2)[239] and CdS/TiO_2 [240] composites. We found that this synthetic route is highly reproducible and leads to the formation of heterostructures with different loading amount of SnS_2. In particular, the SnS_2 content was tuned from 10 to 40 wt%. by varying the concentration of $SnCl_4$ and S_8 precursors, and measured by thermogravimetric analysis (TGA). The TGA results showed that the loading amounts of SnS_2 were very close to the expected compositions from the stoichiometry of reactions (**Table 9** and **Figure 86**). Moreover, energy dispersive X-ray spectroscopy (EDS) also indicated an overall Sn to S composition close to 1:1.7–1.8 (see **Table 9**), that is close to the stoichiometric ratio of SnS_2.

Table 9. Chemical composition of the as-prepared SnS_2/GCN catalysts.

Sample	**mg SnO_2/ mg catalyst[a]**	**SnS_2 content[a] (wt%)**	**Atomic ratio[b] Sn/S**
1-SnS_2/GCN	2.0/25.1	9.7	1.69
2-SnS_2/GCN	4.3/25.8	20.2	1.67
3-SnS_2/GCN	6.2/25.6	29.4	1.76
4-SnS/GCN	8.0/24.8	39.1	1.82

[a]Based on TGA results. [b]Based on EDS analysis.

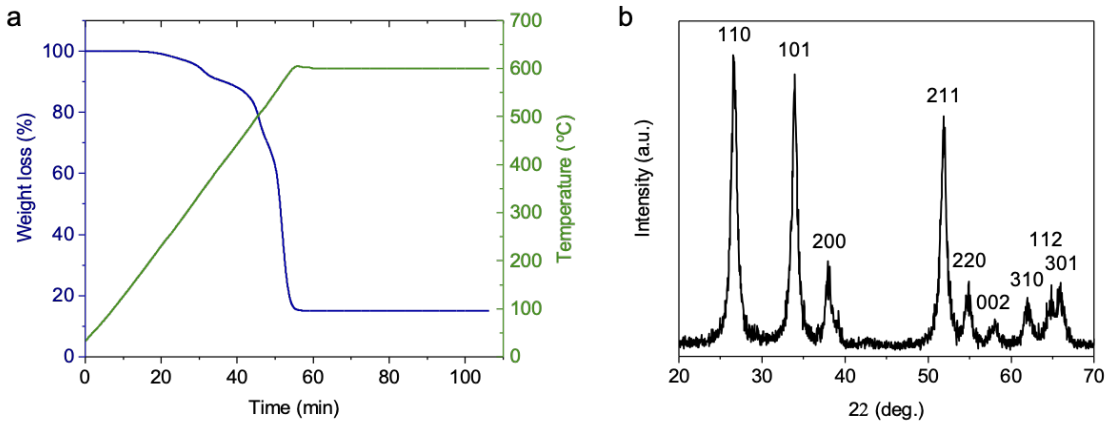

Figure 86. Typical (a) TGA profile and (b) XRD pattern of the inorganic residue (SnO_2) obtained after TGA analysis (up to 600 °C) of the 2-SnS_2/GCN sample.

The crystallinity and morphology of the as-prepared materials were examined by X-ray diffraction (XRD) and transmission electron microscopy (TEM). The XRD patterns of pristine and SnS_2-containing g-C_3N_4 samples in **Figure 87** show two distinctive diffraction peaks at 27.8° and 13.2°, which are assigned to the (002) inter-planar stacking reflection of the conjugated aromatic rings and the (100) in-plane tri-s-triazine packing of the graphitic C_3N_4, respectively (JCPDS card no. 87-1526).[241] The XRD patterns of SnS_2/GCN heterostructures also show two additional peaks at 33.1° and 50.6° due to the (101) and (110) reflections of the hexagonal SnS_2 (JCPDS 23-0677).

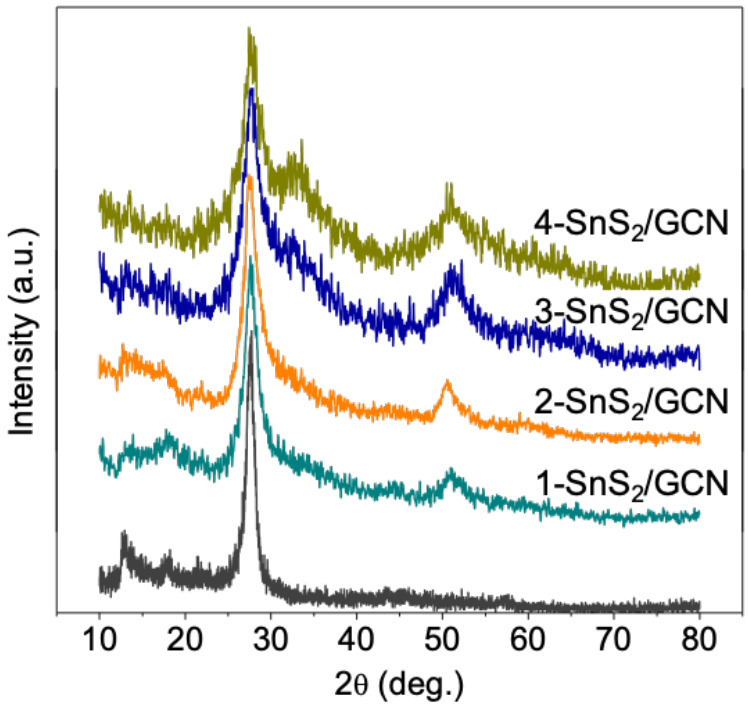

Figure 87. XRD patterns of GCN and SnS_2/GCN materials.

Typical TEM images of the 2-SnS_2/GCN catalyst are shown in **Figure 88a**. The TEM images magnify the hybrid structure of the sample and show SnS_2 nanosheets (appeared as dark areas) that are uniformly decorated on the surface of graphitic C_3N_4 (appeared as white areas). Through this analysis, the size of SnS_2 flakes is approximately 25–30 nm in lateral diameter. In addition, a closer inspection of the heterojunction network with high-resolution TEM (HRTEM) shows lattice fringes with d spacing of ~5.9 Å corresponding to the (120) interplanar distance of hexagonal SnS_2; the region marked by the yellow frame in **Figure 88b** is further enlarged, as shown in inset image. The nanocrystallite feature of SnS_2 can be further discerned from selected-area electron diffraction (SAED) measurements. The SAED pattern recorded on a small area of the 2-SnS_2/GCN structure shows two broad concentric Debye-Scherrer diffraction rings (**Figure 88c**), which, according to the XRD results, can be assigned to the (100) and (102) crystal planes of the hexagonal SnS_2 (space group: $P\bar{3}m1$).

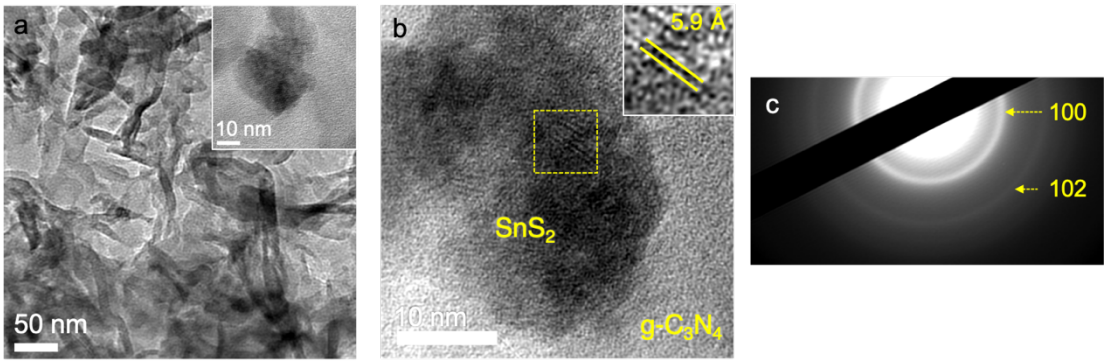

Figure 88. (a) Typical TEM image, (b) high-resolution TEM, showing the lattice fringes of an individual SnS_2 nanosheet, and (c) SAED pattern of 2-SnS_2/GCN catalyst.

The nitrogen adsorption-desorption isotherms of the GCN and SnS_2/GCN samples showed characteristic type IV curves with a small H3 hysteresis loop according to the IUPAC classification (**Figure 89**), suggesting mesoporous structures with slit-shaped pores.[242] The interchannel mesopores in these materials are possibly due to the interstitial voids between the aggregated g-C_3N_4 flakes. The Brunauer–Emmett–Teller (BET) surface areas and pore volumes assessed from the adsorption branch of isotherms were estimated to be ~30–51 $m^2\ g^{-1}$ and 0.05–0.08 $cm^3\ g^{-1}$, respectively, for SnS_2/GCN and 94 $m^2\ g^{-1}$ and 0.15 $cm^3\ g^{-1}$ for GCN. The lower specific surface area of the SnS_2-

containing catalysts could be attributed to the heavy phase (SnS_2) that compose the structure. A summary of the N_2 physisorption results is presented in **Table 10**.

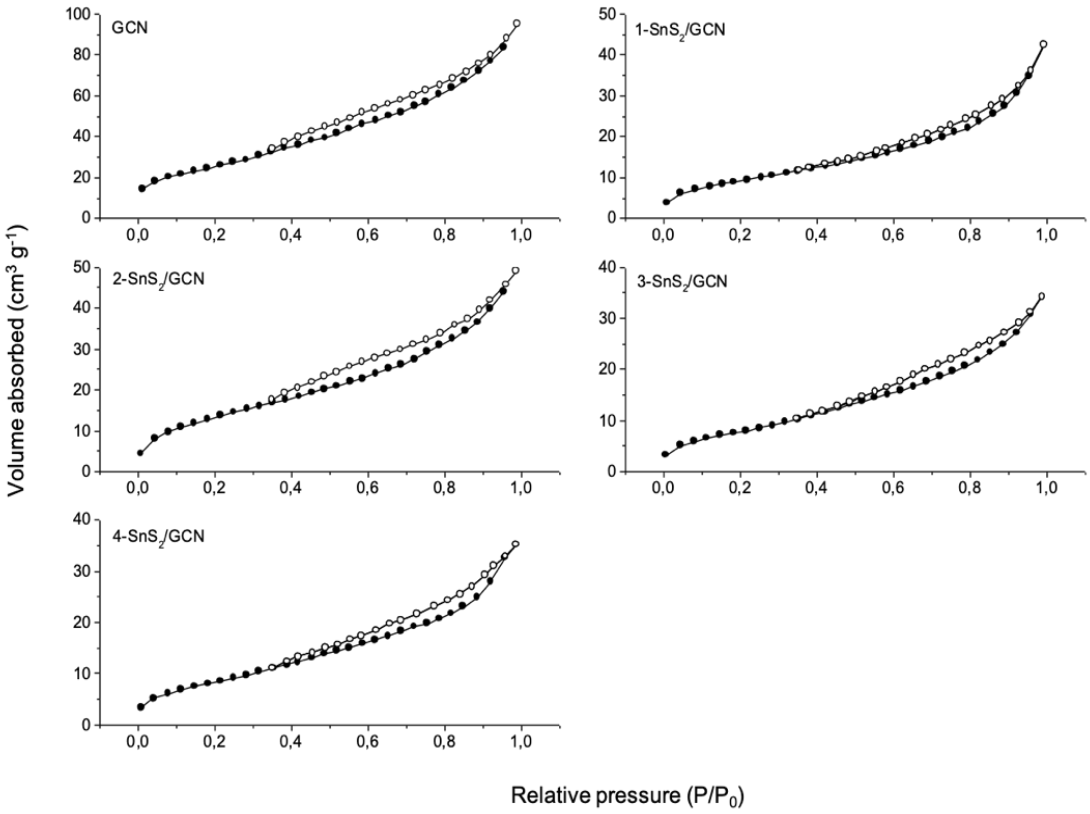

Figure 89. N_2 adsorption (open circles) and desorption (closed circles) isotherms at –196 ºC of the GCN and SnS_2/GCN catalysts.

Table 10. Textural properties of the GCN and SnS_2/GCN catalysts.

Sample	**BET surface area ($m^2\ g^{-1}$)**	**Pore volume ($cm^3\ g^{-1}$)**	**Average pore size[a] (nm)**
GCN	94	0.15	3.2
1-SnS_2/GCN	34	0.06	3.5
2-SnS_2/GCN	51	0.08	3.1
3-SnS_2/GCN	30	0.05	3.3
4-SnS_2/GCN	32	0.05	3.1

[a]The average pore width is given by $w = 2V_p/S_p$, where V_p is the total pore volume at $P/P_0 = 0.98$ and S_p is the pore surface area, assuming slit-shaped pores.

The chemical states of elements at the surface of SnS_2/GCN were investigated by X-ray photoelectron spectroscopy (XPS). **Figures 90a** and **b** display the C 1s and N 1s

core-level spectra for SnS_2/GCN catalyst with 20 wt% SnS_2 content (2-SnS_2/GCN). The C 1s spectrum can be resolved into three peaks at about 284.8, 286.2 and 288.4 ±0.2 eV binding energies, which are attributed to the aliphatic carbon and the sp^2-bonded (N–C=N) and sp^3-bonded (C–N) C atoms in triazine units of g-C_3N_4, respectively. [243,244] As for the N 1s signal, a prominent peak at 398.9 ±0.3 eV and a broad shoulder at 400.8 ±0.3 eV was observed, which can be assigned to the pyridinic (C–N sp^2) and pyrrolic (C–N sp^3) like nitrogen, respectively. [245] In respect of the Sn 3d XPS signal (**Figure 90c**), the SnS_2/GCN manifests a single doublet peak at binding energies of 486.8 and 495.2 ± 0.2 eV, consistent with the Sn $3d_{5/2}$ and Sn $3d_{3/2}$ spin-orbit components of the Sn^{4+} states in SnS_2.[246] Besides, the S 2p core-level spectrum (**Figure 90d**) shows one peak around 162.3 ±0.2 eV, which agree with the literature data for the S^{2-} ions. [247] Inevitably, surface oxidation of SnS_2 particles is plausible, however, this is minimal (less than 10%) as confirmed by XPS analysis.

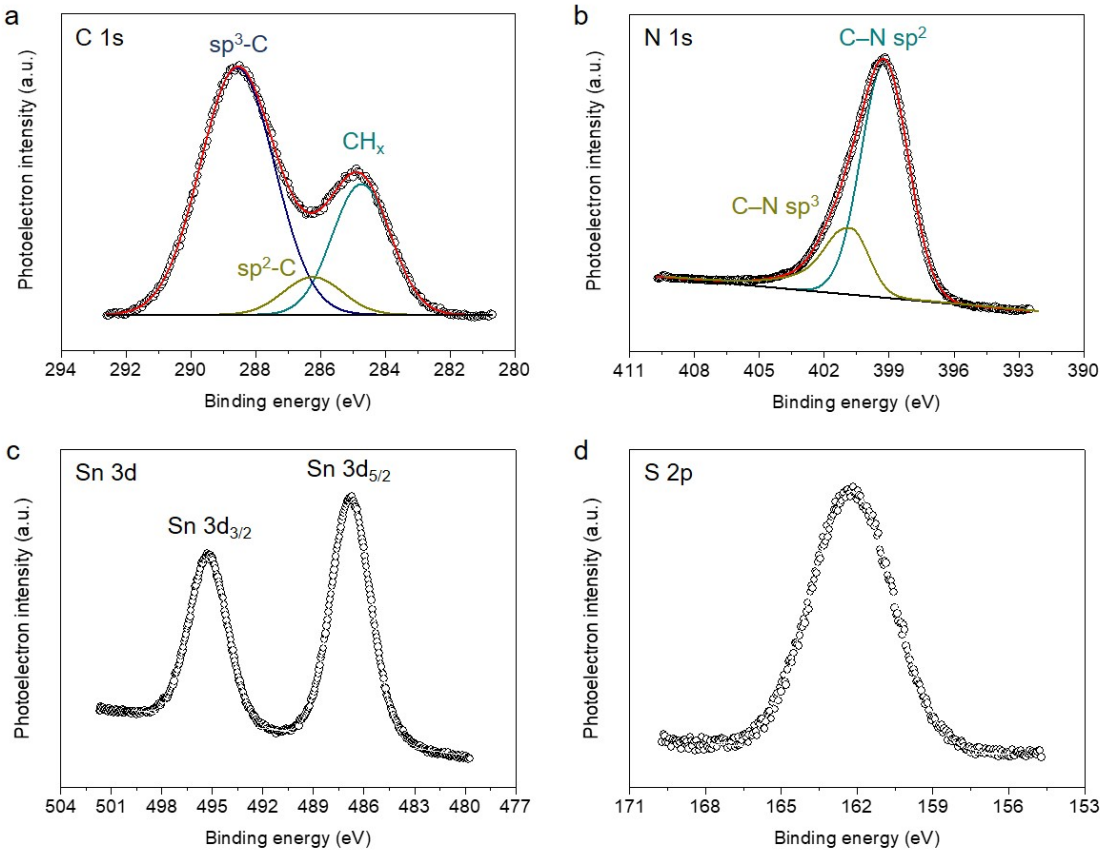

Figure 90. XPS core-level spectra of the (a) C 1s, (b) N 1s, (c) Sn 3d and (d) S 2p region for the 2-SnS_2/GCN catalyst. The white circles are XPS data, while the green, blue and yellow curves are the fitting of the experimental data.

3.4.2 Photocatalytic study of n-SnS_2/GCN

3.4.2.1 Photocatalytic Cr(VI) reduction

The photocatalytic activity of the SnS_2/GCN heterostructures were evaluated in the reduction of aqueous Cr(VI) solution under irradiation of $\lambda > 360$ nm light. The catalytic results in **Figure 91** show that deposition of SnS_2 nanosheets have a significant effect on the photocatalytic performance of g-C_3N_4. In particular, photoreduction of Cr(VI) was complete (>99%) after 1.6 h and 1 h for the 10 and 20–40 wt% SnS_2-containing samples, whereas for the pristine g-C_3N_4 under the same reaction conditions, it took nearly 3 h for ~54% Cr(VI) reduction. Under control experimental conditions, no Cr(VI) reduction was observed in the absence of catalyst or light irradiation, signified that this is a photocatalytic process. In consequence, we focused on reactions with 2-SnS_2/GCN catalyst throughout our further photocatalytic studies due to its relatively high activity in Cr(VI) reduction and lower effective load of SnS_2.

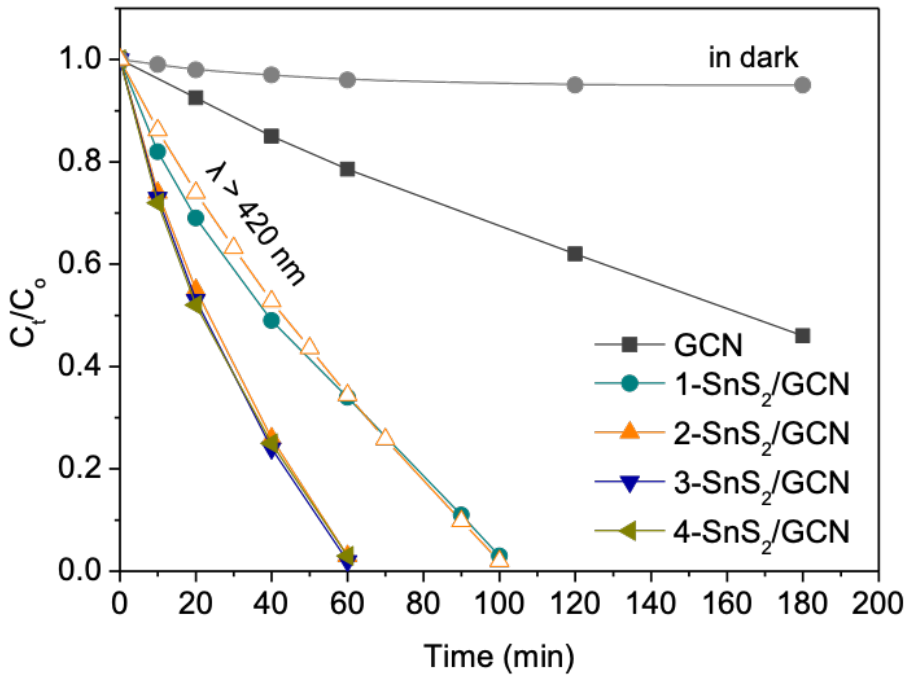

Figure 91. Photocatalytic reduction of aqueous Cr(VI) with GCN and SnS_2/GCN catalysts. The time course of Cr(VI) removal by 2-SnS_2/GCN in the dark is also given.

In the following, we modified the catalyst dosage and pH of the solution to optimize the reaction conditions. **Figure 92** displays the evolution of photocatalytic Cr(VI) reduction over time for different additions of 2-SnS_2/GCN catalyst (from 0.2 to 0.8 g

L^{-1}). It can be perceived that the Cr(VI) reduction efficiency reach a maximum at 0.4 g L^{-1} catalyst concentration. The slightly unaffected photoactivity with higher loadings (0.4–0.8 g L^{-1}) can be attributed to the contradictory effect of more available active sites and light scattering from the particles surface.

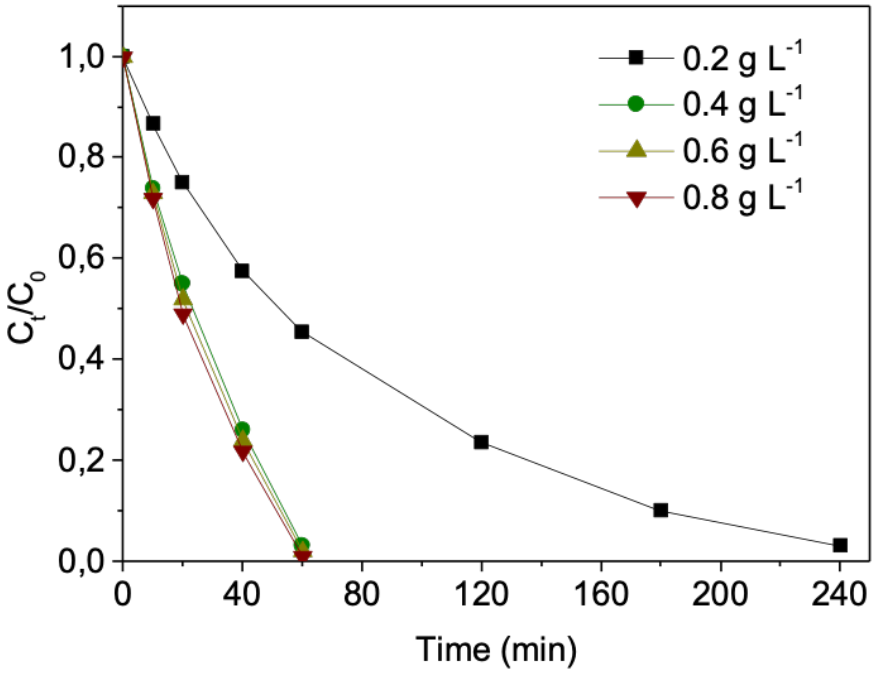

Figure 92. Concentration dependent photocatalytic Cr(VI) reduction activity of 2-SnS_2/GCN. Reaction conditions: 0.2–0.8 g L^{-1} catalyst, 50 mg L^{-1} Cr(VI) aqueous solution, pH = 2, $\lambda > 360$ nm light irradiation, 20 ºC.

The pH of the solution has also a pronounced effect on the photocatalytic activity. As shown in **Figure 93**, the 2-SnS_2/GCN catalyst exhibits a remarkably increased Cr(VI) photoreduction yield as the solution pH decreases from 6 to 1. Notably, in pH 1 solution, 2-SnS_2/GCN reduces Cr(VI) (50 mg L^{-1}) with a >99% conversion yield after 40 min. This behavior can be attributed to the favorable adsorption of Cr(VI) ions on the catalyst surface. Specifically, at acid pH (pH < 4), the Cr(VI) species, mainly in the $HCrO_4^-$ form [248], tend to absorbed on the positively charged surface of g-C_3N_4 (the point of zero charge (pH_{pzc}) of g-C_3N_4 is reported to be between 4 and 5) [249] and, therefore, this process can enhance the Cr(VI) photoreduction efficiency. Moreover, in acidic solutions, the excessive concentration of protons (H^+) is beneficial to the reduction of Cr(VI) to Cr(III) (see Eq. (11)). Thus, under optimal conditions (0.4 g L^{-1} catalyst dose, pH 2), the Cr(VI) reduction rate for the system reaches 21.2 μmol h^{-1}

within 1 h under λ > 360 nm light. When using a monochromatic light source, the apparent quantum yield (QY) for Cr(VI) reduction, defined as the ratio between the amount of reduced Cr(VI) and the flux of incident photons, is as high as 16.4% at 375 nm and 12.1% at 410 nm. It is worth noting that the efficiency of 2-SnS_2/GCN is superior to almost all of the reported Cr(VI) reduction catalysts, operating even with the aid of sacrificial regents (see **Table 11**).

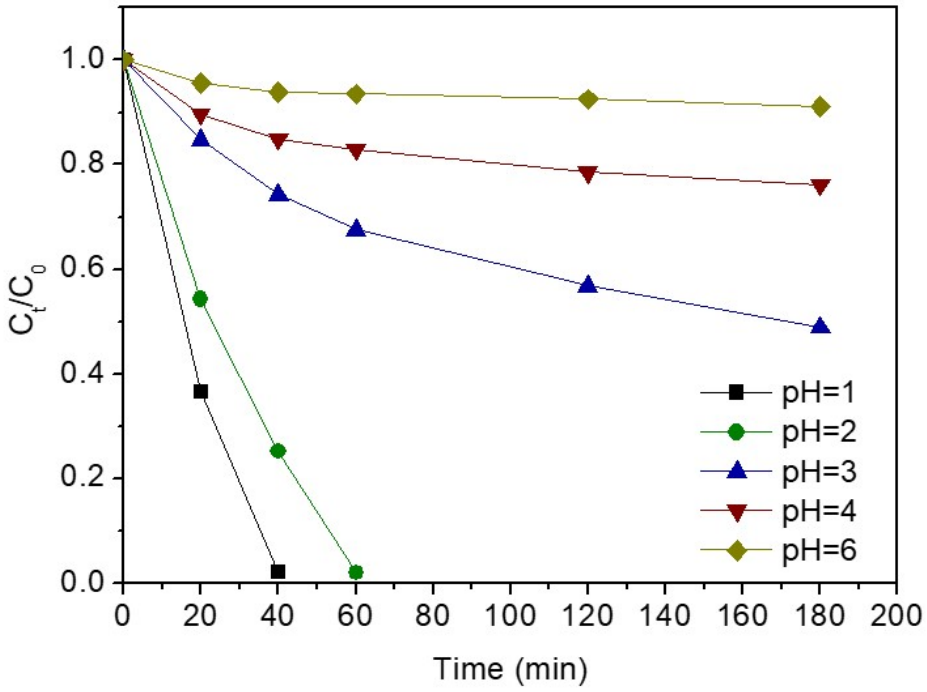

Figure 93. Effect of the solution pH on the photocatalytic Cr(VI) reduction performance. Reaction conditions: 0.4 g L^{-1} catalyst (2-SnS_2/GCN), 50 mg L^{-1} Cr(VI) aqueous solution, pH = 1–6, λ > 360 nm light irradiation, 20 ºC. The pH of the solution was adjusted with 2 M H_2SO_4 or 2 M NaOH.

Table 11. Comparison of photocatalytic efficiency between 2-SnS_2/GCN and other reported Cr(VI) reduction catalysts.

Photocatalyst	**Reaction conditions**	**Photocatalytic reduction of Cr(VI)**		**Ref.**
		QY	**Cr(VI) reduction/ Time**	
Ag_3PO_4/AgBr/ $Ti_3C_2T_x$ composite	15 mg L^{-1} Cr(VI)/EDTA	12.5% at λ > 420 nm	~76%/1h	[250]
AgCl:Ag hollow nanocrystals	10 mg L^{-1} Cr(VI)/10 mM EDTA	7.5% at λ > 420 nm	>99%/10min	[251]
Porous Ag/Ag_3PO_4/rGO microspheres	10 mg L^{-1} Cr(VI)/methylene blue (MB)	2.37% at λ > 400 nm	>99%/16min	[252]

$CuFe_2O_4$/CdS heterostructure	0.5 mM Cr(VI)/0.5 mM salicylic acid	1.1% at λ = 430 nm	~72%/6h	[253]
TiO_2/formic acid (FA) composite	1.92 mM Cr(VI)/286 mM FA	1.58% at λ = 365 nm	>99%/8h	[254]
Co_3O_4/g-C_3N_4 heterojunction	15 mg L^{-1} Cr(VI)/tetracycline	30% at λ = 420 nm	>90%/2.5h	[255]
Ni-doped MoS_2/g-C_3N_4 hetero-nanostructures	50 mg L^{-1} Cr(VI) aqueous solution	29.6% at λ = 375 nm, 23.7% at λ = 410 nm	>99%/40min	[256]
Mesoporous $Co_{1-x}Ni_xO$	50 mg L^{-1} Cr(VI) aqueous solution	1.5% at λ = 375 nm, 0.8% at λ = 410 nm	~90%/4h	[257]
Mesoporous CoO	50 mg L^{-1} Cr(VI) aqueous solution	1.61% at λ = 375 nm	~92%/4h	[258]
Au/TiO_2-Pt nanocomposites	1 mM Cr(VI) aqueous solution	1% at λ = 550 nm	>99%/0.5h	[259]
2-SnS_2/GCN heterostructure	**50 mg L^{-1} Cr(VI) aqueous solution**	**16.4% at λ = 375 nm 12.1% at λ = 410 nm**	**>99%/1h**	**In this work**

Further experiments were also performed to explore practical application of the present catalytic system in detoxification of wastewaters. In this context, 2-SnS_2/GCN was tested for Cr(VI) reduction in the presence of various ions as competing agents. Measurements were conducted using the same dose of catalyst (0.4 g L^{-1}) in 50 mL of Cr(VI) aqueous solution (100 mg L^{-1}) without and containing 50 mg L^{-1} for each SO_4^{2-}, CO_3^{2-}, NO_3^-, Cl^-, Na^+, Cu^{2+}, Zn^{2+} and Mn^{2+} ion, which are typical concentrations in industrial wastewaters. [260,261] In general, the presence of interfering ions, such as SO_4^{2-}, NO_3^-, Cl^-, Zn^{2+} and Mn^{2+}, may have a negative effect on the photocatalytic reduction of Cr(VI) due to their competitive adsorption and redox behavior with Cr(VI) at the catalyst's surface. [262,263] Throughout these experiments, 2-SnS_2/GCN catalyst exhibited persistent high Cr(VI) photoreduction activity (>99% Cr(VI) conversion in 2.5 h), even though excess amount of competing ions are present (**Figure 94**).

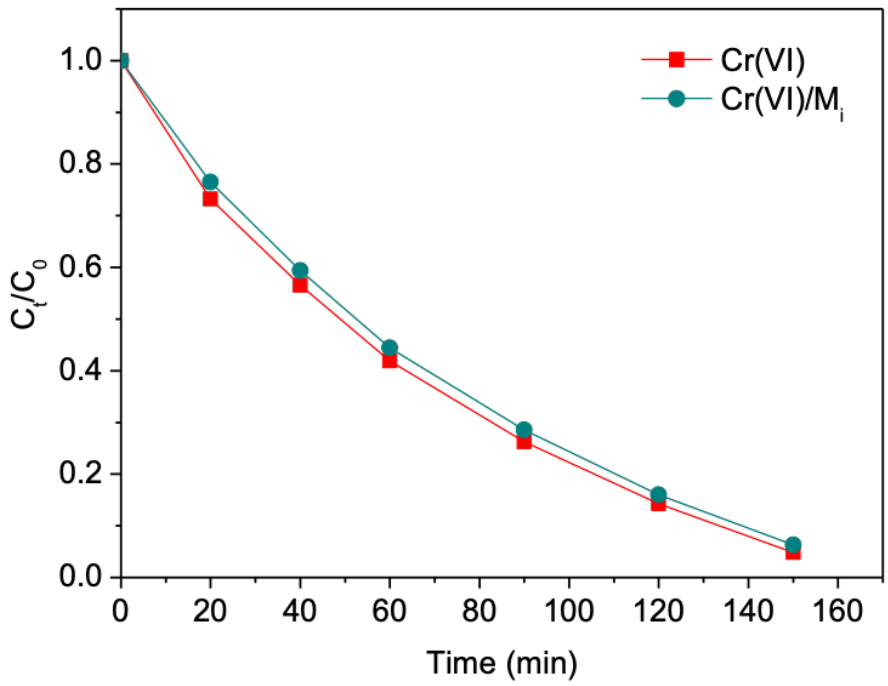

Figure 94. Comparison of Cr(VI) reduction in the absence and presence of different interfering ions (M_i = SO_4^{2-}, CO_3^{2-}, NO_3^-, Cl^-, Na^+, Cu^{2+}, Zn^{2+} and Mn^{2+}) (C_{Cr}/C_{Mi} = 1:4, where C_{Cr} and C_{Mi} are the total concentration of Cr(VI) and impurity ions).

The results of cycling tests of the reduction of Cr(VI) over 2-SnS/GCN are shown in **Figure 95**. After completion of reaction, the catalyst was isolated from the reaction mixture by centrifugation, washed with water, and re-dispersed in a fresh Cr(VI) solution. As shown in **Figure 95**, the 2-SnS/GCN catalyst did not exhibit any significant decrease of its activity throughout the testing cycles and its Cr(VI) conversion efficiency remains stably high (>98%) after three 1-h photocatalysis runs. In addition, no obvious changes in crystallinity and surface chemical states were observed after the recycling tests, as shown by the TGA, XRD and XPS spectra, substantiating the excellent stability of the 2-SnS_2/GCN catalyst (see **Figures 96, 97** and **98**). In the deconvoluted C 1s spectrum, the peaks located at 284.8, 286.2 and 288.4 ±0.2 eV binding energies are assigned to the C–C bond of aliphatic carbon and the N–C=N and C–N bonds in triazine units of g-C_3N_4, respectively. The N 1s spectrum displays the fitting peaks at 398.9 and 400.8 ±0.3 eV, which are attributed to the pyridinic (C–N sp^2) and pyrrolic (C–N sp^3) N atoms of g-C_3N_4. The Sn 3d spectrum shows two peaks corresponding to Sn $3d_{5/2}$ (486.8 ±0.2 eV) and Sn $3d_{3/2}$ (495.3 ±0.2 eV) core levels of Sn^{4+}. In the S 2p region, the signal at 162.2 ±0.2 eV binding energy is assigned to the Sn–S bonding, indicating the existence of SnS_2.

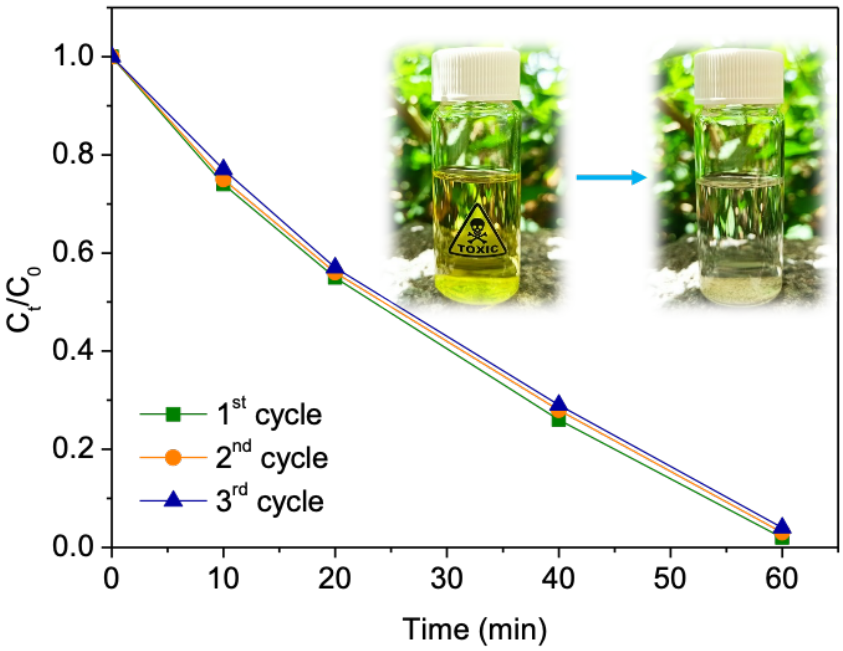

Figure 95. Cycling tests of photocatalytic Cr(VI) reduction with 2-SnS_2/GCN catalyst. Inset: typical photographic images of a Cr(VI) aqueous solution before (left) and after (right) catalysis. Reaction conditions: 0.4 g L^{-1} catalyst, 50 mg L^{-1} aqueous Cr(VI) solution, pH = 2, $\lambda > 360$ nm light, 20 °C.

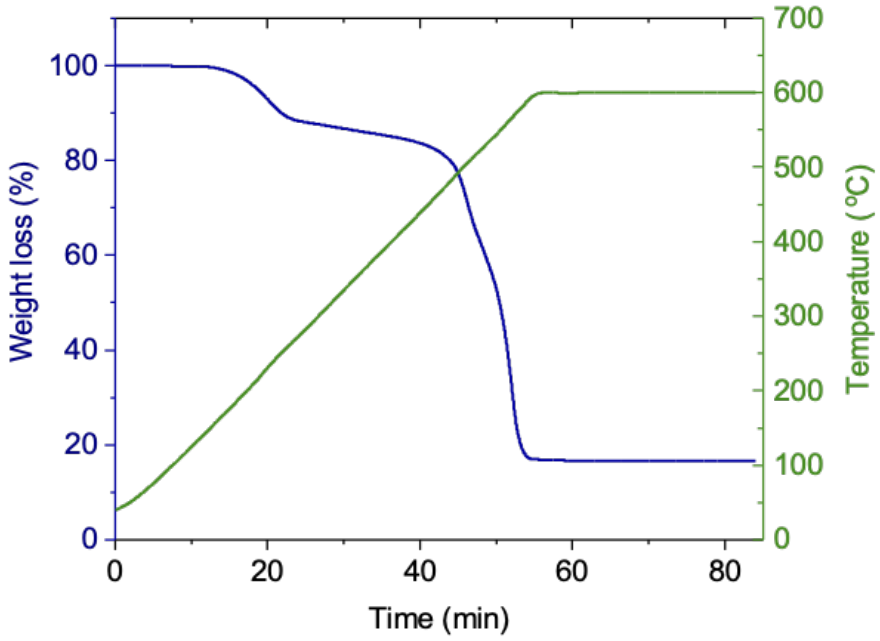

Figure 96. TGA profile of the three-times reused 2-SnS_2/GCN catalyst. The TGA shows a weight loss of 83.5% between 50 and 600 °C due to the oxidation of SnS_2 and combustion of g-C_3N_4 in air. The mass difference before and after calcination indicates a weight fraction of SnS_2 of ~20.1 wt%.

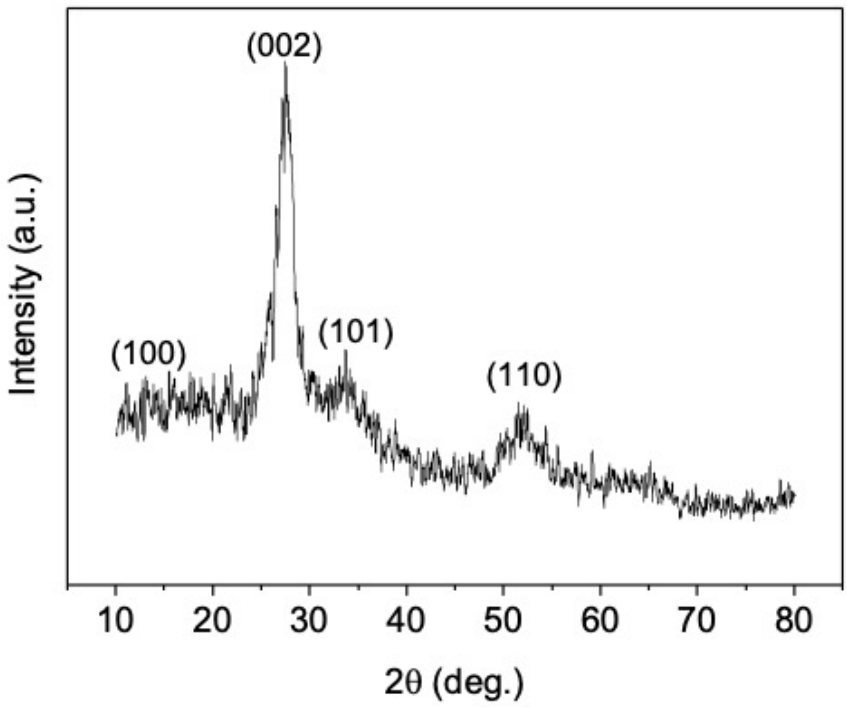

Figure 97. XRD pattern of the 2-SnS_2/GCN catalyst after recycling tests.

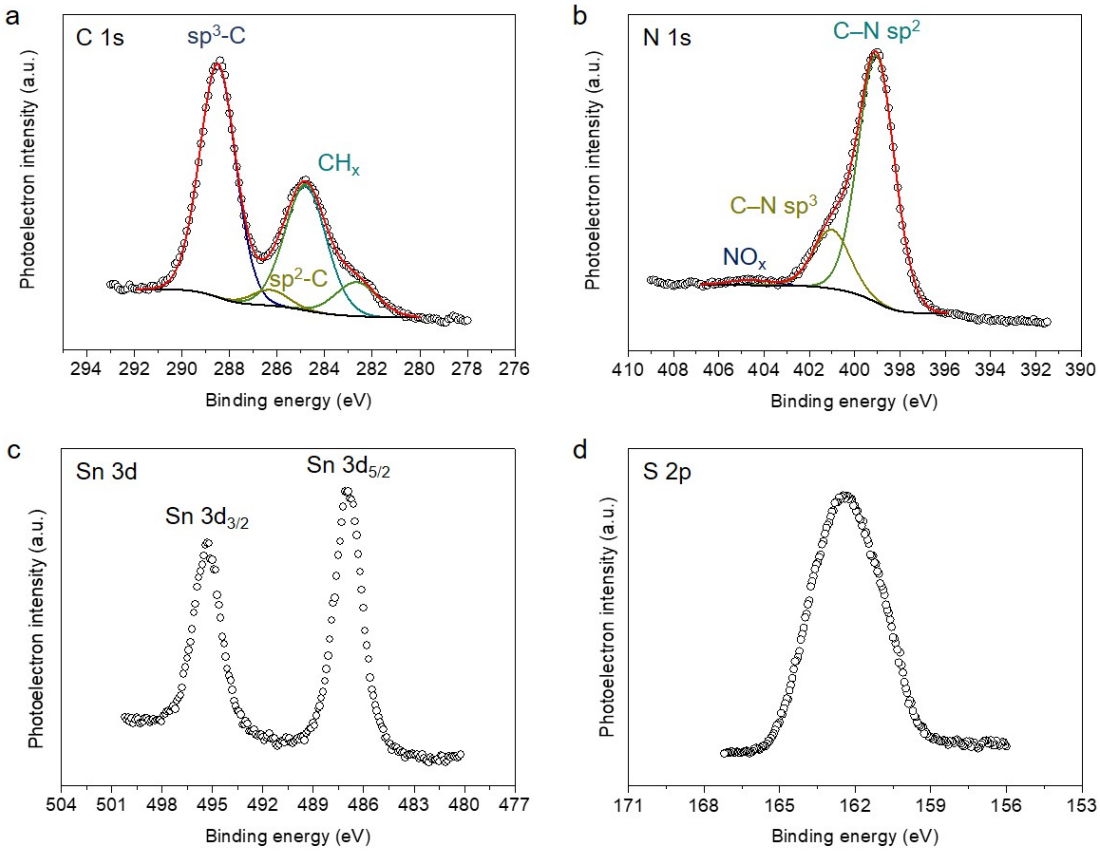

Figure 98. XPS core-level spectra of the (a) C 1s, (b) N 1s, (c) Sn 3d and (d) S 2p region for the 2-SnS_2/GCN catalyst after recycling tests. The white circles are XPS data, while the red, green, blue and yellow curves are the fitting of the experimental data.

3.4.2.2 Mechanism of photocatalytic reactions

The 2-SnS_2/GCN catalyst exhibited substantial activity in the photocatalytic oxidation of H_2O to O_2 under UV–vis light illumination. The photocatalytic oxidation experiment was carried out in an air-tight quartz cell filled with an aqueous solution of Cr(VI) (50 mg L^{-1}) and the evolved oxygen was analyzed by gas chromatography (GC). We found that 1 h of $\lambda > 360$ nm irradiation generated 15.1 μmol of O_2 with 0.4 mg L^{-1} catalyst dispersion; meanwhile, no other gas (e.g., CO_2, N_2) was detected by GC. The O_2 evolution rate is consistent with the expected production of oxygen derived from the stoichiometry of the overall Cr(VI)/Cr(III) reaction; assuming a 21.2 μmol h^{-1} Cr(VI) reduction rate, the O_2 production based on Eq. (9) is 15.9 μmol h^{-1}. This suggests that the main oxidation reaction occurring on the 2-SnS_2/GCN surface is the oxidation of water to oxygen ($2H_2O \rightarrow O_2 + 4H^+ + 4e^-$), and the overall photocatalytic reaction can be expressed by the equation: $2HCrO_4^- + 8H^+ \rightarrow 2Cr^{3+} + \frac{3}{2} O_2 + 5H_2O$.

The Cr(VI) reduction activity of 2-SnS_2/GCN in the presence of phenol, EDTA and citric acid as organic pollutants was also examined. Since oxidation of these compounds is kinetically more propitious than oxidation of water, it is anticipated that the Cr(VI) reduction process will be accelerated. As expected, the rate of Cr(VI) degradation is increased significantly with the addition of 2 eq. of the above pollutants, resulting in complete conversion of Cr(VI) in only 10–30 min (**Figure 99**). The rate constants of the these reactions were determined using a first-order kinetic model $\ln(C_t/C_o) = -k_{app}t$, where, C_o and C_t is the concentration of Cr(VI) at initial time and time t, respectively, and k_{app} is the apparent reaction rate constant). Thus, fitting results show that the photocatalytic reduction of Cr(VI) proceeds at a rate (k_{app}) of ~7.8×10^{-2} min^{-1} and ~11.5×10^{-2} min^{-1} with EDTA and citric acid, respectively (**Figure 100**), which is higher by a factor of about 2.4–3.5 than that obtained in pure water (3.3×10^{-2} min^{-1}). Due to the very fast reduction of Cr(VI) in presence of phenol, the determination of the rate constant for this reaction is difficult; however, a rough value of ~15.5×10^{-2} min^{-1} is assessed based on initial limited data. This demonstrates that presence of organic pollutants in Cr(VI)-containing wastewaters clearly enhance the catalytic propensity of SnS_2/GCN.

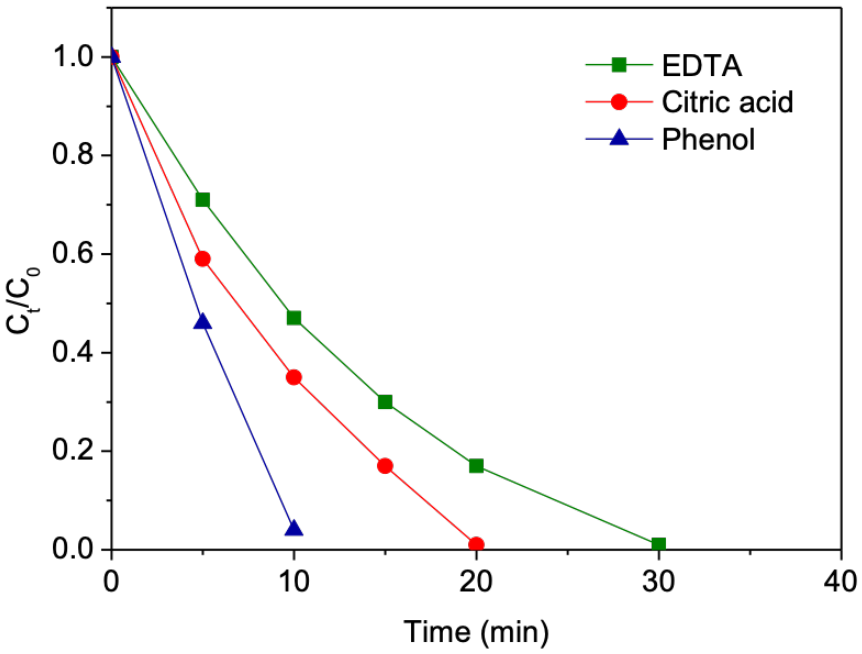

Figure 99. Time courses for the photocatalytic reduction of aqueous Cr(VI) over 2-SnS_2/GCN catalyst in the presence 2 eq. of EDTA, citric acid and phenol under λ > 360 nm light irradiation. Reaction conditions: 0.4 g L^{-1} catalyst, 50 mg L^{-1} Cr(VI) solution, pH = 2, 20 °C.

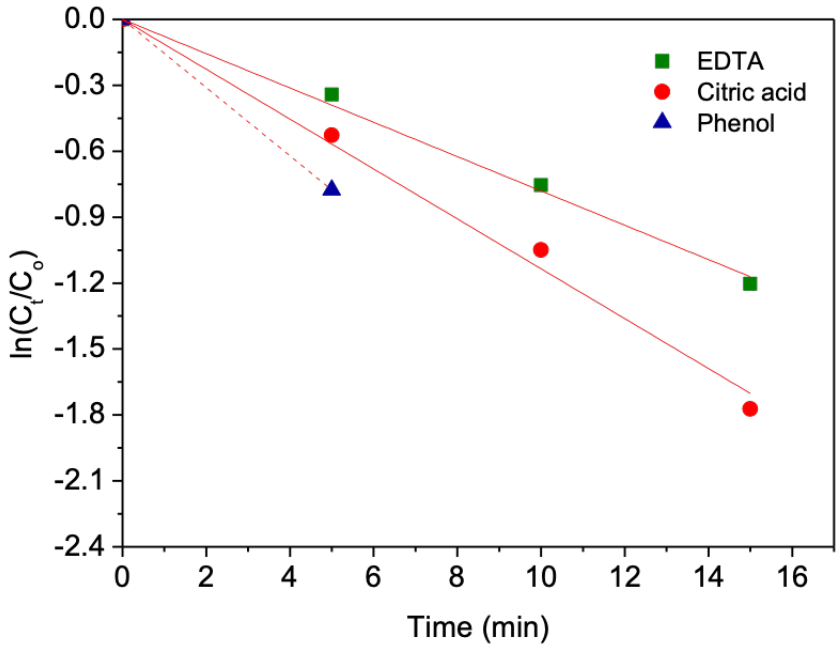

Figure 100. kinetic profiles for the photocatalytic reduction of aqueous Cr(VI) over 2-SnS_2/GCN catalyst in the presence 2 eq. of EDTA, citric acid and phenol under λ > 360 nm light irradiation. Reaction conditions: 0.4 g L^{-1} catalyst, 50 mg L^{-1} Cr(VI) solution, pH = 2, 20 °C.

3.4.2.3 Electronic band structure of the catalysts

We used electrochemical impendence (EIS) and optical absorption spectroscopy to examine the electron band structure and interfacial charge separation efficiency of the

SnS_2/GCN catalysts. **Figure 101** shows the Mott-Schottky plots of GCN and SnS_2/GCN samples (drop-casted as thin films on FTO substrates). The flat band potentials (E_{FB}) of the electrodes were obtained as extrapolation of the linear portion of $1/C_{sc}^2$ versus applied potential (E) curves to zero. The $1/C_{sc}^2$–E plots slow positive slopes claiming GCN and SnS_2/GCN to be n-type semiconductors. The E_{FB} values for the SnS_2/GCN are estimated to be –0.86 V to –1.28 V, while the E_{FB} position of pure GCN locates at –1.33 V (see **Table 12**). All electrochemical potentials are referred to the normal hydrogen electrode (NHE) at pH 7. Apparently, deposition of SnS_2 nanosheets onto the GCN surface causes an anodic shift in the E_{FB} potential of g-C_3N_4, which is consistent with the lower Fermi level of SnS_2 than that of g-C_3N_4 (–6.2 eV vs –4.2 eV vacuum scale) [264,265]. In particular, the SnS_2/g-C_3N_4 contact forms a built-in electric field, which account for the electron flow from g-C_3N_4 to SnS_2 until the Fermi levels reach equilibrium. Moreover, the slopes of the curves in **Figure 101** indicate a much higher donor density (N_d) for SnS_2/GCN catalysts compared to GCN. Specifically, the N_d values for SnS_2/GCN were determined as ~0.9–2.2×10^{18} cm^{-3}, superior to that of GCN (~7.1×10^{17} cm^{-3}), see **Table 12**. This is most likely due to the improved charge dissociation at the SnS_2/g-C_3N_4 interface (see below).

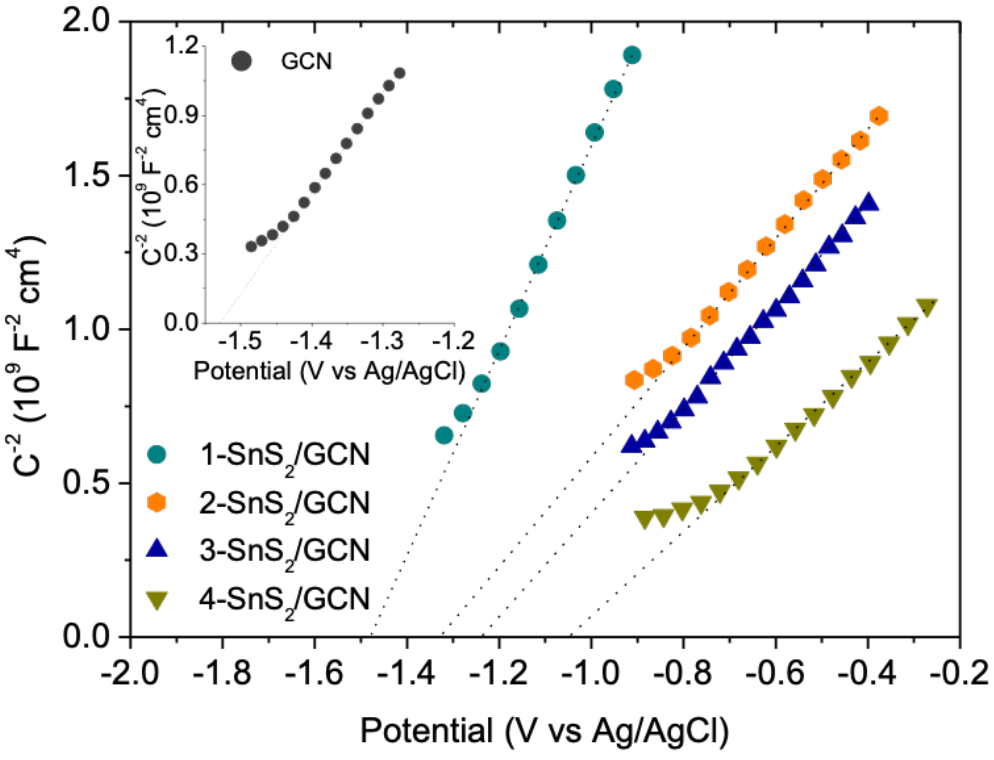

Figure 101. Mott-Schottky plots of GCN and SnS_2/GCN catalysts.

Table 12. Optical absorption and electrochemical data for the GCN and SnS_2/GCN catalysts.

Sample	E_g (eV)	E_{FB} (V vs NHE)	E_{VB} (V vs NHE)	N_d (cm^{-3})	R_{ct} (kΩ)	w_{SCL}[a] (nm)
GCN	2.72	–1.33	1.39	7.10×10^{17}	1241.2	30.9
1-SnS_2/GCN	2.73	–1.28	1.45	8.94×10^{17}	19.2	27.0
2-SnS_2/GCN	2.88	–1.13	1.75	1.74×10^{18}	11.6	18.2
3-SnS_2/GCN	2.92	–1.04	1.88	1.85×10^{18}	31.3	16.9
4-SnS_2/GCN	2.92	–0.86	2.06	2.23×10^{18}	28.7	14.0

[a]Width of space charge layer (w_{SCL}) calculated by $w_{SCL} = (2\varepsilon\varepsilon_0(E–E_{FB})/e_0N_d)^{1/2}$, where, E is the applied potential, E_{FB} is the flat band potential of the semiconductor, ε is the relative dielectric constant, ε_0 is the permittivity under the vacuum, N_d is the donor density of electrode material and e_0 is the elementary charge.

Measurements of the optical band gap (E_g) were performed using UV–vis diffuse reflectance spectroscopy, as shown in **Figure 102**. The absorption spectra revealed that the energy gap of the heterostructured catalysts range from ~2.73 to ~2.92 eV, which is slightly larger than the band gap of GCN sample (~2.72 eV). This small, yet noteworthy, blue shift in energy gap suggests strong interlayer coupling between the g-C_3N_4 and SnS_2 layers, which enables interfacial electronic interactions. The UV–vis spectra of SnS_2-containing samples also show an apparent tail between 2.2 and 2.5 eV due to the optical absorption of SnS_2 nanosheets; SnS_2 has an energy gap of ~2.2–2.4 eV. For heavily doped n-type semiconductors (such as the SnS_2/GCN), the flat band position lies very close to the CB edge. Thus, combined with the results from optical absorption measurements, the valence band-edge energy (E_{VB}) of GCN and SnS_2/GCN was obtained by subtracting the E_g from the E_{FB} energy level (**Table 12**), and the band diagrams for each catalyst are shown in **Figure 103**. The results show that the CB and VB levels of SnS_2/GCN meet the redox potentials of Cr(VI)/Cr(III) (0.92 V vs NHE) and O_2/H_2O (0.82 V vs NHE) couples, thus demonstrating the ability of these materials for the remediation of aqueous Cr(VI) under irradiation.

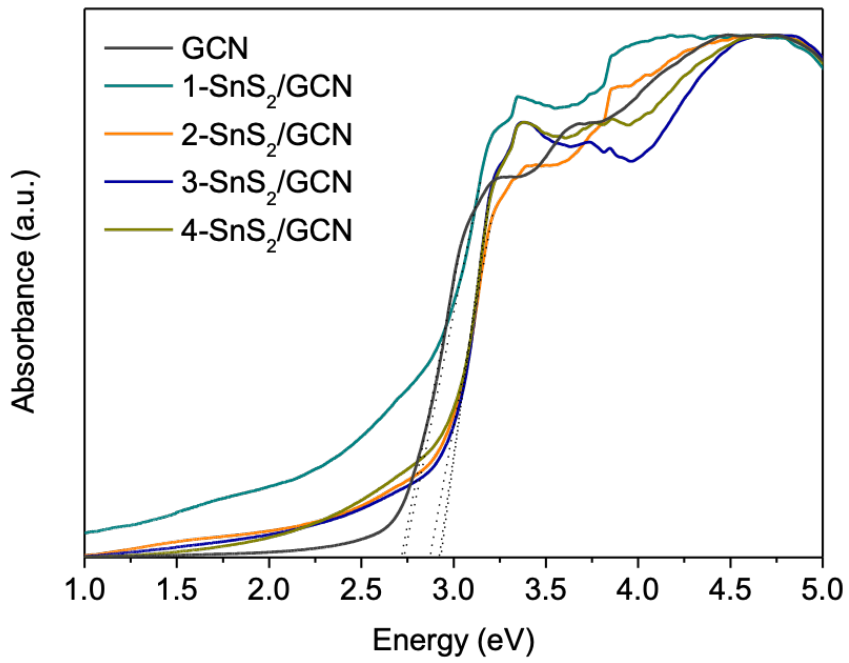

Figure 102. Optical absorption spectra of GCN and SnS_2/GCN catalysts.

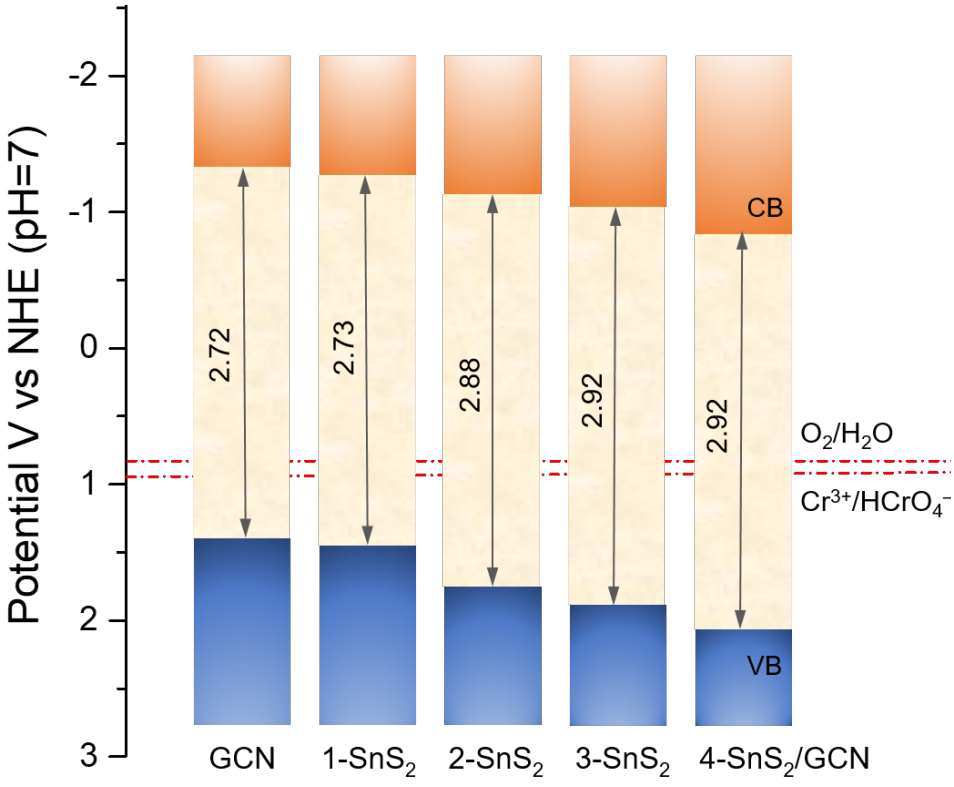

Figure 103. Energy band diagrams of GCN and SnS_2/GCN catalysts.

EIS Nyquist measurements were also performed to extract the charge-transfer resistance (R_{ct}) at the catalyst/electrolyte interface. All measurements were conducted

in 0.5 Na_2SO_4 electrolyte at open circuit potential from 1 Hz to 1 MHz using an alternating current amplitude of 10 mV. **Figure 104** shows Nyquist plots for pure GCN and SnS_2/GCN catalysts. We interpret the experimental data using a typical Randles electrical circuit (inset of **Figure 104**), and found that 2-SnS_2/GCN exhibits the lowest resistance among the studied materials. **Table 13** depicts the EIS parameters obtained by fitting the impendence data. Nyquist plots unveiled a R_{ct} for SnS_2/GCN at ~11.6–31.3 kΩ, dramatically lower than GCN at ~1241.2 kΩ (**Table 13**), suggesting an accelerated electron transfer along the SnS_2/g-C_3N_4 interface. The space-charge layer thickness (w_{SCL}) at the electrode/electrolyte interface was further evaluated to understand the charge transfer ability of the catalysts [266]. Based on E_{FB} and N_d values, the space charge layer of SnS_2/GCN samples is calculated to be 14–27 nm at an applied potential of 0 V (vs NHE), which is thinner than that of GCN (ca. 30.9 nm), see **Table 12**. This reflects a lower energy barrier between the SnS_2-containing catalysts and electrolyte, further manifesting a more efficient charge transfer towards the redox species in solution, in line with above results.

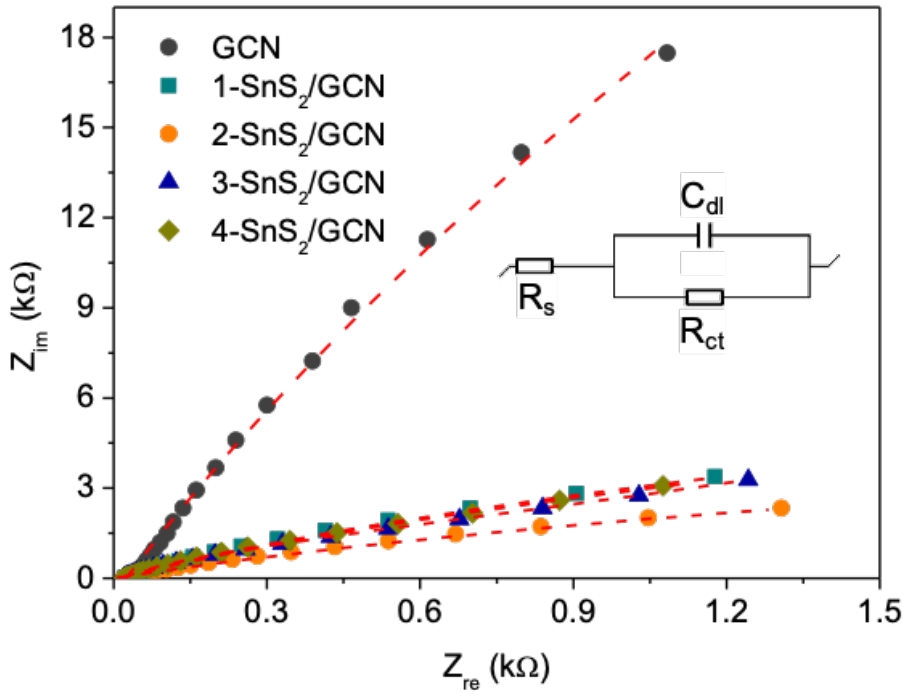

Figure 104. Nyquist plots of GCN and SnS_2/GCN catalysts. Inset of panel: Randles equivalent circuit where R_s is the electrolyte resistance, R_{ct} is the charge-transfer resistance and C_{dl} is the double layer capacitance.

Table 13. EIS equivalent circuit fitted parameters for GCN and SnS_2/GCN catalysts.

Sample	R_s (Ω)	C_{dl} (F)	R_{ct} (Ω)	x^2
GCN	24.71	9.5×10^{-6}	1241.2	5.04×10^{-5}
1-SnS_2/GCN	20.75	21.9×10^{-6}	19.2	4.32×10^{-4}
2-SnS_2/GCN	15.54	29.3×10^{-6}	11.6	5.29×10^{-5}
3-SnS_2/GCN	6.85	18.4×10^{-6}	31.3	1.74×10^{-4}
4-SnS_2/GCN	11.58	9.5×10^{-6}	28.7	5.20×10^{-4}

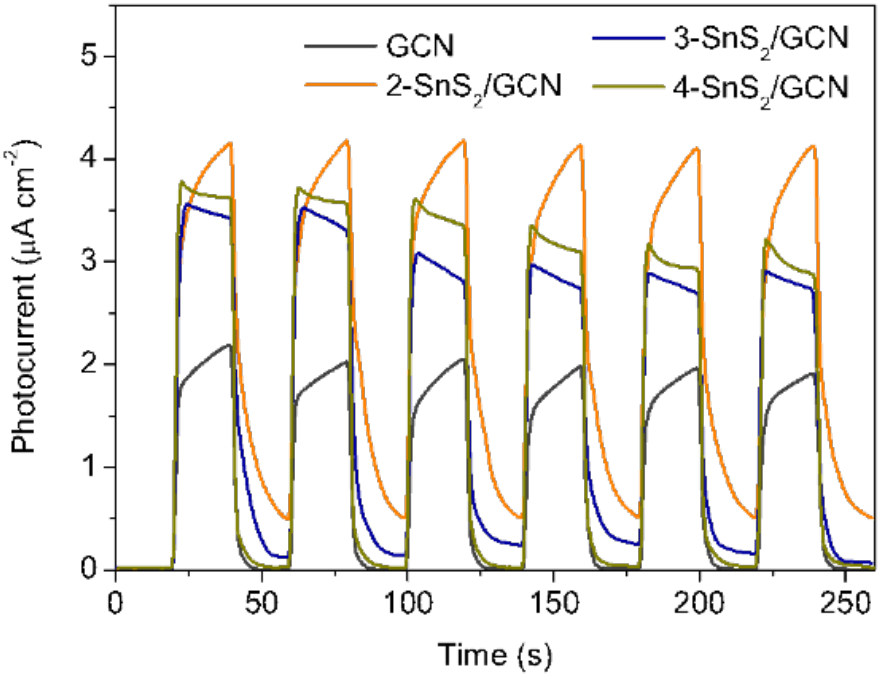

Figure 105. Transient photocurrent profiles measured at a bias of 0.2 V (vs Ag/AgCl) under light and dark conditions for the GCN and SnS_2/GCN catalysts.

To obtain further information about the charge transport dynamics in SnS_2/GCN heterostructures, we performed photoelectrochemical measurements in 1 M Na_2SO_4 solution. In **Figure 105** we compare the photocurrent response curves of various SnS_2-containing catalysts with that of unmodified g-C_3N_4 under visible (380–780 nm) light irradiation. Evidently, deposition of 20 wt% SnS_2 on g-C_3N_4 makes a stronger contribution to photocurrent generation; 2-SnS_2/GCN exhibited a markedly higher photocurrent density than the other samples. This suggests a more efficient separation

of the photogenerated electron–hole pairs in this catalyst. Open-circuit photovoltage (OCP) decay analysis was also performed to obtained further information on the exciton separation along the electrode/electrolyte interface. OCP experiments were conducted in a 1 M Na_2SO_4 electrolyte under light on and off conditions, and the potential-dependent lifetime (τ_n) of the photogenerated electrons (both free and trapped electrons) of the samples was calculated by the equation: $\tau_n = -(k_BT/e_0)(dV_{oc}/dt)^{-1}$, where, k_B is the Boltzmann's constant, T is the temperature, e_0 is the electron charge and dV_{oc}/dt is the photovoltage decay over time when the light is turned off.[267] As shown in **Figure 106**, the electrodes based on SnS_2-containing catalysts, especially 2-SnS_2/GCN, produce longer electron lifetimes than that of g-C_3N_4 (τ_n values measured as ~15, ~80, ~72 and ~69 s for GCN, 2-SnS_2/GCN, 3-SnS_2/GCN and 4-SnS_2/GCN, respectively obtained from the OCP decay profiles (**Figure 107**); consequently, this may contribute to the observed trends in photocatalytic performance. Therefore, the high photo-responsive activity of SnS_2/GCN heterostructures, once again, indicates the electron transportation from g-C_3N_4 to SnS_2 that prolongs the electron lifetime and eventually improves the utilization of charge carriers for interfacial chemical reactions. On the basis of the above characterizations, the excellent photocatalytic activity of 2-SnS_2/GCN was largely associated with the lower charge-transfer resistance through the catalyst/electrolyte interface, relative high electron density, and low electron-hole recombination rate. The high SnS_2-loaded catalysts (>30 wt% SnS_2), although possess more active sites for Cr(VI) reduction (SnS_2), the interface states formed at the SnS_2/g-C_3N_4 junction can serve as trap centers and cause recombination of the photogenerated electron-hole pairs. This is supported by the relatively higher electron-transfer resistance, shorter electron lifetime and lower photocurrent generation efficiency in these materials, as indicated by the above-mentioned results.

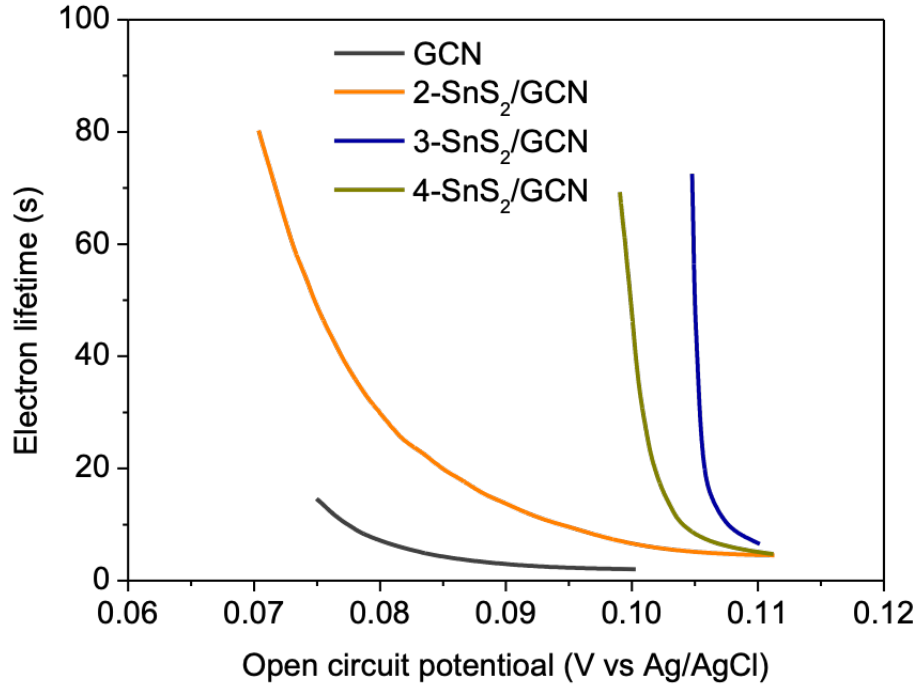

Figure 106. Electron lifetime determined from the OCP decay curves for the GCN and SnS_2/GCN catalysts.

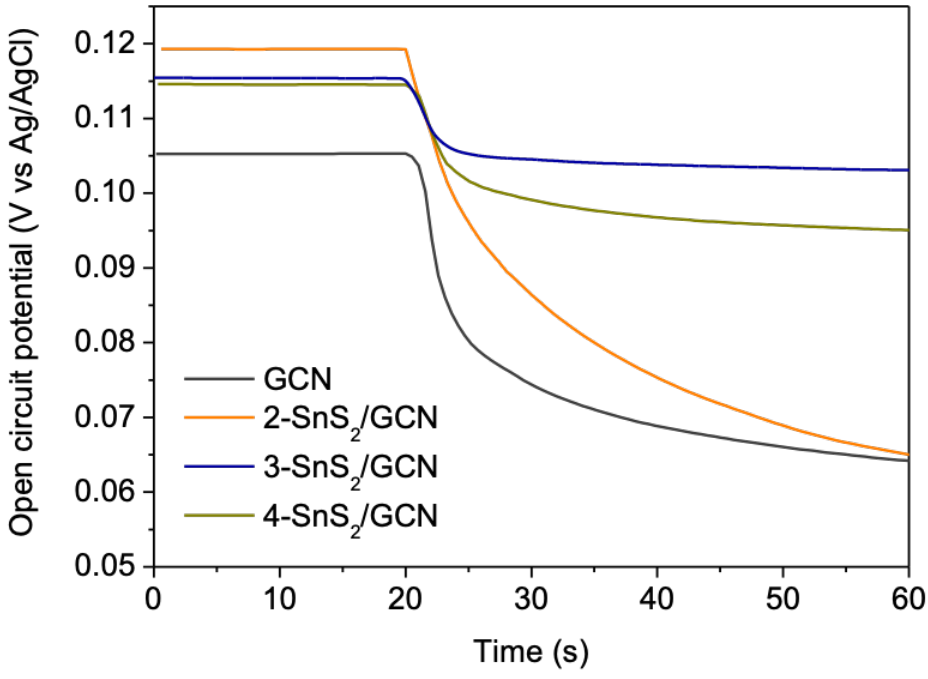

Figure 107. Open-circuit photovoltage (OCP) decay curves of GCN, 2-SnS_2/GCN, 3-SnS_2/GCN and 4-SnS_2/GCN catalysts in 1 M Na_2SO_4 solution.

Figure 108 illustrates a proposed reaction mechanism for reduction of Cr(VI) and oxidation of H_2O in aqueous suspension of SnS_2/GCN under UV-visible light

irradiation. In short, under illumination conditions, both g-C_3N_4 and SnS_2 components get excited and produce electrons and holes. Because of the potential drop at the SnS_2/g-C_3N_4 interface, electrons are injected from g-C_3N_4 into the CB of SnS_2, where they reduce Cr(VI) (mainly in $HCrO_4^-$ form) to Cr(III). Whereas the photogenerated holes in the VB of SnS_2 transfer to the g-C_3N_4 at which oxidation of H_2O to O_2 occurs. As g-C_3N_4 has a higher CB and VB edge position, a type II heterostructure is formed between g-C_3N_4 and SnS_2. Specifically, the CB and VB potentials of SnS_2 are estimated as –0.75 V and 1.47 V vs NHE (pH 7), respectively, according to Mott-Schottky and optical absorption measurements (see **Figure 109**), which are close to the literature values [268,269]. Such charge transfer pathways within the SnS_2/GCN catalysts are evidenced from electrochemical and photoelectrochemical studies.

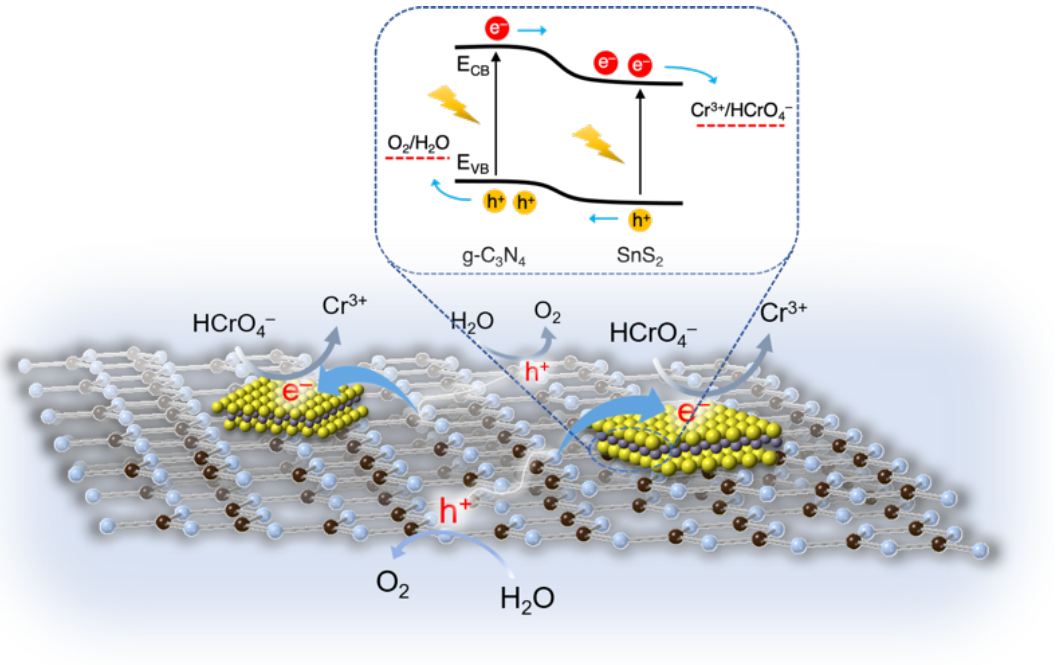

Figure 108. Expected reaction mechanism for reduction of Cr(VI) and oxidation of H_2O over SnS_2/GCN catalysts under irradiation of UV-visible light.

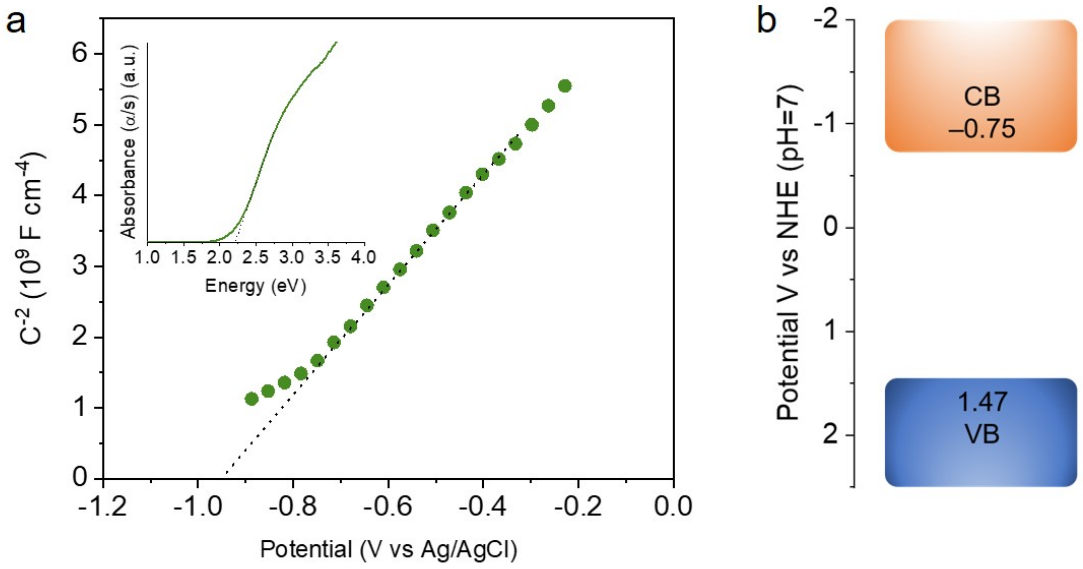

Figure 109. (a) Mott-Schottky plot and UV-vis diffuse reflectance spectrum (inset), and (b) energy band diagram of SnS_2. The EIS measurements yield a flat band potential (E_{FB}) of –0.75 V vs NHE (pH 7), while the UV-vis spectrum shows an energy band gap (E_g) of 2.22 eV. The VB energy level is estimated by subtracting the E_g from the E_{FB} potential.

Chapter 4 – Conclusions

Summing up, 2H MoS_2-modifed few-layer g-C_3N_4 nano-heterostructures with variable area of interlayer contact were synthesized via a two-step hydrothermal sulfurization and liquid-phase exfoliation method. These materials are composed of monodispersed MoS_2 nanolayers with tunable lateral sizes (i.e., ranging from 18 to 52 nm) and show interface size dependence photocatalytic activity. The MoS_2/g-C_3N_4 catalyst at the 20 wt% MoS_2 loading and 39 nm MoS_2 lateral size reaches the highest H_2-production activity, giving a 1497 μmol h^{-1} g_{cat}^{-1} H_2 evolution rate with an apparent QY of 3.3% at 410 nm. The UV-vis/NIR, PL and EIS results affirm an electron-transport mechanism by which photoexcited g-C_3N_4 efficiently transfer electrons to the surface-anchored MoS_2 nanosheets, where they subsequently react with protons to produce hydrogen. According to this reaction scheme, the electronic compatibility between g-C_3N_4 and MoS_2 layers plays a significant role in dictating charge transport and separation processes and, thus, overall photocatalytic conversion efficiency. Besides the increased interlayer contact area, the enhanced activity of these catalysts for hydrogen evolution is also correlated to the increased number of exposed MoS_2 edge sites created at the interface of the MoS_2/g-C_3N_4 heterojunction, which is affected by the size of MoS_2 nanolayers. This study provides new insights into engineering the MoS_2/g-C_3N_4 junctions, thus guiding on the importance of interface interactions in layers heterostructures for the development of future light energy conversion devices.

A series of 2D/2D layered metal-doped MoS_2/g-C_3N_4 heterostructures with different metal doping level was also prepared via a two-step hydrothermal sulfurization and liquid-phase exfoliation process. These materials exhibit high efficiency in photocatalytic reduction of Cr(VI) with excellent stability. As a result, the Ni-MoS_2/g-C_3N_4 catalyst with 30 wt% concentration of 3% Ni-doped MoS_2 nanosheets (3-NMS/GCN) shows the highest Cr(VI) photoreduction activity, reaching a record-high apparent QY of 29.6% at 375 nm and 23.7% at 410 nm, which to our knowledge is the highest among all reported Cr(VI) reduction nonprecious catalysts. Moreover, direct comparison of the Cr(VI) photoreduction efficiency of 3-NMS/GCN in the absence and presence of different interfering ions demonstrates the great reducing ability and viability of the catalyst for detoxification of Cr(VI)-contaminated industrial effluents. The effect of Ni doping and sulfur vacancies was thoroughly examined experimentally

and theoretically to provide insights into the electronic band structure and photoelectrochemical behavior of Ni-MoS_2 layers. Optical absorption, photo-electrochemical and photoluminescence studies confirm an electron-transport and separation mechanism by which photoexcited electrons are transferred from g-C_3N_4 to the surface-anchored Ni-doped MoS_2 nanosheets. Besides the electronic compatibility between the Ni-MoS_2 and g-C_3N_4 layers, the enhanced Cr(VI) reduction activity of this catalytic system is also arises from fast water oxidation kinetics. Due to the efficient dissociation and transport of free excitons, surface-reaching holes effectively oxidize water to form molecular oxygen. These results provide new insights into understanding and designing low-cost and earth-abundant layered heterostructures for photocatalytic environmental remediation and water treatment.

In addition, 2D/2D SnS_2/g-C_3N_4 heterojunction networks with different composition have been successfully prepared by a photochemical deposition method. In particular, the strong reducing ability of the CB electrons of g-C_3N_4 favors the thermodynamic growth of SnS_2 nanosheets on exfoliated g-C_3N_4. These newly developed heterostructures have an electronic band structure that allows a spatial separation of charge carriers across the SnS_2/g-C_3N_4 interface and promotes high Cr(VI) reduction and water oxidation efficiency of the photogenerated electrons and holes. Owing to these merits, SnS_2/g-C_3N_4 catalysts conduct photocatalytic reduction of Cr(VI) with high energy conversion efficiency of up to 16.4% at 375 nm and 12.1% at 410 nm. The results demonstrate the great potential of the SnS_2/g-C_3N_4 nano-heterostructures as viable photocatalysts for aqueous Cr(VI) reduction. Moreover, by proper selection of the initial precursors, this photo-deposition method can be easily adapted for the synthesis of a range of functional photocatalysts for clean energy conversion and environmental protection.

References

[1] F.J. Clauss, Solid Lubricants and Self-Lubricating Solids Elsevier, New York, **1972**.

[2] K.S. Novoselov, D. Jiang, F. Schedin, T.J. Booth, V.V. Khotkevich, S.V. Morozov, A.K. Geim , Proc. Natl. Acad. Sci. U.S.A. **2005**, 102 , 10451.

[3] A. Geim, K.S. Novoselov, Nature Mater., **2007**, 6**,** 183–191.

[4] K.S. Novoselov, et al., Proc. Natl. Acad. Sci., **2005**, 102, 10451–10453.

[5] G. Fiori, F. Bonaccorso, G. Iannaccone, T. Palacios, D. Neumaier, A. Seabaugh, S.K. Banerjee, L. Colombo, Nat. Nanotechnol., **2014**, 9, 768.

[6] G. Giovannetti, P. Khomyakov, G. Brocks, P. Kelly, J. van den Brink, Phys. Rev. B: Condens. Matter Mater. Phys. **2007**, 76, 073103.

[7] A. K. Geim, I. V. Grigorieva, Nature, **2013**, 499, 419–425.

[8] Q. Li, S.M. Koo, C.A. Richter, M.D. Edelstein, J.E. Bonevich, J.J. Kopanski et al., IEEE Trans Nanotechnol., **2007**, 6, 256–62.

[9] H. Liu et al., ACS Nano, **2014**, 8, 4033–4041.

[10] K.S. Kim, Y. Zhao, H. Jang, S.Y. Lee, J.M. Kim, K.S. Kim et al., Nature, **2009**, 457, 706–10.

[11] F. Lévy, Springer Netherlands, Dordrecht, **1976**.

[12] J.A. Wilson, A.D. Yoffe, Adv. Phys., **1969**, 18, 193.

[13] H. Zeng, X. Cui, Chem. Soc. Rev., **2015**, 44, 2629–2642.

[14] R.J. Toh, Z. Sofer, J. Luxa, D. Sedmidubský, M. Pumera, Chem. Commun., **2017**, 53, 3054–3057.

[15] S. Manzeli, D. Ovchinnikov, D. Pasquier, O.V. Yazyev, A. Kis, Nat. Rev. Mater., **2017**, 2, 17033.

[16] M.Y. Han, B. Ozyilmaz , Y.B. Zhang , P. Kim , Phys. Rev. Lett., **2007**, 98, 206805.

[17] K.F. Mak, C. Lee, J. Hone, J. Shan, T.F. Heinz, Phys. Rev. Lett., **2010**, 105, 136805.

[18] D. Dumcenco, et al., ACS Nano, **2015**, 9, 4611–4620.

[19] J.N. Coleman, M. Lotya, A. O'Neill, S.D. Bergin, P.J. King, U. Khan et al., Science, **2011**, 331, 568–71.

[20] J.A. Wilson, A.D. Yoffe, Adv Phys, **1969**, 18, 193–335.

[21] Y. Li, H. Wang, L. Xie, Y. Liang, G. Hong, H. Dai, J Am. Chem. Soc., **2011**, 133, 7296–9.

[22] M. Wu, L. Li, Y. Xue, G. Xu, L. Tang, N. Liu, W. Huang, Appl. Cat. B: Environ., **2018**, 228, 103–112.

[23] B. Poudel, Q. Hao, Y. Ma, Y. Lan, A. Minnich, B. Yu et al., Science, **2008**, 320, 634–8.

[24] Novoselov KS, Geim AK, Morozov SV, Jiang D, Zhang Y, Dubonos SV, et al., Science, **2004**, 306, 666–9.

[25] R. Van Noorden, Nature, **2012**, 483**,** S32–S33.

[26] M. Thripuranthaka, D.J. Late, ACS Appl. Mater. Interf., **2014**, 6, 1158–63.

[27] B.K. Miremadi, S.R. Morrison. J. Catal., **1987**, 103, 334–45.

[28] D. Pacile, J.C. Meyer, C.O. Girit, A. Zettl, Appl. Phys. Lett., **2008**, 92, 133107.

[29] J. N. Coleman et al., Science, **2011**, 331, 568–571.

[30] V. Nicolosi, M. Chhowalla, M.G. Kanatzidis, M. S. Strano, J. N. Coleman, Science, **2013**, 340, 1226419.

[31] A. Jawaid, D. Nepal, K. Park, M. Jespersen, A. Qualley, P. Mirau, L.F. Drummy, R.A. Vaia, Chem. Mater., **2016**, 28, 337–348.

[32] S. Yang, Y. Gong, J. Zhang, L. Zhan, L. Ma, Z. Fang, R. Vajtai, X. Wang and P. M. Ajayan, Adv. Mater., **2013**, 25, 2452–2456.

[33] Y. Yan, X. Ge, Z. Liu, J. –Y. Wang, J. –M. Lee, X. Wang, Nanoscale, **2013**, 5, 7768–7771.

[34] M. Osada, T. Sasaki, J. Mater. Chem., **2009**, 19, 2503–11.

[35] L. Hu, R. Ma, T.C. Ozawa, T. Sasaki, Chem. Asian J., **2010**, 5, 248–51.

[36] T. Sasaki, M. Watanabe, H. Hashizume, H. Yamada, H. Nakazawa, J. Am. Chem. Soc., **1996**, 118, 8329.

[37] J.N. Coleman, M. Lotya, A. O'Neill, S.D. Bergin, P.J. King, U. Khan et al., Science, **2011**, 331, 568–71.

[38] J.N. Coleman, Acc. Chem. Res., **2013**, 46, 14–22.

[39] C.Y. Zhi, Y. Bando, C.C. Tang, H. Kuwahara, D. Golberg, Adv. Mater., **2009**, 21, 2889–93.

[40] J. Feng, L. Peng, C. Wu, X. Sun, S. Hu, C. Lin et al., Adv. Mater., **2012**, 24, 1969–74.

[41] A. O'Neill, U. Khan, J.N. Coleman, Chem. Mater., **2012**, 24, 2414–21.

[42] Y. Peng, Z. Meng, C. Zhong, J. Lu, W. Yu,Y. Jia et al., Chem. Lett., **2001**, 30, 772–3.

[43] K. Chang et al., J. Mater. Chem., **2011**, 21, 6251.

[44] X.D. Xu et al. J. Mater. Chem. A, **2013**, 1, 14548.

[45] K. Chang, et al. J. Power Sources, **2012**, 201, 259.

[46] H. Pan, Y.W. Zhang, J. Phys. Chem. C, **2012**, 116, 11752–11757.

[47] E. Benavente, M. Santa Ana, F. Mendizábal, G. González, Coord. Chem. Rev., **2002**, 224, 87–109.

[48] Z. He, W. Que, Appl. Mater. Today, **2016**, 3, 23–56.

[49] K. F. Mak, C. Lee, J. Hone, J. Shan, T. F. Heinz, Phys. Rev. Lett., **2010**, 105, 136805–136808.

[50] B. Radisavljevic, A. Radenovic, J. Brivio, V. Giacometti, A. Kis, Nat. Nanotechnol., **2011**, 6, 147–150.

[51] C. Ling, Y. Ouyang, L. Shi, S. Yuan, Q. Chen, J. Wang, ACS Catal., **2017**, 7, 5097–5102.

[52] A.Y. Liu, M.L. Cohen, Science, **1989**, 245, 841−842.

[53] J.J. Zhu, Y.C. Wei, W.K. Chen, Z. Zhao, A. Thomas, Chem. Commun., **2010**, 46, 6965−6967.

[54] X. C. Wang, K. Maeda, A. Thomas, K. Takanabe, G. Xin, J.M. Carlsson, K. Domen, M. Antonietti, Nat. Mater., **2009**, 8, 76−80.

[55] P. Zhou, J.G. Yu, M. Jaroniec, Adv. Mater., **2014**, 26, 4920.

[56] X. Wang, K. Maeda, A. Thomas, K. Takanabe, G. Xin, J.M. Carlsson, K. Domen, M. Antonietti, Nat. Mater., **2009**, 8, 76−80.

[57] A. Walsh, S.M. Woodley, Phys. Chem. Chem. Phys., **2010**, 12.

[58] L.E. Burton, D. Colombara, R.D. Abellon, F.C. Grozema, L.M. Peter, T.J. Savenije, G. Dennler, A. Walsh, Chem. Mater., **2013**, 25, 4908−4916.

[59] D. Avellaneda, M.T.S. Nair, P.K. Nair, J. Electrochem. Soc., **2008**, 155, D517–D525.

[60] H. Noguchi, A. Setiyadi, H. Tanamura, T. Nagatomo, O. Omoto, Sol. Energy Mater. Sol. Cells, **1994**, 35, 325–331.

[61] W. Albers, C. Haas, F. Van der Maesen, **1960**, 15, 306–310.

[62] W. Albers, C. Haas, H.J. Vinx, J.D. Wasscher, J. Appl. Phys., **1961**, 32, 2220.

[63] J.M. Gonzalez, J. Chem. Phys., **2018**, 148, 194701.

[64] Y. Huang, E. Sutter, J. T. Sadowski, M. Cotlet, O. L. A. Monti, D. A. Racke, M. R. Neupane, D. Wickramaratne, R. K. Lake, B. A. Parkinson, and P. Sutter, ACS Nano, **2014**, 8, 10743.

[65] B. Palosz, E. Salje, J. Appl. Crystallogr., **1989**, 22, 622.

[66] Y. Liu, G. Qiu, D. Kong, B. Hu, Y. Li, J. Su, C. Xia, Superlattices and Microstructures, **2017**, 111, 480–486.

[67] F. Wang et al., Nano Lett., **2015**, 15, 7558–7566.

[68] Sneha Sinha et al., Materials Today: Proceedings, **2020**, 21, 1840–1845.

[69] L. Ma et al., J. Power Sources, **2015**, 285, 274–280.

[70] L. Ge, C. Han, X. Xiao, L. Guo, Int. J. Hydrogen Energy, **2013**, 38, 6960–6969.

[71] M. Wu, L. Li, Y. Xue, G. Xu, L. Tang, N. Liu, W. Huang, Appl. Catal. B: Environ., **2018**, 228, 103–112.

[72] M.R. Hoffmann, S.T. Martin, W. Choi, D.W. Bahnemann, Chem. Rev., **1995**, 95, 69.

[73] Y. Cui, Z. Ding, P. Liu, M. Antonietti, X. Fu, X. Wang, Phys. Chem. Chem. Phys., **2012**, 14, 1455−1462.

[74] J. Liu, Y. Zhang, L. Lu, G. Wu, W. Chen, Chem. Commun., **2012**, 48, 8826−8828.

[75] J. Mao, T. Peng, X. Zhang, K. Li, L. Ye, L. Zan, Catal. Sci. Technol., **2013**, 3, 1253−1260.

[76] S. Ghosh, John Wiley & Sons, **2018**.

[77] O. Ola, M.M. Maroto–Valer, Journal of Photochemistry and Photobiology C: Photochemistry Reviews, **2015**, 24, 16–42.

[78] J.Li, N. Wu, Catal. Sci. Technol., **2015**, 5, 1360–1384.

[79] See, e g., D. V.. Lang, in Roditttiott sects itt Semiconductors, Vol. 31 of Institute of Physics Conference Series, IOD, London, 70, **1976**.

[80] X. Q. Chen, D. H. Deng, X.L. Pan, Y. F. Hu, X.H. Bao, Chem. Commun., **2015**, 51, 217–220.

[81] A.K. Geim, I.V. Grigorieva, Nature, **2013**, 499, 419–425.

[82] Z. Zou, J. Ye, K. Sayama, H. Arakawa, Nature, **2001**, 414, 625– 627.

[83] M. W. Kanan, D. G. Nocera, Science, **2008**, 321, 1072 –1075.

[84] P. Kuang, M. Sayed, J. Fan, B. Cheng, J. Yu, Adv. Energy Mater., **2020**, 10, 1903802.

[85] E. Pulido Melian, O. Gonzalez Dıaz, A. Ortega Mendez, R. Lopez Cristina, M. Nereida Suarez, J.M. Dona Rodrıguez et al., Int. J. Hydrogen Energy, **2012**.

[86] C.H. Liao, C.W. Huang, C.S. Wu Jeffrey, Catalysts, **2012**, 490–516.

[87] J.S. Jang, H.G. Kim, J.S. Lee, Catal. Today, **2012**, 185, 270–7.

[88] A. Fujishima, K. Honda, Nature, **1972**, 238, 37–38.

[89] J. Yang, D. Wang, H. Han and C. Li, Acc. Chem. Res., **2013**, 46, 1900–1909.

[90] M.R. Hoffmann, S.T. Martin, W. Choi, D.W. Bahnemann, Chem. Rev., **1995**, 95, 69–94.

[91] J. Wang, T. van Ree, Y. Wu, P. Zhang, L. Gao, Metal Oxides, Metal Oxides in Energy Technologies, Elsevier, **2018**, 205–249.

[92] X. Li, J. Yu, J. Low, Y. Fang, J. Xiao and X. Chen, J. Mater. Chem. A, **2015**, 3, 2485–2534

[93] X. Duan, C. Wang, A. Pan, R. Yu, X. Duan, Chem. Soc. Rev., **2015**, 44, 8859–8876.

[94] M. Acerce, D. Voiry, M. Chhowalla, Nat. Nanotechnol., **2015**, 10, 313–318.

[95] K. F. Mak, C. Lee, J. Hone, J. Shan, T. F. Heinz, Phys. Rev. Lett., **2010**, 105, 136805–136808.

[96] S. Kim, A. Konar, W. S. Hwang, J. H. Lee, J. Lee, J. Yang, C. Jung, H. Kim, J. B. Yoo, J. Y. Choi, Y. W. Jin, S.Y. Lee, D. Jena, W. Choi, K. Kim, Nat. Commun., **2012**, 3, 1011–1017.

[97] H. Yu, R. Yuan, D. Gao, Y. Xu, J. Yu, Chem. Eng. J., **2019**, 375, 121934.

[98] L. Wang, X. Liu, J. Luo, X. Duan, J. Crittenden, C. Liu, S. Zhang, Y. Pei, Y. Zeng, X. Duan, Angew. Chem. Int. Ed., **2017**, 129, 7718–7722.

[99] Y. C. Kim, V. T. Nguyen, S. Lee, J.–Y. Park, Y. H. Ahn, ACS Appl. Mater. Interfaces, **2018**, 10, 5771–5778.

[100] K. Wang, Q. Li, B.S. Liu, B. Cheng, W. Ho, J. G. Yu, Appl. Catal. B: Environ., **2015**, 176–177, 44–52.

[101] H. Zhao, Y. Dong, P. Jiang, H. Miao, G. Wang, J. Zhang, J. Mater. Chem. A, **2015**, 3, 7375–7381.

[102] L. Ye, D. Wang, S. Chen, ACS Appl. Mater. Interfaces, **2016**, 8, 5280–5289.

[103] M. Li, L. Zhang, X. Fan, M. Wu, Y. Du, M. Wang, Q. Kong, L. Zhang, J. Shi, Appl. Catal. B: Environ., **2016**, 190, 36–43.

[104] Y. Hou, A. Laursen, J. Zhang, G. Zhang, Y. Zhu, X. Wang, S. Dahl, I. Chorkendorff, Angew. Chem., Int. Ed., **2013**, 52, 3621–3625.

[105] H. Xu, J. Yi, X. She, Q. Liuc, L. Song, S. Chen, Y. Yang, Y. Song, R. Vajtai, J. Lou, H. Li, S. Yuan, J. Wue, P.M. Ajayan, Appl. Catal. B: Environ., **2018**, 220, 379–385.

[106] D. Lu, H. Wang, X. Zhao, K. K. Kondamareddy, J. Ding, C. Li, P. Fang, ACS Sustainable Chem. Eng., **2017**, 5, 1436–1445.

[107] F. Fu, Q. Wang, J. Environ. Manag., **2011**, 92, 407–418.

[108] P.M. Fernández, M.E. Cabral, O.D. Delgado, J.I. Fariña, L.I.C. Figueroa, Int. Biodeterior. Biodegrad., **2013**, 79, 28–35.

[109] K.P. Lee, C.E. Ulrich, R.G. Geil, H.J. Trochimowicz, Sci. Total Environ., **1989**, 86, 83–108.

[110] A. Zhitkovich, Chem. Res. Toxicol., 2011, 24, 1617–1629.

[111] J. Nriagu, E. Nieboer, Wiley Series, New York, **1988**.

[112] N. Takeno, Atlas of Eh-pH diagrams, National Institute of Advanced Industrial Science and Technology, Japan, **2005**.

[113] L. Dupont, E. Guillon, Environ. Sci. Technol., **2003**, 37, 4235–4241.

[114] L. Levankumar, V. Muthukumaran and M. B. Gobinath, J. Hazard. Mater., **2009**, 161, 709–713.

[115] International Agency for Research on Cancer, **1990**, 49, 49–256, World Health Organization, Lyon, France.

[116] C.E. Barrera-Diaz, V. Lugo-Lugo, B. Bilyeu, J. Hazard. Mater., **2012**, 223–224, 1–12.

[117] B.A. Marinho, R.O. Cristóvão, R.A.R. Boaventura, V.J.P. Vilar, Environ. Sci. Pollut. Res., **2019**, 26, 2203–2227.

[118] Y. Li, W. Cui, L. Liu, R. Zong, W. Yao, Y. Liang, Y. Zhu, Appl. Catal. B: Environ., **2016**, 199, 412–423.

[119] Z. Wan, G. Zhang, X. Wu, S. Yin, Appl. Catal. B: Environ., **2017**, 207, 17–26.

[120] Y.C. Zhang, J. Li, M. Zhang, D.D. Dionysiou, Environ. Sci. Technol., **2011**, 45, 9324–9331.

[121] S. Wang, Z. Wang, W. Zhuang, Appl. Catal. B: Environ., **1992**, 1, 257–270.

[122] Y. Pang, L. Kong, D. Chen, G. Yuvaraja, Appl. Surf. Sci., **2019**, 471, 408–416.

[123] Y. Li, W. Cui, L. Liu, R. Zong, W. Yao, Y. Liang, Y. Zhu, Appl. Catal. B: Environ., **2016**, 199, 412–423.

[124] Y. Pang, L. Kong, D. Chen, G. Yuvaraja, Appl. Surf. Sci., **2019**, 471, 408–416.

[125] S. Polisetti, P.A. Deshpande, G. Madras, Ind. Eng. Chem. Res., **2011**, 50, 12915–12924.

[126] Zhu, M., Liu, Q., Chen, W., Yin, Y., Ge, L., Li, H., Wang, K., ACS Appl. Mater. Interfaces, **2017**, 9 (44), 38832–38841.

[127] Y. Yang, G. Wang, Q. Deng, D.H. Ng, H. Zhao, Acs. Appl. Mater. Inter., **2014**, 6, 3008–3015.

[128] A. Zhu, L. Qiao, P. Tan, J. Pan, Inorg. Chem. Front., **2020**, 7, 4754–4793.

[129] R. Malik, V.K. Tomer, Renew. Sustain. Energy Rev., **2021**, 135, 110235.

[130] K. Maeda, X. Wang, Y. Nishihara, D. Lu, M. Antonietti, K. Domen, J. Phys. Chem. C, **2009**, 113, 4940–4947.

[131] J. Yan, Z. Chen, H. Ji, Z. Liu, X. Wang, Y. Xu, X. She, L. Huang, L. Xu, H. Xu, H. Li, Chem. Eur. J., **2016**, 22, 4764–4773.

[132] H. Jin, C. Guo, X. Liu, J. Liu, A. Vasileff, Y. Jiao, Y. Zheng, S. Z. Qiao, Chem. Rev., **2018**, 118, 6337–6408.

[133] K. F. Mak, C. Lee, J. Hone, J. Shan, T. F. Heinz, Phys. Rev. Lett., **2010**, 105, 136805.

[134] T. F. Jaramillo, K. P. Jørgensen, J. Bonde, J. H. Nielsen, S. Horch, I. Chorkendorff, Science, **2007**, 317, 100–102.

[135] H. Qiu, T. Xu, Z. Wang, W. Ren, H. Nan, Z. Ni, Q. Chen, S. Yuan, F. Miao, F. Song, G. Long, Y. Shi, L. Sun, J. Wang, X. Wang, Nat. Commun., **2013**, 4, 2642.

[136] L. Wang, X. Liu, J. Luo, X. Duan, J. Crittenden, C. Liu, S. Zhang, Y. Pei, Y. Zeng, X. Duan, Angew. Chem. Int. Ed., **2017**, 129, 7718–7722.

[137] Q. H. Wang, K. Kalantar-Zadeh, A. Kis, J. N. Coleman, M. S. Strano, Nat. Nanotech., **2012**, 7, 699–712.

[138] M. L. Tsai, S. H. Su, J. K. Chang, D. S. Tsai, C. H. Chen, C. I. Wu, L. J. Li, L. J. Chen, J. H. He, ACS Nano, **2014**, 8, 8317–8322.

[139] A. Gupta, V. Arunachalam, S. Vasudevan, J. Phys. Chem. Lett., **2016**, 7, 4884–4890.

[140] A. Ambrosi, M. Pumera, Chem. Soc. Rev., **2018**, 47, 7213–7224.

[141] X. Zhang, Z. Lai, C. Tan, H. Zhang, Angew. Chem. Int. Ed., **2016**, 55, 8816–8838.

[142] Y.C.Zhang, Z.N.Du, S.Y.Li, M.Zhang, Appl.Catal.B:Environ., **2010**, 95, 153–159.

[143] J. Li, X. H. Du, L. Yao and Y. C. Zhang, Mater. Lett., **2014**, 121, 44.

[144] J. Liu, G. Huang, W. Huang, Mater. Lett., **2015**, 161, 480–483.

[145] X. Li, J. Zhu, H. Li, Appl. Catal. B, **2012**, 123–124, 174–181.

[146] R. Wei, J. Hu, T. Zhou, Acta Mater., **2014**, 66, 163–171.

[147] L. Deng, Z. Zhu, L. Liu, H. Liu, Solid State Sci., **2017**, 63, 76–83.

[148] Q. Xie, H. Zhou, Z. Lv, H. Liu, H. Guo, J. Mater. Chem. A, **2017**, 5, 6299–6309.

[149] Y. Yang, X.A. Yang, D. Leng, S.B. Wang, W.B. Zhang, Chemical Engineering Journal, **2018**, 335, 491–500.

[150] Maeda K., Wang X., Nishihara Y., Lu D., Antonietti M., Domen K., J. Phys. Chem. C, **2009**, 113, 4940−4947.

[151] S. Pathan, A. Patel, Dalton Trans., **2011**, 40, 348 –355.

[152] P. Kubelka, J. Opt. Soc. Am., **1948**, 38, 448–457.

[153] J. Tauc in Amorphous and Liquid Semiconductors, Plenum Press, New York, **1974**.

[154] G. Kresse, J. Hafner, Phys. Rev. B, **1993**, 47, 558.

[155] P. E. Blöchl, Phys. Rev. B, **1994**, 50, 17953.

[156] P. Perdew, K. Burke, M. Ernzerhof, Phys. Rev. Lett., **1996**, 77, 3865.

[157] E.D. Koutsouroubi, I. Vamvasakis, I.T. Papadas, C. Drivas, S.A. Choulis, S. Kennou, G.S. Armatas, ChemPlusChem, **2020**, 85, 1379–1388.

[158] H. Ou, L. Lin, Y. Zheng, P. Yang, Y. Fang, X. Wang, Adv. Mater., **2017**, 29, 1700008.

[159] Y. Yin, J. Han, Y. Zhang, X. Zhang, P. Xu, Q. Yuan, L. Samad, X. Wang, Y. Wang, Z. Zhang, P. Zhang, X. Cao, B. Song, S. Jin, J. Am. Chem. Soc., **2016**, 138, 7965–7972.

[160] D. Kong, H. Wang, J. J. Cha, M. Pasta, K. J. Koski, J. Yao, Y. Cui, Nano Lett., **2013**, 13, 1341–1347.

[161] S. Yang, Y. Gong, J. Zhang, L. Zhan, L. Ma, Z. Fang, R. Vajtai, X. Wang, P. Ajayan, Adv. Mater. **2013**, 25, 2452–2456.

[162] H. Tributsch, J. C. Bennett, J. Electroanal. Chem., **1977**, 81, 97–111.

[163] J. Xie, J. Zhang, S. Li, F. Grote, X. Zhang, H. Zhang, R. Wang, Y. Lei, B. Pan, Y. Xie, J. Am. Chem. Soc. **2013**, 135, 17881–17888.

[164] J. S. Zhang, F. S. Guo, X. C. Wang, Adv. Funct. Mater., **2013**, 23, 3008−3014.

[165] H. Bian, Y. Ji, J. Yan, P. Li, L. Li, Y. Li, S. Liu, Small, **2018**, 14, 1703003.

[166] a) E. G. Gillan, Chem. Mater., **2000**, 12, 3906. b) Q. Guo, Y. Xie, X. Wang, S. Zhang, T. S. Hou, Chem. Commun., **2004**, 26.

[167] F. Rouquerol, J. Rouquerol, K. S. W., Academic Press, London, **1999**, 191–218.

[168] a) D. Marton, K. J. Boyd, A. H. Al-Bayati, S. S. Todorov, J. W. Rabalais, Phys. Rev. Lett., **1994**, 73, 118–121. b) J. R. Shi, Y. J. Xu, J. Zhang, Thin Solid Films, **2005**, 483, 169–174.

[169] M. Tabbal, P. Mérel, S. Moisa, M. Chaker, E. Gat, A. Ricard, M. Moisan, S. Gujrathi, Surf. Coat. Technol., **1998**, 98, 1092–1096.

[170] N. Y. Cui, N. M. D. Brown, A. McKinley, Appl. Surf. Sci., **1999**, 151, 17–28.

[171] S. Haldar, H. Vovusha, M.K. Yadav, O. Eriksson, B. Sanyal, Phys. Rev. B: Condens. Matter Mater. Phys., **2015**, 92, 1–12.

[172] P. A. Spevack, N. S. McIntyre, J. Phys. Chem., **1993**, 97, 11031–11036.

[173] Y. H. Chang, C. T. Lin, T. Y. Chen, C. L. Hsu, Y. H. Lee, W. Zhang, K. H. Wei, L. J. Li, Adv. Mater., **2013**, 25, 756–760.

[174] P. A. Spevack, N. S. McIntyre, J. Phys. Chem., **1993**, 97, 11031–11036.

[175] J. Bisquert, H. Randriamahazaka, G. Garcia-Belmonte, Electrochim. Acta, **2005**, 51, 627–640.

[176] T. F. Jaramillo, K. P. Jørgensen, J. Bonde, J. H. Nielsen, S. Horch, I. Chorkendorff, Science, **2007**, 317, 100–102.

[177] J. Zhang, J. Wu, H. Guo, W. Chen, J. Yuan, U. Martinez, G. Gupta, A. Mohite, P. M. Ajayan, J. Lou, Adv. Mater., **2017**, 29, 1701955.

[178] a) H. Liu, N. Han, J. Zhao, RSC Adv., **2015**, 5, 17572–17581. b) J. Martincov, M. Otyepka, P. Lazar, Chem. Eur. J., **2017**, 23, 13233–13239.

[179] E. D. Koutsouroubi, I. Vamvasakis, M. G. Minotaki, I. T. Papadas, Ch. Drivas, S. A. Choulis, G. Kopidakis, S. Kennou, G. S. Armatas, Appl. Catal. B: Environ., **2021**, 297, 120419.

[180] W. Fu, H. He, Z. Zhang, C. Wu, X. Wang, H. Wang, Q. Zeng, L. Sun, X. Wang, J. Zhou, Q. Fu, P. Yu, Z. Shen, C. Jin, B. I.Yakobson, Z. Liu, Nano Energy, **2016**, 27, 44–50.

[181] Y. Qi, Q. Liang, R. Lv, W. Shen, F. Kang, Z.-H. Huang, R. Soc. Open Sci., **2018**, 5, 180187.

[182] J. Zhang, F. Guo, X. Wang, Adv. Funct. Mater., **2013**, 23, 3008–3014.

[183] H. Bian, Y. Ji, J. Yan, P. Li, L. Li, Y. Li, S. Liu, Small, **2018**, 14, 1703003.

[184] V. N. Khabashesku, J. L. Zimmerman, J. L. Margrave, Chem. Mater., **2000**, 12, 3264–3270.

[185] G. Ye, Y. Gong, J. Lin, B. Li, Y. He, S. T. Pantelides, W. Zhou, R. Vajtai, P. M. Ajayan, Nano Lett., **2016**, 16, 1097–1103.

[186] Z. Qiao, L. Lin, X. Yan, W. Guo, Q. Chen, Q. Xie, X. Han, J. Lin, L. Wang, D. L. Peng, Chem. Asian J., **2020**, 15, 3620–3636.

[187] H. Ou, L. Lin, Y. Zheng, P. Yang, Y. Fang, X. Wang, Adv. Mater., **2017**, 29, 1700008.

[188] N. Y. Cui, N. M. D. Brown, A. McKinley, Appl. Surf. Sci., **1999**, 151, 17–28.

[189] S. Haldar, H. Vovusha, M. K. Yadav, O. Eriksson, B. Sanyal, Phys. Rev. B, **2015**, 92, 235408.

[190] P. A. Spevack, N. S. McIntyre, J. Phys. Chem., **1993**, 97, 11031–11036.

[191] A. Syariati, S. Kumar, A. Zahid, A. Ali El Yumin, J. Ye, P. Rudolf, Chem. Commun., **2019**, 55, 10384–10387.

[192] Y. H. Chang, C. T. Lin, T. Y. Chen, C. L. Hsu, Y. H. Lee, W. Zhang, K. H. Wei, L. J. Li, Adv. Mater., **2013**, 25, 756–760.

[193] F. Rouquerol, J. Rouquerol, K. S. W. Sing, Academic Press, London, UK, **1999**.

[194] B. Zhu, P. Xia, W. Ho, J. Yu, Appl. Sur. Sci., **2015**, 344, 188–195.

[195] S. Wang, Y. Wang, J. Wan, Y. Ma, Z. Yan, G. Zhang, Sep. Purif. Technol., **2020**, 253, 117486.

[196] H. Li, T. Wu, B. Cai, W. Ma, Y. Sun, S. Gan, D. Han, L. Niu, Appl. Catal. B: Environ., **2015**, 164, 344–351.

[197] Y. Liu, D. Yang, T. Xu, Y. Shi, L. Song, Z. Z. Yu, Chem. Engin. J., **2020**, 379, 122200.

[198] N. Nasrallah, M. Kebir, Z. Koudri, M. Trari, J. Hazard. Mater., **2011**, 185, 1398–1404.

[199] Y. Wang, Z. Cui, G. Xiao, Y. Zhao, Y. Jin, Z. Wang, H. Su, T. Tan, Sep. Purif. Technol., **2019**, 227, 115727.

[200] W. Zhao, J. Li, T. She, S. Ma, Z. Cheng, G. Wang, P. Zhao, W. Wei, D. Xia, D. Y. C. Leung, J. Hazard. Mater., **2021**, 402, 123839.

[201] G. Velegraki, I. Vamvasakis, I.T. Papadas, S. Tsatsos, A. Pournara, M. J. Manos, S. Choulis, S. Kennou, G. Kopidakis, G. S. Armatas, Inorg. Chem. Front., **2019**, 6, 765–774.

[202] G. Velegraki, J. Miao, C. Drivas, B. Liu, S. Kennou, G. S. Armatas, Appl. Catal. B: Environ., **2018**, 221, 635–644.

[203] A. Tanaka, K. Nakanishi, R. Hamada, K. Hashimoto, H. Kominami, ACS Catal., **2013**, 3, 1886–1891.

[204] Q. Meng, Y. Cai, B. Cong, W. Xing, G. Chen, Mater. Res. Bull., **2020**, 122, 110681.

[205] X. H. Yi, F. X. Wang, X. D. Du, P. Wang, C. C. Wang, Appl. Organomet. Chem. **2019**, 33, e4621.

[206] X. Hu, W. Wang, G. Xie, H. Wang, X. Tan, Q. Jin, D. Zhou, Y. Zhao, Chemosphere, **2019**, 216, 733–741.

[207] W. Huang, N. Liu, X. Zhang, M. Wu, L. Tang, Appl. Surf. Sci., **2017**, 425, 107–116.

[208] Q. Wang, P. Xu, G. Zhang, L. Hu, P. Wang, Appl. Surf. Sci., **2019**, 488, 360–369.

[209] M. Ye, W. Wei, L. Zheng, Y. Liu, D. Wu, X. Gu, A. Wei, J. Hazard. Mater., **2019**, 365, 674–683.

[210] S. Patnaik, K. K. Das, A. Mohanty, K. Parida, Catal. Today, **2018**, 315, 52–66.

[211] X. Wang, Y. Liang, W. An, J. Hu, Y. Zhu, W. Cui, Appl. Catal. B: Environ., **2017**, 219, 53–62.

[212] M. Wu, L. Li, Y. Xue, G. Xu, L. Tang, N. Liu, W. Huang, Appl. Catal. B: Environ., **2018**, 228, 103–112.

[213] K. Li, Z. Huang, S. Zhu, S. Luo, L. Yan, Y. Dai, Y. Guo, Y. Yang, Appl. Catal. B: Environ., **2019**, 243, 386–396.

[214] Z. Wang, M. Murugananthan, Y. Zhang, Appl. Catal. B: Environ., **2019**, 248, 349–356.

[215] X. H. Yi, S. G. Ma, X. D. Du, C. Zhao, H. Fu, P. Wang, C. C. Wang, Chem. Eng. J., **2019**, 375, 121944.

[216] B. Ou, J. Wang, Y. Wu, S. Zhao, Z. Wang, Chem. Eng. J., **2020**, 380, 122600.

[217] G. Li, Y. Wu, M. Zhang, B. Chu, W. Huang, M. Fan, L. Dong, B. Li, Ind. Eng. Chem. Res., **2019**, 58, 8979–8989.

[218] P. Babu, S. Mohanty, B. Naik, K. Parida, Inorg. Chem., **2019**, 58, 12480–12491.

[219] X. Wang, M. Hong, F. Zhang, Z. Zhuang, Y. Yu, ACS Sustainable Chem. Eng., **2016**, 4, 4055–4063.

[220] M. Sun, Q. Yan, T. Yan, M. Li, D. Wei, Z. Wang, Q. Wei, B. Du, RSC Adv., **2014**, 4, 31019–31027.

[221] S. Patnaik, G. Swain, K. M. Parida, Nanoscale, **2018**, 10, 5950–5964.

[222] X. Ding, D. Xiao, L. Ji, D. Jin, K. Dai, Z. Yang, S. Wang, H. Chen, Catal. Sci. Technol., **2018**, 8, 3484–3492.

[223] X. Zhao, Y. Zhang, Y. Zhao, H. Tan, Z. Zhao, H. Shi, E. Wang, Y. Li, Dalton Trans., **2019**, 48, 6484–6491.

[224] F. Liu, S. Dong, Z. Zhang, X. Li, X. Dai, Y. Xin, X. Wang, K. Liu, Z. Yuan, Z. Zheng, RSC Adv., **2019**, 9, 25750–25761.

[225] J. Qiu, P. Fan, C. Yue, F. Liu, A. Li, J. Mater. Chem. A, **2019**, 7, 7053–7064.

[226] Z. D. Lei, Y. C. Xue, W. Q. Chen, L. Li, W. H. Qiu, Y. Zhang, L. Tang, Small, **2018**, 14, 1802045.

[227] S. Li, Z. Hu, S. Xie, H. Liu, J. Liu, Int. J. Electrochem. Sci., **2018**, 13, 655–663.

[228] N. Adhoum, L. Monser, N. Bellakhal, J. E. Belgaied, J. Hazard. Mater., **2004**, 112, 207–213.

[229] R. Djellabi, M. F. Ghorab, Desalin. Water Treat., **2015**, 55, 1900–1907.

[230] R. A. Burns, J. C. Crittenden, D. W. Hand, V. H. Selzer, L. L. Sutter, S. R. Salman, J. Environ. Eng., **1999**, 125, 77–85.

[231] A. Tanaka, K. Nakanishi, R. Hamada, K. Hashimoto, H. Kominami, ACS Catal., **2013**, 3, 1886–1891.

[232] Y. Nakabayashi, Y. Nosaka, J. Phys. Chem. C, **2013**, 117, 23832–23839.

[233] Y. Zhang, H. Zhang, A. Liu, C. Chen, W. Song, J. Zhao, J. Am. Chem. Soc., **2018**, 140, 3264–3269.

[234] R. Kuriki, T. Ichibha, K. Hongo, D. Lu, R. Maezono, H. Kageyama, O. Ishitani, K. Oka, K. Maeda, J. Am. Chem. Soc., **2018**, 140, 6648–6655.

[235] J. Bisquert, H. Randriamahazaka, G. Garcia-Belmonte, Electrochim. Acta, **2005**, 51, 627–640.

[236] D.A. Harrington, P. Van den Driessche, Electrochim. Acta, 2011, 56, 8005–8013.

[237] A. Zaban, M. Greenshtein, J. Bisquert, ChemPhysChem, **2003**, 4, 859–864.

[238] H. He, F. Ren, J. Zhu, Y. Xiang, B. Zheng, S. Li, S. Chen, Y. Li, Q.H. Wu, Y. Yang, Nano Energy, **2020**, 72, 104679.

[239] H. Wang, X. Yuan, Y. Wu, X. Chen, L. Leng, G. Zeng, RSC Adv., **2015**, 5, 32531–32535.

[240] M. Fujii, K. Nagasuna, M. Fujishima, T. Akita, H. Tada, J. Phys. Chem. C, **2009**, 113, 16711–16716.

[241] J. Zhang, F. Guo, X. Wang, Adv. Funct. Mater., **2013**, 23, 3008−3014.

[242] Y. Zhang, J. Liu, G. Wu and W. Chen, Nanoscale, **2012**, 4, 5300–5303.

[243] D. Marton, K.J. Boyd, A.H. Al-Bayati, S.S. Todorov, J.W. Rabalais, Phys. Rev. Lett., **1994**, 73, 118–121.

[244] J.R. Shi, Y.J. Xu, J. Zhang, Thin Solid Films, **2005**, 483, 169–174.

[245] M. Tabbal, P. Mérel, S. Moisa, M. Chaker, E. Gat, A. Ricard, M. Moisan, S. Gujrathi, Surf. Coat. Technol., **1998**, 98, 1092–1096.

[246] F.S. Ohuchi, W. Jaegermann, B.A. Parkinson, Surf. Sci., **1988**, 194, L69–L76.

[247] Y.C. Zhang, J. Li, M. Zhang, D.D. Dionysiou, Environ. Sci. Technol., **2011**, 45, 9324–9331.

[248] A. Zhitkovich, Chem. Res. Toxicol., **2011**, 24, 1617–1629.

[249] B. Zhu, P. Xia, W. Ho, J. Yu, Appl. Sur. Sci., **2015**, 344, 188–195.

[250] S. Wang, Y. Wang, J. Wan, Y. Ma, Z. Yan, G. Zhang, Sep. Purif. Technol., **2020**, 253, 117486.

[251] H. Li, T. Wu, B. Cai, W. Ma, Y. Sun, S. Gan, D. Han, L. Niu, Appl. Catal. B: Environ., **2015**, 164, 344–351.

[252] Y. Liu, D. Yang, T. Xu, Y. Shi, L. Song, Z. Z. Yu, Chem. Engin. J., **2020**, 379, 122200.

[253] N. Nasrallah, M. Kebir, Z. Koudri, M. Trari, J. Hazard. Mater., **2011**, 185, 1398–1404.

[254] Y. Wang, Z. Cui, G. Xiao, Y. Zhao, Y. Jin, Z. Wang, H. Su, T. Tan, Sep. Purif. Technol., **2019**, 227, 115727.

[255] W. Zhao, J. Li, T. She, S. Ma, Z. Cheng, G. Wang, P. Zhao, W. Wei, D. Xia, D. Y. C. Leung, J. Hazard. Mater., **2021**, 402, 123839.

[256] E. D. Koutsouroubi, I. Vamvasakis, M. G. Minotaki, I. T. Papadas, Ch. Drivas, S. A. Choulis, G. Kopidakis, S. Kennou, G. S. Armatas, Appl. Catal. B: Environ., **2021**, 297, 120419.

[257] G. Velegraki, I. Vamvasakis, I.T. Papadas, S. Tsatsos, A. Pournara, M. J. Manos, S. Choulis, S. Kennou, G. Kopidakis, G. S. Armatas, Inorg. Chem. Front., **2019**, 6, 765–774.

[258] G. Velegraki, J. Miao, C. Drivas, B. Liu, S. Kennou, G. S. Armatas, Appl. Catal. B: Environ., **2018**, 221**,** 635–644.

[259] A. Tanaka, K. Nakanishi, R. Hamada, K. Hashimoto, H. Kominami, ACS Catal., **2013**, 3, 1886–1891.

[260] S. Li, Z. Hu, S. Xie, H. Liu, J. Liu, Int. J. Electrochem. Sci., **2018**, 13, 655–663.

[261] N. Adhoum, L. Monser, N. Bellakhal, J.E. Belgaied, J. Hazard. Mater., **2004**, 112, 207–213.

[262] R. Djellabi, M.F. Ghorab, Desalin. Water Treat., **2015**, 55, 1900–1907.

[263] R.A. Burns, J.C. Crittenden, D.W. Hand, V.H. Selzer, L.L. Sutter, S.R. Salman, J. Environ. Eng., **1999**, 125, 77–85.

[264] H. Li, H. Yu, X. Quan, S. Chen, Y. Zhang, ACS Appl. Mater. Interfaces, **2016**, 8, 2111–2119.

[265] C. Gong, H. Zhang, W. Wang, L. Colombo, R. M. Wallace, K. Cho, Appl. Phys. Lett., **2013**, 103, 053513.

[266] J.J. Kelly, D. Vanmaekelbergh, Electrochim. Acta, **1998**, 43, 2773–2780.

[267] A. Zaban, M. Greenshtein, J. Bisquert, ChemPhysChem, **2003**, 4, 859–864.

[268] P.C. Huang, Y.M. Shen, S. Brahma, M.O. Shaikh, J.L. Huang, S.C. Wang, Catalysts, **2017**, 7, 252.

[269] L. A. Burton, T. J. Whittles, D. Hesp, W. M. Linhart, J. M. Skelton, B. Hou, R. F. Webster, G. O'Dowd, C. Reece, D. Cherns, D. J. Fermin, T. D. Veal, V. R. Dhanak, A. Walsh, J. Mater. Chem. A, **2016**, 4, 1312–1318.